Università degli Studi di Milano

Doctoral Thesis

Emergent phenomena in condensed matter, soft matter and complex systems

---

Settore Scientifico Disciplinare FIS/03

Author:
Francesco Mambretti

Supervisor:
Prof. Davide Emilio Galli

February 25, 2021

"*Quel che mi piace dell'esperienza è che si tratta di una cosa così onesta. Potete fare un mucchio di svolte sbagliate; ma tenete gli occhi aperti e non vi sarà permesso di spingervi troppo lontano prima che appaia il cartello giusto. Potete aver ingannato voi stessi, ma l'esperienza non sta cercando di ingannarvi. L'universo risponde il vero . . . "*

Clive Staples Lewis

"*Non c'è niente di meglio di una tazza di caffè per stimolare il cervello."*

Sherlock Holmes

"*Se tutte le volte che ho guardato il cielo, il cielo ha guardato me, io sono un uomo benedetto."*

Davide Van De Sfroos

UNIVERSITÀ DEGLI STUDI DI MILANO

Abstract

Facoltà di Scienze e Tecnologie
Dipartimento di Fisica "Aldo Pontremoli"

Doctor of Philosophy

Emergent phenomena in condensed matter, soft matter and complex systems

by Francesco Mambretti

Physical systems composed of a large number of reciprocally interacting constituents provide the natural context for the rise of *emergent phenomena*. Despite the intrinsic difficulty in providing a mathematical definition of what is meant for 'emergence' (see [Baas, in Langton, Alife III, Santa Fe Studies in the Sciences of Complexity, Proc. Volume XVII, Addison-Wesley, (1994)]), the intuitive notion of emergent property is that of a collection of interacting objects showing a novel collective behavior, qualitatively different from and not immediately attributable to the behaviors of the individual components. Non-linear interactions among elements of the system, or interactions between the system and the environment, or merely the large number of constituents are usually the motivations addressed to be responsible for emergent behavior. It is important to remark that emergent properties can only be inferred from a comprehension of the collective properties of the microscopic constituents [Kivelson *et al*, npj Quant. Mater. 1, 16024 (2016)].

In this regard, computer simulations provide a unique tool to support experimental observation, develop abstract models and investigate systems properties at a microscopic level. In general, condensed matter, particularly soft matter but also the complex systems studied in Physics, are necessarily described via simplified models, which include the key features of the corresponding real systems. On the one hand, this certainly represents a powerful approach when it finds its roots in the concept of universality, connected with critical phenomena, but this also turns into a limiting factor for the realistic description of the considered phenomena. On the other hand,it makes the properties of such abstract simulated systems calculable and investigable via computer simulations. As a consequence, the simulations assume a key role in complementing the comparison between experiments and theory [Frenkel and Smit, *Understanding Molecular Simulations*, Academic Press (2002); Allen and Tildesley, *Computer simulation of liquids*, Oxford University Press (2017)]. In this sense, simulations are often regarded as being *computer experiments*, in which materials properties and novel phases of matter can be investigated.

The present PhD thesis is a collection of the main results coming from four different research lines which I have been involved into in the last 3 years. The topics could appear to be rather diverse but they are all connected by the presence of emergent phenomena which were studied via computer simulations (Molecular Dynamics and Monte Carlo methods, mainly). Three of these four research lines are related to collaborations with as many experimental groups. The first group I started collaborating with is led by dr. R. Grisenti, at the University of Frankfurt (`https://www.atom.uni-frankfurt.de/hhng-grisenti/index.html`). As reported in Chapter 1 and in a recent paper which I contributed to as first co-author [Schottelius, Mambretti *et al.*, Nat. Mat. (2020)], we studied the **crystal growth**

of supercooled Ar–Kr liquid mixtures by means of a micro–jet experiment, Molecular Dynamics simulation and thermodynamic analysis. The second ongoing collaboration is with the group of prof. P. Milani, which is the leader of the CIMaINa laboratories (http://cimaina.unimi.it/) at the Università degli Studi di Milano. We developed an abstract stochastic model of resistive switching devices that they are characterizing for neuromorphic applications (see Chapter 3). More recently, I started a collaboration with the group led by prof. T. Bellini at the Università degli Studi di Milano (https://sites.google.com/site/unimisoft/), in order to investigate the spinodal decomposition of mixtures of DNA nanostars via light scattering experiments and Monte Carlo simulations, as described in Chapter 4. I will now provide a brief overview of the contents of each Chapter, where each Chapter corresponds to a different research line.

Crystal growth from a supercooled melt is of fundamental theoretical and practical importance in many fields, ranging from materials science to the production of phase–change memories. To date, the temperature dependence of the growth rates of many materials, including pure metals, metallic alloys, colloids and many others are still under intense scrutiny (see e.g. Tang *et al.*, Nat. Mat. (2013) and Sun *et al.*, Nat. Mat. (2018)). The majority of systems display a maximum growth rate at a temperature located between the melting point and the glass transition [Orava *et al.*, J. Chem. Phys. (2014)]. Several materials are characterized by a range of many orders of magnitude between this maximum value and the crystal growth rates measured in other regimes. We still lack a deep comprehension of the mechanism underlying this phenomenology, which emerges from experiments and simulations both. Classical models of crystal growth from a melt hypothesize either a diffusion–limited process, or a collision–limited one, but for a lot of materials them both fail to fit the available data. This situation claims for further investigation about the key elements that tune the crystal growth rates from supercooled liquids, extending the current theoretical framework. Jointly with the experimental group of dr. Grisenti (which performed measurements at the EU-XFEL facility https://www.xfel.eu/), we studied the crystallization of supercooled mixtures of argon and krypton via Molecular Dynamics. Our results showed that their crystal growth rates (obtained from the analysis of simulated configurations exploiting Steinhardt angular order parameters) can be reconciled with existing crystal growth models only by explicitly accounting for the non–ideality of the mixtures. Our theoretical and computational contribution aided in highlighting the importance of thermodynamic aspects in describing the crystal growth kinetics, yielding a substantial step towards a more sophisticated theory of crystal growth.

A second project concerns the study of **soft matter systems in one dimension** (1D), detailed in Chapter 2. Soft matter systems are made of particles which can overlap by paying a finite energy cost and they are renowned

for being able to display complex emerging phenomena. Some of them, for example, are characterized by the presence of clustering phases [Prestipino, Phys. Rev. E (2014)]. Recently, a surprising quantum phase transition has been revealed in a 1D system composed of bosons interacting via a pairwise soft potential in the continuum. It was shown that the spatial coordinates undergoing two-particle clustering could be mapped into quantum spin variables of a 1D transverse Ising model [Rossotti *et al.*, Phys. Rev. Lett. (2017)]. Extending the description and the results provided in a very recent paper I contributed to as first author [Mambretti *et al.*, Phys. Rev. E (2020)], in the second Chapter we investigate the manifestation of an analogous critical phenomenon in 1D classical fluids of soft particles in the continuum. In particular, we studied the low–temperature behavior of three different classical models of 1D soft matter, whose inter–particle interactions allow for clustering. The two–particle cluster phase is largely explored, by simulating the systems at the commensurate density via Monte Carlo and Simulated Annealing methods. The same string variables exploited in the aforementioned quantum case highlight that, at the right commensurate density, the peculiar pairing of neighboring soft particles can be nontrivially mapped onto a 1D discrete classical Ising model. We also observe a related phenomenon, i.e. the presence of an anomalous peak in the low–temperature specific heat, thus indicating the emergence of Schottky phenomenology in a non–magnetic fluid.

The third Chapter presents the case of an electrical resistor network featuring novel emergent properties, such as memristivity and the possibility to be used as a self–assembled logic gate; an article on this topic is currently in preparation. The growing difficulties arising in the improvement of the performance of standard computing architectures encouraged the quest for different approaches aiming at reproducing the computational capability and energy efficiency of the human brain, by mimicking neurons and synapses as probabilistic computing units [Marković *et al.*, Nat. Rev. Phys. 2, 499–510 (2020)]. Networks based on the bottom–up assembling of nanoscale building blocks and characterized by resistive switching (RS) activities are becoming increasingly popular as possible solutions for a straightforward fabrication of complex architectures with neuromorphic features [Wang *et al.*, Nat. Rev. Mat. 5, 173-195 (2020)]. Specifically, it has recently been demonstrated that metallic nanostructured Au films, under certain conditions show a non–ohmic electrical behavior and complex and reproducible resistive switching, which can be exploited for the innovative realization of logic gates. In these devices, the nonlinear dynamic switching behavior resulting from an applied input voltage can be exploited for developing hardware for reservoir computing applications. In Chapter 3, I show how it is possible to **simulate a complex model** (Stochastic Resistor Network Model, SRNM) able to imitate the phenomenology and give hints for the development of experiments

ongoing at the CIMaINa research laboratories, regarding the **electrical current passage through nanostructured cluster gold films** [Mirigliano *et al.*, Nanotechnology, 31, 23, (2020)]. To this purpose, I personally contributed to develop from scratch a `C++` code, parallelized via the Armadillo library (`http://arma.sourceforge.net/`). To study the electrical transport properties of this system, we modeled the experimental sample as a network of interconnected resistors whose effective resistance under a given voltage can be determined using spectral graph theory. The network state evolves stochastically via random physically–inspired update moves, and its effective total resistance (and the related Power Spectral Density) has been analyzed. The structure and the topology of the network were studied via the investigation of the shortest path connecting the source and the sink of the system, thus exploring the possible paths in which the current could flow. Moreover, we also applied Information Theory entropy–based tools to investigate the time evolution of network resistance at a local, coarse–grained, scale. We observed that specific input signals corresponding to 2 logical 'bits' produce rich outputs associable to a logical NAND gate, which posses functional completeness. Given that relevant differences could be detected between the behavior of the network at low voltage before and after the so called 'writing' step (where the system is under a high applied voltage), memristive effects naturally emerge in the study of network properties. These results encourage further investigations, both experimental and via the innovative SRNM approach we developed, in order to exploit these RS devices in hardware computing applications as self–assembled logic gates.

Last, in Chapter 4 I focus on another soft matter system, that I have started to investigate during my PhD research activity, regarding Monte Carlo simulations of **low valence DNA–based colloidal particles**. This last Chapter is mainly devoted to the description of the simulation method I have been developing during my more recent PhD research activities, while the preliminary results presented obviously need to be confirmed and extended by further studies. Particles with a limited number of attractive spots (patches) on their surface are generally characterized by non–crystalline low energy states; they rather generate a disordered 3D network in which all the sticky sites are engaged in (mutually exclusive) patch–patch bonds [Bianchi *et al.*, Phys. Rev. Lett. (2006)]. One of the most promising experimental realizations of such peculiar colloids is extremely recent: laboratory synthesized DNA nanostars (NS) with fixed valence [Biffi *et al.*, PNAS (2013)]. In this field the landmark is represented by our collaborators from the group led by prof. T. Bellini. Recently, they started to investigate the behavior of mixtures of nanostars with leftwise or rightwise chirality of the DNA strands, characterized by a merely repulsive interspecies interaction. To date, our contribution mainly consisted in the development of an abstract model of these DNA nanostars, schematized as limited valence soft patchy particles,

whose equilibrium configurations are sampled via a canonical Monte Carlo program. Their different chirality is represented by a mixed interaction which only comprises excluded volume terms. Our goal in this project is twofold: on the one hand, we aim to reconstruct the temperature–density phase diagram of such mixtures, also depending on the mixing ratio. Experiments revealed a critical behavior and a phase separation processes for dilute mono–component DNA solutions; the properties of a mixture of two components, each found in critical conditions, are studied in this work. In this Chapter, after a detailed overview of the experimental, computational and theoretical studies regarding low valence particles, the simulation code is described and it is presented a comparison between the simulation results and the experimental measurements at equilibrium. The peculiar structures found in the patchy particles network claim for further analysis, as well as the interesting behavior near the critical point for mono–component and bi–component systems both. The second perspective of this research regards the unexplored aggregation and cluster growth process of such particles. In this concern, part of the future research effort will be devoted to the transformation of our custom code into a Brownian Monte Carlo in order to unveil the mechanisms underlying the dynamics of such particles during their aggregation stages.

The conclusions and further perspectives concerning each of the four topics addressed in this work can be retrieved at the end of each Chapter.

Contents

Chapter 1

Crystal growth in supercooled Argon-Krypton liquids

1.1 Crystal growth in supercooled liquids: motivation

Crystal growth from a supercooled melt is a extremely relevant process in materials science, providing the primary route for the realization of a wide range of new materials [1–5]. The crystallization of melts is crucial in many fields, ranging from the microstructural control in engineering alloys and polymers, and phase selection in organic electronics and pharmaceuticals, to the analysis of geological processes (e.g. magma flows) up to the formation of ice in living systems [1, 3]. The technological relevance of supercooled binary alloys is complemented by their theoretical importance in studies of the glass-forming ability in few-component liquids [3, 4, 6]. In particular, as underlined by Tang *et al.*, our possibility to exploit the benefits of metallic glasses depends on the identification of alloys with incredibly low crystal growth rates, i.e. good glassformers [6]. Crystallization rates are thus also considered to be useful probes of the glass-forming ability (GFA) of a given material [3, 6–8]. In a simplified picture, one shall imagine that an extreme reduction of the crystallization rate can induce a complete arrest of the crystal propagation into the liquid (the so called 'dynamical arrest')[9]. Glasses can then be regarded as 'failed crystals', where a material is cooled from the liquid phase without freezing, and so it remains stuck, being not completely liquid due to the scarce mobility of the particles and its solid–like mechanical response, but also not being a crystal due to the lack of long–range order. The GFA of pure metals and of binary metallic alloys, related to their crystal growth rates, raised considerable interest in recent years, from a theoretical/computational [6–8, 10–15] and also from an experimental [3, 4, 16, 17] point of view.

All these systems display a growth rate whose maximum value is found at a temperature that lies between the glass-transition temperature and the melting temperature, as appears from Fig. 1.1. The downward arrows in Fig. 1.1 mark the glass transition temperature for each alloy, while upward arrows indicate the temperatures corresponding to the maximum crystal growth rates. Some data reported in this picture come from MD simulations, other from theoretical calculations, but the majority was experimentally determined. The logarithmic scale on y-axis highlights that these growth rates span several orders of magnitude, even for the same material. The origin of this remarkable variation is still not completely understood, and the classical models (largely described in the next section, Sec. 1.2) fail to fit the available data [3]. For example, aiming to account for the very different values of the maximum growth rates for a rich glassformer (CuZr), opposed to a poor glassformer (NiAl), Tang and collaborators indicated a different structure of the supercooled liquid as the main cause for the observed behavior, but were

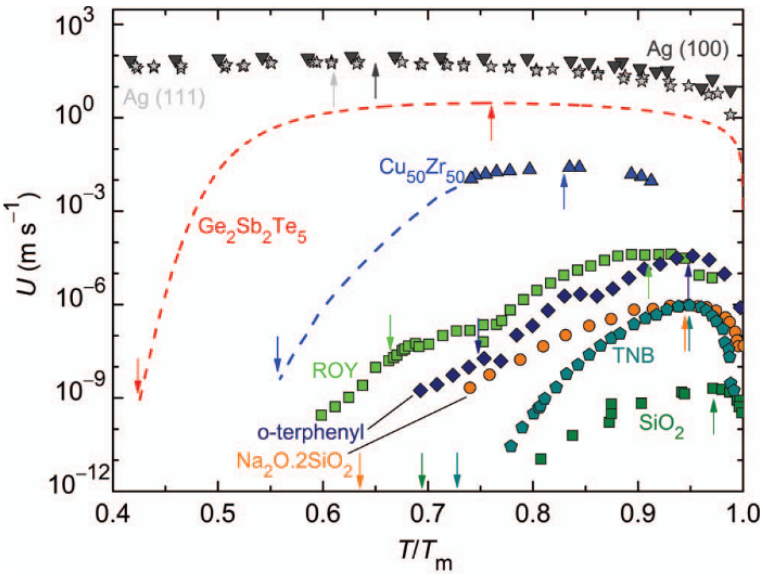

FIGURE 1.1: Crystal growth rates of many metallic alloys as a function of the temperature over melting temperature ratio. Reprinted from [3]

not able to completely reconcile their data with existing growth theories [6].

Therefore, the currently available theoretical models of crystal growth appear to not always be able to capture the complexity of the crystal growth mechanisms. The degree of supercooling can certainly be a limiting factor to the applicability of classical crystal growth formulas, as evidenced for example by the study of Sun *et al.* on pure metals [12]: great supercooling degrees not only are hardly experimentally accessible, but also the crystal growth in these regimes shows even larger deviations from the models. Despite many trials have been attempted in recent years to extend classical theories, we still lack a unified picture of crystal growth mechanisms [5].

An interesting approach to this problem is represented by the simulations of model systems, such as the well–known Kob–Andersen (KA) mixture, which is a merely abstract system loosely based around the metallic glassformer Ni_{80} P_{20} but using Lennard-Jones (LJ) interactions with the non-additivity where the cross-attraction is stronger than the attraction between each species (in other words, the KA mixture tends to phase–separate into two coexisting fcc lattices) [9]. This binary mixture is intensively studied from a computational and theoretical perspective as a model glassformer [9, 18–23], which shows a significant variability in its crystal growth rate as a function of temperature and supercooling degree [24]. The great popularity of such a model is undoubtedly due also to the usage of the simple LJ pair potential,

instead of the complicated potentials of metallic alloys which may involve three-body interactions, electronic contributions and other complex terms. Pioneering studies in the field of crystal growth from the melt were mono–component LJ systems which displayed a relevant temperature dependence of the growth rates [25, 26], which however did exhibit variations of a factor of 10 or less. Also experimental measurements about apparently different regimes crystal growth of charged colloids [27] are an additional point that challenges our current understanding of crystallization.

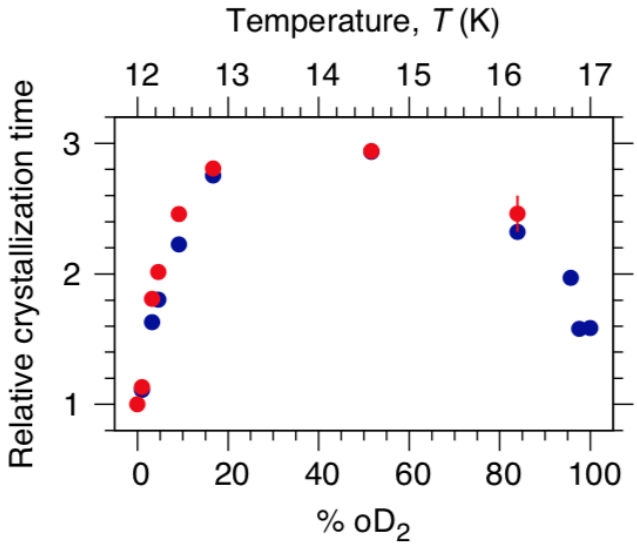

FIGURE 1.2: pH_2–oD_2 system crystallization time as a function of composition (and temperature, as consequence). Reprinted from [28]

Moreover, some recent studies focused on the crystal growth in supercooled quantum pH_2–oD_2 mixtures [28, 29], evidencing a temperature dependence of the measured crystal growth rate. The authors also studied the behavior of the system upon changing the relative concentration of the two components of the mixture, which is clearly another element that controls crystallization rates (see Fig. 1.2). The equimolar mixture was found to be about 3 times slower than the 100% pH_2 in crystallizing; surprisingly, upon further increasing the oD_2 percentage, the crystallization time started again to decrease. The pure oD2 displayed a crystallization rate of about 1.5 times slower than the pH_2 case (see Fig. 1.2), despite being hotter (17 K vs 12 K). The origin of this non–monotonic behavior as a function of temperature and composition was investigated via Quantum Monte Carlo simulations, revealing that differences in quantum delocalization between the

two isotopic species translate into different effective particle sizes, thus hindering the crystallization rate when mixing the two types of particles. Moreover, these simulations suggested that a minor fraction of non crystalline (icosahedral) structures could be responsible for a geometric frustration of the long–range order, but the presence of these structures was far too small and the issue remained partially open. The argument of the so–called locally favored structures (LFS), which are not compatible with the growth of a long–range ordered lattice, but are found at a lower or comparable free energy, and thus obstacle crystallization, was largely addressed also in the aforementioned studies about KA mixture [9, 18, 21]. The presence of icosahedra, bicapped square antiprisms and in general other structures that generate geometric frustration was often identified as the motivation behind the observed crystal growth slowdown in some temperature (and/or mixing ratio) regimes. As evidenced e.g. by Crowther *et al.* also the model glassformer KA mixture is characterized by different properties, growth regimes and LFS depending on the mixture composition and on the supercooling temperature [18].

Summarizing, there are many examples of materials whose crystal growth rates, experimentally measured and/or derived from simulations, which do not fit into the classical models formulas (detailed in the next section of this Chapter) and whose crystal growth mechanisms are not fully understood.

1.2 The classical models

As largely explained in the previous section, many mono–component systems as well as many few–component alloys display a crystallization slowdown as a function of temperature, passing from surprisingly high crystal growth rates (see e.g. [12] about velocities in the range of $10 - 100$ m/s for pure metals) to extremely low growth processes. We still lack a comprehension of the microscopic motivation of this behavior. Classically, crystallization is usually described by the *phenomenological crystal nucleation and growth theories*, yet in general solid formation is a far more complex process.

These theories give an account of the microscopic steps by which a solid phase spontaneously forms in the supercooled liquid at some temperature T below melting. Homogeneous crystal nucleation is defined as the process of the formation by thermal fluctuations of a small, localized nucleus of the newly ordered phase in the metastable liquid [30]. Once the nucleus has reached its critical size, it grows at a rate which the kinetic theory of crystal growth expresses as [2]:

$$u(T) = f a(T) \nu(T) \exp\left(-\frac{\Delta S_{\mathrm{m}}}{R}\right) \left\{1 - \exp\left[-\frac{\Delta G(T)}{RT}\right]\right\} \tag{1.1}$$

where $f \leq 1$ is a geometrical factor representing the fraction of atomic collisions with the crystal surface that actually contribute to the growth, $a(T)$

is a characteristic interatomic spacing that can be identified with the lattice constant, $\nu(T)$ is the *crystal addition rate* at the crystal–liquid interface, ΔS_m is the molar entropy of fusion, R is the universal gas constant and $\Delta G(T) = G^L(T) - G^C(T)$ is the difference in liquid ^{L} and crystal ^{C} molar Gibbs free energies G. Usually f is a fit parameter, or it is estimated from approximated considerations about the fraction of active sites at the crystal–liquid interface. Conversely, $a(T)$, ΔS_m and $\Delta G(T)$ are, in principle, experimentally accessible observables (they are, however, seriously hard to obtain in the majority of systems, even in the simplest). But the key term in 1.1 is represented by the addition rate $\nu(T)$, whose value dramatically changes from material to material (see e.g [31]; for a detailed discussion about ν, see Jackson's book [2]. In the *Wilson–Frenkel* (WF) theory [32, 33], it is proportional to the atomic diffusivity $D(T)$:

$$\nu_{\mathrm{WF}}(T) = 6\frac{D(T)}{\Lambda^2(T)} \tag{1.2}$$

hence exhibiting the strong temperature dependence associated with an activated process (i.e. a process with an energy barrier to overcome). In this work, the thermal length Λ is assumed to be an average atomic displacement proportional to $a(T)$: $\Lambda = ca(T)$, with the ratio f/c^2 in this model being a free fittable parameter. The diffusion coefficient $D(T)$ has an Arrhenius–like shape, being proportional to $e^{-E/(k_B T)}$, where E identifies the activation energy of each species and k_B is Boltzmann's constant. The calculation of the attachment rate according to this model, when applied to a binary AB mixture requires the determination of the diffusion coefficient $D(x_A, T)$ for the mixture. A simple possibility is to apply a geometric average of the pure substances diffusion coefficients based upon the mole fraction of A and B. In particular:

$$D(x_A, T) = D_A^{x_A}(T)\, D_B^{1-x_A}(T) \tag{1.3}$$

We verified that usual mutual diffusion coefficients (i.e. defined as $D(x_A, T) = D_A^{x_B}(T)\, D_B^{x_A}(T)$) and also arithmetically averaged ones lead to results comparable to the ones detailed in the remainder of this Chapter.

On the contrary, in the *collision-limited* (CL) scenario [25], the crystal addition rate is proportional to the average thermal velocity of the particles:

$$\nu_{\mathrm{CL}}(T) = \frac{\sqrt{3k_{\mathrm{B}}T/m}}{\Lambda(T)} \tag{1.4}$$

where m is the particle's mass. When calculating ν in this framework, for binary mixtures we used the weighted mass $m(x_A)$ defined as:

$$m(x_A) = m_A\, x_A + m_B\, x_B$$

but very similar results could be obtained by using thermal velocities instead that masses. Another possibility, as pointed out e.g. by Tang *et al.* [6], would have been to use the slowest rate (i.e. Kr one, in this case), as the rate determining process. However, we decided not to opt for such a choice, because it treats in equal way any mixture, regardless of its effective composition. In brief, this formula represents the extreme case in which there is no activation barrier for ordering. Again, f/c here is a fit parameter that should be determined. These two different models of ν provide rather different growth rates, and the competition between them is still ongoing, due to the apparent effectiveness and predictivity of one model or the other, alternatively, depending on the peculiar system studied. At the microscopic level, the WF and CL models can be characterized by limiting time scales associated with particle motion [31]. The weak dependence ($\sim \sqrt{T}$) on the temperature T of the particle's velocity for a Boltzmann distribution describes ballistic motion on short time scales, without any activation barrier. On longer time scales, the particle motion becomes, on average, diffusive, exhibiting an Arrhenius-like dependence on temperature (a decaying exponential as in eq. 1.2). Sun *et al.* [12] recently found by Molecular Dynamics simulations that the barrier-less crystal growth kinetics in supercooled Lennard–Jones liquids and pure metals might arise from a crystalline ground state of the atoms in the disordered liquid state adjacent to the crystal–liquid interface, effectively reducing the time required for transforming the liquid to crystal. However, many crystal growth rates are difficult to treat with these classical models, especially when key variables such as composition and particle size ratio are varied in binary systems (see examples in Figs. 1.1 and 1.2). Note that, in dealing with binary mixtures made of type-A and type-B particles, the growth rate u of eq. 1.1 becomes not only a function of T but also a function of x_A, $u(x_A, T)$, being $x_B = 1 - x_A$. For each mixture composition, the above formula can be used, as a function of temperature; vice versa, another possibility is to study the composition dependence of u, with the temperature fixed for each mixture and chosen according to experimental or simulated conditions.

Let us delve deeper into the details of the calculation of $u(x_A, T)$, according to eq. 1.1, by inspecting each term appearing in that formula. To begin, f is left as a fit parameter for the *absolute* crystal growth rates, while it does not matter for the *relative* crystal growth rates $\left(\text{i.e.}\frac{u(x_A,T)}{u(0,T)}\right)$. In the present Chapter the major attention is paid to relative crystal growth rates. The expression for the lattice constant $a(T)$ can be derived from experimental measurements based on sample temperature (see equation A.1 in Appendix A). $a(T)$ also appears in the expression of the thermal length $\Lambda(T)$, therefore possible simplifications have to be taken into account. The entropy of fusion ΔS_{m} present in the first exponential term in equation 1.1 is a simply function

of the mole fraction of the A mixture component:

$$\Delta S_{\mathrm{m}}(x_A) = \frac{H^{\mathrm{L}}\left[x_A, T_{\mathrm{m}}(x_A)\right] - H^{\mathrm{C}}\left[x_A, T_{\mathrm{m}}(x_A)\right]}{T_{\mathrm{m}}(x_A)} \tag{1.5}$$

with the enthalpies

$$H^{\mathrm{L,C}}(x_A, T) = G^{\mathrm{L,C}}(x_A, T) - T\frac{\partial G^{\mathrm{L,C}}(x_A, T)}{\partial T}$$

evaluated at the melting temperature $T_{\mathrm{m}}(x_A)$.

As explained for example in the book of Porter [34], the variation of the Gibbs free energy appearing in the second exponential term of eq. 1.1 provides the driving force for solidification. $\Delta G(T)$ for a binary mixture AB can be rewritten as:

$$\Delta G = G^{\mathrm{L}}(x_A, T) - G^{\mathrm{C}}(x_A, T)$$

with the apexes ^{L} and ^{C} indicating the liquid and the crystal phases[35] and where

$$\begin{aligned} G^{\mathrm{L,C}}(x_A, T) = x_A\, g_{\mathrm{A}}^{\mathrm{L,C}}(T) + (1 - x_A)\, g_{\mathrm{B}}^{\mathrm{L,C}}(T) \\ + g_{\mathrm{mix}}(x_A, T) + g_{\mathrm{E}}^{\mathrm{L,C}}(x_A, T) \end{aligned} \tag{1.6}$$

where $g_{\mathrm{B}}^{\mathrm{L,C}}(T)$ and $g_{\mathrm{A}}^{\mathrm{L,C}}(T)$ are the Gibbs free energies for the elements of the mixture A and B considered separately. Both the g_{mix} and the $g_{\mathrm{E}}^{\mathrm{L,C}}$ terms appearing in eq. 1.6 require further explanations. A detailed review of the thermodynamics and the kinetics of binary alloys can be found in the exhaustive book of Jackson [2]. Following Jackson's approach to this issue, we can starts from the chemical potential distinguishing between *ideal* and *regular* mixtures. For a binary ideal phase with a mole fraction x_A of atoms of type A, the chemical potential of the species A, μ_A, is given by:

$$\mu_A(x_A, T) = \mu_A^0(T) + k_B T \ln x_A \tag{1.7}$$

$\mu_A^0(T)$ being the chemical potential of the pure A element at temperature T. Note that the previously introduced $g_{\mathrm{A}}^{\mathrm{L,C}}(T)$ is equal to $n_A\, \mu_A^0$, where n_A is the number of moles. The non ideality in regular mixtures chemical potential, $\mu_A(x_A, T) - \mu_A^0(T)$ is expressed via an *activity coefficient* γ_A:

$$\mu_A(x_A, T) - \mu_A^0(T) = k_B T \ln \gamma_A(x_A, T) \tag{1.8}$$

γ_A replaces x_A in non–ideal alloys in eq. 1.7 and allows to keep the same form for the chemical potential value. The activity coefficients are all equal to 1 in ideal mixtures, while in regular mixtures they become functions of temperature and composition. In principle, γ_A also (weakly) depends on pressure [35] but in most theoretical treatments this will not be explicitly taken into account and approximately constant zero pressure is assumed.

When two (or more) phases are in equilibrium, the activity of any component is the same in all phases, provided that the activity in every phase is expressed with respect to the same standard state [36]. As a consequence, exploiting the thermodynamic relationship between the chemical potential and the Gibbs free energy [35], the following equation for g_{mix} is easily derived from the second term in eq. 1.7:

$$g_{\text{mix}}(x_A, T) = (1 - x_A)\ \ln(1 - x_A) + x_A\ \ln x_A RT \tag{1.9}$$

which represents the *ideal free energy of mixing*.

For what concerns $g_{\text{E}}^{\text{L,C}}(x_A, T)$, it is a composition-dependent energy term, called *excess free energy*, which describes the departure from ideality. It is very similar to eq. 1.9 and it depends on the activity coefficients of A and B species:

$$g_{\text{E}}^{\text{L,C}}(x_A, T) = \left[(1 - x_A) \ln \gamma_{\text{B}}^{\text{L,C}} + x_A \ln \gamma_{\text{r}}^{\text{L,C}}\right] RT \tag{1.10}$$

Therefore, expliciting $G^{\text{L}}(x_A, T)$ and $G^{\text{C}}(x_A, T)$:

$$\begin{gathered} \Delta G = G^{\text{L}}(x_A, T) - G^{\text{C}}(x_A, T) = \\ x_A \Delta g_{\text{A}}^{\text{L,C}} + (1 - x_A)\Delta g_{\text{B}}^{\text{L,C}} + \Delta g_{\text{E}}^{\text{L,C}}(x_A, T) \end{gathered} \tag{1.11}$$

with the ideal free energy of mixing vanishing (because it appears both in $G^{\text{L}}(x_A, T)$ and $G^{\text{C}}(x_A, T)$).

For practical calculations of the growth rate, $g_{\text{B}}^{\text{L,C}}(T)$ and $g_{\text{A}}^{\text{L,C}}(T)$ are usually obtained from their respective heat capacities $c_p^{\text{L,C}}(T)$, since $g^{\text{L,C}}(T) = h^{\text{L,C}}(T) - Ts^{\text{L,C}(T)}$, as remarked in the work of Pelton [36] for regular solutions. In fact, the enthalpies and entropies appearing in $g_{\text{B}}^{\text{L,C}}(T)$ and $g_{\text{A}}^{\text{L,C}}(T)$ expressions are given by:

$$h^{\text{L,C}}(T) = h^{\text{L,C}}\left(T_{\text{m}}\right) - \int_T^{T_{\text{m}}} \mathrm{d}T' c_p^{\text{L,C}}\left(T'\right)$$

and

$$s^{\text{L,C}}(T) = s^{\text{L,C}}\left(T_{\text{m}}\right) - \int_T^{T_{\text{m}}} \mathrm{d}T' \frac{c_p^{\text{L,C}}\left(T'\right)}{T'}$$

being T_{m} the melting temperature (which is, in general, different for the two mixture components).

A final consideration about the physical meaning of the regular solution term is worth: $g_{\text{E}}^{\text{L,C}}(x_A, T)$ has a simple interpretation with reference to the interactions among atoms. Let us follow Schirmacher's description [37] and introduce the quantity U_{ij}:

$$U_{ij} = \rho \int d^3\mathbf{r} g_{ij}(r) V_{ij}(r) \tag{1.12}$$

i.e. the integral of the pair interaction potential between an atom of type i and one of type j weighted over the radial distribution function. This multiplication is necessary to guarantee the existence of the primitive function. U_{ij} is then employed to build the *Flory–Huggins interaction parameter* for AB mixture:

$$\omega = U_{AB} - \frac{1}{2}(U_{AA} + U_{BB}) \tag{1.13}$$

Now, ω appears in the expression of the stability function g_{xx} which essentially is the second derivative with respect to the concentration x_A of the Gibbs free energy difference reported in eq. 1.11:

$$g_{x_A x_A} = -2\omega + k_B T \frac{1}{x_A(1 - x_A)}$$

From this expression, by integrating twice with suitable boundary conditions (see [37]) it is possible to retrieve the following formula:

$$\Delta G = x_A(1 - x_A)\omega + k_B T(x_A \ln x_A + (1 - x_A) \ln(1 - x_A)) \tag{1.14}$$

which is equal to the expression for ΔG of eq. 1.11 for the Gibbs free energy difference, containing the excess term. Remarkably, we have just established a link between the interparticle interactions (embedded in the Flory-Huggins parameters) and the Gibbs free energy excess term, which is a key ingredient of the crystal growth rate formula. Interestingly, in the $s_0 \to 0$ limit (largely valid for the systems we are investigating), the expression for the excess Gibbs free energy simplifies as $g_{\mathrm{E}}^{\mathrm{L,C}}(x_A, T) = x_A\,(1 - x_A)\,h_0^{\mathrm{L,C}}$. Therefore, $\omega = h_0^{\mathrm{L,C}}$, in this limit.

Now, for all the binary systems for which the previous quantity are available (from theoretical estimations or experimental measurements), one is able to perform analytical calculations of the crystal growth rate expected by classical model in eq. 1.1, both in its CL and WF flavors, for each mixture with A mole fraction x_A as a function of temperature T. This allows to generate either

1. either the crystal growth rate u as a function of x_A, with T for each mixture fixed for instance at the experimental value for that A mole fraction

2. or a set of curves $u(T)$, with a parametric dependence on the mixture composition x_A

More frequently, one is interested in exploring the temperature dependence of the properties of a given material (at fixed composition), but it is important to remark that the crystal growth rates depends on mixing ratio and temperature *both*.

Moving back to the possible interpretation of simulated or measured crystal growth rates via classical formulas, it turns out that frequently neither the CL nor the WF expressions fit the available data. For example, simulations do show that crystal growth rates in binary alloys can be much lower than those predicted by the CL model [6, 8, 11, 15] but the WF model also fails to describe crystal growth in these systems [11, 14]. In particular, let us consider the case investigated by Tang and collaborators in [6] and already mentioned in the previous section: in this paper, the authors exploit Molecular Dynamics simulations to show that the crystal growth rate for an important binary glassformer, CuZr, is significantly slower than that of a poor glassformer, NiAl. In particular, they keep the *composition* of each mixture fixed, while changing the supercooling *temperature*.

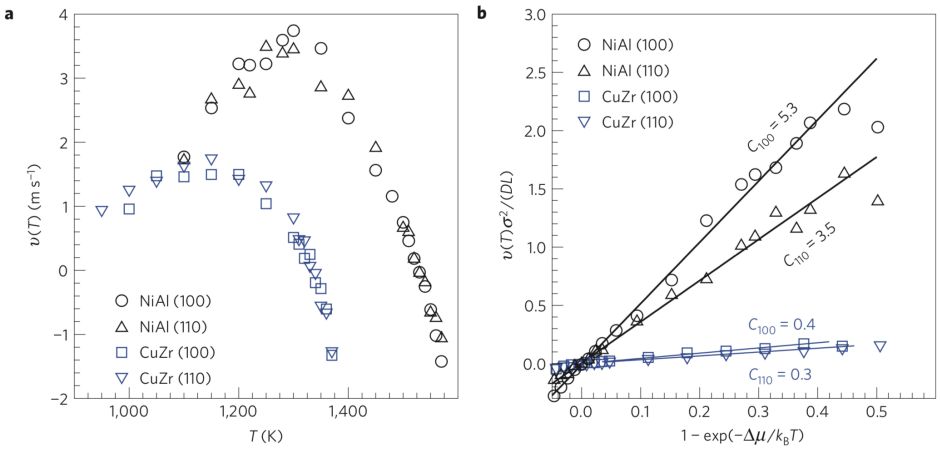

FIGURE 1.3: a) Crystal growth rates for NiAl and CuZr as a function of temperature. The growth rates for CuZr have been multiplied by a factor of 10 for clarity. b) Crystal growth rates for NiAl and CuZr as a function of $1-e^{-\frac{\Delta\mu}{k_B T}}$ Reprinted from [6].

The left picture (Fig. 1.3a) represents the physical growth rates (measured in m/s, and magnified by a factor of 10 for the CuZr) extracted from the MD simulations for the studied mixtures: the datasets both exhibit a well-defined peak, about 20 times higher for NiAl than for CuZr. The authors, compared the MD data with the two formulas introduced above; as a result, the WF formula fitted the majority of the data quite accurately (the straight lines in Fig. 1.3b are linear fits of the data along different growth axes). A deeper investigation (see Fig. 1.4) proved that the barrier–less picture (CL framework) completely missed a proper description of the significant temperature dependence of the crystal growth of these alloys. The quantity

reported in the abscissa of Figs. 1.3b and 1.4 ($1 - e^{-(\Delta\mu)/(k_B T)}$) is an equivalent formulation of the Wilson–Frenkel model, where the Gibbs free energy has been replaced by the chemical potential μ.

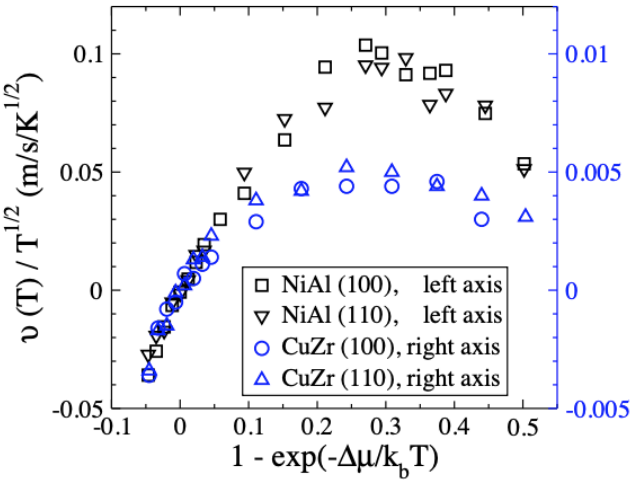

FIGURE 1.4: Crystal growth rates for NiAl and CuZr for (100) and (110) surfaces normalized by the square root of the temperature. Reprinted from [6]

As the authors state, if the CL model did fit the growth rate then they would find a linear relationship when plotting $v(T)/\sqrt{T}$ with respect to $1 - e^{-(\Delta\mu)/(k_B T)}$, regardless of the values of other constants. This, clearly, does not happen, even at small undercoolings, neither for (110) nor for (100) surfaces: thus, it was possible to conclude that the collision–based model was not consistent with the growth data for the alloys considered in that study.

Quite surprisingly, on the contrary, the growth of other systems such as pure metals is well described by the collision–limited formula, while the WF model turns out to be inadequate to account for their reported growth rates [12]. Even concerning the crystallization of much simpler, monoatomic LJ systems, Burke *et al.* pointed out that the WF model should be replaced by CL one [26]. The more recent work of Sun *et al.* investigated the growth rates of a set of pure metals, as a function of the supercooling degree, via Molecular Dynamics. Here, they tried to fit the simulated data via three models: the already presented WF and CL, and also the Ginzburg–Landau (GL) framework (an approach where the kinetic coefficient is governed by the relaxation rate of density fluctuations in the liquid). Last, they also considered the possibility of having a constant $\nu(T)$ in eq. 1.1. This last hypothesis was apparently correct for some of the systems explored (such as pure copper), but failed at high supercoolings for others (e.g. Ag) as reported in Fig. 1.5). Also here, none of the (four) models was able to account for the

data on the full temperature range [12], but it resulted necessary to suggest a crossover from one regime to another.

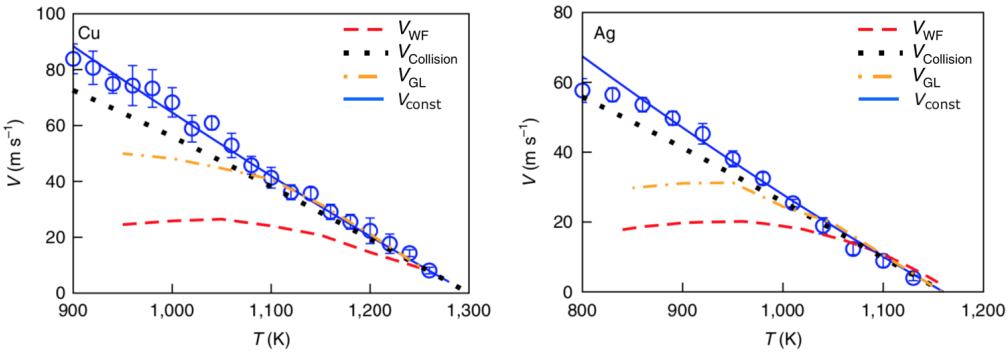

FIGURE 1.5: Crystal growth rates for Cu and Ag as a function of T. The blue straight line is a fit, in the hypothesis of constant attachment rate of the atoms to the interface. Red, black and orange dashed lines correspond to WF, CL and GL models. Reprinted from [12]

To date, many other studies [3, 4, 31] showed that there is a widespread impossibility to reconcile experimental and/or simulated data with the classical model of crystal growth. The current situation is that there is no comprehensive theory that is able to explain such differences in crystal growth rates arising in entirely metallic liquids: both CL and WF models, apparently, sometimes utterly fail.

The project of the present PhD thesis is meant to investigate if it is possible to get to a unified picture of crystal growth from supercooled melts or, at least, to provide a deeper comprehension of the microscopic mechanisms regulating crystal growth in binary mixtures. In particular, together with our collaborators from the Frankfurt Goethe Universität, led by dr. Robert Grisenti (`https://www.atom.uni-frankfurt.de/hhng-grisenti/index.html`), we focus here on Argon-Krypton supercooled liquid mixtures. We studied their crystallization by experiments, theory, and computer simulations: the main results of this investigation have been reported in a recent article [5].

1.2.1 Why Argon-Krypton?

The choice of such a simple system is rooted in several different motivations.

- First, rare-gas liquids are particularly attractive model systems because Molecular Dynamics simulations indicate that crystal growth rates in supercooled Lennard-Jones liquids are comparable to those in pure metals [12, 25, 26], whose technological relevance is undoubtedly higher. Furthermore, condensed argon and krypton are miscible in the whole

range of composition in both the liquid and solid phases, with a phase diagram approaching that of an ideal mixture (i.e. a mixture whose gas phase has thermodynamic properties analogous to those of a mixture of ideal gases) [38]. These features, combined with the roughly 8% difference between the argon and krypton atomic radii and the absence of chemical order, make liquid mixtures of these two elements the ideal laboratory realization of the simplest atomic binary systems.

- From a simulation perspective, Argon and Krypton are relatively easily modeled via a simple LJ pair potential whose parameters have been optimized since many years and whose effectiveness has been strengthened by several comparisons with experimental measurements.

- Last, many experimental data concerning the thermodynamic quantities comprised in eq. 1.1 are available for this system, which is quite uncommon. In particular, the diffusion coefficients for Ar and Kr as a function of T were obtained as zero-pressure linear extrapolations of experimental diffusivity data at higher pressures [39] by assuming a temperature dependence of the usual Arrhenius form, $D_0 e^{-Q/T}$, with $D_0 = 1.21 \times 10^{-7}\mathrm{m^2 s^{-1}}$ and $Q = 350.77\,\mathrm{K}$ for argon, and $D_0 = 0.51 \times 10^{-7}\mathrm{m^2 s^{-1}}$ and $Q = 402.51\,\mathrm{K}$ for krypton.

  Concerning the melting entropy, it was possible to derive an analytic expression for $T_\mathrm{m}(x_A)$ by fitting a sixth–order polynomial to the experimental phase-equilibrium data [38]. The experimental phase diagram for Ar-Kr mixtures is reported in Fig. 1.9, whose other contents will be clarified in next sections. The enthalpy of fusion $\Delta h_\mathrm{m} = h^\mathrm{L}(T_\mathrm{m}) - h^\mathrm{C}(T_\mathrm{m})$ is instead equal to $1.180\,\mathrm{J mol^{-1}}$ for argon and $1.640\,\mathrm{J mol^{-1}}$ for krypton. We assumed the heat capacities of the supercooled liquids as linear extrapolations for $T < T_m$ of experimental data at higher temperatures [40–42], which are fitted by $c_p^\mathrm{L}(T) = a_0 + a_1 T + a_2 T\, e^{a_3 T}$. Analogously, the experimental heat capacities of the pure solids [40, 43] were fitted for $T > 10$ K by the fourth-order polynomial $c_p^C(T) = \sum_{k=0}^{4} b_k T^k$. Major details are provided in Appendix A with tables containing the fit parameters and a pictures of the heat capacities for Ar and Kr.

  For practical purposes, the excess term of equation 1.10 is better expressed as a series expansion:

$$g_\mathrm{E}^\mathrm{L,C}(x_{Kr}, T) = (1 - x_{Kr}) x_{Kr} \Big[\xi_0^\mathrm{L,C}(T) +$$

$$\xi_1^\mathrm{L,C}(T)(1 - 2x_{Kr}) + \xi_2^\mathrm{L,C}(T)(1 - 2x_{Kr})^2 + \ldots \Big] RT$$

where $\xi_0^{\mathrm{L,C}}(T), \xi_1^{\mathrm{L,C}}(T), \xi_2^{\mathrm{L,C}}(T), \ldots$, are empirical coefficients that depend on temperature. Davies *et al.* [44] measured the excess free energy for equimolar liquid mixtures of argon and krypton at two different temperatures, providing the first three coefficients in the expansion of $g_{\mathrm{E}}^{\mathrm{L}}(x_{Kr}, T)$. The experimental values indicate that such mixtures closely approach the already discussed limit of regular solutions [35] for which:

$$\xi_0^{\mathrm{L,C}}(T)RT = h_0^{\mathrm{L},C} - Ts_0^{\mathrm{L,C}}$$

and $\xi_1^{\mathrm{L,C}}(T) = \xi_2^{\mathrm{L,C}}(T) = \ldots = 0$. The data reported in [44] yield $h_0^{\mathrm{L}} = 279.07\,\mathrm{Jmol}^{-1}$ and $s_0^{\mathrm{L}} = -0.49\,\mathrm{Jmol}^{-1}\mathrm{K}^{-1}$. Similarly, Fender and Halsey investigated solid solutions of argon and krypton, and, in the regular solution approximation, they found $h_0^{\mathrm{C}} = 1163.15\,\mathrm{Jmol}^{-1}$ and $s_0^{\mathrm{C}} = 5.48\,\mathrm{Jmol}^{-1}\mathrm{K}^{-1}$ [45].

For both species, $|s_0| \ll |h_0|$ and the excess free energy g_E can be approximately rewritten as [37]:

$$\mathrm{E}^{\mathrm{L,C}}(x_{Kr}, T) \approx x_{Kr}\,(1 - x_{Kr})\,h_0^{\mathrm{L,C}}$$

We therefore managed to calculate the explicit analytic dependence on x_{Kr} and T of each of the quantities appearing in equation 1.1.

However, cooling rare-gas liquids to temperatures appreciably below their melting points is difficult, not to mention the subsequent probing of the rapidly evolving liquid-to-solid phase transition. These reasons, clearly, make these experimental measurements a challenge. Our work, in this sense, represent the first case of such measurements on Ar–Kr supercooled liquids and it is highly innovative [5]. In the next section, only the essential points concerning experiments are provided, while further details can be found in Appendix A and in our paper recently published on *Nature Materials* [5].

1.3 The experiments

The approach of our experimental collaborators from Frankfurt was based on the generation of a microscopic laminar jet in vacuum, which offers a powerful method to investigate fast structural transformations in simple supercooled atomic and molecular liquids [29, 46]. The X-ray scattering experiments were performed during some experimental sessions held at the P03 beamline of the PETRA III synchrotron at DESY, Hamburg (`https://photon-science.desy.de/facilities/petra_iii`), between 2015 and 2018. I actively joined the majority of these experimental campaigns, since my Master thesis (see the inset of Fig. 1.6 for a partial view of the experimental hutch).

Fig. 1.6 shows a schematic representation of the experiment. Liquid jets of varying krypton mole fraction x_{Kr} between $x_{Kr} = 0$ (pure argon

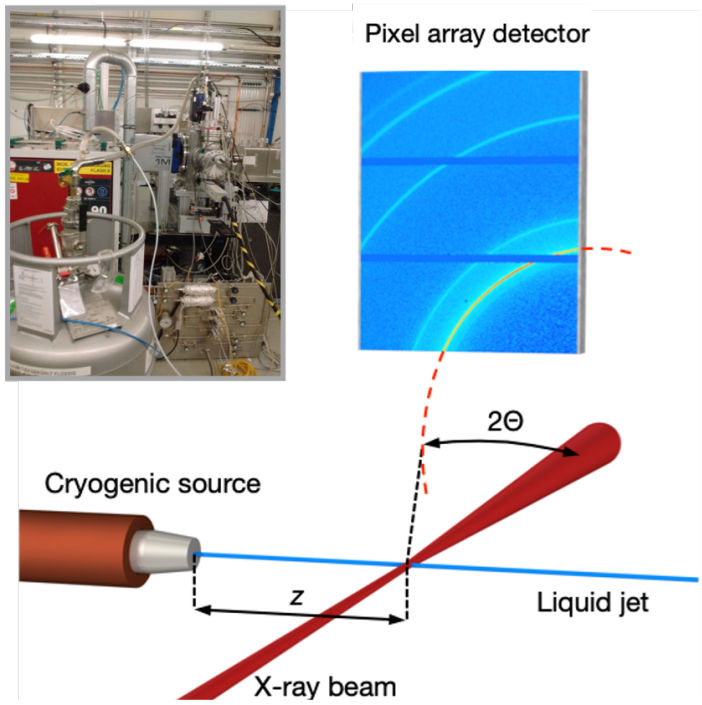

FIGURE 1.6: Sketch of the experimental setup, adapted from [5]. In the inset (top left), my own picture of the experimental hutch at DESY.

jet) and $x_{Kr} = 1$ (pure krypton jet) were generated in a vacuum chamber. In particular, the jets diameters were uniformly micrometer–sized ($\sim 5\mu$m). We verified that the calculated jet velocities were consistent with those determined by mass conservation from the pressure rise in the experimental vacuum chamber.

The jets cooled rapidly by surface evaporation until they crystallized spontaneously by homogeneous crystal nucleation, forming continuous solid filaments [46]. We used 13 keV X-rays to probe the crystallization process by adjusting the distance z between the orifice and the interaction region, effectively changing the time $t = z/v$, where v is the jet velocity, with a resolution of $\sim 0.5\mu$s. In fact, since the velocity v of the jet into the chamber is constant, if you scan the filament at increasing distance z from nozzle, it is equivalent to the study of the time evolution of the system. Near the cryogenic source, the microjet is substantially liquid; as long as z grows, the liquid fraction that crystallizes becomes more and more relevant (from the outer surface towards the inner core). The scattered X-rays were detected by a two-dimensional pixel array detector covering the 10° to 40 ° 2Θ diffraction angular range

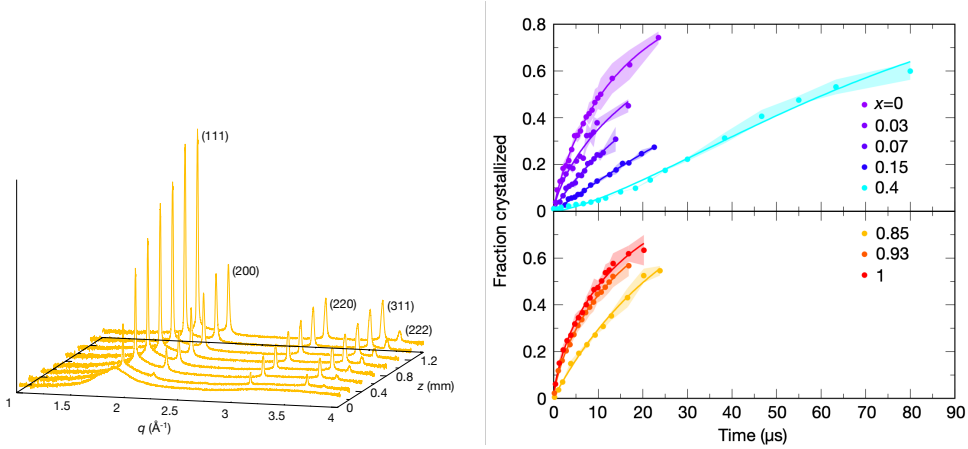

(a) (b)

FIGURE 1.7: (a): Selection of area-normalized of experimental diffracted intensity profiles in a mixture with $x = 0.85$. The abscissa axis contains the wavectors $q = 4\pi sin(\Theta)/\lambda$, where λ is the radiation wavelength. (b): Experimental crystallization processes of the 8 mixtures studied here. y–axis: crystallized fraction of the sample; x–axis, time in μs. Reprinted from [5]

(see Fig. 1.6 for an overall view of the process). Beyond all the technical details specified in Appendix A concerning image acquisition and related data analysis, an example of reduced diffraction profiles obtained by azimuthal integration of two-dimensional scattering images from a jet with $x_{Kr} = 0.85$ is reported in Fig. 1.7a.

At small distances from the orifice, the diffraction curves exhibit a broad main peak characteristic of short-range order in the disordered liquid state. By increasing z, a reduction in the diffuse scattering from the liquid is accompanied by the rise in intensity of five sharp peaks, which become the dominant feature at the largest distances. We identified these peaks with reflections of the fcc crystal structure, into which rare-gas liquids crystallize under equilibrium conditions [47]. There are also some weak signals of hexagonal close packed (hcp) structures. Note that several growth surfaces have been investigated, because they are all present in the experimental sample, but the (111) and the (200) give signals with higher intensity.

1.3.1 Experimental crystal growth rates

These diffraction profiles allowed us to obtain the time evolution of the converted liquid fraction in the scattering volume, as shown in Fig. 1.7b.

The explanation of the analysis procedure employed to separate the contributions to the diffraction intensity of the disordered liquid and crystalline phases is available in Appendix A. The experimental data were fitted by the Johnson–Mehl–Avrami–Kolmogorov (JMAK) rate equation:

$$X(t) = 1 - \exp\{-[k(t-\tau)^n]\} \tag{1.15}$$

[2], where k is the characteristic crystallization rate, τ and n are fit parameters and $X(t)$ is the measured solid fraction. In particular, as described in [2], the Avrami exponent n usually is comprised between 1 and 4, and encodes information about where the nucleation takes place (it can happen near dislocations, or near grain-boundaries) and about the underlying physical mechanism (diffusion-controlled growth, or constant nucleation rate). The τ parameter is a sort of delay, related to the fact that in each mixture the growth process starts at different times. The fits with the JMAK formula are shown as solid curves in Fig. 1.7b, where $x = x_{Kr}$, with the values of the fit parameters presented in Tab. A.3 in Appendix A. Interestingly, the Avrami exponent n typically contains information on the crystal nucleation and growth topologies. We found that n is close to unity for the investigated jets, a result that might be associated with surface nucleation [48]; this is consistent with the evaporative cooling ongoing in our samples. This means that the external region of the microjets starts to crystallize, in general, earlier than the core regions. Referring to Fig. 1.7b, the symbols represent the time evolution of the fraction crystallized for argon– (top panel) and krypton–rich (bottom panel) mixtures obtained from the analysis of the experimental diffraction profiles. The figure provides clear information about the time evolution of each system, if one considers (as also mentioned before) that an increasing z is equivalent to a later stage of the crystallization process $t = z/v$. Note that the light-shaded regions around the solid lines represent the estimated uncertainties in the evaluation of the fraction of the sample that crystallized. The fitted values of τ were used to shift the experimental datasets to a common origin. The JMAK model provides also a widely used approach to obtain a reliable estimation of the characteristic crystallization rate constant k. In Fig. 1.8, the ratio of k to the crystallization rate constant for the pure argon jet is plotted for each mixture as a black circle, in the range $x_{Kr} \in [0, 1]$. Blue and green solid lines represent the CL and WF classical models, respectively, for relative crystal growth rates. As shown in the following (see Fig. 1.9), the temperature dependence on the mixing ratio can be linearly interpolated. Therefore, all the plots of theoretical curves contained in this chapter use the interpolated temperatures so obtained.

In Tab. 1.1, some data about the experimental growth rates are reported.

The first feature emerging from these data is that the pure argon system is the fastest, faster than all mixtures and also faster than the 100% krypton sample. Besides, a slowdown in the crystallization rate is evident by adding

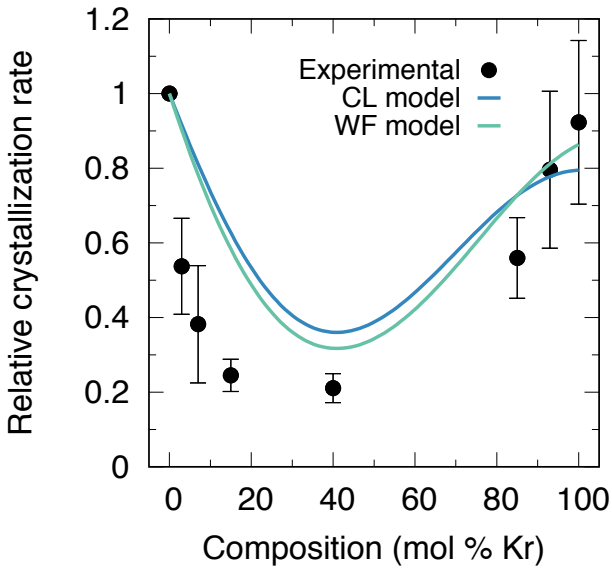

FIGURE 1.8: Experimental growth rates for the eight Ar-Kr supercooled liquid mixtures investigated in our experiments, compared with CL (blue) and WF (green) classical models.

Ar to Kr and by adding Kr to Ar as well: this rules out the simplistic hypothesis that this could be a mere increasing temperature effect (note that temperature grows from the left to the right of the picture). The reader should note that the usage of the word 'crystallization' in an experimental context is due to the compresence of nucleation events and subsequent crystal growth in the measurements, and these two contributions can not be effectively disentangled. Furthermore, we observed that the mixture that took more time to crystallize was the 40% Kr – 60% Ar: its rate k is five times smaller than the pure argon one. We underline that the errorbars of each data point are huge, owing to uncertainties in the experimental fraction crystallized related also to the jet temperature estimation. The trend of the data displayed in Fig. 1.8 is qualitatively similar to that reported for diverse binary systems at various mixing ratios, such as colloids [27], hard spheres [49] and quantum liquids [28] (see also section 1.1).

We remark that, in general, a direct comparison with equation 1.1 is in general precluded because the explicit calculation of the crystal growth rate requires thermodynamic data that are either difficult to obtain or unavailable, so that several approximations must be introduced [2]. Condensed argon and krypton and their mixtures represent a fortunate exception, as phase-equilibrium thermodynamic data are available for these systems: we were

x_{Kr}	u [1/s]	$u/u_{x_{Kr}=0}$
0	60206	1.0
0.03	25287	0.42
0.07	22300	0.38
0.15	14756	0.25
0.4	12683	0.21
0.85	33696	0.56
0.93	47919	0.8
1	55569	0.92

TABLE 1.1: Experimental crystal growth rates, in 1/s (first column) and relative to pure Argon sample (second column).

hence able to calculate the exact growth rates forecast by eq. 1.1 and to compare these curves with our experimental growth rates. The details of the exact analytic calculation of $u(x_{Kr}, T)$ we carried out were provided in the previous section (1.2).

Since the crystal growth rate is a function of temperature, to allow for comparison with the experimental data we determined the average jet temperature at the onset of crystallization on the basis of the lattice constants extracted from the diffraction profiles. Consider that the jet experiences a temperature gradient, going inwards from the surface; the estimated average temperature is, then, slightly hotter than the T of the external surface of the microjet. The complete process for the determination of jet temperatures is retrievable in Appendix A, see in particular eq. A.1 and Fig. A.2. The calculated temperatures are plotted as colored circles in Fig. 1.9 (each mixture is represented by the same color used in Fig. 1.7b and in Fig. A.2). The error bars on these data result from the uncertainty in the distance between the liquid jet and the detector. Moreover, the solid black lines are sixth-order polynomial fits to the experimental liquidus and solidus Ar–Kr boundaries [38], shown instead as black dots. To a good approximation, their dependence on the krypton mole fraction can be treated as linear [28], as shown by the fit $T(x_{Kr}) = 74.7 + 28.7x_{Kr}$ (dashed line). We used this linear interpolation when comparing the theoretical calculations with the experimental data.

Here, it has to be underlined that all the temperatures are located below the coexistence zone of the phase diagram: this ensures that our experimental samples are mostly avoiding that region, while trying to crystallize. Differently, with systems whose average T was found in the region inside the liquidus and solidus boundaries, we would have detected the impossibility for those samples to proceed with the crystal growth due to location into the phase coexistence.

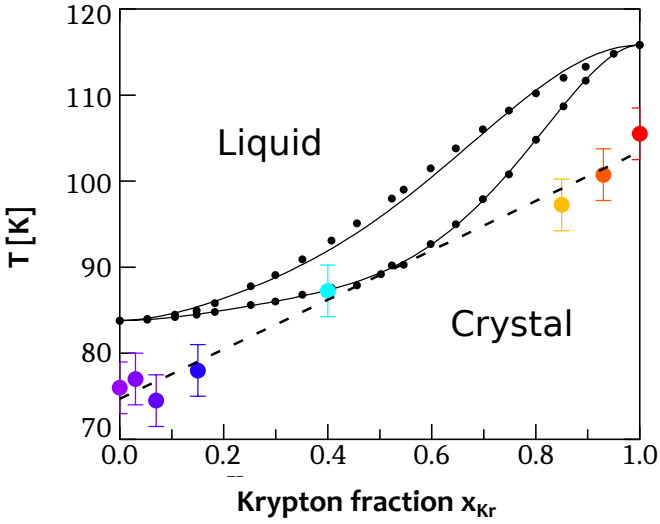

FIGURE 1.9: Estimated experimental jet temperatures, and Ar–Kr phase diagram (liquid, solid and liquid/solid coexistence region). Solid lines are fits to the experimental data. Reprinted from [5]

1.3.2 Experimental growth rates vs the models

Note that, in the analysis of the experimental data, the outcome is an estimation of u as a function of x_{Kr}. The possibility to vary the temperature at will is only limited to theoretical calculations and computer simulations. As a consequence, here the experimental growth rates are going to be confronted only with the theoretical model $u(x_{Kr})$; in particular, the relative crystal growth rates $u(x_{Kr})/u(0)$ will be the subject of the present discussion. The choice not to look at absolute growth rates allows not to fit the unknown parameters f and c in the classical model equation 1.1. The relative crystallization rates in the CL and WF formulations are shown in Fig. 1.8 as blue and green solid lines, respectively, with both models giving a reasonable account of the experimental data. Evidently, the agreement between real data and theoretical curves is not quantitative, but both models forecast a trend similar to the one retrieved in the experiments. Obviously, both CL and WF frameworks indicate higher growth rates for almost all the systems studied; this is due to the fact that the experimental samples are affected by many sources of noise. In fact, we believe that the real systems hosted the growth of many crystallites with different directions, which is a clear source of further slowdown in the measured growth rate. Moreover, we have the already discussed uncertainties about the jet temperature (which is evidently

not constant).

An important last point is that our data also include *nucleation* events, which are not explicitly considered in the models. In particular, this is confirmed by a preliminary set of results of the experiment conduced by the group of Dr. Grisenti at the EU-Xfel (https://www.xfel.eu/) in March and October, 2019 (in which I also took part). Some preliminary calculations seem to indicate the great relevance of the nucleation process in the determination of the experimental crystallization rates, as also supposed by Tang *et al.* for other systems [6]. We then stress that the discrepancy observed for the argon–rich mixtures, for which the experimental rates are systematically smaller than those predicted by equation 1.1, might then arise from the slightly different physical meaning of k and $u(T)$, the former also implicitly including the contribution from the nucleation rate. As a consequence, the experimental and theoretical relative rates in Fig. 1.8 would be directly comparable only if the nucleation rate were independent on composition; our results indicate that for mixtures of argon and krypton this may in fact not be the case. Interestingly, the krypton–rich mixtures display instead crystallization rates closer to the theoretical ones. The comparison reported here between the experimental data and theoretical calculations does not allow assessing which of the two crystal growth models effectively describes the kinetics of crystallization. This can be understood by the fact that at the temperatures at which crystallization occurred in the liquid jets the crystal growth rate is largely determined by the thermodynamic factor in the curly brackets of equation 1.1 and only at lower temperatures does the kinetic contribution from the crystal addition rate become dominant. Being ν the key term that distinguishes the collision–limited model from the diffusion–limited one, obviously this comparison does not allow us to discern which model is best suited to our data. Concerning this, another possibility would have been to use, for ν in eq. 1.1, an average weighted over the thermal velocities for pure Ar and Kr (and not over the masses as we chose). We estimated that the WF $u(x_{Kr})$ curve in the above picture would always be found above the CL curve and partially deviate from the experimental growth rates at high Kr concentration, with an inflection point and a concavity shift around $x_{Kr} = 0.9$. On the contrary, the CL model curve would not be affected by such a choice.

1.4 Simulations of crystal growth in supercooled Ar-Kr liquids

To discern between the two models, and also to get microscopic information during the crystal growth process, we performed state-of-the-art Molecular Dynamics simulations of a seeded fcc crystal growth (similar to [6, 25]) in

supercooled liquid mixtures of argon and krypton. In order to skip the long–lasting stages of nucleation, i.e. the birth of the first critical nucleus preceding the crystal growth, a crystal seed was already present in the box at the beginning of the simulation. In fact, aiming to measure the crystal growth rate *after* the nucleation, we put some slabs with a fcc crystal geometry in the middle of the simulation box. In this way, the particles in the supercooled liquid surrounding this inner crystal wall could attach to these slabs, making the crystal effectively start to grow.

The simulation tool we developed demanded a huge amount of computing resources; this need had to be faced exploiting computer clusters and using an efficiently parallelized code. These MD simulations exploited the well–established and highly–parallelized software LAMMPS (`http://lammps.sandia.gov`, [50]) on CINECA high-performance computing facilities (`https://www.cineca.it`). In particular, the MARCONI and GALILEO clusters at CINECA were hugely exploited, via the projects *LISA–PUMAS* (2016), *IscraC–GLEMD* (2017) and *IscraB-MEMETICO* (2018). This research required approximately 1 million of core–hours, roughly equivalent to a century of calculations on a single–core computer.

In the following, the principles of MD will be assumed as basic knowledge. It is worth to underline that the protocol developed here for the MD simulations is quite similar, in its nature, to those employed by other works in the field, such as [6, 8, 12, 21–23, 31, 51, 52] and many other articles. The method we have developed is supported by clear physical motivations described in the following; at the same time, this could appear to be elaborate also because of the fact that the LAMMPS package serves for a wide range of applications, but some functionalities must be customized. The crucial point is that, as largely remarked in the next pages, our aim is to guarantee almost constant chemical potential and pressure along crystallization axis, which is a standard procedure for ensuring a uniform crystal growth (on average).

1.4.1 Simulation parameters

All the particles interacted via a classical Lennard–Jones pair potential:

$$V_{\alpha\beta}(r) = 4\epsilon_{\alpha\beta} \cdot \left[\left(\frac{\sigma_{\alpha\beta}}{r} \right)^{12} - \left(\frac{\sigma_{\alpha\beta}}{r} \right)^{6} \right] \tag{1.16}$$

with α and β referring to the chemicals element involved. The parameters for the pure systems were $\epsilon_{ArAr} = 0.996$ kJ/mol , $\sigma_{ArAr} = 3.405$ Å, $\epsilon_{KrKr} = 1.33$ kJ/mol and $\sigma_{KrKr} = 3.636$ Å(respectively taken from [53] and [54]). The parameters for the interactions between distinct species obey the Lorentz-Berthelot rules, i.e. $\epsilon_{ArKr} = \sqrt{\epsilon_{ArAr}\,\epsilon_{KrKr}}$ and $\sigma_{ArKr} = (\sigma_{ArAr} + \sigma_{KrKr})/2$. The potential cut-off was set at 20.4 Å(equal to about $6\,\sigma_{Ar}$) for all simulated systems, much larger than what is usually done; a significant subset of all the

simulations was then run with a smaller cutoff (13.6 Å), finding equivalent results. Note that we have also carried a relevant number the simulations using a more accurate pair potential, i.e. Aziz's one [55]. The results did not vary appreciably, thus we decided to get back to LJ interaction, which is simpler and more general. The atomic masses were set to $m_{Ar} = 39.948$ and $m_{Kr} = 83.798$ amu.

Concerning the time–integration of the atomic coordinates, the standard velocity Verlet integration scheme with a time step of 2 fs was employed. The neighbor list for each atom was updated every 10 steps, after checking if any atom has moved beyond half the skin distance (equal to $0.5\,\sigma_{Ar}$).

The typical simulation box for the growth of the (100) surface was constituted by $36 \times 8 \times 8$ conventional unit cells, where a unit cubic cell's side is equal to the target lattice constant. Being our reference lattice a fcc (i.e. in each conventional cell two distinct atomic planes are present), it means that a perfect crystal of $72 \times 16 \times 16$ layers could be exactly hosted in our simulation box, corresponding to a total of 9216 atoms at the beginning of the simulation. Conversely, for the growth along the (111) direction, 8640 atoms were found in the initial box, constituted by $36 \times 10 \times 6$ unit cells (in this case, the scaling factors for each axis were chosen to provide almost cubic unit cells). This, again, is equivalent to have $72 \times 20 \times 12$ layers. The details about LAMMPS implementation of these oriented crystals are given in Appendix B.

To rule out size effects, we also performed more computationally demanding simulations with larger systems containing 20736 atoms, finding similar results. However, aiming to get the output of our computations within a reasonable amount of time, it is necessary to time–integrate a lower number of atoms (as exposed above). This corresponds to a simulation box of a few tens of nanometers, which is about 10^3 times less than the experimental diameter of the filament. Therefore, our simulations will be able to reproduce only what happens in a small part of the jet: nonetheless, the three–dimensional Periodic Boundary Conditions (PBC) guarantee that our small box is infinitely replicated in the space, thus strengthening the validity of our findings.

1.4.2 Simulation details and methods

Here follows a brief sketch of the schedule of the MD simulations (valid for (100) and (111) growth directions both):

(i) start from a perfect fcc crystal, made by 72 single–atom layers orthogonal to x axis

(ii) keep the 4 central layers at the target crystal density (established from experimental data), and expand the remainder up to a liquid typical

density, increasing the distance between consecutive layers (see Table 1.2)

(iii) melt all the system at a $T > T_{\text{melting}}$, except for the inner solid slabs, and equilibrate the high–temperature liquid for 8×10^3 fs, during which the central seed retained its crystal structure because of an harmonic confinement (see below)

(iv) perform the supercooling of the liquid, so to bring it out of equilibrium. This takes about 100 fs, having to be extremely fast with respect to the typical timescales of the system.

(v) let the supercooled system evolve in time, so to observe its solidification (as detailed below). Due to the layout of the simulation box, our systems crystallize via the stacking of layers one on the top of the previous ones, starting from the inner seed.

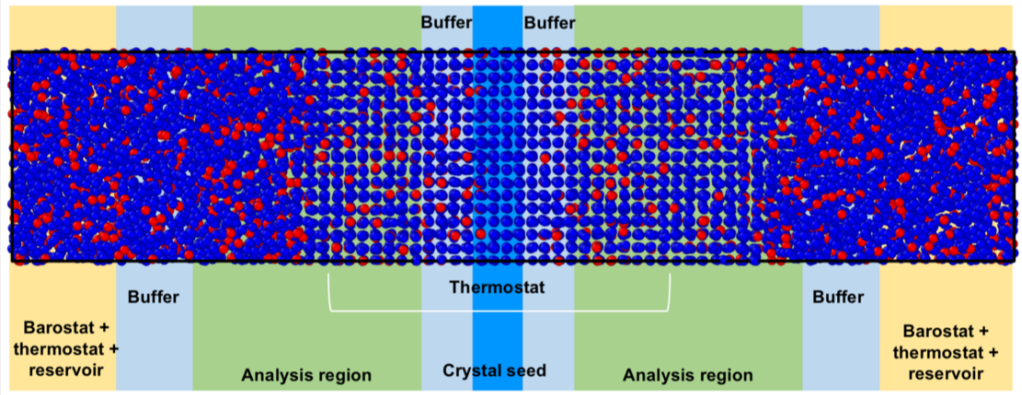

FIGURE 1.10: Example of our typical simulation box, projected on xy plane. There are about 10^4 atoms. Background colors mark the different regions.

Let us get deeper into the description of the computational setup, referring to Fig. 1.10. We underline that the box has an elongated geometry, with the x axis much longer than the other directions, aiming at a better measurement of the crystal growth rate along the (100) face (analogous to the (200) experimental one), and along the (111) face, for comparison with the two main experimental sources of signal. From Fig. 1.10, the box is evidently built in a symmetric fashion, with the crystal seed in the middle and two independent crystals growing at the two sides, left and right. The motivation for this is that, aiming to investigate the highest possible number of statistically independent configurations, in this way we can exploit a single MD run for collecting two uncorrelated set of data. This is possible thanks

to the fact that the crystal growth on each side of the crystalline wall is not influenced by the growth on the other side.

The following description holds, then, for both halves of the box, on each side of the central crystal seed.

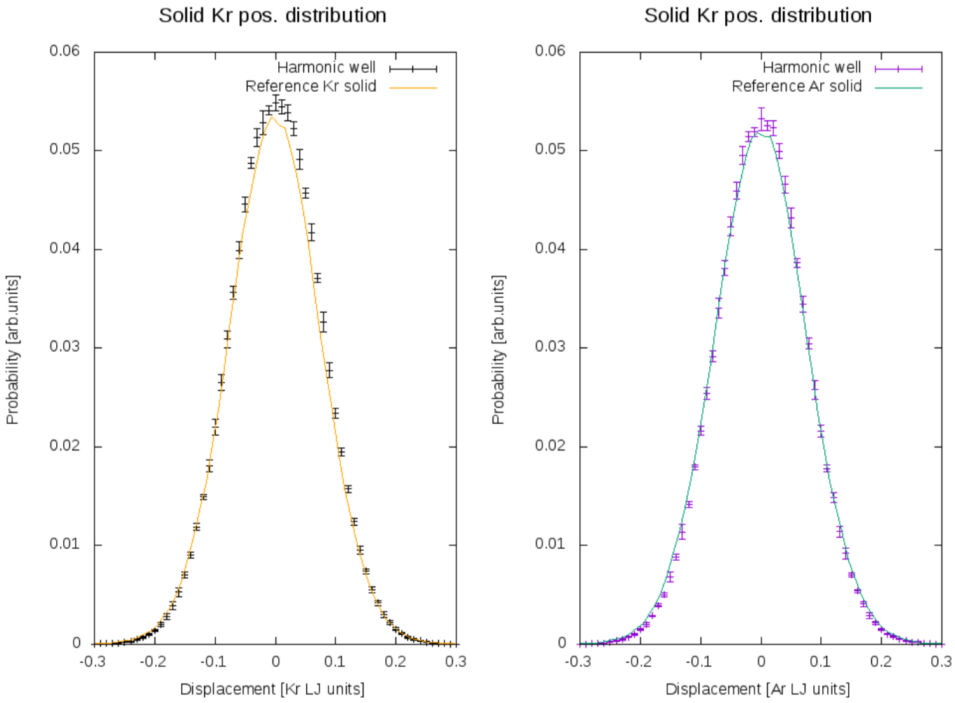

FIGURE 1.11: Solid lines: distributions of the displacements of solid–like atoms in perfect fcc Krypton (left) and Argon (right crystals), with respect to their own equilibrium positions. Data points: distributions of the same displacements for atoms confined via harmonic wells.

- The *crystalline seed* is composed of 4 layers (2 on each half), with a fcc perfect crystalline geometry; the spacing between two consecutive layers is equal to half the target lattice constant of each mixture (blue background area in Fig. 1.10). The particles of the seed mutually interacted via the standard Lennard–Jones potential, but they were additionally confined to their equilibrium positions by a single–particle harmonic potential whose elastic constant was pre–determined to reproduce the average atomic positions of a reference crystalline fcc phase at fixed temperature. At the beginning, the density here is higher (i.e. it is the density of the target crystal) than in the rest of the system: these slabs are intended to act as a guidance for the crystal growth process of all

the other atoms. Note that the central crystalline seed was made of either pure argon, for argon-rich systems, or pure krypton, for krypton-rich systems. In particular, the LAMMPS command `fix spring/self` served to this purpose. At each MD timestep, the magnitude of the elastic three-dimensional force on each atom is $F_{spring} = -k_{spring} r$, where r is the displacement of the atom with respect to its initial position. The elastic constant k_{spring} here is a free fit parameter: the aim was to find the right value for k_{spring} such that the average position distribution of the atoms confined by the harmonical well closely resembled the one of a typical crystal phase (previously simulated as a reference). In Fig. 1.11 it is reported the distribution of the displacements of the atoms confined to their equilibrium positions by springs with suitable k_{spring} values, in black (left) and purple (right) dots, with their own errorbars. Solid orange and green lines represent, respectively, the same quantity calculated for atoms in a perfect fcc crystal, simulated in the same thermodynamic conditions with MD.

In the end, the harmonic constant for Krypton is 2.088 Kcal/mol Å^2 , while for Argon it is 1.776 Kcal/mol Å^2.

- It follows a thin region used as a *buffer* (the x-width of this zone is equal to 2 lattice steps), where the measurements of the physical observables are not used for output, due to the proximity to the crystal seed. In this way, also the measurement of the crystal growth rate in the simulations should not be seriously biased by the presence of the inner wall.

- Then the *analysis region* is found (green background areas in Fig. 1.10); at each MD step, the atoms belonging to this region are the only ones actually contributing to the calculation of the physical interesting quantities. The x-width of this zone is equal to 9 lattice constants (i.e. 18 layers, once the crystal is fully formed). The number of atoms comprised in this volume is not constant, because particles are free to enter and exit this regions. Therefore, this number must be recovered at each step, in order to normalize the observables calculated.

  Here, all the atoms were time–evolved in a microcanonical ensemble; in addition, a Bussi–Parrinello thermostat [56] was employed for draining from the box the extra–energy due to the latent crystallization heat. This thermostat was initially applied only to the crystal seed and the related buffer regions; during the simulation, this 'adaptive thermostat' was also progressively applied to a growing volume in the analysis zone. In this way, the stability of the crystal layers as–solidified should not be affected too much by the slight increase in temperature present at the crystal–liquid interface (i.e. the latent solidification heat). For each mixture, we first estimated a reasonable growth rate and then we

ran all the respective simulations with a lower rate of the expansion of the thermostatted area. A too fast adaptive thermostat would indeed precede the crystal front (CF) propagation, thus haltering the physical process. The atoms in the analysis region were then time–integrated at constant atom number, volume and energy, but with this additional adaptive thermostat following the CF movement towards outermost regions.

- After the analysis region, another *buffer* (light blue background in the picture) is found, so to separate the analysis region from the external part of the box. Again, the atoms found here do not contribute to the calculation of any of the observables that are being analyzed after the simulations.

- Last, the outermost zone of the box (the so called *control region*) plays a fundamental role in guaranteeing a *uniform* crystallization process, which would in turn ensure a good set of growth rates measurements. The control region, in fact, acts as a particle reservoir, barostat, and thermostat (for a comparison with similar MD methods, see e.g. [6, 12, 21, 51, 52]). Consider that, as long as more and more atoms join the growing crystal front, the liquid is deprived of particles. It is then mandatory to have an external reservoir of atoms, so to guarantee a continuous supply of particles of both chemical elements; not only, it was also necessary to maintain approximately constant pressure and temperature in the control region. In this way, not only the composition of the mixture is almost exactly preserved, but, more importantly, the crystal growth conditions are uniform for the whole duration of the simulation.

  From a computational point of view, the control over the chemical potential is achieved via the random insertion of new particles in the control regions (see Appendix B). These new particles have an initial velocity compatible with the temperature of the control regions, are tentatively inserted in empty points of these regions (the trial is rejected in case of overlaps) and their type is chosen randomly so to preserve the mixture composition. We highlight that this tool is separately activated in the left and right control regions. In any case, it is activated only if the number of atoms in these regions is below the target one, calculated via the equation:

$$N_{\text{target}} = \rho_{\text{liquid}} \cdot n_z \cdot n_y \cdot n'_x \cdot V_{\text{unit cell}}$$

  where n'_x is the number of unit cells along the x axis (limited to the control region and its buffer), while n_y and n_z represent the (fixed) number of unit cells along the other axes. The densities here have to

read as numerical ones. The uniform crystal growth was achieved also through the application of a Berendsen barostat [57] acting only on the x coordinate of the atoms found in the control region. The y and z dimensions of the box are kept constant, while the x axis, orthogonal to the growing surface, adapts to the ongoing process: the mathematical restraint is $P = 0$ in the whole box, where P is the total scalar pressure measured at each step. It is worth stressing that the trajectories of the atoms in the analysis region are not affected by the barostat corrections, which are effective only for the atoms found in the control region. The parameters of the barostat (i.e. the stress damping parameter and the bulk modulus of the system, for the LAMMPS `fix press/berendsen` instruction) were chosen after many tests; a slight variation of their numerical values yields however similar results. Additionally, the control regions are thermostatted via a Bussi–Parrinello thermostat. The amount of particles in the control regions, clearly, increases with time: we end up with more particles than the initial number. The final x dimension of these regions is also smaller than at the beginning, due to the box shrinkage upon crystallization of the inner volume. One could state that our simulations are then approximately performed at constant *chemical potential*, *pressure* and *temperature*, even if the corrections effectively take place only in the control volumes. As a general check that all this computational machinery was effectively providing an approximately uniform crystal growth, the pressure of the liquid subregion in the analysis region was monitored. In particular, for a relevant subset of all the simulations performed, we computed the average pressure of those atoms whose x coordinate was greater than the x coordinate of the crystal front at that step, finding that this pressure was very small and essentially constant along the duration of the MD simulation. This guaranteed us that our setup was effectively able to accommodate a physically reasonable crystal growth. As a consequence, we could exactly locate the solid–liquid interface position inside the simulation box step by step (see next section for the corresponding mathematical criterion). These almost homogeneous conditions of the bulk supercooled liquid allowed us to safely perform averages of the growth rate taking different spatial positions.

With the input parameters reported in Table 1.2, the time for crystallization of the supercooled liquid varied between $\sim 3.6 \times 10^5$ fs for pure argon and $\sim 2.2 \times 10^6$ fs for the $x_{Kr} = 0.4$ mixture.

See Appendix B for the whole LAMMPS input script, with comments.

x_{Kr}	(100) Lattice constant (Å)	ρ (g cm $^{-3}$)	$T(x_{Kr})$ (K)
0	5.44755	1.461	74.7
0.03	5.45839	1.49307	75.6
0.07	5.48366	1.53583	76.7
0.15	5.52351	1.62135	79.0
0.4	5.62953	1.886	86.2
0.85	5.77935	2.36965	99.1
0.93	5.79966	2.45517	101.4
1	5.81686	2.530	103.4

TABLE 1.2: Physical input parameters for the MD simulations. The density refers to the that of the supercooled liquid. The temperatures of the simulated systems correspond to the linear fit $T(x_{Kr}) = 74.7 + 28.7 \times x_{Kr}(K)$ to the experimental data shown in Fig. 1.9

1.5 Analysis of the atomic configurations

All the MD trajectories obtained via LAMMPS simulations were analyzed aiming to obtain the crystal growth rates as a function of Kr mole fraction, starting from the atomic configurations produced.

1.5.1 Local Bond Order Parameters

In this regard, the Local Bond Order Parameters (LBOP) and their Averaged (ALBOP) version represent a very effective tool for inspecting of the angular order in atomic systems. These order parameters, originally introduced by Steinhardt *et al.* [58], are linear combinations of the spherical harmonics able to identify the crystal structures around each atom. The Averaged LBOP were introduced by Lechner *et al.* [59], and they were shown to be even better in distinguishing the various possible types of crystal lattices. Here follows a brief mathematical description of these parameters, valid for a generic system. Later, we will explain how they have been exploited in this research; their role as order parameters for MD-simulated configurations has become a well–established standard (see e.g. [60]), but in the present work the ALBOP were used in some innovative ways.

First of all, define the components of the $(2l+1)$–dimensional complex vector $\mathbf{q}_l(i)$

$$q_{lm}(i) = \frac{1}{N_b(i)} \sum_{j=1}^{N_b(i)} Y_{lm}\left(\theta\left(\mathbf{r}_{ij}\right), \phi\left(\mathbf{r}_{ij}\right)\right) \tag{1.17}$$

where $N_b(i)$ is the number of first neighbors of particle i (usually the maximum number is 12, which is the case of a close-packed configuration [61]) l

is a free integer (eigenvalue of square angular momentum - its correspondent eigenvalues for $\mathbf{L}$ run from -m to m), the functions Y_{lm} are the spherical harmonics and the 3D distance between particles i and j is represented by vector $\mathbf{r}_{ij}$. The quantum rotational number l can only be chosen even [58], due to the fact that we target quantities which are invariant under spatial inversion. Steinhardt parameters can identify crystal particles inside a liquid and they are defined as follows:

$$q_l(i) = \sqrt{\frac{4\pi}{2l+1} \sum_{m=-l}^{l} |q_{lm}(i)|^2} \tag{1.18}$$

with q_{lm} as in eq. 1.17. The key features of these parameters are the independence from the reference frame (they only depend on the angles between the vectors to the neighboring atoms - i.e. they are rotational invariants) and the possibility to distinguish between various crystal symmetries. For example, as it will be shown in the following, the typical q_6 values of crystalline structures are much higher than those of a liquid phase. Once introduced the q_l, the following scalar product is defined:

$$S(i,j) = \sum_{m=-6}^{6} q_{6m}(i) q_{6m}^*(j) \tag{1.19}$$

which brings information about the correlation between structures belonging to i's environment and those surrounding its neighbors j. The neighbors are selected through a Delaunay triangulation, within a sphere of given cutoff radius (in this work, it is 5.1 Å, equal to 1.5 σ_{Ar}). Usually, S_{ij} is normalized as:

$$s(i,j) = \frac{S(i,j)}{|\mathbf{q}_6(i)||\mathbf{q}_6(j)|} \tag{1.20}$$

with $s(i,j)$ carrying information about the bond between atoms i and j (clearly, this bond is not related to chemical bonding, this is just structural ordering). Conventionally, if s_{ij} is greater than a given value ($s(i,j) = 0.7$ in the present work, in general a value in the range 0.5-0.7 is used [61, 62]) the bond between atoms i and j is considered crystalline, i.e. the two atoms are said to be *connected*. In this way, each atom i has its own list of $s(i,j)$ values with its neighbors j; this means that $s(i,j)$ is an array, thus difficult to be represented in a picture or even analyzed. We could then get rid of the j dependence taking the sum over that index:

$$S(i) = \sum_{j=1}^{N_b(i)} s(i,j) = \sum_{j=1}^{N_b(i)} \frac{\mathbf{q}_6(i) \cdot \mathbf{q}_6(j)}{|\mathbf{q}_6(i)|\,|\mathbf{q}_6(j)|} \tag{1.21}$$

thus defining a scalar parameter computable for each atom, called *structural order parameter*. Here, the same idea of the threshold introduced for $s(i,j)$

also holds, with the same values. When there are more than a certain number of connections involving the i-th atom (typically 6, 7 or 8, depending on the chosen threshold) that particle is classified as solid-like. Other useful quantities, which are often together q_l, are the w_l parameters, defined as follows:

$$w_l(i) = \sum_{m_1,m_2,m_3} \begin{pmatrix} l & l & l \\ m_1 & m_2 & m_3 \end{pmatrix} q_{lm_1} q_{lm_2} q_{lm_3} \tag{1.22}$$

and their normalized variants:

$$\hat{w}_l = \frac{w_l}{\left(\sum_m |q_{lm}|^2\right)^{3/2}} \tag{1.23}$$

where the parentheses stand for the so-called Wigner $3j$ symbol, which can be calculated using the Racah formula. Omitting the mathematical details (that can be found e.g. here https://mathworld.wolfram.com/Wigner3j-Symbol.html), it should be underlined that the values assumed from w_6 are especially interesting, since w_6 is a good signal of the presence of icosahedral arrangements within the sample [58]. Icosahedra are low–energy structures but, unfortunately, not able to completely fill the space. They usually induce geometric frustration within crystallizing liquid samples; according to some theoretical models [9] this is the main reason behind the crystallization slowdown observed in some systems [62]. In Steinhardt's picture, for a perfect icosahedron we have $\hat{w}_6^{icos} = -0.169754$ while other crystals exhibit lower absolute values $\hat{w}_6^{fcc} = -0.013161$, $\hat{w}_6^{hcp} = -0.012442$. Note that others, e.g. Leocmach *et al.* [62], use w_6 and not $\hat{w}_6$ in their investigation for the possible presence of icosahedra and work then with different values, such as $w_6^{icos} = -0.023$. In this work, we will adopt the choice of Steinhardt and $\hat{w}_4$ and $\hat{w}_6$ will be employed. In 2008, Lechner *et al.* improved this set of angular parameters by defining their averaged (ALBOP) version [59]. In fact, they considered an average of q_{lm} over the neighbors of the atom i plus i itself:

$$Q_{lm} = \frac{1}{\tilde{N}_b(i)} \sum_{k=0}^{\tilde{N}_b(i)} q_{lm}(k) \tag{1.24}$$

with $\tilde{N}_b(i)$ representing exactly i and its neighbors. One can then explicit the other Averaged Local Bond Order Parameters as:

$$Q_l(i) = \sqrt{\frac{4\pi}{2l+1} \sum_{m=-l}^{l} |Q_{lm}(i)|^2} \tag{1.25}$$

and

$$W_l(i) = \sum_{m_1,m_2,m_3} \begin{pmatrix} l & l & l \\ m_1 & m_2 & m_3 \end{pmatrix} Q_{lm_1} Q_{lm_2} Q_{lm_3} \tag{1.26}$$

analogous to what was done with the original Steinhardt parameters. In practice, you are averaging the local orientational order vectors q_{lm} over i and its first–neighbors shell; in this way, one is taking into account also the second shell of atoms surrounding the particle under consideration. These ALBOP have proven to be much better in distinguishing liquid from crystalline (bcc, hcp or fcc) order [59]. We verified with our own MD simulations the validity of the typical ranges proper of these Q_l and W_l parameters they report. In particular, reasonable intervals of Q_4 and Q_6 corresponding to the main lattice geometries are synthesized in Tab. 1.3.

lattice	Q_4 **range**	Q_6 **range**
liquid	0.015-0.06	0.09-0.31
bcc	0.015-0.07	0.36-0.44
fcc	0.125-0.18	0.43-0.55
hcp	0.07-0.11	0.38-0.45

TABLE 1.3: Typical range of Q_4 and Q_6 parameters, based on [59] and on our own MD simulations.

In this work, these parameters have been repeatedly used in several ways for the analysis of the configurations generated via the MD simulations. The main exploitation of the ALBOP here concerns $S(i)$, whose values typically range from ~ 0.2 for a disordered liquid to ~ 0.9 for a solid (1 for a perfect crystal). After the calculation, for every frame, of the $S(i)$ of each atom, we spatially averaged this parameter, defining its layer average S_l. Note that a 'layer' here stands for a spatial bin, with x-width equal to the target lattice constant and y and z dimensions equal to the full corresponding box sides. This calculation allowed us to examine the time evolution of the crystal growth of each portion of the analysis region as a function of time. In Fig. 1.12 two systems are compared: a pure Ar simulation vs a 40% Kr - 60% Ar one. For each system, the time evolution of the various S_l calculated in each simulation is shown. We represent here just a half of the box, and only the odd–index layers for a better view. It is apparent that, for the mixture (right panel), it takes much more time to complete the crystallization of the analysis region. Obviously, this is just a comparison between two single MD runs and it lacks any statistical relevance, but it clearly highlights that the two mixtures experience quite a different path towards crystallization (similar results hold for the even–index layers). Apparently, the growth of each S_l is not always monotonic; sometimes S_l gets lower as a function of time, and then it increases again. These 'uncertainties' in the crystallization process are an interesting feature, and part of this research was dedicated to a statistical study of these collapses in S_l time evolution. In particular, a classification of the so–called 'drops' and 'rises' of S_l (growths and decreases of S_l as a

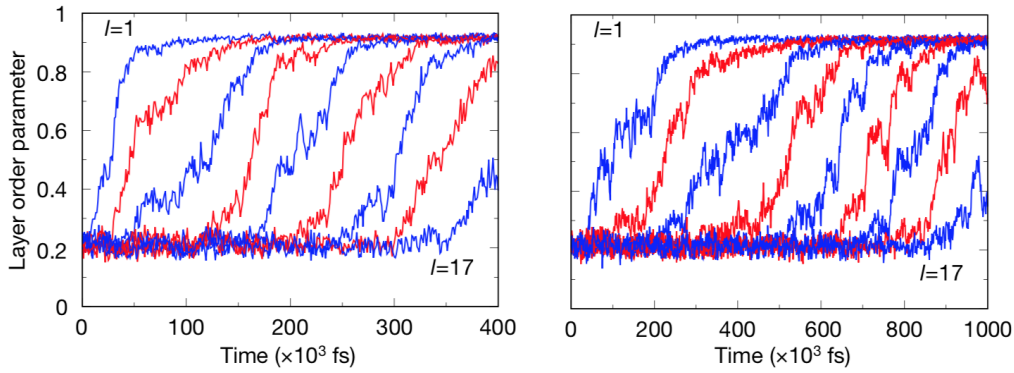

FIGURE 1.12: Order parameter $S(i)$ averaged over one layer (i.e. S_l) shown as a function of time for the odd–index layers for a pure argon MD simulation (left panel) and a simulation of the $x_{Kr} = 0.4$ mixture (right panel). Note the different time-axis ranges in the left and right panels. Blue and red colors are used for clarity.

function of time) was attempted, but it did not yield any clear indication of differences among the various systems studied. It was not possible to detect any systematic trend or effect dependent on x_{Kr}, neither in the duration nor in the frequency of these sudden decreases of S_l. In a simplified picture, they correspond to fluctuations of the crystal–liquid interface, that are present in any mixture. But the structural order parameter was the key ingredient for the computation of the crystal growth rate. A very recent article by Ouyang *et al.* [60] suggest an alternative approach to measure the growth rate by using the linear fit to the temporal evolution of the growing nucleus radius (their simulations include part of the nucleation process), but exploiting S seemed to us a choice with a rich physical meaning. To this extent, we labeled a layer with index l as the crystal front if the crystallinity condition $S(i) \geq 0.7$ was satisfied by at least 50% of the atoms belonging to the two layers with indices l and $l-1$. In this way, we were able to locate, for every MD configuration, the CF in the left and right halves of the box both. The requirement that also the layer $l-1$ satisfies the same condition on $S(i)$ was found to be necessary for high mixing ratio systems with very unstable and irregular crystal–liquid interfaces. (One could think to the mixing ratio as equal to x_{Kr}/x_{Ar} if $x_{Ar} > x_{Kr}$, and vice versa. A null mixing ratio indicates a mono–component system, while a mixing ratio approaching 1 describes an equimolar binary system.) Indicating by τ_l^{CF} the time at which the layer of index l became the crystal front, we computed the crystal growth rate

according to

$$u_{l'} = \frac{L}{\tau^{\mathrm{CF}}_{l'+9} - \tau^{\mathrm{CF}}_{l'}} \tag{1.27}$$

with $l' = 1, \ldots, 9$, and where L is half the length of the analysis region. In this way, we obtained a total of 18 independent estimations of the crystal growth rate for each simulation run, 9 for each half of the box. Therefore, we obtained a full set of crystal growth rates as a function of the mixing ratio x_{Kr}, to be compared with the experimental data.

1.6 Simulated crystal growth rates

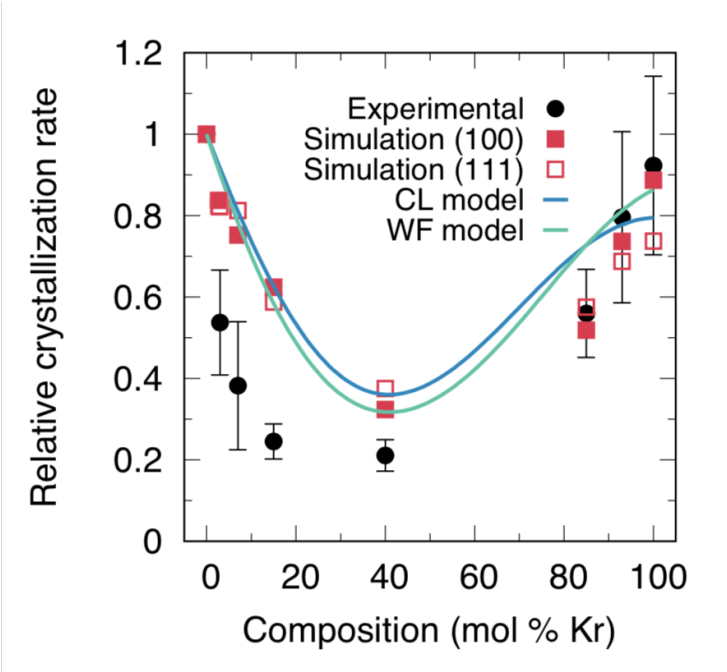

FIGURE 1.13: Reduced experimental (black circles) and MD–simulated (empty and filled red squares, according to the growth surface) crystal growth rates, compared with CL (blue line) and WF (green line) models.

In Fig. 1.13 are collected the data from the simulations of the crystal growth along (100) and (111) surfaces both. For each mixture and for both growth directions simulated, the value shown in the picture is the ratio between absolute growth rate (in m/s) divided by the corresponding value for the pure Argon system (13.3 and 8.0 m/s for (100) and (111) surfaces respectively), so to deal only with the relative growth rates.

x_{Kr}	$u_{(100)}$ [m/s]	$u_{(111)}$ [m/s]
0	13.3 ± 0.4	8.0 ± 0.2
0.03	11.1 ± 0.1	6.6 ± 0.1
0.07	10 ± 0.1	6.5 ± 0.2
0.15	8.3 ± 0.4	4.7 ± 0.1
0.4	4.3 ± 0.2	3.1 ± 0.1
0.85	6.9 ± 0.1	4.6 ± 0.2
0.93	9.8 ± 0.4	5.5 ± 0.2
1	11.8 ± 0.2	5.9 ± 0.4

TABLE 1.4: Absolute crystal growth rates from MD simulations, obtained via eq. 1.27, for (100) and (111) axes.

First of all, the reader should take into account that the experiments are extremely different from the simulations. In fact, the crystal growth observed in the experiment is mixed together with the crystal nucleation; moreover, in the real sample there are lots of crystallites growing in several directions. Conversely, MD simulations provide an incredibly 'clean' environment: PBC impose the growth of a lattice with a given geometry, there are not many sources of noise, the latent heat is efficiently dissipated and the system is quite small, if compared to the typical experimental sample. Thus, the mere *qualitative* agreement between computational and experimental growth rates is remarkable. The growth rates calculated from the MD runs display a concave shape as a function of x_{Kr}, even if the Ar–rich systems crystallize more rapidly in the computer simulations than in the experimental measurements. Nonetheless, the trend is much similar, the pure Ar system is the fastest and the 40%-60% mixture is the slowest in both cases. The growth along (100) and (111) is, obviously, different for what concerns the absolute values, but the relative growth rates do not exhibit any significant different trend. Tab. 1.4 collects the numerical values for crystal growth rates of the mixtures.

The most important feature, i.e. the slowdown of the crystal growth rate u upon increasing the mixing ratio, is anyway present in these simulations. Thus, our computational setup allowed us to retrieve the key ingredients of the experiments: our Molecular Dynamics machinery is not an exact copy of the experimental sample, but rather a precious tool for capturing the relevant details. The MD runs and their analysis show furthermore that this phenomenology can not be attributable to a mere temperature effect: the pure krypton is found at a higher temperature than the $x_{Kr} = 0.4$ mixture but $u(x_{Kr} = 1) \simeq 1/3u(x_{Kr} = 0.4)$.

Let us move to the comparison of our experimental and computational crystal growth rates with the analytical models (see eq. 1.2 and eq. 1.4).

Looking at the solid curves in Fig. 1.13, it appears that the simulation results agree reasonably well with the theoretical calculations, without evidencing any significant difference between the mechanisms underlying the crystal growth rates of the two surfaces. Concerning absolute growth rates (see Tab. 1.4), instead, the growth along (111) was found to be systematically slower than the growth along (100). This could be argued from the fact that many stacking faults can form while growing the (111) surface. In fact, along this direction, hcp and fcc slabs can easily alternate, leading to mismatches (see for example Fig. 1.21 in the following, for a more detailed discussion about this) and a general slowdown of the process. The random alternation of fcc–like and hcp–like layers originates the so called random hexagonal close–packed (rhcp) structure. Once again, as for the comparison between experimental data and theoretical calculations, there are no evidences that either the WF or the CL models fit definitely better the data. It was then fundamental to make a step further, comparing our growth rates with the models under a different perspective. In particular, if one takes into account the fact that eq. 1.1 describe u as a function of x_{Kr} and T both, the importance of a comparison with u as a function of temperature becomes clear.

Therefore, we now turn to the analysis of the temperature dependence of the simulated crystal growth rates of the surface (100), plotted in Figs. 1.15a and 1.15b for five representative systems, together with the CL and WF models respectively (solid lines). It is worth to stress here that this comparison would not be possible, if it was not for the computational growth rates. In fact, in the experiments we can not modify the temperature of the sample as we wish. On the contrary, MD simulations allow to set up the target crystal lattice and all the other parameters, so to reach the desired temperature. As a consequence, we widely explored a temperature range of some tens of K for each mixture. Going to lower T correspond to a deeper supercooling degree (a regime where classical theories are particularly known to fail, as highlighted e.g. by Sun *et al.*, [12]), clearly unreachable in the experiments. We also studied some cases at temperatures higher than the experimental estimations. Let us provide some more details about these simulations: some physical input parameters, such as the lattice constant, strongly depend on the temperature at which the simulation is conducted. From the experiments, the lattice step a is only available at a given T. Therefore, for each temperature T investigated only in the simulations and not in the experiments, we had to determine $a(T)$. For each x_{Kr} and T, the method used was to equilibrate a system of 512 particles, coupled to an external barostat (imposing $P = 0$) and thermostat. The equilibrium lattice constant a reached in this way was used as input for the large–scale simulations of the crystal growth. Then, each of this new computer simulations was analyzed via the same tools exposed in the previous section. In Appendix D it is possible to find the table (Tab. D.1) with the lattice steps (for the growth perpendicular to the (100)

face) used for the simulations of the mixtures at temperatures different from the experimental estimated T. It should be considered that, in order to bring the system to the desired temperature after the supercooling, some parameters in the supercooling process itself have to be modified. In particular (see Appendix B), the variable `T_scale` had to be varied accordingly. Details are not provided here, because it is just a matter of computational tricks and not a physically relevant problem. The last parameter that we had to adjust was the expansion rate of the adaptive thermostat, empirically found for each mixture. Crystal growth rates were thus calculated for each of these systems in the way described in the previous section, via eq. 1.27.

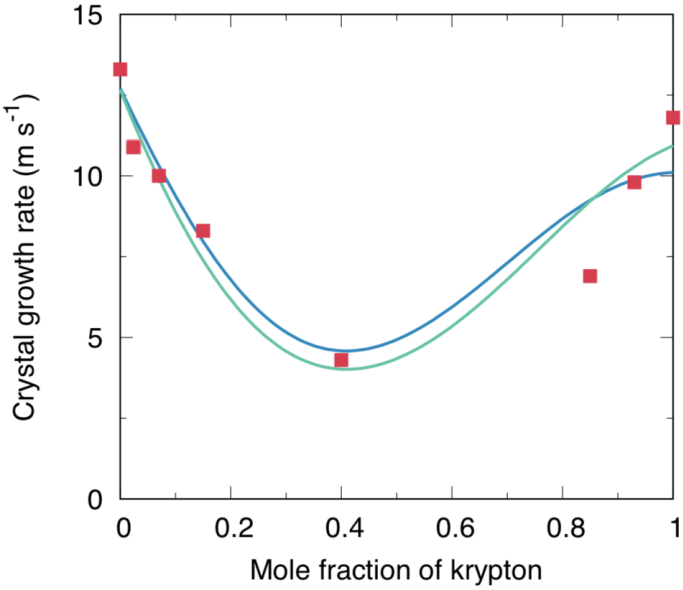

FIGURE 1.14: The red symbols are the absolute simulated crystal growth rates of the (100) surface at the interpolated temperature $T(x)$ (see Fig. 1.9). The solid lines are fits of the CL (blue) and WF (green) models, to the simulated absolute crystal growth rates with f/c and f/c^2 as fit parameters, respectively. Reprinted from [5]

Here, it is worth underlining that the comparison will take place between the simulated and theoretical *absolute* crystal growth velocities. One consequence of this fact is that some parameters that are not relevant when considering relative growth rates, have now to be determined. More precisely, we need to determine f and the proportionality constant c relating $\Lambda(T)$ with the lattice step $a(T)$. We determined the unknown parameters f/c^2 and f/c of the WF and CL models, respectively, by fitting u_{Kr} in either case to the simulated crystal growth rates, obtaining $f/c^2 = 31.4$ and $f/c =$

1.8 (see Fig. 1.14).

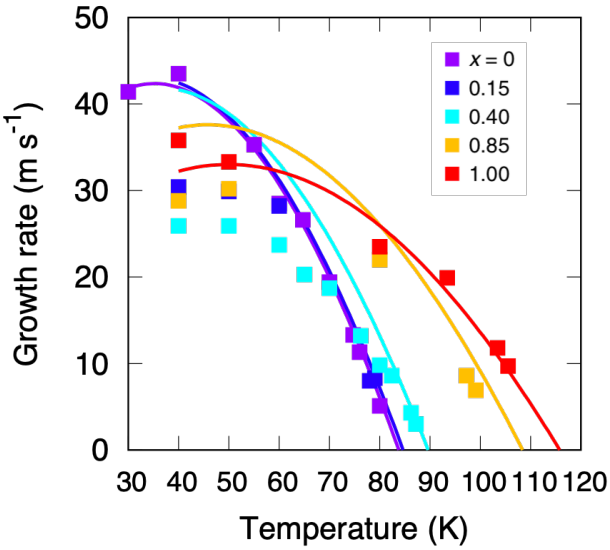

(a)

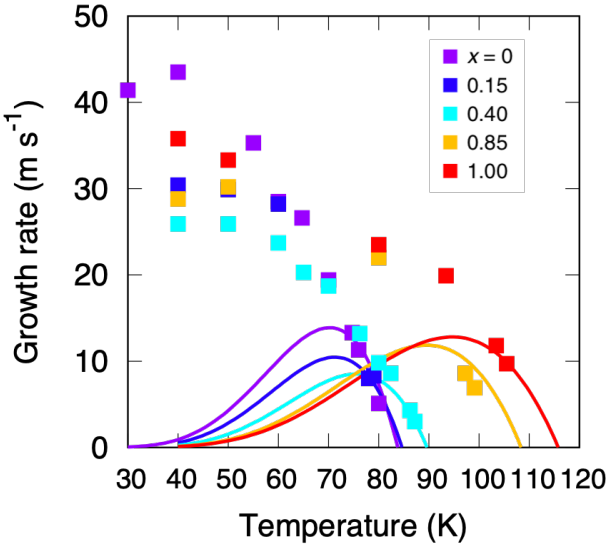

(b)

FIGURE 1.15: Simulated $u(T)$ along (100) in m/s, for five representative mixtures, colored based on the mixing ratio. Solid lines are the theoretical calculations for the CL (top) and the WF models (bottom). Reprinted from [5]

In this part of the study, we restricted ourselves to the investigation of five

systems, i.e. the pure Ar and Kr and the three mixtures where the effects of a second component are more evident. This choice, then, resulted as a compromise between the computational weight of these simulations and the highest crystallization slowdown detected in samples with higher mixing ratio. Concerning the comparison with the CL model (Fig. 1.15a), it is interesting to note that the pure Ar and Kr data are described almost perfectly by the theoretical function (violet and red solid lines). Conversely, the mixtures tend to deviate from the model already at intermediate supercoolings. The model overestimates the growth rates, and the discrepancy with the simulated growth rates increases at lower temperatures. In particular, the maximum theoretical crystal growth rate predicted for the $x_{Kr} = 0.4$ mixture (cyan solid line) is roughly 80% larger than that found in the simulations. Note that in these calculations we used the slightly different value $f/c = 1.9$, as obtained independently by a direct fit of the CL model to the temperature dependence of the simulated crystal growth rates of pure argon.

The WF model, instead, fails already at small supercoolings also for $x_{Kr} = 0$ and $x_{Kr} = 1$, let alone the mixtures (see Fig. 1.15b). The shape of $u(T)$ described by diffusion–limited model is completely different from our results, thus indicating the total inadequacy of these formulas in this case. This failure of the WF model was already detected for other systems such as simpler monoatomic LJ liquids [25]. All these features are fully retrieved for the growth along (111) direction, where the models behave in a much similar way. We shall also note that, as already discussed for the analysis of u_{Kr} (Fig. 1.8), the attachment rate ν could also be calculated weighing over thermal velocities and not over the masses of the pure substances. In this case, it turns out that the $u(T)$ curves of CL and WF models would not be appreciably modified. Therefore, apparently, the collision–limited framework works well only for pure systems while the diffusion–limited theory is not able to describe the crystal growth in any case. The situation is not different from the various examples of metallic systems, e.g., described at the beginning of this work: the experimental and/or simulated growth rates are irreconcilable with the models. Our results and subsequent analysis provide in fact clear evidence that neither the WF nor the CL model can properly describe the crystal growth kinetics in the simplest supercooled atomic liquid mixtures of the present study. Are both models wrong? We are certainly missing some key ingredient.

1.7 Extended collision–limited model

The CL model, at least, provides a reasonably accurate description for the crystal growth in mono–component systems. Therefore, our guess was that an appropriate modification of eq. 1.4 could continue to describe correctly the

pure systems and also be predictive about the mixtures. As a consequence, we wondered about how to extend the CL formula for crystal growth rates.

To this extent, a central intuition was that Ar-Kr binary systems had been treated as being *ideal* mixtures. We introduced *non–ideality* in the model, so to modify the crystal addition rate accordingly. The essential idea is to multiply ν by a factor accounting for the non–ideal effects. In particular, this multiplicative correction is the same approach that could be used for the diffusion coefficient of non–ideal binary mixtures. We clarify that diffusion here is not involved at all, but it is just invoked for the sake of comparison. Eq. 1.3 assumes that a geometric average is a good formula for diffusion in an ideal system with components A and B. Non–ideality is usually embodied in such a formula by multiplying the previous expression by a multiplicative factor Φ:

$$D_{\text{non-ideal}}(x_A, T) = [D_A^x(T)]\,[D_B^{1-x}(T)]\,\Phi \tag{1.28}$$

where

$$\Phi = 1 + x_\alpha \frac{\partial \ln \gamma_\alpha^{\mathrm{L}}}{\partial x_\alpha} \tag{1.29}$$

with x_α is the mole fraction of each species α and $\gamma_\alpha^{\mathrm{L}}$ represents the activity coefficient [35]. The multiplicative correction by the factor Φ is known to be effective for taking into account non–idealities in diffusion coefficients, so we finally applied the same correction to ν in eq. 1.4 and developed a *modified collision–limited model*. Therefore, a modified CL crystal addition rate can be defined as:

$$\widetilde{\nu}_{\mathrm{CL}}(T) = \nu_{\mathrm{CL}}(T)\Phi \tag{1.30}$$

and employed in eq. 1.1. Note that, by construction, $\widetilde{\nu}(T) = \nu(T)$ for $x = 0, 1$. Before showing the theoretical predictions of this new framework, let us delve deeper into the rationale behind this extended CL model.

First of all, recall that in a liquid mixture a force $\mathbf{F}_\alpha = -\nabla\mu_\alpha^{\mathrm{L}}$ on an atom of species $\alpha \in \{\text{Ar, Kr}\}$ is generated by the gradient of its chemical potential $\mu_\alpha^{\mathrm{L}} = \mu_{0\alpha}^{\mathrm{L}} + k_{\mathrm{B}}T \ln\left(x_\alpha \gamma_\alpha^{\mathrm{L}}\right)$ where $\mu_{0\alpha}^{\mathrm{L}}$ is the potential of pure species α at the same thermodynamic conditions of the mixture, and x_α and $\gamma_\alpha^{\mathrm{L}}$ have been already defined. An elementary calculation yields the expression for the gradient (and then for the force) $\nabla\mu_\alpha^{\mathrm{L}} = k_{\mathrm{B}}T\Phi\nabla \ln x_\alpha$, being Φ as in eq. 1.29. Since in a pure Lennard-Jones liquid the crystal growth kinetics as described by the CL model is determined by the short-time thermal motion characteristic of an ideal gas [31], the question arises how the particle's velocity is affected by the force $\mathbf{F}_\alpha$ in the mixture. To determine which is the effect of this force on particle velocities, it can be shown that a multiplicative correction to the average thermal velocity of the particles is appropriate. This multiplicative factor appears than suitable for a correction such as the one proposed in eq. 1.30. Let us derive this through some calculations:

- the scalar version of $\mathbf{F}_\alpha = -\nabla\mu_\alpha^{\mathrm{L}}$ reads: $F_\alpha = m_\alpha\, a = m_\alpha \dfrac{dv}{dt} = -\dfrac{d\mu_\alpha}{dx}$
- using the chain rule, along x direction $\dfrac{d\mu_\alpha}{dx} = \dfrac{d\mu_\alpha}{dc_\alpha}\dfrac{dc_\alpha}{dx}$, where c_α is the number of particles of species α, normalized by the total number of particles.
- recalling the expression for non–ideal chemical potential in mixtures (see Section 1.2), i.e. $\mu_\alpha^0(T) + k_B T \ln\gamma_i(c_\alpha, T)$, the derivative of the chemical potential with respect to the x coordinate becomes:

$$
\begin{aligned}
-\frac{d\mu_\alpha}{dx} = k_B T\left(\frac{d\ln(\gamma_\alpha)}{dc_\alpha} + \frac{1}{c_\alpha}\right)\frac{dc_\alpha}{dx} = \\
k_B T\left(\frac{d\ln(\gamma_\alpha)}{dx} + \frac{d\ln(c_\alpha)}{dx}\right) = \\
k_B T\left(\frac{d\ln(\gamma_\alpha)}{d\ln c_\alpha} + 1\right)\frac{d\ln(c_\alpha)}{dx} = \\
k_B T\Phi\frac{d\ln c_\alpha}{dx}
\end{aligned}
$$

  where we have introduced the quantity $\Phi = \left(\dfrac{d\ln(\gamma_\alpha)}{d\ln c_\alpha} + 1\right)$
- returning to the general vectorial expression, $\mathbf{F}_\alpha = -m_\alpha k_B T\Phi\nabla\ln c_\alpha$. Given that $\nabla\ln c_\alpha$ is approximately constant, we can write a general expression for atomic velocity:

$$
\begin{aligned}
v \approx \frac{k_B T}{m}\Phi(-\nabla\ln c_\alpha t + C) = \\
C\frac{k_B T}{m}\Phi\left(1 - \frac{\nabla\ln c_\alpha t}{C}\right)
\end{aligned}
\tag{1.31}
$$

  Now, the determination of the exact C value depends on the boundary conditions, which can be synthesized as:

  1. if $t = 0$ and $\gamma_\alpha = 1$ (i.e. ideal mixture case), the average thermal velocity $v := \langle v\rangle$ must be equal to $\sqrt{\dfrac{3k_B T}{m}}$ for the equipartition theorem, with $m = c_1 m_1 + c_2 m_2$ for a generic binary mixture
  2. if $c_\alpha = 1$, $v = \sqrt{\dfrac{3k_B T}{m_\alpha}}$

  These conditions yield $C = \sqrt{3m}k_B T$. For $t \approx 0$, $v \approx \sqrt{\dfrac{3k_B T}{m}}\Phi$, i.e. a multiplicative correction term Φ accounts for non–ideality in the velocities of particles belonging to a binary mixture; the expression proposed in eq. 1.30 comes then from the as–discussed considerations.

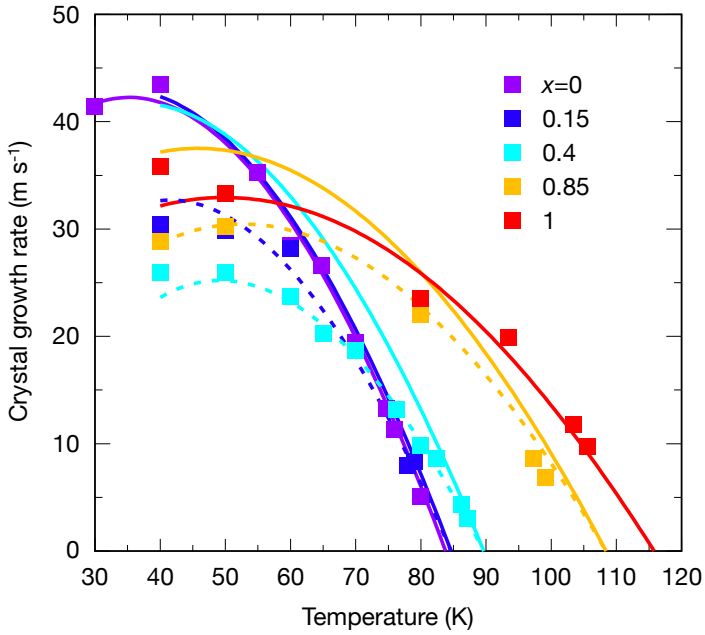

FIGURE 1.16: Simulated $u(T)$ along (100) in m/s, for five representative systems. The solid lines are the theoretical calculations for the CL model, while the dashed lines are the ones for the modified CL formula. The color code indicates the Kr mole fraction. Reprinted from [5]

Note that, to evaluate the thermodynamic factor Φ of equation 1.30 in terms of the experimental excess data for mixtures of argon and krypton, we first write the excess free energy for the liquid as

$$g_{\mathrm{E}}^{\mathrm{L}}(x_{Kr},T) = (1-x_{Kr})x_{Kr}\xi_0^{\mathrm{L}}(T)RT = \left[(1-x_{Kr})x_{Kr}^2\xi_0^{\mathrm{L}}(T) + x_{Kr}(1-x_{Kr})^2\xi_0^{\mathrm{L}}(T)\right]RT$$

By comparing the last expression in this equation with equation 1.10, we find for example $\ln\gamma_{\mathrm{Kr}}^{\mathrm{L}} = (1-\mathrm{x_{Kr}})^2\xi_0^{\mathrm{L}}(\mathrm{T})$, and thus

$$\Phi(x_{Kr},T) = 1 + x_{Kr}\frac{\partial \ln\gamma_{\mathrm{Kr}}^{\mathrm{L}}}{\partial x_{Kr}} = 1 - 2(1-x_{Kr})x_{Kr}\xi_0^{\mathrm{L}}(T) \tag{1.32}$$

The dashed lines in Fig. 1.16 represent the just introduced model, which now displays a remarkable agreement with the simulation results, for all x_{Kr} values. This indicates that the modified CL model successfully captured the full temperature dependence of the crystal growth rate in our supercooled mixtures.

In particular, this modified model performs much better than the original CL formula in locating the peak growth rate. We extended the comparison

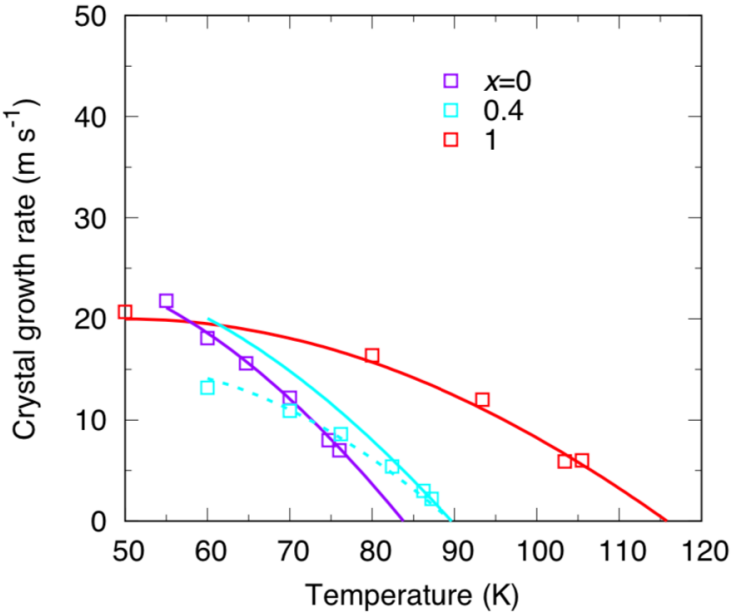

FIGURE 1.17: Simulated $u(T)$ along (111) in m/s, for five representative systems. The solid lines are the theoretical calculations for the CL model, while the dashed lines are the ones for the modified CL formula. The color code indicates the Kr mole fraction. Reprinted from [5]

between theory and simulations also to the growth of the (111) surface. The results, shown in Fig. 1.17, clearly show that the dependence on temperature of the crystal growth rate of the (111) surface is also well described by the modified CL model. In these calculations we used $f/c = 1.1$, reflecting the smaller absolute crystal growth rates found in the simulations when compared to the (100) surface. It is noteworthy that our results are in sharp contrast to those reported by Burke *et al.* [26], who found that the crystal growth rate of the (111) surface in a pure supercooled Lennard-Jones liquid was described by the WF model.

Concerning the relative growth rates, instead, here follows the picture showing the comparison between experimental/simulated data and all the three models (WF, CL and CL modified). The dashed blue line in Fig. 1.18 represents indeed the theoretical calculation based on the modified CL model at the interpolated temperature $T(x)$ (see Fig. 1.9), showing also here a slightly improved agreement with both the experimental data and simulation results for the krypton-rich mixtures.

Here, it is important to underline that the peculiar shape of the crystal growth rates, widely discussed in the previous pages, is essentially originated

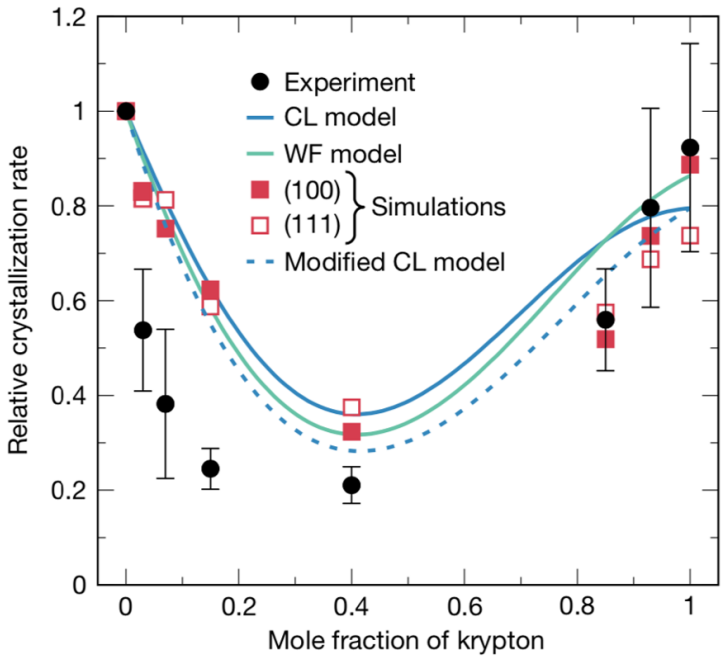

FIGURE 1.18: Reduced experimental (black circles) and simulated (empty and filled red squares, according to the growth surface) crystal growth rates, compared with WF (green line), CL (blue line) and modified CL (dashed blue line) models. Reprinted from [5]

by the particular temperature and density experimental conditions. This also underlines the role of the thermodynamic driving force in affecting the solid growth: at the experimental temperatures, WF and CL model are extremely close in their predictions, and the peculiar shape of the curve is only determined by jet temperatures (which are partly closer to the coexistence region for intermediate mixtures). The lower degree of supercooling of the $x = 0.4$ mixture naturally determines the value of the minimum crystal growth rate. The classical theoretical approaches fail in the comparison with the simulated growth rates at fixed concentration and variable temperature (see Figs. 1.15a and 1.15b), asking for an extension of the CL theory.

1.8 Searching local structures with ALBOP

In parallel to the analysis of the simulated crystal growth rates, which provided an encouraging improved version of the CL model, we carried out an extended analysis of the structures of the supercooled liquids and growing crystals simulated. In particular, we leveraged the ALBOP with the purpose

of evidencing possible traces of *geometric frustration*, and searching for elements capable of distinguishing the crystallization process of the mixtures from the one of pure systems.

Concerning geometric frustration, one of the main reasons usually addressed in literature for the crystal growth slowdown in liquids concerns the presence of 3D structures not fully able to fill the space with a periodic arrangement, in particular icosahedra [9, 63]. Icosahedra are indeed five-fold symmetric, and thus do not tile Euclidean space; this generates geometric frustration, thus hindering system's crystallization. According to Frank [64], the ground state of 13 atoms of the monoatomic Lennard-Jones model is the icosahedron, and not fcc or hcp crystals. As a consequence, in this view, upon supercooling such atoms should first form icosahedra rather than crystals, as for example happens in the Wahnström LJ model [19, 65]. These icosahedra are a renowned example of the family of the so-called *locally favored structures* (LFS): these are peculiar forms of atomic ordering which minimize the free energy of a small number of particles and compete with other forms of (usually crystalline) ordering. These LFS do not tile Euclidean space and then the growth of domains of LFS, which induces strain, is the essence of geometric frustration. In this framework, this strain (free) energy suppresses the formation of an 'LFS-state'. There are many other LFS found e.g. in recent works about the Kob-Andersen LJ model, such as the bicapped square antiprism [18, 20, 21, 23, 65]. Leocmach *et al.* [62] investigated as well the roles of icosahedral and crystal-like order in the hard spheres glass transition, trying to quantify the importance of LFS in crystallization and in the glass transition.

In order to quantitatively unveil the possible presence of icosahedra in our supercooled mixtures, an analysis based on the Local Bond Order Parameter $\hat{w}_6$ was conducted, looking for $\hat{w}_6$ values in the range directly associable to the presence of icosahedral structures. Being interested in what happens in the neighborhoods of the CF, we plot in Fig. 1.19b an histogram of the $\hat{w}_6$ values averaged over layers preceding and following the CF, in (100) simulations. This is similar to a kind of analysis performed by Tang *et al.*, which detected a considerably different ordering in the supercooled liquid in fron of the CF, when comparing a fast crystallizing mixture with a very slow one [6].

The data reported only refer to the significant $x_{Kr} = 0, 0.4, 1$ systems, but analogous results were found for all the other intermediate mixture compositions studied. Clearly, the range visited by the $\hat{w}_6$ parameter in the neighborhoods of the CF is far from the typical values of icosahedra. Conversely, the values recorded for $\hat{w}_6$ are much closer to the ones proper of the fcc/hcp crystal phases, with the broadness of the distribution which is larger for the liquid region after the CF. The distribution is instead sharper and peaked approximately around $\hat{w}_6^{fcc}/\hat{w}_6^{hcp}$ values for the as–crystallized

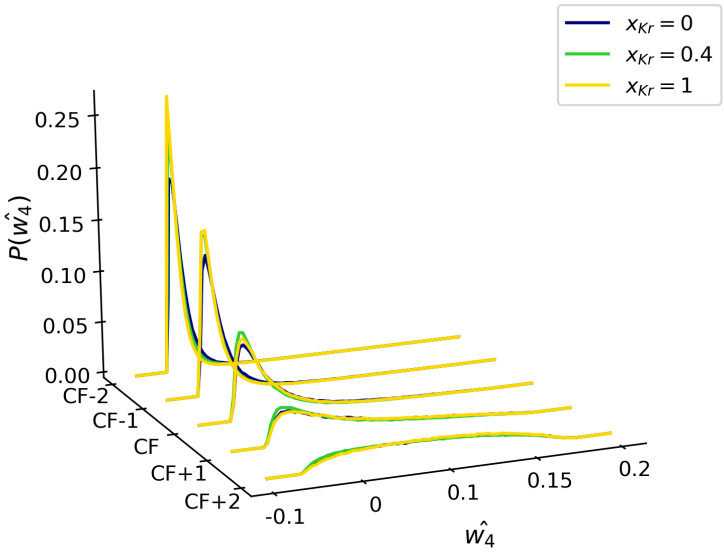

(a)

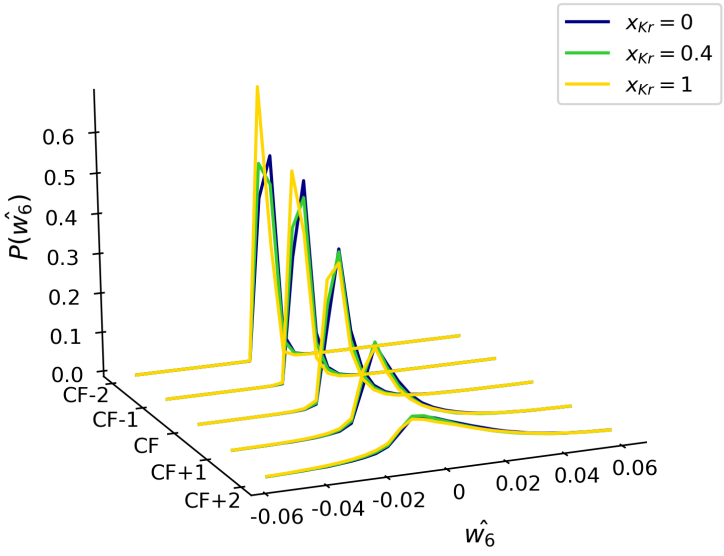

(b)

FIGURE 1.19: Probability distribution of the $\hat{w}_4$ and $\hat{w}_6$ Steinhardt parameters, averaged over layers immediately before and after the CF in (100) simulations. Only data for $x_{Kr} = 0, 0.04, 1$ are reported.

layers indicated via the 'CF-1' and 'CF-2' labels. There are no evident differences among the three systems investigated, apart from a slight tendency of

the pure krypton crystal to be more structured than the others. The liquid phase, oppositely, is apparently identical for all mixture compositions. Concerning the analogous calculations performed for $\hat{w}_4$, from Fig. 1.19a clearly appears that this parameter is very similar amongst all the systems studied, near the CF. The layers already crystallized present a sharp distribution peaked around crystalline $\hat{w}_4$ values, while the layers in front of the solid–liquid interface are characterized by a flatter and broader $\hat{w}_4$ distribution, indicating the prevalent disordered liquid component.

The same analysis was then conducted for Q_4 and Q_6 parameters (see Figs. 1.20a, 1.20b), in simulations of the (100) surface growth. Here some differences dependent on x_{Kr} are more evident, especially in the distribution of Q_4; the pure Kr displays a distribution which is always slightly right–shifted, compared to the other two cases. This may indicate a greater homogeneity in the single layers considered; not only, this also means that - on average - the pure krypton forms structures with a higher fraction of fcc regions. However, for all the three compositions studied, the transition of the system from the liquid phase ('CF+1' and 'CF+2' layers) to the crystalline one is easily detectable, with a predominant fraction of atoms in a fcc arrangement and some others which are hcp-like and a minority which are still liquid–like. The analysis of the Q_6 parameter, instead, does not reveal any peculiar differences depending on the Kr fraction. The data highlight a transition from broad Q_6 histograms, in the range $\sim (0.1, 0.3)$ after the CF, up to narrow distributions approximately in the range $\sim (0.3, 0.5)$. Some minor features underline again a tendency of the pure krypton to form slightly more structured fcc crystals.

Q_4 and Q_6 parameters were also used to observe the presence of defects and stacking faults in the growth of the (111) surface. In fact, along that direction and for LJ systems, fcc and hcp structures possess very close free energies: therefore it should be easy to detect the presence of fcc planes alternated with hcp ones, similar to the observations of Burke *et al.* [26]. As noticed before, if fcc and hcp layers constitute approximately the 50% each of the layers, we are in presence of a structure known as rhcp. Labeling $Q_{4,l}$ and $Q_{6,l}$ the layer averages of Q_4 and Q_6, we show in Fig. 1.21 the distributions of $Q_{4,l}$ and $Q_{6,l}$ in three simulations of the crystal growth along (111) surface, for $x_{Kr} = 0, 0.4, 1$. The data included in each histogram belong only to the measurement region and were collected all along the crystallization process. Counts on y axis are scaled between 0 and 1. The temperatures for the thermostats in these simulations are those listed in Tab. 1.2.

The $Q_{4,l}$ distribution shows that some layers form fcc structures, other form hcp structures, and other are probably characterized by fcc and hcp subdomains within the same layer, thus generating slabs which are neither fully hcp nor fully fcc (note the presence of structures in the transition regions between hcp and fcc). Pure argon rarely forms fully fcc structures, in the example reported, but this can depend on many factors (included the

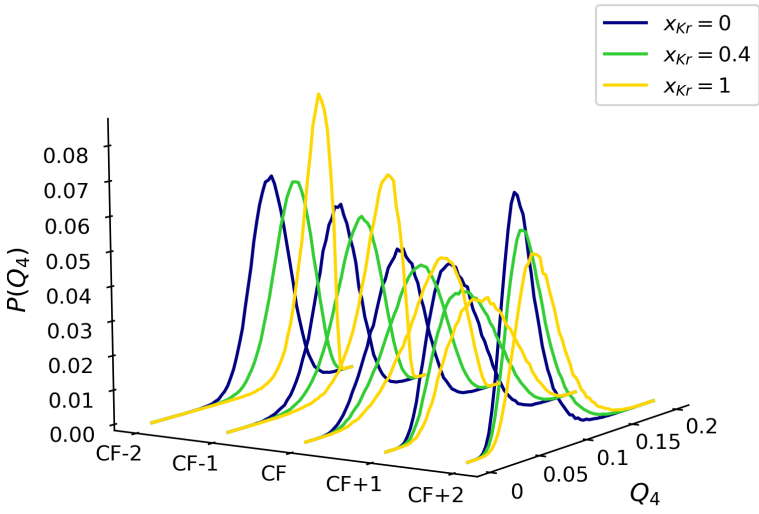

(a)

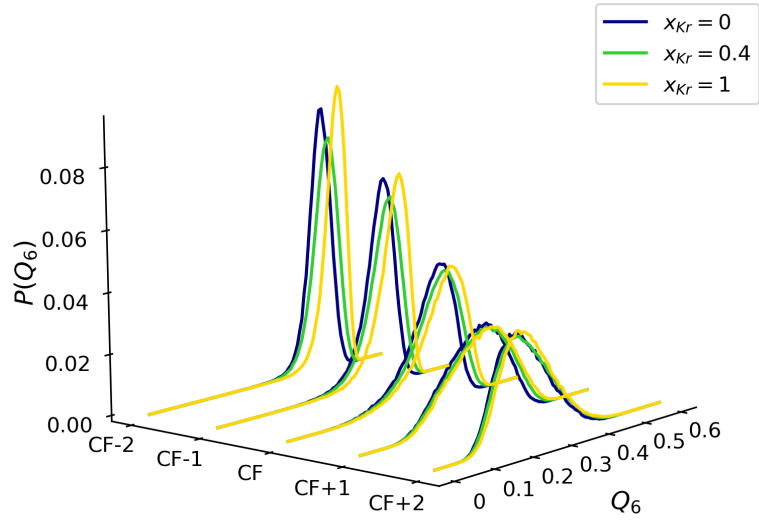

(b)

FIGURE 1.20: Probability distribution of the Q_4 and Q_6 Steinhardt parameters, averaged over layers immediately before and after the CF in (100) simulations. Only data for $x_{Kr} = 0, 0.04, 1$ are reported.

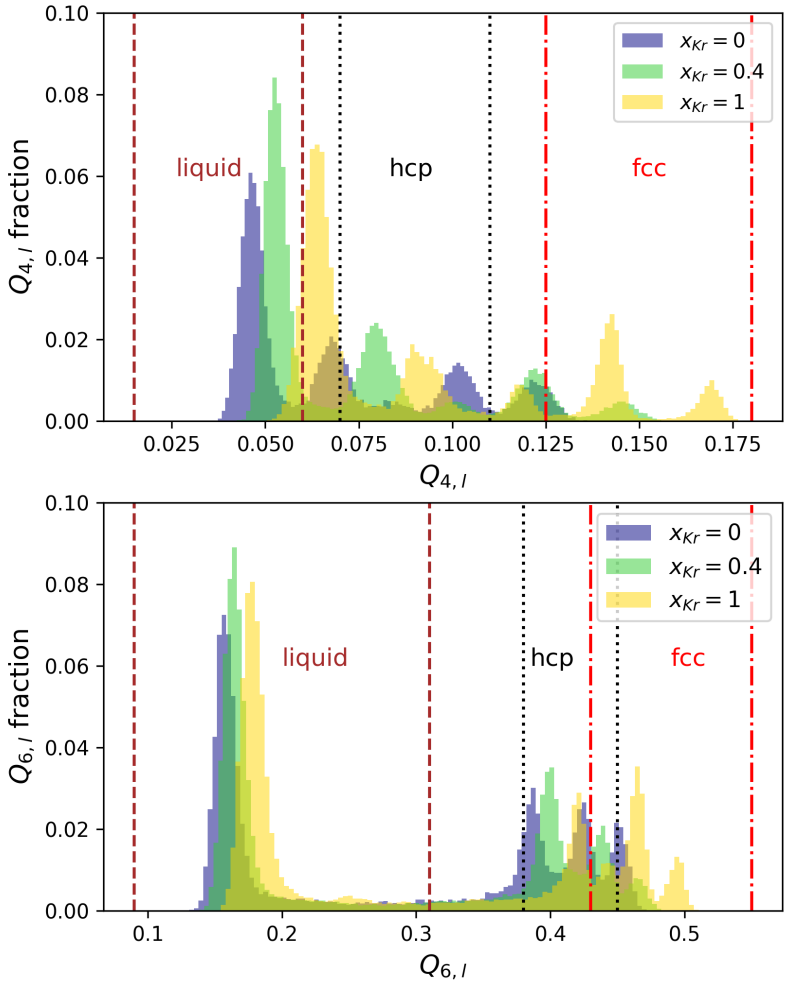

FIGURE 1.21: Distributions of $Q_{4,l}$ and $Q_{6,l}$ values in simulations of the growth along (111) surface, for $x_{Kr} = 0, 0.4, 1$. Ranges typical of liquid, hcp and fcc lattices are marked.

temperature and the fact that the ALBOP ranges are approximate and could depend on external conditions, such as density and temperature). This consideration holds also for pure Kr, whose corresponding liquid range should probably be slightly shifted towards higher values. Analogously, there are

signals of hybrid structures also in the corresponding histogram for $Q_{6,l}$ values; here, this is less evident than in the case of $Q_{4,l}$ because of the *a priori* overlap existing between fcc and hcp regions. We note that the pure Kr system forms the fcc and hcp layers with the highest $Q_{6,l}$. It is also important to underline that the values reported in Fig. 1.21 are not atomic values for ALBOP, but averages performed within spatial regions; individual values could, in principle, have a different distribution.

On the other hand, many other analyses were performed exploiting the structural order parameter; for example, the same histograms exposed above were built also for $S(i)$ and for $s(i,j)$, yielding results qualitatively similar to those found for Q_6. We also investigated the distribution of these parameters in the neighborhoods of the CF by separating the contributions due to Ar and Kr atoms in each single layer, but without finding remarkable differences. Apparently, the volume regions around argon atoms do not differ that much from the corresponding surroundings of krypton atoms.

1.9 Conclusion and further perspectives

In conclusion, we have shown that the departure from ideality provides a simple, clear physical account of the crystal growth rates in supercooled mixtures of argon and krypton, thereby significantly improving the canonical view of crystallization. We believe that the crystal addition rate in equation 1.30 might be especially relevant to the description of crystal growth in regular (non ideal) solutions. As described in detail in previous sections, regular solutions are described as ideal solutions including in their free energy a further term, which depends on the composition as: $\omega\, x_A\, x_B$ [2, 37]. Here, ω is the Flory–Huggins interaction parameter and $x_{A,B}$ represent the concentration of the A and B components of the mixture. Is is worth to underline again the connection between Φ and ω [37]:

$$\Phi = 1 + \frac{x_A\, x_B}{k_B\, T}(-2\omega) \tag{1.33}$$

As a further important example of a binary system for which our new model holds, the explicit calculation of Φ for alloys of copper and nickel has been performed. Based on available assessed data [66], extrapolated to supercooled temperatures, our analysis does indicate that the modified CL model can consistently explain experimental [16, 17] and simulation[10] results on crystal growth in these liquids. Having established the key role played by the thermodynamic complexity that distinguishes binary liquid mixtures in the kinetics of crystal growth, the opportunity now exists for a quantitative description of crystal growth in binary systems beyond the simplest atomic liquids discussed in the present thesis, and particularly in strongly non–ideal

alloys exhibiting several intermediate solid phases and extended eutectic regions. It is fundamental to observe here that our modified model only works for systems whose enthalpic therm h_0 in the expression of the excess free energy 1.10 is strictly positive. If $h_0 < 0$, our modified model reveals the need for further improvements: in fact, in that case, the thermodynamic factor Φ becomes a parabola with negative curvature [37] and eq. 1.30 is no more an adequate description of the crystal growth rate behavior. We recall that, for regular mixtures, $g_{\mathrm{E}}^{\mathrm{L,C}}(x_{Kr}, T) \approx x_{Kr}\,(1 - x_{Kr})\,h_0^{\mathrm{L,C}}$, i.e. a negative h_0 value implies that also the excess Gibbs free energy becomes negative. According to Pelton [36], this means that the real mixture is thermodynamically more stable than an ideal solution. This happens when the interspecies interaction dominates over the intraspecies one, which is clearly not the case of Ar–Kr mixtures. In this sense, it is important to remark that the issue addressed in the work by Tang *et al.* [6] is still an open question. For those systems, in fact, the parabola is negatively curved, and CuZr and NiAl mixtures can not be regarded as being regular. However, the reader has to take into account that even our extended CL model is phenomenological: it is of course not expected to provide a correct and complete physical description of the crystal growth in *any* regime.

Where does the crystal growth break down? Concerning this, an interesting limit case is verified when $\Phi = 0$; if eq. 1.30 holds, $\tilde{\nu} = 0$ for a given temperature $\overline{T}$ for which $\Phi|_{\overline{T}} = 0$ (see eq. 1.32). In particular, eq. 1.33 clearly states that the critical temperature is equal to $\overline{T} = \dfrac{\omega}{2\,k_B}$. As a consequence, from a theoretical point of view, the crystal growth process should completely arrest in such conditions; for our supercooled mixtures, this would happen at temperatures of few ($\sim 10/20$) K. Is the as–introduced model still valid in these conditions? Clearly, answering to such a question is not possible in an experimental framework, while simulations would naturally deal with this problem. Probably our simulation method, described in Sec. 1.4, would have to be partially adjusted, at such low temperatures; assuming to have a still effective computational tool, it is difficult to predict if the crystal growth would be completely hindered in these simulations, thus leading to the extreme case of a phase separation along a spinodal line. However, if one was able to correctly simulate Ar-Kr supercooled liquid mixtures where $\Phi \to 0$, the computed crystal growth would be probably extremely small, due to the reduced atomic mobility. Therefore, in principle, we expect the systems to remain approximately stuck in a disordered configuration, and it would be interesting to test this hypothesis in specific simulations. Nonetheless, we recall that our simulation tool partially forces the supercooled liquid, even at very low temperatures, to crystallize by stacking solid–like layers above the inner crystalline wall. This is quite a strong bias and, probably, we should

change approach in order to study the crystallization at extremely low T. In particular, it would be useful to include spontaneous nucleation events in the simulation process, without the preliminary insertion of an already formed crystal seed. The tendency towards an arrested dynamics is partly retrievable for example in Fig. 1.16, where all the reported curves show a peak growth rate and then it starts to decrease upon further lowering T. Surely, it would be extremely stimulating to investigate the behavior of Ar–Kr supercooled liquid mixtures in such conditions. However, as already stated, in a real sample it is impossible to perform and maintain such a high supercooling degree. Not only, also from a theoretical point of view, these conditions could be favorable to the glass transition, or however should induce a dynamical arrest in the sample [9]. This would lead the systems into a completely different situation, far away from the cases explored in the present work.

Mind the Gibbs free energy! A similar question arises when the Gibbs free energy difference between the crystal and the liquid phases vanishes. Referring to Fig. 1.9, there is a line in the (T, x_B) phase diagram, called 'T_0 line', along which $\Delta G(T) = 0$ for the corresponding concentration of the B species. Simple calculations derived from the expression of $\Delta G(x_A, T) = x_A \Delta g_A(T) + x_B \Delta g_B(T) + \Delta g_E(x_A, t)$ for a generic $A - B$ mixture provide the following expression:

$$T_0(x_A) = \frac{x_A \Delta h_A + x_B \Delta h_B + x_A x_B \Delta h_0}{x_A \frac{\Delta h_A}{T_{m,A}} + x_B \frac{\Delta h_B}{T_{m,B}} + x_A x_B \Delta s_0} \tag{1.34}$$

where $\Delta g(T) = \Delta h \frac{T_m - T}{T_m}$ with T_m as the melting temperature and $\Delta g_E(x_A, t) = x_A x_B (\Delta h_0 - T \Delta s_0)$ In such conditions, the solid front gains no free energy, on average, by growing into the liquid, and the crystallization does not proceed. In Fig. 1.22, the first row shows, for the examples of Ar-Kr and CuNi, the T_0 line in red; from this perspective, the two systems present evident similarities. The T_0 line lays in the coexistence region of the phase diagram, and thus a small supercooling is sufficient to avoid the case $\Delta G(T) = 0$.

Both Ar–Kr and CuNi binary phases are characterized by simple diagrams; many systems, especially metallic alloys, have much richer phase diagrams. Two core examples, in this regard, are reported in the bottom row of Fig. 1.22: CuZr and AlSm. It is important to recall that copper–zirconium alloy (bottom left picture) is a widely studied system, also due to its technological potentiality [1, 6, 14, 15]. CuZr is a promising glassformer, and many structural analysis have been performed on this alloy [6]; all these studies introduced interesting observations, but they probably lack one key element. Here, the phase diagram of CuZr it is shown: the three colored lines correspond to three different crystal lattices that CuZr can form, and represent the T_0 line for each case, for systems with low concentrations of the minority

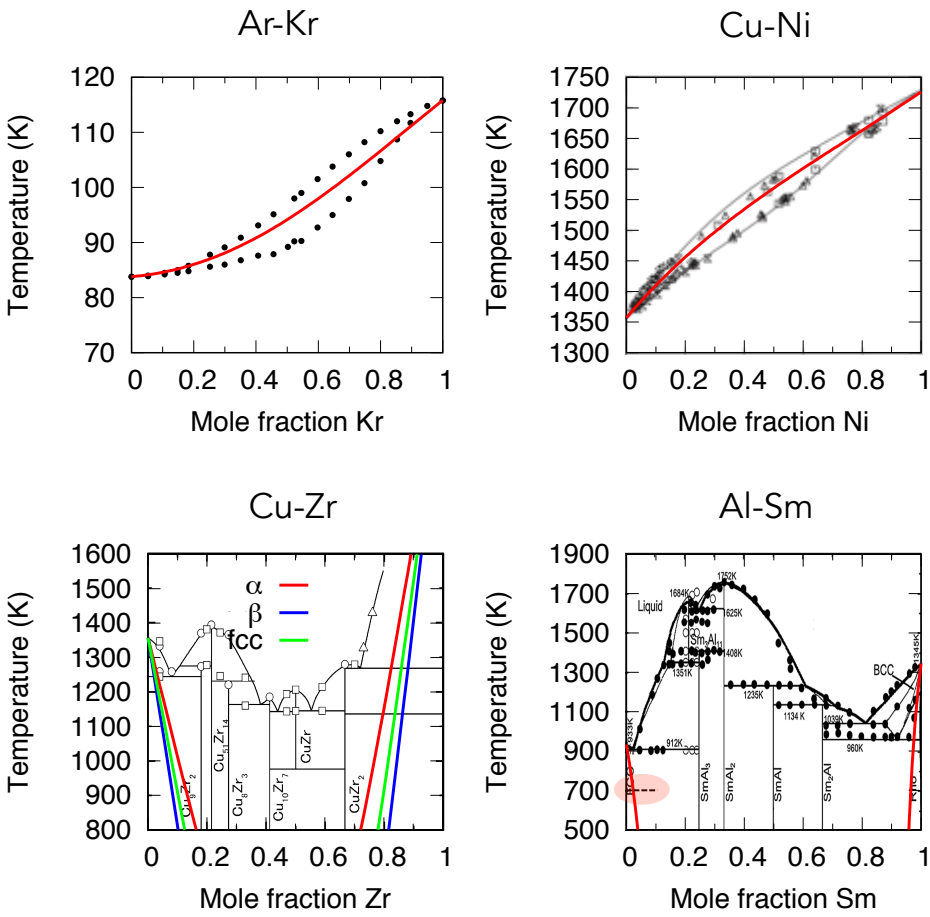

FIGURE 1.22: Figure reproduced by courtesy of R. Grisenti. T_0 line for Ar–Kr and CuNi mixtures (first row). Second row: CuZr and AlSm phase diagrams with T_0 lines evidenced (the different lattices have slightly different T_0 lines in the CuZr case).

species. The three crystal structures that CuZr usually forms are all characterized by T_0 lines with a rapid decrease upon growing Zr concentration in Cu (and, almost symmetrically, with a rapid increase as a function of Cu concentration in Zr). Clearly, if one would know the corresponding T_0 lines for almost equimolar mixtures, it would be necessary to consider the free energies of the crystals indicated in the phase diagram, such as $Cu_{10}Zr_7$ or $CuZr_2$; our hypothesis is that, in this case, these curves will be much more complicated, with many local maxima and minima. Tang *et al.* [6] simulated equimolar mixtures, finding a significant crystallization slowing down; it would be intriguing to relate this behavior to how close to the respective

T_0 line the temperature of the simulation is.

The intimate relation between the T_0 line and the crystallization rate is made even more evident in the last subfigure, which contains the AlSm phase diagram with its T_0 line. In a recent paper, Sun *et al.* studied the effects of Mg and Sm dopants on the crystal nucleation in Al [8]. What is interesting (and missed by the authors) is that their AlSm crystallization simulations are located in a region of the phase diagram where the T_0 line is rapidly met, around 700 K. According to the authors, the addition of only 8% Sm dramatically hinders the crystallization process of the system. This was addressed to the intolerance (i.e. scarce miscibility of the two elements) of Al to this dopant: the increase in the solid–liquid interfacial free energy was identified as the reason for the extremely small nucleation rate and subsequent slow crystal growth observed in AlSm alloys. Conversely, according to the picture we are summarizing here, supported also by our experiments and simulations, the motivation can simply be associated to the fact that a small Sm fraction into the Al matrix leads to a region where $\Delta G = 0$ and the crystal growth can not proceed. The bottom right subfigure in Fig. 1.22 highlights the region where the simulations of that study have been conducted: the reason behind the observed phenomenology appears straightforward, in our new framework.

Fine tuning interaction parameters Furthermore, an exciting possibility would be, in this regard, to explore the role of the interaction parameters in tuning the crystal growth rate in such systems. In the interesting essay of Pelton [36], it is possible to find an exhaustive discussion about the connection between the Gibbs free energy of eq. 1.1 and the interaction potential. In particular, it is reported how, by simply modifying the enthalpic therms $h_0^{\mathrm{L,C}}$ in g_E, a vast number of phase diagrams for binary mixtures can be retrieved, each of them corresponding to a richly diverse phase of the system. Something similar was recently explored by Sun *et al.* [13], who systematically studied the crystal growth rates from a binary LJ model liquid as a function of the variation of the interspecies interaction length. They perform the so called assignment analysis, to investigate the origin of the slowdown detected at the crossover between two different crystal structures, dependent on the mixed interaction length σ_{AB}. First of all, importantly, their growth profiles (Fig. 3 of their paper) resemble quite closely our data, as a function of T at fixed mixing ratio. There is also a second and deeper connection with the present study: the change of σ_{AB} implies a variation in the excess free energy, as highlighted by eq. 1.12. It is quite challenging to exactly determine the scaling of the excess free energy as a function of σ_{AB}. Nonetheless, it is clear that a variation of g_E dependent on the interspecies interaction length generates a subsequent modification of the thermodynamic factor Φ,

which in turn is reflected into the crystallization rate. This approach to the physical origin of the crystal growth slowdown is much different from the one adopted by the author, but both methods can unveil different details of this complicated phenomenon.

It is worth mentioning an alternative approach to the topics of crystal growth, dynamical arrest and glass formation. The above discussed central role of the interaction parameters induced many scientists to address the Potential Energy Landscape, PEL, (or the Free Energy Landscape, FEL) as the natural candidate for the explanation of the revealed slowdown of the crystal growth rate in supercooled condensed matter systems [9]. For a simple liquid in three dimensions, the total potential energy is a function of the $3N$ atomic coordinates; each configuration could then be represented by a point in phase space, and the dynamics of the system can be thought of as the motion of this point over this PEL. The local minima of the potential energy correspond to locally stable configurations of the system and one of these is the crystal, which in turn corresponds to the absolute minimum. There will also be many local minima corresponding to particle arrangements that lack crystalline order, i.e. glasses or amorphous solids, characterized by a potential energy that is extensively larger than the crystal one. The complete description of the theory is well beyond the aim of this thesis, but its core idea is clearly interesting. Obviously, the behavior of the system is determined by the interactions among its constituents; the Hamiltonian stores all the relevant information and the PEL (or FEL) is a good way to synthesize this information. Concerning crystal growth in supercooled liquids (above the glass transition temperature [9]), it is possible that structural fluctuations in the crystal/liquid interface could be intimately related to variations as a function of composition in the underlying PEL. Upon cooling, the particles have to jump over higher barriers in order to reach the lowest energy minima and this naturally provokes a delay in the propagation of the ordered solid into the disordered liquid. This is a clear and neat framework but it somehow lacks the possibility of a quantitative description, even though some trials have been attempted in this sense [67–71]. On the other hand, producing a glass in an experiment is extremely challenging and requires that the liquid is cooled fast enough to prevent the nucleation and subsequent growth of the crystal [69].

The regime in which we have studied argon-krypton mixtures is not characterized by easily accessible glassy states and we observed that the crystal growth is present, even if the opportunity of arbitrarily changing the interparticle potential provided by the simulations is stimulating. To this extent, while the experiments could obviously never have such a freedom in choosing the mixed interaction parameters, the results of simulations with arbitrary interaction parameters could still be compared with the theoretical models; this would strengthen and widen the validity our findings.

Bibliography

[1] T. S. Ingebrigtsen, J. C. Dyre, T. B. Schrøder, and C. P. Royall. Crystallization Instability in Glass-Forming Mixtures. *Physical Review X*, 9(3):031016, 1–11, 2019.

[2] K. A. Jackson. *Kinetic Processes: Crystal Growth, Diffusion, and Phase Transitions in Materials*. 2nd edition, 2005.

[3] J. Orava and A. L. Greer. Fast and slow crystal growth kinetics in glass-forming melts. *Journal of Chemical Physics*, 140(21), 2014.

[4] J. Orava and A. L. Greer. Fast crystal growth in glass-forming liquids. *Journal of Non-Crystalline Solids*, 451:94–100, 2016.

[5] A. Schottelius, F. Mambretti, A. Kalinin, B. Beyersdorff, A. Rothkirch, C. Goy, J. Müller, N. Petridis, M. Ritzer, F. Trinter, J. M. Fernández, T. A. Ezquerra, D. E. Galli, and R. E. Grisenti. Crystal growth rates in supercooled atomic liquid mixtures. *Nature Materials*, 19(May 2020):512–516, 2020.

[6] C. Tang and P. Harrowell. Anomalously slow crystal growth of the glass-forming alloy CuZr. *Nature Materials*, 12(6):507–511, 2013.

[7] J. C. E, L. Wang, Y. Cai, H. A. Wu, and S. N. Luo. Crystallization in supercooled liquid Cu: Homogeneous nucleation and growth. *Journal of Chemical Physics*, 142(6), 2015.

[8] Y. Sun, F. Zhang, L. Yang, H. Song, M. I. Mendelev, C. Z. Wang, and K. M. Ho. Effects of dopants on the glass forming ability in Al-based metallic alloy. *Physical Review Materials*, 3(2):023404, 2019.

[9] C. P. Royall and S. R. Williams. The role of local structure in dynamical arrest. *Physics Reports*, 560:1–75, 2015.

[10] T. Fang, L. Wang, and Y. Qi. Molecular dynamics simulation of crystal growth of undercooled liquid Co. *Physica B: Condensed Matter*, 423:6–9, 2013.

[11] A. Kerrache, J. Horbach, and K. Binder. Molecular-dynamics computer simulation of crystal growth and melting in Al50Ni50. *Europhysics Letters*, 81(5):58001, 2008.

[12] G. Sun, J. Xu, and P. Harrowell. The mechanism of the ultrafast crystal growth of pure metals from their melts. *Nature Materials*, 17(10):881–886, 2018.

[13] G. Sun and P. Harrowell. Crystal growth rates and liquid dynamics at the crossover between stable crystal phases. *Journal of Chemical Physics*, 164505(March), 2020.

[14] Q. Wang, L.M. Wang, M. Z. Ma, S. Binder, T. Volkmann, D. M. Herlach, J. S. Wang, Q. G. Xue, Y. J. Tian, and R. P. Liu. Diffusion-controlled crystal growth in deeply undercooled melt on approaching the glass transition. *Physical Review B*, 83(1):1–5, 2011.

[15] X. Q. Yan and Y. J. Lü. Mechanism of abnormally slow crystal growth of CuZr alloy. *Journal of Chemical Physics*, 143(16), 2015.

[16] P. R. Algoso, W. H. Hofmeister, and R. J. Bayuzick. Solidification velocity of undercooled Ni-Cu alloys. *Acta Materialia*, 51(14):4307–4318, 2003.

[17] R. Willnecker, D. M. Herlach, and B. Feuerbacher. Evidence of nonequilibrium processes in rapid solidification of undercooled metals. *Physical Review Letters*, 62(23):2707–2710, 1989.

[18] P. Crowther, F. Turci, and C. P. Royall. The nature of geometric frustration in the Kob-Andersen mixture. *Journal of Chemical Physics*, 143(4), 2015.

[19] A. Malins, J. Eggers, C. P. Royall, S. R. Williams, and H. Tanaka. Identification of long-lived clusters and their link to slow dynamics in a model glass former. *Journal of Chemical Physics*, 138(12):12A535, 2013.

[20] A. Malins, J. Eggers, H. Tanaka, and C. P. Royall. Lifetimes and lengthscales of structural motifs in a model glassformer. *Faraday Discussions*, 167(0):405–423, 2013.

[21] U. R. Pedersen, T. B. Schrøder, and J. C. Dyre. Phase Diagram of Kob-Andersen-Type Binary Lennard-Jones Mixtures. *Physical Review Letters*, 120(16):165501, 2018.

[22] U. R. Pedersen, N. P. Bailey, J. C. Dyre, and T. B. Schrøder. Crystallization of the Wahnström Binary Lennard-Jones Liquid. *arXiv*, (arXiv:0706.0813v2):1–4, 2007.

[23] S. Toxvaerd, T. R. Pedersen, T. B. Schrøder, and J. C. Dyre. Stability of supercooled binary liquid mixtures. *Journal of Chemical Physics*, 130(22):224501, 2009.

[24] J. R. Fernández and P. Harrowell. Crystallisation and local order in glass-forming binary mixtures. In *AIP Conference Proceedings*, volume 708, pages 496–502. American Institute of Physics Inc., 2004.

[25] J. Q. Broughton, G. H. Gilmer, and K. A. Jackson. Crystallization rates of a Lennard-Jones liquid. *Physical Review Letters*, 49(20):1496–1500, 1982.

[26] E. Burke, J. Q. Broughton, and G. H. Gilmer. Crystallization of fcc (111) and (100) crystal-melt interfaces: A comparison by molecular dynamics for the Lennard-Jones system. *Journal of Chemical Physics*, 89(2):1030–1041, 1988.

[27] A. Stipp and T. Palberg. Crystal growth kinetics in binary mixtures of model charged sphere colloids. *Philosophical Magazine Letters*, 87(11):899–908, 2007.

[28] M. Kühnel, J. M. Fernández, F. Tramonto, G. Tejeda, E. Moreno, A. Kalinin, M. Nava, D. E. Galli, S. Montero, and R. E. Grisenti. Observation of crystallization slowdown in supercooled parahydrogen and orthodeuterium quantum liquid mixtures. *Physical Review B*, 89(18):1–6, 2014.

[29] M. Kühnel, J. M. Fernández, G. Tejeda, A. Kalinin, S. Montero, and R. E. Grisenti. Time-resolved study of crystallization in deeply cooled liquid parahydrogen. *Physical Review Letters*, 106(24):2–5, 2011.

[30] K. F. Kelton and A. L. Greer. *Nucleation in Condensed Matter Applications in*, volume Volume 15. New York, 1 edition, 2010.

[31] A. Hawken, G. Sun, and P. Harrowell. Role of interfacial inherent structures in the fast crystal growth from molten salts and metals. *Physical Review Materials*, 3(4):43401, 2019.

[32] H. A. Wilson. On the velocity of solidification and viscosity of supercooled liquids. *Philosophical Magazine*, 50:238–250, 1900.

[33] J Frenkel. Note on the relation between the speed of crystallization and viscosity. *Phys. Z. Sowjet Union*, 1:498, 1932.

[34] D. A. Porter, K. E. Easterling, and M. Y. Sherif. *Phase transformations in metals and alloys, third edition.* 2009.

[35] J. S. Rowlinson and F. L. Swinton. *Liquids and Liquid Mixtures - Butterworths Monographs in Chemistry.* 1982.

[36] A. D. Pelton. Thermodynamics and Phase Diagrams of Materials. In *Phase Transformations in Materials*, pages 1–81. 2001.

[37] W. Schirmacher. *Theory of Liquids and Other Disordered Media*, volume 887. 2015.

[38] R. Heastie and G. O. Jones. Solid Solutions of Argon and Krypton. *Del Nuovo Cimento*, IX(1), 1958.

[39] J. Naghizadeh and S. A. Rice. Kinetic theory of dense fluids. X. Measurement and interpretation of self-diffusion in liquid Ar, Kr, Xe, and CH4. *Journal of Chemical Physics*, 36(10):2710–2720, 1962.

[40] P. Flubacher, A. J. Leadbetter, and J. A. Morrison. A low temperature adiabatic calorimeter for condensed substances. Thermodynamic properties of argon. *Proceedings of the Physical Society*, 78(6):1449–1461, 1961.

[41] C. Gladun and F. Menzel. The specific heat and some other thermodynamic properties of liquid krypton. *Cryogenics*, 10(3):210–213, 1970.

[42] C. Gladun. The specific heat of liquid argon. *Cryogenics*, 11(3):205–209, 1971.

[43] R. H. Beaumont, H. Chihara, and J. A. Morrison. Thermodynamic properties of krypton. Vibrational and other properties of solid argon and solid krypton. *Proceedings of the Physical Society*, 78(6):1462–1481, 1961.

[44] R. H. Davies, A. G. Duncan, G. Saville, and L. A.K. Staveley. Thermodynamics of liquid mixtures of argon and krypton. *Transactions of the Faraday Society*, 63(0):855–869, 1967.

[45] B. E. F. Fender and G. D. Halsey. Solid solution of argon and krypton; refined measurements. *Journal of Chemical Physics*, 42(1):127–131, 1965.

[46] R. Grisenti, A. Kalinin, C. Goy, and A. Schottelius. Evaporating laminar microjets for studies of rapidly evolving structural transformations in supercooled liquids. *Advances in Physics: X*, 3:1418183, 2018.

[47] G. L. Pollack. The solid state of rare gases. *Reviews of Modern Physics*, 36(3):748–791, 1964.

[48] J.W. Cahn. Transformation kinetics during continuous cooling. *Acta Metallurgica*, 4(6):572–575, 1956.

[49] S. R. Williams, C. P. Royall, and G. Bryant. Crystallization of Dense Binary Hard-Sphere Mixtures with Marginal Size Ratio. *Physical Review Letters*, 225502(June):4–7, 2008.

[50] S. Plimpton. Fast parallel algorithms for short-range molecular dynamics. *Journal of Computational Physics*, 117(1):1–19, 1995.

[51] C. Perego, M. Salvalaglio, and M. Parrinello. Molecular dynamics simulations of solutions at constant chemical potential. *Journal of Chemical Physics*, 142(14), 2015.

[52] G. C. Sosso, M. Salvalaglio, J. Behler, M. Bernasconi, and M. Parrinello. Heterogeneous crystallization of the phase change material GeTe via atomistic simulations. *Journal of Physical Chemistry C*, 119(11):6428–6434, 2015.

[53] L. A. Rowley, D. Nicholson, and N G Parsonage. Monte Carlo grand canonical ensemble calculation in a gas-liquid transition region for 12-6 Argon. *Journal of Computational Physics*, 17(4):401–414, 1975.

[54] O. Talu and A. L. Myers. Reference potentials for adsorption of helium, argon, methane, and krypton in high-silica zeolites. In *Colloids and Surfaces A: Physicochemical and Engineering Aspects*, volume 187-188, pages 83–93, 2001.

[55] R.A. Aziz and M. J. Slaman. Molecular Physics: An International Journal at the Interface Between Chemistry and Physics. *Molecular Physics: An International Journal at the Interface Between Chemistry and Physics*, 58(4):679–697, 1986.

[56] G. Bussi, D. Donadio, and M. Parrinello. Canonical sampling through velocity rescaling. *Journal of Chemical Physics*, 126(1), 2007.

[57] H. J.C. Berendsen, J. P.M. Postma, W. F. Van Gunsteren, A. Dinola, and J. R. Haak. Molecular dynamics with coupling to an external bath. *Journal of Chemical Physics*, 81(8):3684–3690, 1984.

[58] P. J. Steinhardt, D. R. Nelson, and M. Ronchetti. Bond-orientational order in liquids and glasses. *Physical Review B*, 28(2):784–805, 1983.

[59] W. Lechner and C. Dellago. Accurate determination of crystal structures based on averaged local bond order parameters. *Journal of Chemical Physics*, 129(11), 2008.

[60] W. Ouyang, B. Sun, Z. Sun, and S. Xu. Entire crystallization process of Lennard-Jones liquids: A large-scale molecular dynamics study. *Journal of Chemical Physics*, 152(5), 2020.

[61] J. Russo and H. Tanaka. The microscopic pathway to crystallization in supercooled liquids. *Scientific Reports*, 2:1–8, 2012.

[62] M. Leocmach and H. Tanaka. Roles of icosahedral and crystal-like order in the hard spheres glass transition. *Nature Communications*, 3:1–8, 2012.

[63] J. Taffs and C. P. Royall. The role of fivefold symmetry in suppressing crystallization. *Nature Communications*, 7:1–7, 2016.

[64] F. C. Frank and F. C. Supercooling of liquids. *Proceedings of the Royal Society of London. Series A. Mathematical and Physical Sciences*, 215(1120):43–46, 1952.

[65] D. Coslovich and G. Pastore. Understanding fragility in supercooled Lennard-Jones mixtures. I. Locally preferred structures. *Journal of Chemical Physics*, 127(12):124504, 2007.

[66] M. A. Turchanin. Phase equilibria and thermodynamics of binary copper systems with 3d-metals. VII. Concentration-temperature dependences of the thermodynamic functions of mixing for liquid alloys of copper and transition metals. *Powder Metallurgy and Metal Ceramics*, 46(11-12):565–581, 2007.

[67] S. Sastry, P. G. Debenedetti, and F. H. Stillinger. Signatures of distinct dynamical regimes in the energy landscape of a glass-forming liquid. *Nature*, 393(6685):554–557, 1998.

[68] V. K. De Souza and D. J. Wales. The potential energy landscape for crystallisation of a Lennard-Jones fluid. *Journal of Statistical Mechanics: Theory and Experiment*, 2016(7):74001, 2016.

[69] P. G. Debenedetti and F. H. Stillinger. Supercooled liquids and the glass transition. *Nature*, 410(6825):259–267, 2001.

[70] A. Cavagna. Supercooled liquids for pedestrians. *Physics Reports*, 476(4-6):51–124, 2009.

[71] L. C. Valdes, F. Affouard, M. Descamps, and J. Habasaki. Mixing effects in glass-forming Lennard-Jones mixtures. *Journal of Chemical Physics*, 130(15), 2009.

Chapter 2

Emergence of an Ising critical regime in the clustering of 1D soft matter revealed through string variables

2.1 Introduction

Soft matter systems are characterized by an interaction potential which allows for a finite probability for two or more particles to overlap. Thanks to this feature, they may show a tendency to self–organize into mesoscopic structures, and the properties and the interactions of these structures may determine the macroscopic behavior of the system. Recently, the interest in soft potentials has grown: classically they were found to describe the behavior of compenetrating polymers, molecules [2] and liquid crystals [3], while recent applications in quantum physics were devised in the field of ultracold gases [4] and in the search for exotic supersolid phases [5, 6]. In the last few decades the key features of the phase diagram of many quantum and classical soft potentials were studied in three and lower dimensions, mainly with computational methods [5–11]. It was found that not every soft potential shows the tendency to form aggregates at high densities - i.e "clustering" [12] - and that the key feature to observe such behavior is a negative global minimum of the Fourier transform of the potential, as detailed by Likos *et al.* [9]. For such clustering potentials, the average number of particles per cluster increases with density, and homogeneous n–cluster phases (i.e. with n particles per cluster) appear at specific commensurate densities. One dimensional systems, in this respect, are peculiar, because finite–temperature phase transitions are prevented in systems with either hard–core interactions or discrete (spin) degrees of freedom by the van Hove theorem [13] in classical mechanics and Mermin-Wagner theorem [14] in quantum mechanics. There has been debate about whether such theorems can be extended to soft potentials [15–18]. Recently, a new zero–temperature quantum phase transition (QPT) has been discovered in the clustering of a particular quantum soft matter system in one dimension [7]. By means of quantum Monte Carlo simulations it has been observed that, at the commensurate density for the two–particle cluster phase, the soft system has a secondary excitation mode which is gapless only at the transition point. Further analysis showed that this soft excitation can be mapped via string variables onto an effective one–dimensional (1D) quantum transverse Ising model, finding that the tendency of the soft system to form clusters is the crucial feature for this mode to appear. This fascinating fact opens the interesting possibility that these "magnetic-like" excitations could be a common feature of all the clustering potentials, for both classical and quantum systems.

In this work, our aim is to find evidence of the presence of the same kind of excitations in classical clustering fluids in one dimension, using stochastic simulation techniques. By considering three different soft models, we find that at very low temperatures, at the specific commensurate densities, critical two–particle cluster regimes appear. Under these thermodynamic conditions,

via the same string variables introduced for the quantum transition, we observe the emergence of a critical regime related to a one–dimensional Ising model of pseudo–spins, consistent with a zero–temperature critical point. Moreover, the specific heat of the soft system is characterized by a typical phonon contribution at low temperature, while it shows an anomalous peak at intermediate temperatures, similarly to the 1D classical Ising model. The physical properties of the equivalent pseudo–spin system are also measurable as a function of the temperature T. We show here that the values of the susceptibility, energy, specific heat and spin–spin correlation functions approach the theoretical Ising curves in the limit of zero temperature. This leads to a behavior which is model–independent; moreover, at fixed pair potential, from all the physical properties a consistent estimate of the coupling constant J of the Ising Hamiltonian can be extracted. We suggest here that the J parameters calculated from the various physical quantities tend towards a unique $T \to 0$ limit value. Remarkably, a consistent value can be also deduced from a study of the energy of the "defected" configurations of the system, computed via Simulated Annealing (SA) [19]. At relatively higher temperatures, we find that the anomalous specific heat peak is consistently much higher than for the non–clustering Gaussian potential and has surprisingly universal features, similarly to solid–state magnetic systems displaying a Schottky anomaly.

2.2 Physical models and simulation method

In this work, the results for three distinct soft–core pair potentials are reported. We restrict our investigation to 1D systems of particles characterized by limited, positive, purely repulsive and short-range interactions. In particular, we consider the *Generalized Exponential Model of order four* (also known as GEM–4 and extensively studied in [20, 21]) pair interaction, which has the following functional form:

$$v(r) = U\, e^{-(\frac{r}{\sigma})^4} \tag{2.1}$$

and the *Shoulder–4* (SH–4) and *Shoulder–6* (SH–6) potentials, where a *Shoulder–m* pair interaction is described by:

$$v(r) = \frac{U}{1 + (\frac{r}{\sigma})^m} \tag{2.2}$$

In the previous equations, r is the inter–particle distance, σ is the characteristic length scale and U represents the interaction intensity. In the following energy is naturally measured in units of U and the distances are measured in units of σ. Therefore, equations (2.1) and (2.2) become respectively:

$$v(x) = e^{-x^4} \tag{2.3}$$

and

$$v(x) = \frac{1}{1 + x^m} \tag{2.4}$$

where we have set $x = r/\sigma$. As a consequence, physical wavevectors q will be measured in units of σ^{-1}, i.e. $k = q\,\sigma$. The same applies to number densities $\rho = N\,\sigma/L$, in a system with N particles in a box of length L, always in periodic boundary conditions (PBC). Reduced temperatures $t = k_B\,T/U$ are also used throughout this Chapter, also inside Tables and Figures.

All the potentials just described satisfy Likos criterion concerning the presence of a negative part of their Fourier transform [9, 12, 22] and, therefore, admit high–density n–particle clustering phenomena at low temperatures. These pair interactions are said to belong to the $Q^{\pm}$ class: when the particles of a system interact via this kind of potentials, it was shown [12] that the optimal configuration is achieved when certain fractions of lattice sites are occupied by clusters made of more than one particle. The intuitive motivation for this is related to the tendency of particles to create free space by forming full overlaps, which reflects into the aforementioned property of the potential Fourier transform, i.e. to display negative–valued regions [22]. In particular, as shown by Likos and co–worker, the negative minimum k_{min} of the pair potential in Fourier space determines uniquely the length scale and drives the formation of clusters, whose population scales proportionally with density. Fig. 2.1 clarifies why, in a 'mean–field' approach similar to the one exposed in the Supplemental Material of Ref.[7], the cluster phase is energetically favored. Here, the method employed is called 'mean–field' only because the fluctuations with respect to the perfect cluster lattice are neglected. As it is apparent from the picture, the particles found in the positions corresponding to the cluster liquid phase are characterized by a lower potential energy with respect to the ordinary liquid phase, due to the many–body effective potential. The curves in the example refer to the SH–6 pair interaction, but similar curves can be found for SH–4 and GEM–4 potentials. The mean–field approach begins calculating the 1D Fourier transform $\tilde{v}(q)$ of the interaction $v(r)$. At the commensurate density for the n–particle cluster phase, an approximation of the mean–field potential experienced by a particle in the liquid phase can be computed by letting all other particles on a lattice whose spacing (indicated as b_c in the picture) is the inverse of the density. This lattice periodicity is clearly unstable, since a double well appears close to the origin (see SM of Ref.[7]): only the presence of the kinetic energy aids the stabilization of the system. Vice versa, the mean–field potential felt by a particle in the cluster liquid phase can be approximated by letting all other particles on a lattice of spacing $2/\rho$. When pairs of particles overlap, the effective pair potential (orange line in Fig. 2.1) is characterized by a minimum at $r = 0$: the cluster phase is more stable than the single–particle liquid.

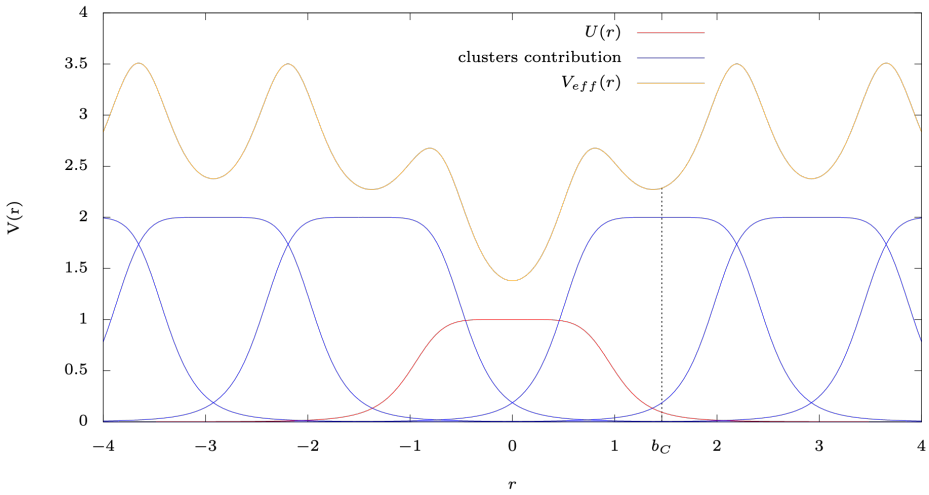

FIGURE 2.1: Mean–field approach for showing the greater stability of the cluster phase at commensurate density $\rho_{(2)}$. The effective potential (yellow curve) presents a global minimum in $r = 0$ and local minima at distances commensurate with b_C.

In Fig. 2.2 we show the three considered potentials and their Fourier transforms.

Table 2.1 displays the values of the wavenumber k_{min} corresponding to the minimum value of the Fourier transform of our potentials and the corresponding optimal reduced densities for the formation of two–particle clusters, where

$$\rho_{(n)} = \frac{n\, k_{\min}}{2\pi} \tag{2.5}$$

and, therefore, $\rho_{(2)} = k_{min}/\pi$.

Pair potential	k_{min}	$\rho_{(2)}$
GEM–4	4.59180	1.46165
SH–4	4.44289	1.41422
SH–6	4.29952	1.36857

TABLE 2.1: k_{min} and $\rho_{(2)}$ for the three pair potentials studied

In our calculations, each of the three systems is studied at its own commensurate numerical density $\rho_{(2)}$, for the two–particle cluster phase. The study of this system at non–commensurate densities is clearly a very interesting topic, which has already been explored [21, 23], and is outside the scope of this work. Low–temperature thermodynamic properties are computed via

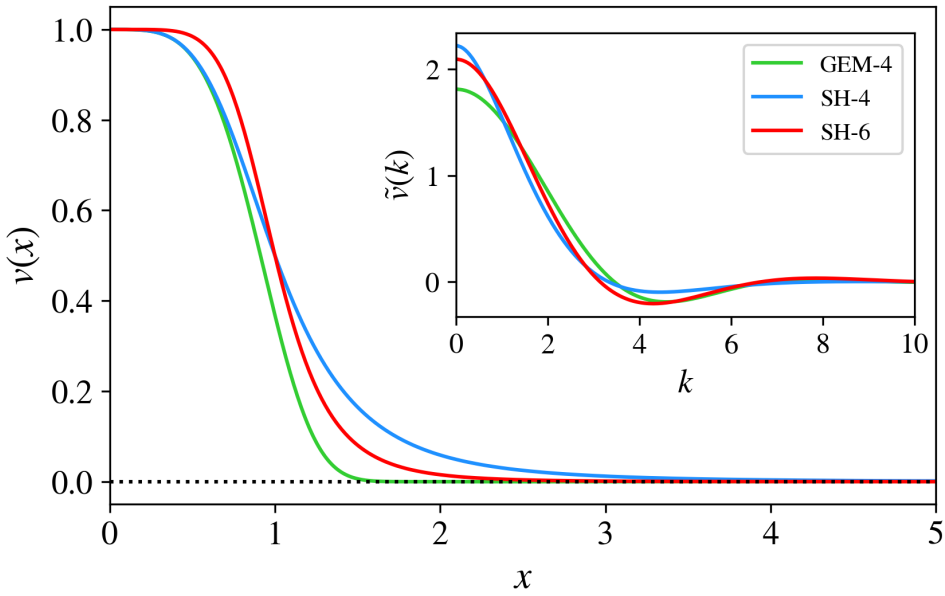

FIGURE 2.2: Inter–particle interaction potentials $v(x)$. In the inset their Fourier transforms, $\tilde{v}(k)$ are drawn. They all display a negative minimum, thus satisfying Likos criterion for clustering. See also Tab. 2.1. Reprinted from [1]

canonical Monte Carlo simulations by using the Metropolis algorithm to sample equilibrium configuration of the N particles.

2.3 Monte Carlo code

In this section the structure of the simulation code will be briefly discussed, and also the observables computed in the program will be described. The software used for the simulations is a `C++` code developed from scratch, which implements Monte Carlo moves of the soft particles in the canonical statistical ensemble; the new configurations proposed are either accepted or rejected via Metropolis criterion, according to their Boltzmann weight. The program uses the so called "data blocking" method, while the equilibrium configurations of the system are sampled (see e.g. [24]). A scheme of the structure of the whole program is depicted in Fig. 2.3, with the s_{tot} steps subdivided in n_b blocks, each one made of $s_b = s_{tot}/n_b$ steps. Essentially, the code exploits the generation of pseudo–random numbers; the sequence of numbers generated starts from a seed and the following numbers are extracted according to a deterministic procedure. This implies that the configurations sampled via moves which are based upon these numbers are, clearly, at least partially

correlated. In fact the MC moves, when they are accepted, produce a local update of the configuration. This phenomenon has a typical timescale related to the specific update moves of the Metropolis algorithm; one can thus group a fixed number of consecutive MC steps into blocks, where data within the same block are - at least partially - not independent. For each observable O, an estimation of its value is computed each step after all the trial moves. The estimations are accumulated and used to generate a single block measurement of that observable (i.e. its average over the steps of the block).

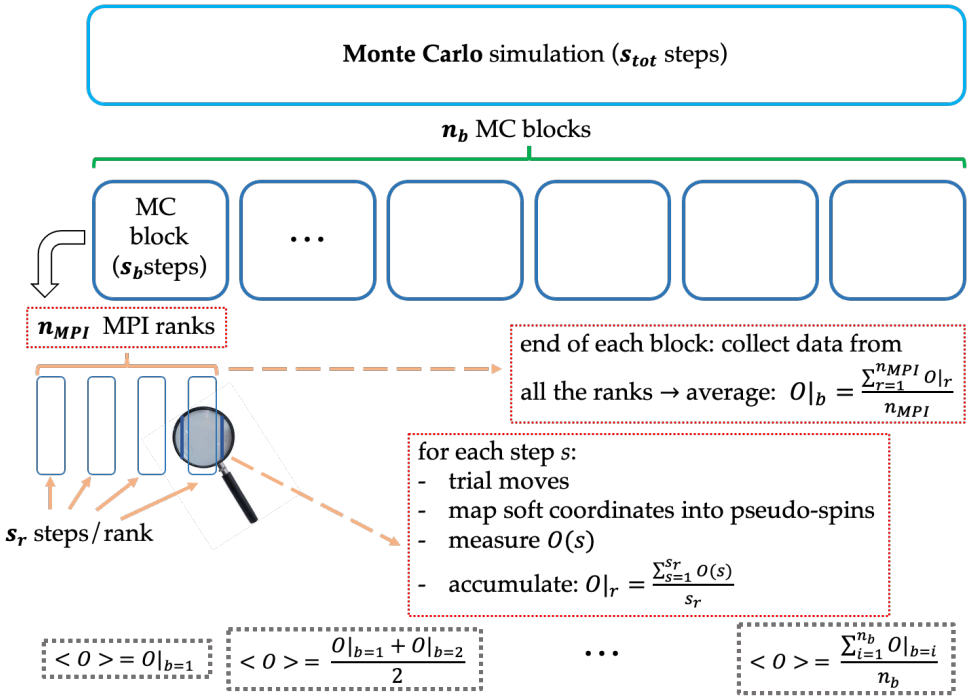

FIGURE 2.3: Scheme of the Monte Carlo code, via a simple MPI parallelization. The simulation is divided into independent blocks, whose steps are split among ranks.

The code has been parallelized in a simple way with MPI libraries (https://www.open-mpi.org/). Each rank (parallel process) performs the same operations on different data and their information are periodically gathered by master rank, which also takes care for statistical analysis and data output. In particular, given the total number of steps in each block, each of the n_{MPI} ranks is assigned $s_r = s_b/n_{MPI}$ steps, to be executed at the same time; then, each rank r averages the observable O over s_r steps, generating a quantity called $O|_r = \frac{\sum_{s=1}^{s_r} O(s)}{s_r}$, $O(s)$ being the single step measurement of

O. Thanks to the fact that each replica of the system is sampled at equilibrium, when a rank completes its s_r steps it sends its $O|_r$ to the master rank, which performs a unique average $O|_b = \frac{\sum_{r=1}^{n_{MPI}} O|_r}{n_{MPI}}$ over the $O|_r$ estimations computed by the single ranks. Note that the choice of the number of concurrent ranks is made in such a way that the resulting s_r is large enough to be meaningful; typically, this value must be larger than the characteristic autocorrelation time of the relevant physical properties. Naturally, as long as the simulation proceeds, the running average of O, $\langle O \rangle = \frac{\sum_{i=1}^{n_b} O|_{b=i}}{n_b}$ improves, because of the increasing number of estimations. Here, $O|_{b=i}$ indicates that O is evaluated at block i.

In the following, it is provided a description of the most important sections of the program:

- input operations → read from file: number of soft particles N, density $\rho_{(n)}$, reduced temperature t, initial soft configuration, number of blocks and steps per block, number of equilibration steps, maximum range of the trial displacement moves.

- after reading the N initial particle coordinates, a function assigns the corresponding $N_s = N/2$ pseudo–spin degrees of freedom. This is a crucial step, and the way in which the soft system can be mapped onto the other is not univocal. Further on, some possible choices about this mapping procedure are discussed.

- perform equilibration of the system. The particles are only randomly moved, without either measuring or averaging the observables. The various moves attempted are explained in the next point.

- using data blocking, the equilibrium configurations of the system are finally sampled. There are four types of trial moves that are applied to the soft degrees of freedom in order to update their positions.

    1. *simple translation* of a particle coordinate by a quantity Δx where $-\delta/2 \leq \Delta x \leq \delta/2$. This move is performed $2N$ times at each step: N random trials are performed with a δ such that the acceptance rate of the move is about 0.5; the next N trials use a larger δ which guarantees about the 20% acceptance rate, increasing the ergodicity of the simulation.
    2. *translation* of a particle coordinate by a quantity which is an *integer multiple of the lattice step* (performed N times per MC step). This move has a very low acceptance rate, but it helps in sampling configurations where a particle belonging to a cluster suddenly

moves to join another already formed cluster, thus leaving a final configuration with 3 particles grouped and a single left alone.

3. to further enhance the configuration–space exploration, the code tries m times for each MC step to perform a *rigid translation of a pair of first neighbors*. This move has been introduced to sample the rigid vibrations of the clusters, which constitute a fundamental improvement in the exploration of the configuration space.
4. n_{split} times per step, a move which tries to *split up clusters* is attempted. In particular, the particles belonging to the randomly chosen cluster are moved in opposite directions by the same amount. The physical rationale behind this move is that, in this way, inner cluster vibrations should be better sampled, thus enhancing the sampling quality of the phase space.

- after all the trial moves, the resulting soft particle configuration of that step is mapped onto the corresponding pseudo–spin system.
- the properties of the soft particles and of the pseudo–spins are measured within each rank. Then, all the n_{MPI} processes gather their own information and send it to master rank, which calculates a unique block average $O|_b$. Then, the running average is updated (the error over $\langle O \rangle$ is computed as standard deviation of the average).
- the software prints output information at the end of each block.

Note that also soft particle configuration is periodically printed for visual inspection.

2.3.1 The reweighting method

We remark that a subset of the simulations was conducted at extremely low temperatures, due to the fact that the correspondence between the soft degrees of freedom and the mapped pseudo–spins is only valid in the $t = k_B T/U \to 0$ limit. At such low temperatures, the computation of equilibrium properties is hindered by the fact that the exploration of the configuration space is slowed down. In fact, the high–energy configurations are visited with exponentially lower probability at such temperatures; an accurate estimation of the expectation values would require extremely long simulations, in order to allow the system to visit rare configurations. This led us to employ a technique called 'reweighting' [25]. In summary, it can be shown that the average value of an observable O at a given reduced temperature t' (where $t' < t$, for us) can be expressed as:

$$\langle O \rangle_{t'} = \frac{\langle OW\,(t,t') \rangle_t}{\langle W\,(t,t') \rangle_t} \tag{2.6}$$

where W is the weight function, written as:

$$W(\vec{R}, t, t') = e^{\frac{t'-t}{tt'}v(\mathbf{R})}$$

with $\vec{R} = x_1, \ldots, x_N$ and v as the total potential interaction of a given particle configuration $\vec{R}$, in units of U. In fact, the statistical average of O at reduced temperature t can be written as:

$$\langle O \rangle_t = \frac{\int d\vec{R}\, O(\vec{R})\, e^{-\frac{v(\vec{R})}{t}}}{\int d\vec{R}\, e^{-\frac{v(\vec{R})}{t}}}$$

which can be transformed by subtracting and adding a quantity $v(\vec{R})/t'$ at the exponent of the numerator and of the denominator exponential terms both:

$$\langle O \rangle_t = \frac{\int d\vec{R}\, O(\vec{R})\, e^{-\frac{v(\vec{R})}{t}+\frac{v(\vec{R})}{t'}-\frac{v(\vec{R})}{t'}}}{\int d\vec{R}\, e^{-\frac{v(\vec{R})}{t}+\frac{v(\vec{R})}{t'}-\frac{v(\vec{R})}{t'}}}$$

$$= \frac{\int d\vec{R}\, O(\vec{R})\, e^{-\frac{v(\vec{R})}{t}+\frac{v(\vec{R})}{t'}}\ \frac{e^{-\frac{v(\vec{R})}{t'}}}{Q}}{\int d\vec{R}\, e^{-\frac{v(\vec{R})}{t}+\frac{v(\vec{R})}{t'}}\ \frac{e^{-\frac{v(\vec{R})}{t'}}}{Q}}$$

where Q is the partition function of the system in the canonical ensemble. This means that we can finally express $\langle O \rangle_t$ as in Eq. 2.6, with $W(\vec{R}, t, t') = e^{-\frac{v(\vec{R})}{t}+\frac{v(\vec{R})}{t'}} = e^{\frac{t'-t}{tt'}v(\vec{R})}$. An important remark, in this context, is that the Metropolis criterion is obviously still valid at low temperatures; the problem resides in the reduced mobility of the particles, which would need energetically expensive moves to better explore the phase space, but at low t the majority of these moves are rejected. Considered that the potential energy surface, with such a number of degrees of freedom, would be quite complex, the presence of local minima is almost guaranteed. In case of low temperatures, it would take a huge computational (and also real) time for the system to escape from a minimum. The reweighting methods helps to compensate for this issue, but one has to be aware that the W function experiences wide fluctuations, according to the values of V along the simulation. This can sometimes generate computational problems (due to finite machine precision), which are usually overcome by rewriting $W(\mathbf{R}, t, t')$ as:

$$W(\mathbf{R}, t, t') = e^{\frac{t'-t}{tt'}(v(\mathbf{R})-A)}$$

where A is a constant whose value is set, in general, equal to a previously determined average potential energy value at that temperature $\langle v \rangle_t$ at the temperature t. In this way, the fluctuations of $V(\mathbf{R}) - A$ should be small, and overflow issues should not occur. Note that the weight function appears

both at the numerator and at the denominator of the fraction in Eq. 2.6; thus, adding the constant A at the exponent is irrelevant and leaves the expectation value of the observable $\langle O \rangle_t$ unaltered. In the rest of the present Chapter, the reweighting method was used:

- for any SH–4 simulation at $t < 0.04$
- for any SH–6 simulation at $t < 0.05$
- for any GEM–4 simulation at $t < 0.055$

while all the GEM–2 simulations were run without employing this tool.

2.4 Results for the soft–particle system

In this section, we show the results of the MC simulations for the thermodynamic quantities calculated from the low–temperature equilibrium configurations of the 1D soft particles system. This first part of the chapter is similar to the analysis performed by Speranza *et al.* [18] on the Gaussian core model. They investigated the properties of the 1D GEM–2 soft fluid, finding anomalies in the specific heat and determining the structural properties of the system via pair correlation functions and static structure factors. In particular, they suggested the presence of traces of the ordered arrangements found in clustered crystals, despite the absence of a true solid–liquid phase transition. The results reported in the following are analogous, but are referred to genuine clustering potentials, at variance with the GEM–2. Van Hove's theorem does not hold, due to the lack of any hard–core interaction in our model, as discussed e.g. in [15], despite being in 1D. Previous studies gave strong evidence that the penetrable spheres and the penetrable square well models do not display a thermal phase transition in 1D [16]; conversely, Acedo *et al.* [17] identified the appearance of a crystalline one–dimensional phase for a step (discontinuous) potential, which is not our case. As a consequence, it is not known *a priori* if a critical finite–temperature phase transition does exist for our models. Our results, in agreement with previous studies [18], show that a phase transition is eventually expected only in the limit $t \to 0$. This is immediately apparent in the features of the two–particle distribution function $g(x)$ upon decreasing t, where $g(x) = \dfrac{\rho^{(2)}(x_1, \ldots, x_N)}{\prod_{i=1}^{N} \rho^{(1)}(x_i)}$ and the p–particles density is equal to $\rho^{(p)} = \dfrac{N!}{(N-p)!} \displaystyle\int \rho(x_1, \ldots, x_N) dx_{p+1} \ldots dx_N$. The temperature dependence of $g(x)$ for the SH–6 potential is shown in Fig. 2.4 for some relevant t values. Results for the other potentials are essentially equivalent. This fluid was simulated at density $\rho_{(2)} = 1.36857$; in these conditions, a perfect single–particle crystal would host a particle about every $\Delta x = 0.73069$.

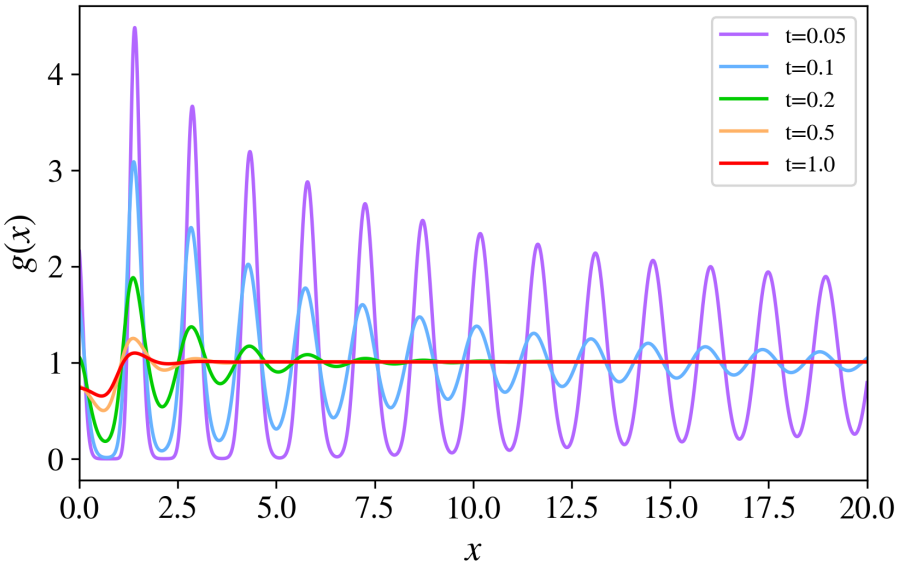

FIGURE 2.4: Temperature dependence of $g(x)$ for the SH–6 potential. Errorbars are smaller than the line width. Reprinted from [1]

A key observation is that $g(x)$, by lowering the temperature, shows the formation of oscillations, damped with increasing distance x, at a spatial separation $2\Delta x$. Moreover, the formation of a peak in the origin can be observed, whose height grows while approaching $t = 0$. These features clearly highlight the tendency of the system to form clusters composed of two particles. The growing height of the peaks of the oscillations in $g(x)$ indicates the emergence of a quasi-long-range order, due to the increasing regularity of the spatial arrangement of the clustering particles. For much higher temperatures, this order is lost and $g(x)$ displays some structure only at small distances.

To further remark this behavior of the clustering potentials, in Fig. 2.5 we compare $g(x)$ for two systems of particles interacting via either the GEM–2 (i.e., Gaussian) or the GEM–4 potential, both simulated at reduced density 1.46165. We considered two simulations at different t for each system, so as to be able to compare the properties at low and at high temperature of a clustering and a non–clustering system. The GEM–2 tends to show ordering at much lower temperatures [26]; for this reason, in Fig. 2.5 we compared a GEM–2 $g(x)$ at $t = 0.01$ to the $g(x)$ for the GEM–4 simulated at $t = 0.06$.

The GEM–2 system displays a minimum for the occupation probability in $x = 0$ (even at low temperature), while the GEM–4 always presents an evident maximum in the pair distribution function at the origin. At low temperatures, the oscillations of $g(x)$ for the GEM–2 case display a periodic spacing which

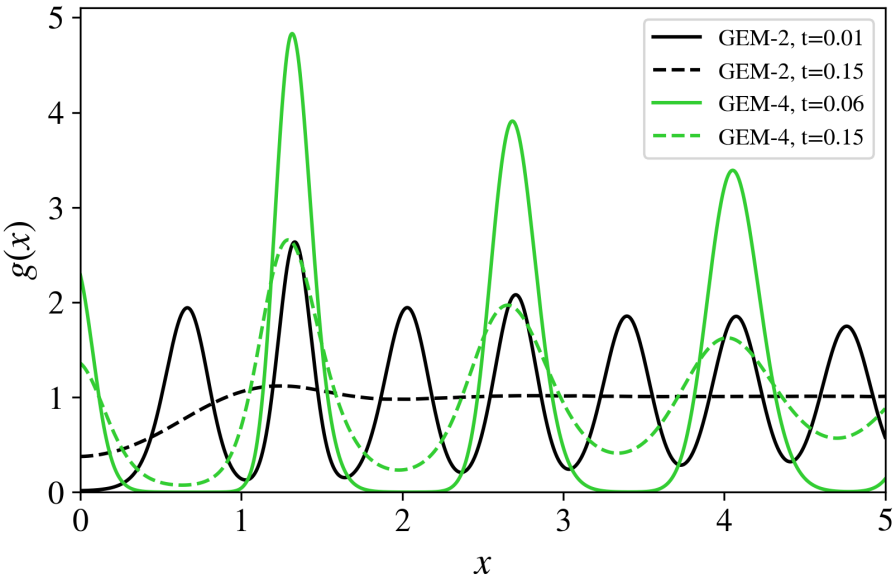

FIGURE 2.5: Comparison between the $g(x)$ of GEM–2 and GEM–4 potentials for some temperatures, at reduced density 1.46165. Errorbars are smaller than the line width. Reprinted from [1]

is one half that of the GEM–4. Therefore, also the particles interacting via the GEM–2 potential have some tendency to solid ordering, but they do not show any clustering tendency. We observe a striking feature: the $g(x)$ peaks of the GEM–2 corresponding to the clustering peaks of the GEM–4 are slightly higher than the other peaks of the GEM–2. Interestingly, as already observed in [18] a non–clustering potential such as the GEM–2 displays, nonetheless, a slightly prevalent spatial ordering in correspondence of the peak positions characteristic of clustering phases. This is remarkable since the GEM–2 does not have any negative component in its Fourier transform. By comparing the $g(x)$ for the two potentials at $t = 0.15$ (dashed lines in the figure), we note that the particles interacting via the GEM–4 already present a partial order and a finite occupation in $x = 0$, while the GEM–2 is still mostly disordered.

Analogous physical information about the soft–particle behavior can be extracted from the static structure factor $S(k)$, where $S(k) = \frac{1}{N}\langle \rho_k \rho_{-k} \rangle$ with $\rho_k = \sum_{l=1}^{N} e^{ikx_l}$, in Figs. 2.6 and 2.7. The wavevector of the first peak in the $S(k)$ (Fig. 2.6) is given by the value of k_{min} for the SH–6 potential, thus underlining that the forming structure is closely related to the two–particle clusters. Moreover, when temperature decreases, the appearance of the second peak at $k = 2\,k_{min}$ highlights the tendency to the crystalline ordering among the clustering particles.

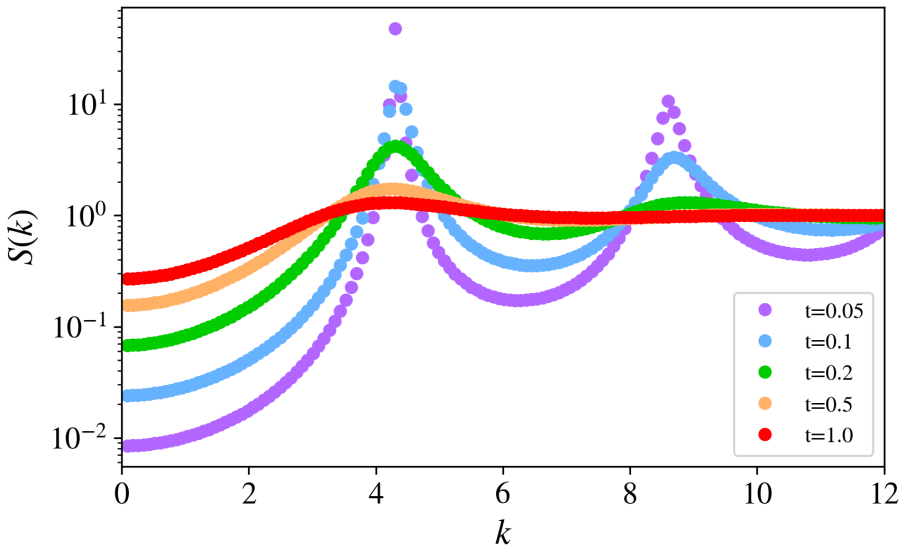

FIGURE 2.6: Temperature dependence of $S(k)$ for the SH–6 potential. Note the log-scale for $S(k)$. Errorbars are smaller than the symbol size. Reprinted from [1]

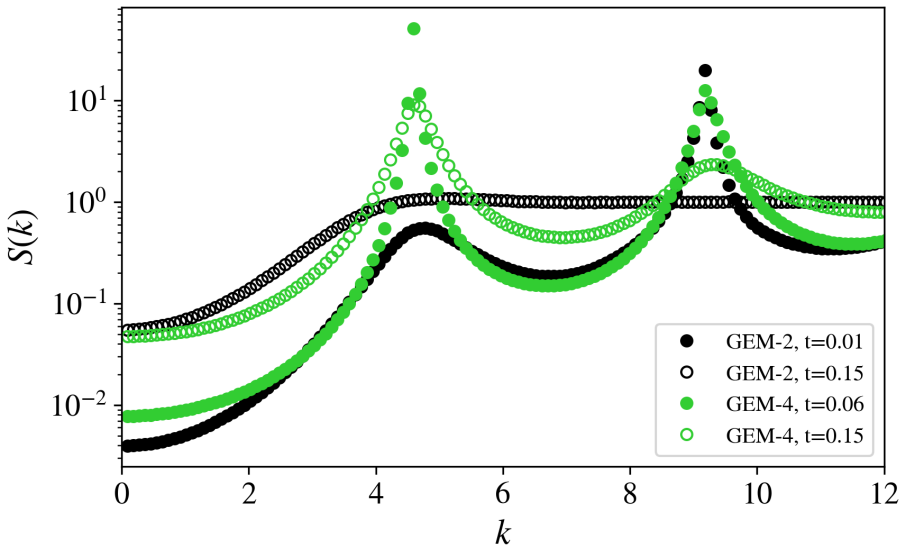

FIGURE 2.7: Comparison between the GEM–2 and GEM–4 $S(k)$ for some temperatures, at reduced density 1.46165. Note the log-scale for $S(k)$. Errorbars are smaller than the symbol size. Reprinted from [1]

We also compare, in analogy with the observations reported for the pair distribution functions, the static structure factors for the GEM–2 and GEM–4 systems at the same temperatures. The peak of $S(k)$ located at k_{min} shown in the picture is again a clear sign of the tendency to clustering; the behavior of the GEM–4 system displayed here (green points in Fig. 2.7) is then similar to the one suggested by the $S(k)$ of the SH–6 potential. Concerning the small-k peak of $S(k)$, at low temperature the GEM–2 also presents some structure which can be interpreted as a signal of the aborted clustering. Both models show the formation of a peak at $k = 2k_{min}$ which represents the tendency to solidification of clustering pairs of particles for the GEM–4 and of particles for the GEM–2.

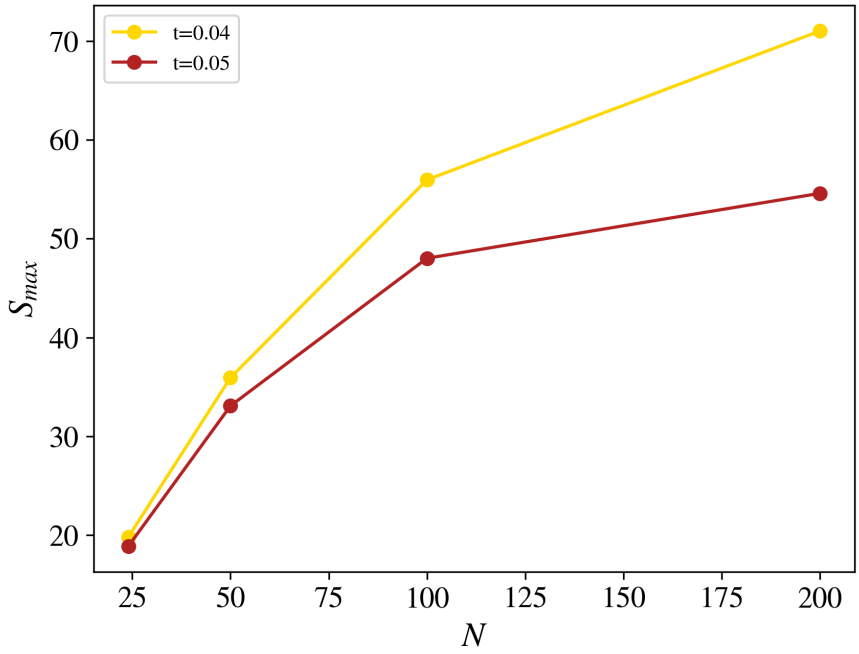

FIGURE 2.8: Maximum height of $S(k)$, S_{max}, as a function of the number of particles in the system N, for Shoulder–6 pair potential at temperature $t = 0.04$ and $t = 0.05$.

Besides, the height of the static structure factor main peak is a useful tool for the identification of possible crystal phases. Plotting the maximum height of $S(k)$ (called S in the picture) as a function of the system size (N going from 20 to 200) at various temperatures reveals a sublinear growth for each temperature, which indicates that our system does not truly crystallize in the low–temperatures explored ($t = 0.04$ and $t = 0.05$ in this case). The example reported in Fig. 2.8 is about the SH–6 simulations, but analogous considerations hold for the other two models investigated in this work.

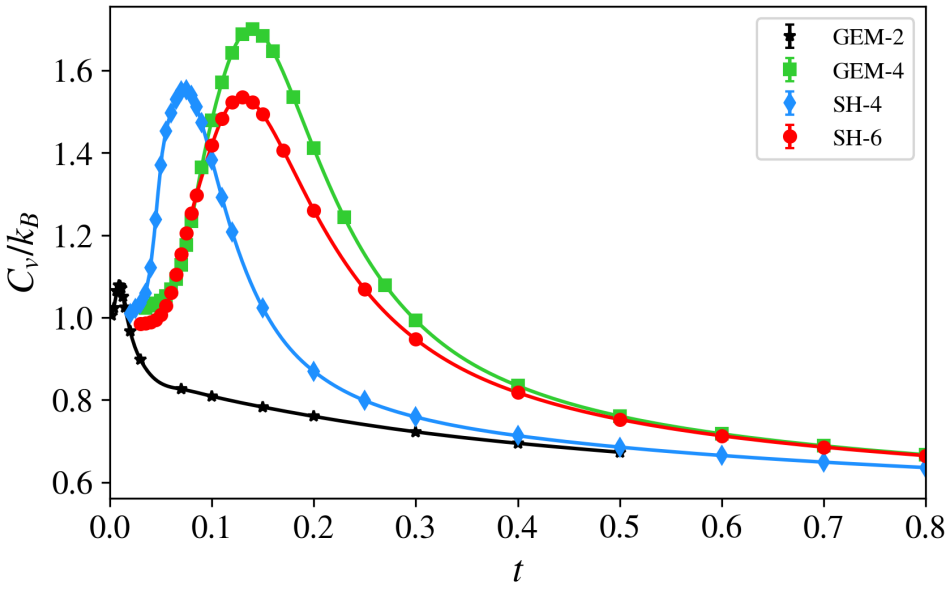

FIGURE 2.9: The specific heat at fixed volume, C_v, for GEM–4, SH–4 and SH–6 over a wide range of temperatures is reported. Also data of C_v for the GEM–2 (non–clustering) potential are reported. Solid lines are guide for the eye. Reprinted from [1]

We also calculate the specific heat for these systems. In particular, Fig. 2.9 contains the simulated values of the specific heat $C_v = C/N$ in units of k_B, for the three aforementioned potentials, where C is the heat capacity:

$$C = \frac{k_B(\langle V^2\rangle - \langle V\rangle^2)}{t^2} + \frac{1}{2}\,N\,k_B\ . \tag{2.7}$$

In this equation, V is the potential energy of the soft-particle system and the second term is the analytical constant kinetic energy contribution to C, which is included for the sake of completeness. The most striking feature in Fig. 2.9 is that, at low temperatures, all the clustering potentials present a well–defined peak in the specific heat curves as a function of t. This behavior is akin to the Schottky anomaly of solid–state spin systems [27], which prompts the investigation of the emergence of spin degrees of freedom in the next Sections. The temperature range relative to the appearance of this peak is potential–dependent. The maximum heights of these curves have similar values for the three models investigated. On the contrary, the non–clustering GEM–2 system shows a much smaller peak at temperatures about one order of magnitude lower than the clustering potentials. A tendency to spatial ordering in the GEM–2 thus occurs at lower temperatures, via single-particle occupation of effective lattice sites. Conversely, the high and broad

peaks present in the other three systems are a sign of the tendency towards the formation of two–particle clusters already at higher temperatures. This emergent phenomenon is more fragile in the SH–4 model, as shown by the C_v peak, whose range is shifted towards lower temperatures. Note also that this peak, as well as the ones of the SH–6 and GEM–4 potentials, is much higher than that of the non–clustering potential, because of the larger energy fluctuations occurring in the clustering phenomena. Approaching the limit of $t = 0$, C_v/k_B approximates the unit value, which corresponds to the value for an ideal harmonic solid; at high t, the simulated data display a convergence towards 1/2, the typical value for the 1D ideal gas with only kinetic contribution.

2.5 Mapping and pseudo–spin observables

Recently, the study of the SH–6 potential was tackled for a fluid of indistinguishable bosons in the continuum at zero temperature [7, 28–30]. The system was investigated upon changing the density and the interaction constant U. In the quantum regime, in fact, properties of the system do not depend only on the reduced temperature $t = k_B T/U$, but also on the dimensionless coupling constant $u = Um\sigma^2/\hbar^2$, where m is the particle mass. The constant u accounts for the relative role of interaction versus quantum delocalization effects. In particular, by fixing the density at the commensurate value $\rho = \rho_{(2)} = 1.36857$, a QPT corresponding to the formation of two–particle clusters was detected at $u = u_c \simeq 18$ [7]. Below this value, a liquid regime was found, where ground state and excited state properties are typical of a Luttinger liquid of single particles, whereas for values above u_c the behavior was the one of a two–boson cluster Luttinger liquid. The transition between these two regimes, at $u = u_c$, is highlighted by a pair distribution function $g(x)$ which develops a peak at zero distance for $u > u_c$, but also by a marked anomaly in the Luttinger parameter, which characterizes the hydrodynamic properties of the fluid, across the transition. Interestingly, across the transition, an analysis of the excited states via extraction of the dynamical structure factor using analytic continuation [31–34] demonstrates a gapped secondary mode connected to the incipient cluster formation. The gap of the secondary mode is found to vanish at the transition; this is the crucial clue for a further investigation of the possible mapping between this system and the quantum Ising model in transverse field, which has a similar behavior in the excited states' spectrum across its QPT [35].

This mapping can be made quantitative by introducing a set of string variables similar to the one discussed in Ref. [36]: first, particles are ordered by their increasing position, $x_1 < x_2 < \cdots < x_N$ and even positions are assigned a lattice index $j = 1, \ldots, N/2$. Second, a pseudo–spin $\sigma_j = 1$ is assigned if

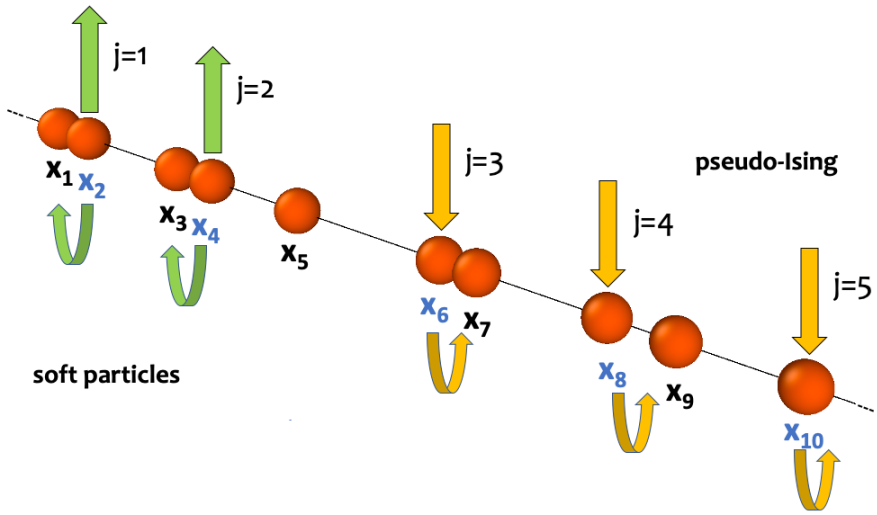

FIGURE 2.10: Schematic representation of the mapping between the soft–particle degrees of freedom and the corresponding pseudo–spins. The assignment of a left/right closest neighbor (lower curved arrows) is done for the particles with even indexes (labeled in blue), and determines the value of the pseudo spin (upper arrows). Considering the odd particles leads to an equivalent result. Reprinted from [1]

$|x_k - x_{k-1}| < |x_k - x_{k+1}|$, or $\sigma_j = -1$ in the opposite case, with $k = 2j$; note that when these operations involve particle 1 and particle N, these are first neighbors in PBC. The last step of the mapping consists in placing these spins onto evenly spaced lattice sites, thus neglecting the fluctuations of the particle coordinates in the original soft system. An equivalent mapping can be done by using only the odd-indexed particles as starting points. The whole procedure is sketched in Fig. 2.10. Note that, given a soft–particle configuration, two different mapping algorithms do not generate, in principle, the same pseudo–spin state. Therefore, each different mapping procedure can not be directly compared with any other; rather, what we verified is that the specific algorithm employed does not yield, in the end, different physical results. When comparing two mapping methods, the two sequences of pseudo–spin states will almost certainly be different, but this is not a problem: both sequences are univocally defined by the particular algorithm and, at equilibrium, the emerging pseudo–spin properties are essentially identical. Moreover, there are several other possible ways in which pseudo–spins can be associated to the degrees of freedom of the original system. For example, we also explored the possibility of a mapping which compares the two methods just exposed

(start from even–indexed or odd–indexed sites) and excludes the configurations where the two mappings do not provide the same result (which, in the temperature range explored, represent a fraction smaller than the 1% of the total number of configurations produced). We also performed a distinguished analysis of the configurations, that accounts twice for a configuration when the original two mapping methods disagree (both the ground state and the first excited state counters are incremented by 1). In both these last methods, if one of the mapping procedures identifies a state as being at least the second excited state, that configuration is discarded. Importantly, all these alternatives provide almost identical results, which means that the final outcome is independent of the particular mapping procedure. As a consequence, it is possible to directly associate these $N_{\rm s} = N/2$ discrete spin variables to the N soft continuous configurational degrees of freedom. This mapping is a surjective function of the spatial coordinates and performs a coarse graining of the configurations, leaving only the relevant "magnetic" degrees of freedom. Note that a completely disordered configuration of soft particles, being the distance between a particle and its two neighbors a random value, would be mapped onto a randomly–oriented pseudo–spin configuration. Conversely, an almost perfectly two–particle clustered configuration would be mapped onto a spin configuration with all the spins aligned in the same direction. The order parameter is essentially the thermal average of these pseudo–spins. Moreover, as it is exemplified in Fig. 2.10, it could happen that a pseudo–spin with a given orientation is followed by a pseudo–spin with the opposite orientation. Remarkably, in the 1D quantum soft system, the pseudo–spin correlation function $\langle \sigma_j^z \sigma_{j+i}^z \rangle$ (averaged over j) behaves as expected for the transverse Ising model. In the paramagnetic phase, which corresponds to a Luttinger liquid of soft particles, it decays exponentially; conversely, in the ferromagnetic phase, which corresponds a two–particle cluster Luttinger liquid, it manifests true long-range order. This procedure allows then to observe the order emerged in this QPT, which is a nonlocal form of ordering evidenced by the procedure employed for mapping the soft system onto a system of pseudo–spins hosted on a regular 1D lattice. All the positions of the soft particles are involved, indeed, in the construction of the string variables: the particles must, in fact, be labeled in increasing order, to be able to define each pseudo–spin via the mapping algorithm.

Concerning the classical 1D soft systems under investigation in this work, a phase transition at finite temperature is not expected, as discussed above; however, at very low temperatures, our systems enter a critical regime corresponding to a tendency to clustering which becomes effective only for $t = 0$. Moreover, the appearance of a Schottky-like anomaly in the specific heat suggests that a discrete number of well-defined metastable states contributes in the low-temperature dynamics of clustering systems. An intriguing possibility is that these soft systems could as well be partially mapped onto the 1D

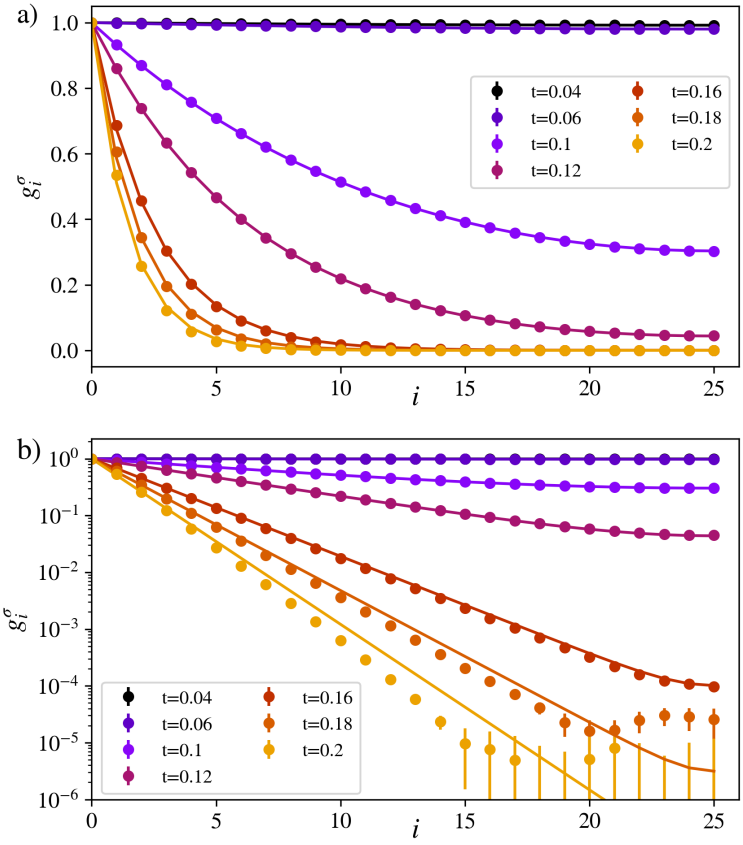

FIGURE 2.11: a): Ising correlation functions for pseudo–spins g^σ are shown in the case of the GEM–4 interaction. Solid lines represent, at each temperature, independent fits with the exact Ising formula up to the largest possible distance in PBC (i.e. half the size of the simulation box). b): same data in linear–logarithmic scale with errorbars. Reprinted from [1]

Ising model, but in this case a classical one. This would imply that the part of the dynamics of a generic soft 1D system on the continuum, pertaining to clustering effects, could be mapped onto a system of discrete variables on a lattice. We notice that there are many instances in statistical physics where a continuous system has the same critical behavior as a discrete model, for example the three-dimensional (3D) liquid-gas transition is in the 3D Ising class. Moreover, discrete variables are customarily introduced in the study of clustering systems, describing the number of particles per cluster. Here, the role of magnetic discrete degrees of freedom can be directly tested by using the mapping of the soft–particle degrees of freedom onto the pseudo–spin variables already exploited in the quantum case. To this aim, via the

mapping procedure just introduced, it is possible to calculate the Ising–like thermodynamic properties of the pseudo–spins. A major advantage of this approach is that it is well-defined for all potentials and temperature regimes that we are considering, without any approximation. We are interested not so much in the characterization of the thermodynamic limit, as in the comparison between the pseudo–spin observables computed in the simulations and the analytical calculations for an analogous Ising system with the same number of spins.

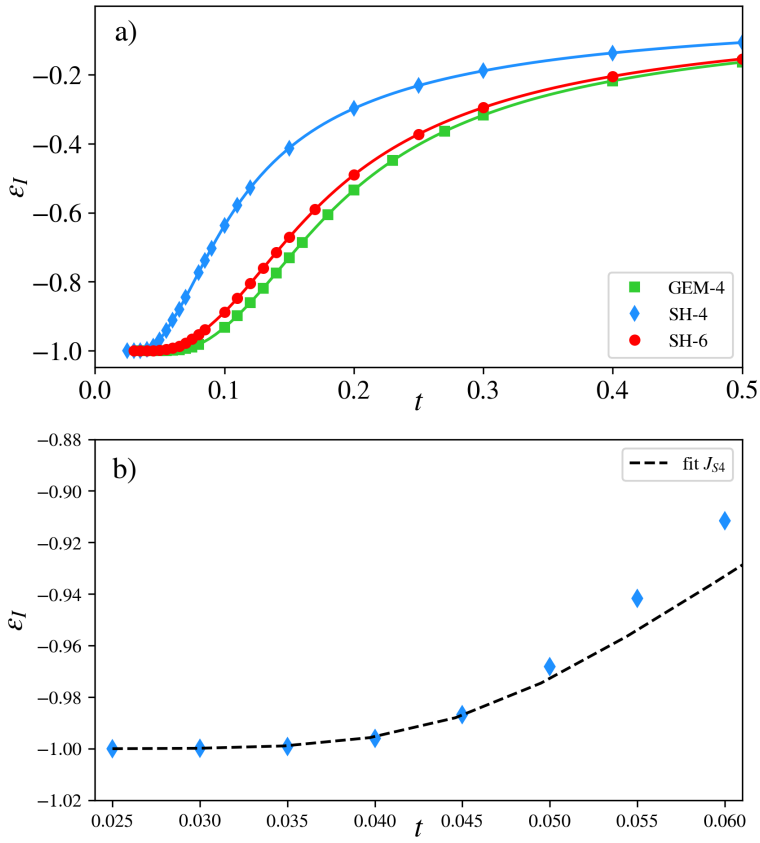

FIGURE 2.12: Ising energy per spin in units of J, obtained from soft–particle configurations via mapping. Solid lines are guide for the eye. The lower panel shows a closer view of the temperature range between 0.025 and 0.06, only for SH–4, and the black dashed line is the Ising result with $J = J_{S4}$. Reprinted from [1]

In parallel to the approach adopted in the study of the 1D quantum system, the first step consists in applying the mapping procedure for the computation of the pseudo–spin correlation functions averaged over the starting

index, $g_i^\sigma = \sum_j \langle \sigma_j \sigma_{j+i} \rangle / N_\mathrm{s}$. As an example, in Fig. 2.11 we report a relevant subset of those computed for the GEM–4. The following considerations hold however for all the three interaction potentials studied in this work. Remarkably, the shape of all these curves closely resembles the behavior expected for a classical Ising model with short range interactions, but with a coupling constant J dependent on temperature. Note, in fact, that we necessarily have to associate the temperature t of the soft system to the one of the pseudo–spin model. This implies that we let the Ising coupling J (assumed to be in U units) as a free parameter to be fitted at each temperature. Clearly, as evidenced by the lin–log scale of Fig. 2.11b) the fit turns out to be very accurate at low t; in particular, at $t = 0.16$ and below the simulated data are fitted quite closely by the theoretical curve, while at higher temperatures the mapping procedure does not generate pseudo–spin variables effectively associable to Ising spins. In fact, the simulated data points deviate from the model, at large i values, for $t = 0.18$ and $t = 0.20$. Noticeably, as it will be shown in the following (see Fig. 2.15), a further temperature lowering is required for pseudo–spin behavior to closely manifest Ising physical properties. As in the Ising model, the pseudo–spins appear to be strongly correlated at very low temperatures, where g^σ is almost flat and slowly decaying; conversely, the pseudo–spins start to assume random relative orientation, as the temperature grows and g^σ rapidly decreases towards zero.

The study of the g^σ functions suggests that the hypothesis of a mapping between the soft system and the Ising model can be quantitative. As a further step in this direction, we also compute other relevant thermodynamical observables of the mapped pseudo–spin system. In Figs. 2.12, 2.13 and 2.14, we show, for all the three interaction models, the pseudo–spin properties of energy, heat capacity and susceptibility, obtained by mapping the configurations of $N = 100$ soft particles onto $N_\mathrm{s} = 50$ pseudo–spins. We define the Ising total energy as $E_I = -J \sum_{i=1}^{N_\mathrm{s}} \sigma_i \sigma_{i+1}$ (with PBC) and the magnetization as $M = \sum_{i=1}^{N_\mathrm{s}} \sigma_i$. Since J is an unknown parameter, in our simulations we evaluate the pseudo–spin thermodynamic quantities by suitably factoring out the trivial J dependence, and thus using the following formula: the energy per spin, in units of J, $\varepsilon_I = E_I / N_\mathrm{s} J$; the specific heat in $k_B J^2$ units $c_I = N_\mathrm{s} \left(\langle \varepsilon_I^2 \rangle - \langle \varepsilon_I \rangle^2 \right) / t^2$; and the magnetic susceptibility, $\chi_I = \langle M^2 \rangle / N_\mathrm{s} t$, where we use $\langle M \rangle = 0$ since we are in the paramagnetic phase.

As an example of the critical Ising regime unveiled via mapping with the string variables, in the insets of Figs. 2.12, 2.13 and 2.14 we also show a curve (black dashed line) obtained by simultaneously fitting ε_I, c_I and χ_I for the SH–4 potential to the corresponding theoretical expressions for the 1D Ising model with nearest–neighbor interaction and PBC (recalled in the Appendix E). The fit is done in the t-range 0.025-0.06 and yields a value $J = J_{S4} = 0.099235$. The results highlight a fairly good agreement between the quantities obtained via mapping and the analytical expressions, by using

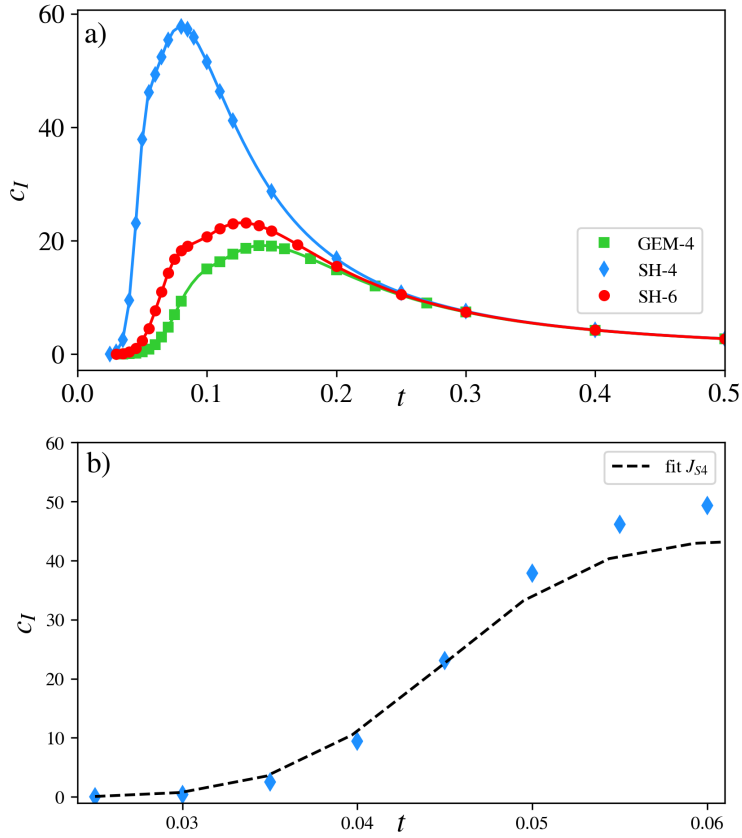

FIGURE 2.13: Ising specific heat in units of $k_B J^2$, obtained via mapping from soft–particle configurations. Solid lines are guide for the eye. The lower panel shows a closer view of the temperature range between 0.025 and 0.06, only for SH–4, and the black dashed line is the Ising result with $J = J_{S4}$. Reprinted from [1]

the same J_{S4} for all the observables. However, this only holds at very low temperatures; upon increasing temperature, in fact, the data points start to deviate from the fitted curve. This is indeed what one should expect, given that the critical regime (marked by the peak in che specific heat) is approached for $t \to 0$. The simple first–neighbor Ising model should not be able to adequately fit a whole range of finite temperatures with a single parameter (J_{S4}, in this case). Therefore, we could expect that the mapping onto the Ising model only becomes exact in the limit $t \to 0$ and that an effective mapping at finite temperature has the spin–spin coupling constants (even beyond first neighbors) significantly dependent on temperature.

The Ising–like energy of the pseudo–spins system reaches -1 in the $t \to 0$

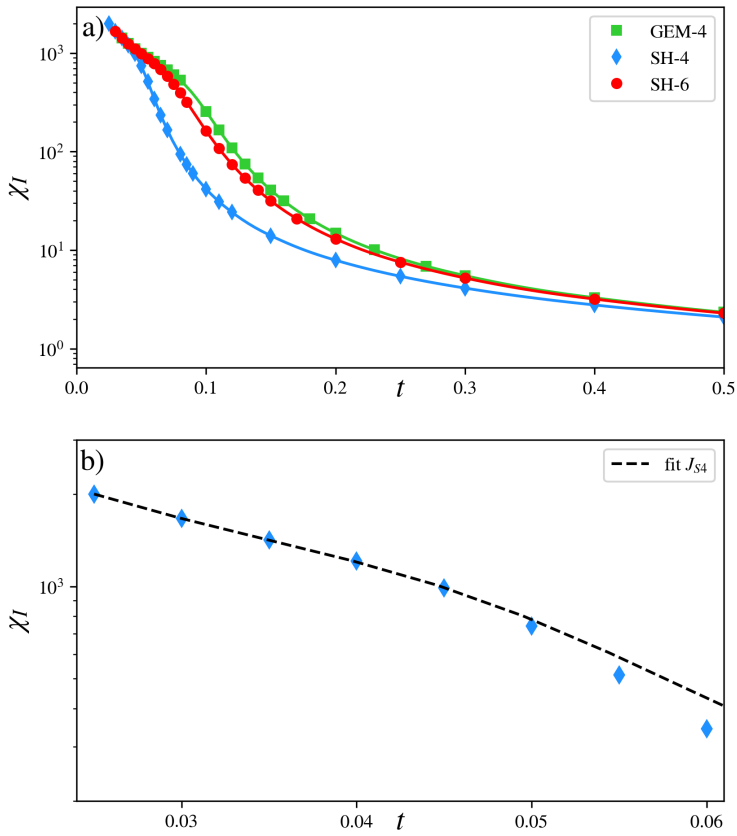

FIGURE 2.14: Ising magnetic susceptibility, obtained via mapping from soft–particle configurations. Solid lines are guide for the eye. The lower panel shows a closer view of the temperature range between 0.025 and 0.06, only for SH–4, and the black dashed line is the Ising result with $J = J_{S4}$. Reprinted from [1]

limit, while it increases for higher temperatures, as expected. Also c_I and χ_I behave like the corresponding observables of a Ising spin system with first–neighbor interactions, but the quantitative agreement with this model only holds at very low temperatures (see Figs. 2.12b), 2.13b) and 2.14b)), thus highlighting that the soft system at high temperatures departs from the critical regime. The specific heat tends to 0 as $t \to 0$, and then it grows up to a maximum value located between $t = 0.1$ and $t = 0.15$, depending on the soft interaction considered; then, it starts to decrease. For $t \to 0$, the susceptibility experiences a considerable growth (note the y–log scale), revealing a magnetic ordering of the pseudo–spin system.

2.6 Search for the Hamiltonian coupling constant

We have shown that the critical low–temperature regime (identified by the specific heat behavior) of the soft systems under investigation can be approximately mapped onto an Ising model with first–neighbor interactions via a temperature dependent coupling constant. This procedure effectively traces out the continuous phononic degrees of freedom, and the result is very interesting, because it shows that also in the 1D classical case, on approaching the zero–temperature clustering regime, a mapping onto a discrete Ising model can be found, starting from a continuous fluid. It is therefore possible to compare the data in Figs. 2.11-2.14 to the theoretical curves for the Ising model with $N_s = 50$. This way, the value of J as a function of t can be determined for each observable as follows. Concerning specific heat, energy and susceptibility, we determine the value of J for which the theoretical curve exactly coincides with the simulated data at each t. On the other hand, pseudo–spin correlation functions directly provide a J value for each t via the fit with the exact Ising formula for g^{σ}, as detailed in the previous Section. This procedure provides a set of discrete data points which are drawn in Figs. 2.15, 2.16 and 2.17 for the three interaction models. At high temperatures, the estimates of J extracted from different physical observables are different from each other. Quite remarkably, by lowering t, the four curves collapse onto a unique curve that still displays a dependence on temperature. In the light of the exponential decay of the spin–spin correlation function, it is not surprising that it can be fitted by its Ising form with a suitable value of J. However, it is noticeable that this precise value is almost identical to the three J values estimated from the specific heat, energy and susceptibility. This holds for all the potentials studied and this remarkable collapse marks the entry in the critical regime.

At this point, it is fundamental to assess whether the mapping of the soft system onto the Ising model is trivial, i.e., if only low–energy soft configurations are sent onto the pseudo–spin ground state, while only high–energy soft configurations are mapped onto the Ising states with defects. Fig. 2.18 shows, as an example, two histograms of the soft particles energies from a $t = 0.05$ simulation of the SH–6 interaction model. These distributions collect all the potential energy values of the soft configurations sent onto the Ising ground state (yellow) or onto an Ising first excited state (blue), i.e. a pseudo–spin configuration with two domain walls. In this analysis, the soft configurations mapped onto more defected Ising states have not been considered. Evidently, there is a substantial overlap between the yellow and the blue histograms and not two neatly distinguishable distributions, which means that the mapping is highly nontrivial. This strongly indicates that the mapping procedure via the string variables establishes a complex relation between the physical system of soft particles and the equivalent system of pseudo–spins. We however expect that such distributions become less and less overlapping as temperature

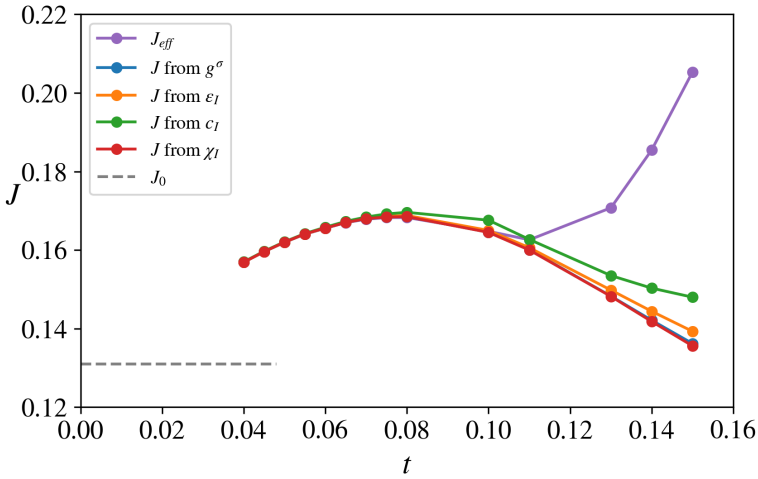

FIGURE 2.15: For the GEM–4 potential, estimates of coupling constant J as a function of t extracted from the pseudo–spin thermodynamic properties, from the defects' occurrence analysis and from SA. Solid lines are guide for the eye. The meaning of J_0 will be exposed in the following. Reprinted from [1]

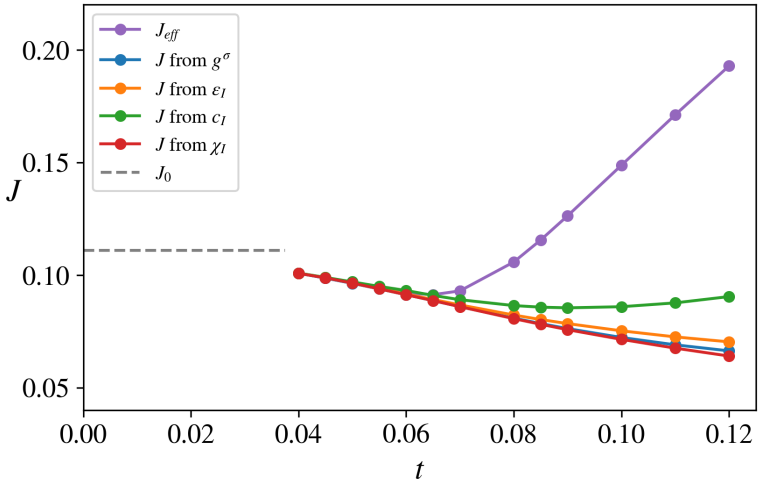

FIGURE 2.16: Estimates of J for potential SH–4, analogous to Fig. 2.15. The meaning of J_0 will be exposed in the following. Reprinted from [1]

decreases to regimes which are not accessible to our simulations.

Thus, the characterization of the $t \to 0$ limit of the mapping, and then of the coupling constant J, becomes an interesting further step. At such low

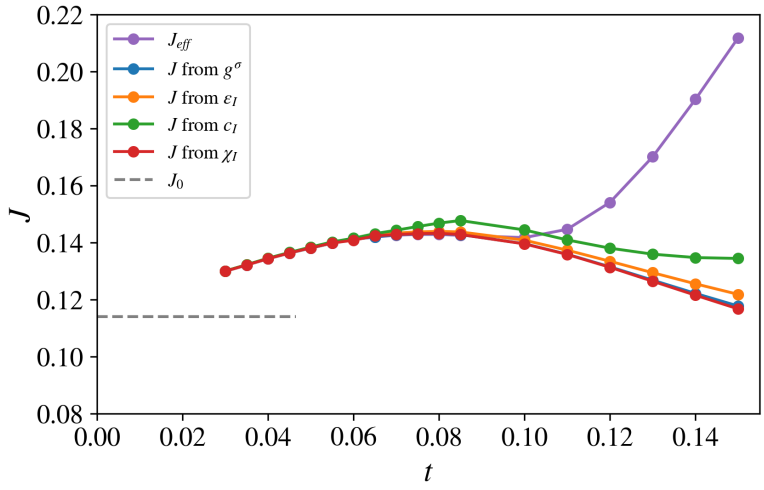

FIGURE 2.17: Estimates of J for potential SH–6, analogous to Fig. 2.15. The meaning of J_0 will be exposed in the following. Reprinted from [1]

temperatures, the kinetic energy contribution to the Hamiltonian is negligible and the potential energy term dominates. In these conditions, an energy variation in the soft system is directly associable to an energy variation in the pseudo–spin mapped system. This provides us with an indirect method for the determination of J. In fact, let us recall that the energy cost for a single domain wall in the Ising model with nearest–neighbor coupling is equal to $2J$. Considering PBC, the first excited Ising state has two domain walls in our simulations. This means that the minimum cost of a defect in the pseudo–spin model is equal to $4J$. The integral of the occurrence distribution of soft configurations that map to this lowest energy defected pseudo–spin configurations, at a given temperature, can thus be matched to a Boltzmann weight with potential energy equal to exactly $4J$. This means that the relative probability of the first exited Ising state with respect to the Ising ground state, written as $e^{-4J/t} w_{\text{def}}/w_{\text{gs}}$, can be identified as the ratio between the number of fluid configurations that are sent into the first state and into the Ising ground state. In particular, this last fraction reads as $\langle e^{-(V_{\text{def}}-V_{\text{gs}})/t} \rangle$, where the energies V_{gs} and V_{def} are the total potential energies (i.e. $\sum_{i<j}^{N} v(|x_i - x_j|)$) of the soft configurations which are mapped, respectively, onto the Ising ground state and onto the first excited Ising state, i.e. the one with two domain walls, while $w_{\text{def}} = N_s(N_s - 1)$ and $w_{\text{gs}} = 2$ are the degeneracies of, respectively, the defected and ground states in the 1D Ising model with PBC. The right member can be determined by assuming that - for a long MC simulation - $\langle e^{-V_{\text{gs}}/t} \rangle$ is proportional to the total number of configurations sent onto the Ising ground state, n_{gs}, namely the sum of an

histogram like the one in Fig. 2.18, and the same holds for the lowest–energy defected state (with the corresponding n_{def}). The previous considerations allow us to introduce the definition of an *effective coupling constant* J_{eff} as:

$$J_{\text{eff}} = \frac{t}{4} \ln\Big(\frac{n_{\text{gs}}}{n_{\text{def}}} \frac{w_{\text{def}}}{w_{\text{gs}}}\Big) \tag{2.8}$$

where J_{eff} depends on t. Therefore, this method not only provides the numerical value of J in the $t \to 0$ limit, but also gives a physical insight into the coupling constant relation with the soft–particle properties. J_{eff} as a function of temperature in the range of interest is shown in purple color in Figs. 2.15-2.17. These curves differ from the ones computed from the soft system observables at high t, but noticeably, at low temperatures, they collapse onto the other ones, despite being computed in a completely different way. Remarkably, the two different approaches yield almost indistinguishable results for the estimation of $J(t)$. This establishes a link between the thermodynamic properties of the pseudo spins and those of the soft particles.

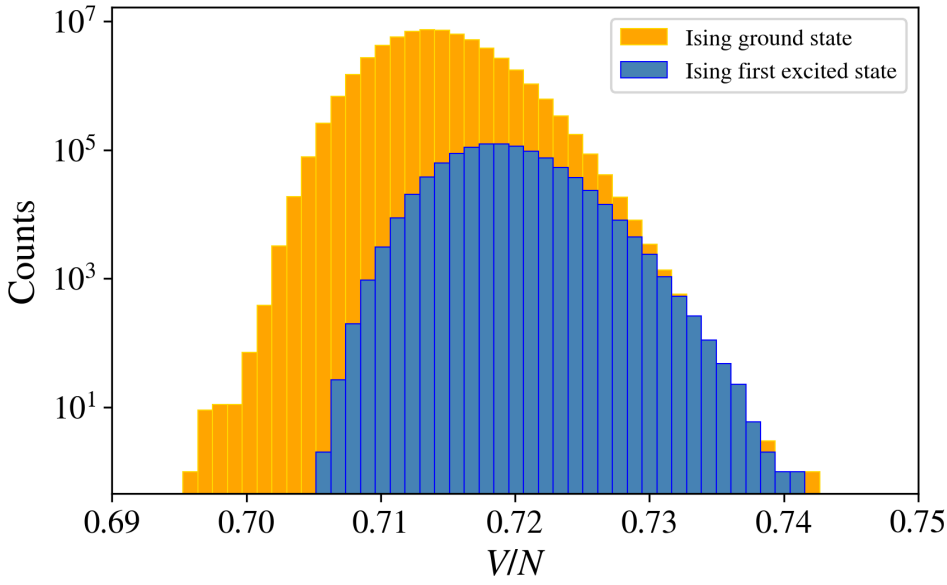

FIGURE 2.18: Histogram of the soft potential energy per particle, V/N for SH–6 at $t = 0.05$. The energies of the soft configurations belong either to the group of those mapped onto a Ising ground state (yellow) or to the group of those with two domain walls in the corresponding Ising system (blue). Reprinted from [1]

We have also extracted the $t \to 0$ limit value for J using Simulated Annealing [19]. I implemented a simple `C++` code which is able to optimize

the configuration of the soft system under investigation, thus allowing the identification of the soft–particle configurations corresponding to the lowest energy excitation of the system, which are mapped onto an Ising state with a single defect (namely two domain walls, in PBC). Starting at low temperature from a non perfectly clustered soft–particle configuration, the system is annealed towards the $t = 0$ limit, storing the positions of the particles and their potential energy. Essentially, the SA methods works at fixed commensurate density, the temperature is progressively lowered, according to a given schedule, and the potential cutoff is the same used in the MC simulations ($r_{\rm cut} = 8$, in units of r/σ). The particular schedule chosen should not affect the final result; however, our typical run was constituted of 100 iterations, the temperature being scaled by a factor 1/1.25 at the end of each iteration. The optimal starting temperature is about 0.001 (which is very low with respect to the typical energy scale of the system). The code proposes random particle displacements in a given range, and the moves are accepted according to the Boltzmann weight of the energy difference between the previous and the new configuration. We realized that the quality of the sampling was dramatically improved thanks to cluster moves, which move two particles at the same time. The algorithm is built in such a way that the energy of the system usually decreases, because at such low temperatures all the moves which would raise the energy are almost certainly rejected. A key point lies in the initial configuration; it is useful to have a guess about it, because placing the particles in a some configurations could greatly help the optimization process. For example, after several trials, it seemed evident that starting with two single soft particles very far away one from each other (e.g. at half the box length) gave the lowest final energy. We also had a guess about another type of defect: a cluster of 3 particles, far away from a singlet. The SA method, in this case, outputs a larger final energy with respect to the case with two singlets. From this analysis, we have therefore obtained that the lowest energy defect corresponds to an arrangement of two single particles and $(N_{\rm s} - 1)$ two–particle clusters.

We observe that the defect is highly localized: the particles immediately near the two single particles experience a huge displacement with respect to their position in a perfect lattice, due to the local depletion of the density. In turn, a few lattice steps away from the defect, the displacement are very small, and consistent with a slightly higher uniform cluster density. Where the single particles are found, the relative pseudo–spin is flipped; the pseudo–spin is reverted again when the other defect is encountered. Consistently, starting from the first single particle, one of the two particles of each cluster is moved into the next cluster. Fig. 2.19 shows the coordinates $x(i)$ of the soft particles as a function of the particle index i, for a simulation of the SH–4 model with $N = 100$. Evidently, there is a local rearrangement in the immediate neighborhood of each single particle, as evidenced by the blue circles in the

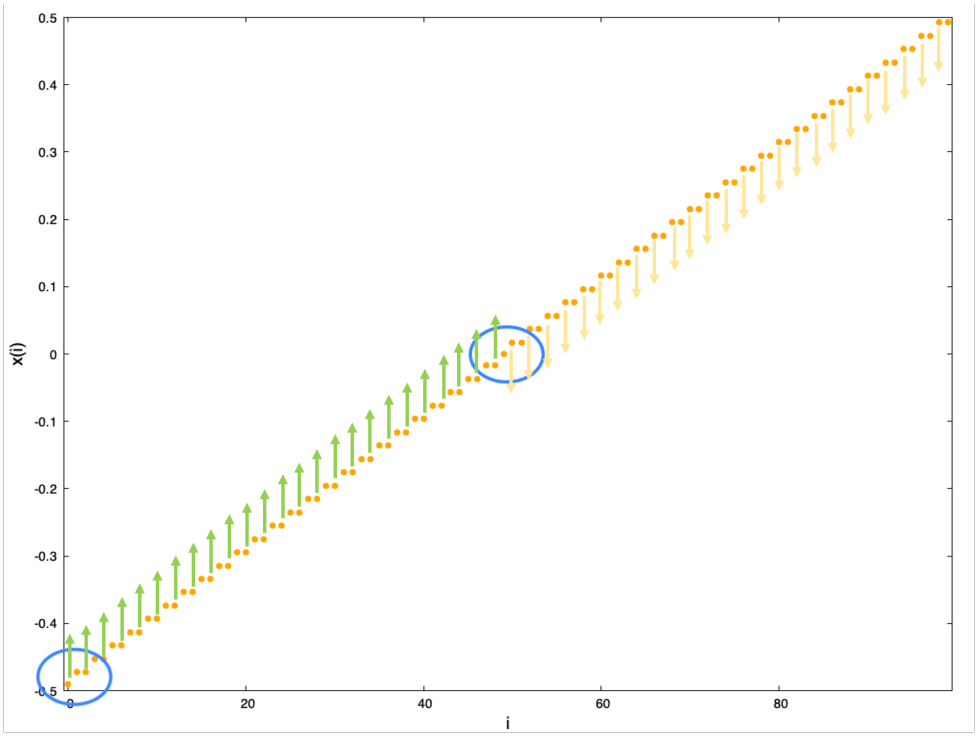

FIGURE 2.19: Configuration of the SH–4 model with two particles which do not join any $n = 2$ cluster. Green/yellow arrows indicate, respectively, pseudo–spin up and down.

picture. The configuration shown is the typical result of a SA optimization where the two singlets are already at the largest possible distance in PBC at the beginning of the simulation. We added green/yellow up/down arrows to indicate the corresponding value of the pseudo–spin degree of freedom, assigned according to the previously exposed mapping procedure. The two domain walls are encircled in blue.

The energy of the defect as a function of the distance between the two single particles rapidly tends to a constant value which characterizes the energy gap with respect to the ground state, as illustrated in Fig. 2.20.

The defect energy thus corresponds to a well–defined local minimum of the potential energy landscape, which is relevant at low temperatures since it provides metastability. With this energy gap, we computed a temperature–independent $J = J_0$ value via the relation $J_0 = (V_{\mathrm{def}} - V_{\mathrm{gs}})/4$, for each model. These $t \to 0$ limit values of J are included in Figs. 2.15-2.17 as horizontal gray dashed lines, and are also listed in Tab. 2.2, for $N_{\mathrm{s}} = 50$. Ideally, all the J values estimated from the soft physical observables and J_{eff} should approximately tend, at low temperatures, to J_0. Reasonable extrapolations for $t \to 0$ of the previously discussed J and J_{eff} curves seem to be in good

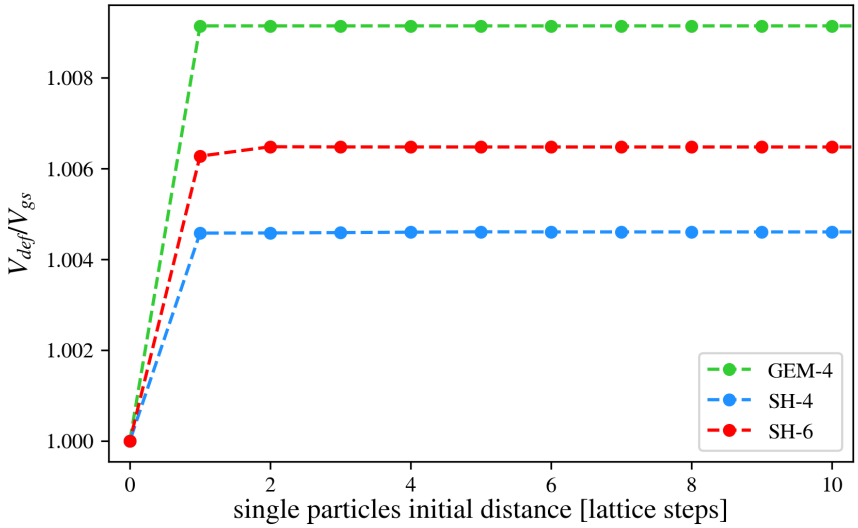

FIGURE 2.20: $V_{\text{def}}/V_{\text{gs}}$ as a function of the reciprocal distance (expressed in lattice steps) of the two single soft particles, for the three potentials investigated. Only range 0-10 is shown on x axis.

agreement with this hypothesis.

Pair potential	J_0
GEM–4	0.130975
SH–4	0.110975
SH–6	0.114025

TABLE 2.2: J_0 values calculated via Simulated Annealing for $N_{\text{s}} = 50$.

As all the other observables involved in the mapping, J_0 naturally depends on the system size. A good final point consists in investigating the J_0 limit as the number of constituents of the 1D system increases. Simulations via SA of the soft system with growing number of particles N yield the results reported in Fig. 2.21. The figure highlights how, for all the interaction potentials, J_0 as a function of N tends to a finite asymptotic value typical of each model; this evidences that, for large N, the energy of the defect converges to a finite value (which corresponds to a classical metastable state) and J_0 becomes almost independent of the number of soft particles.

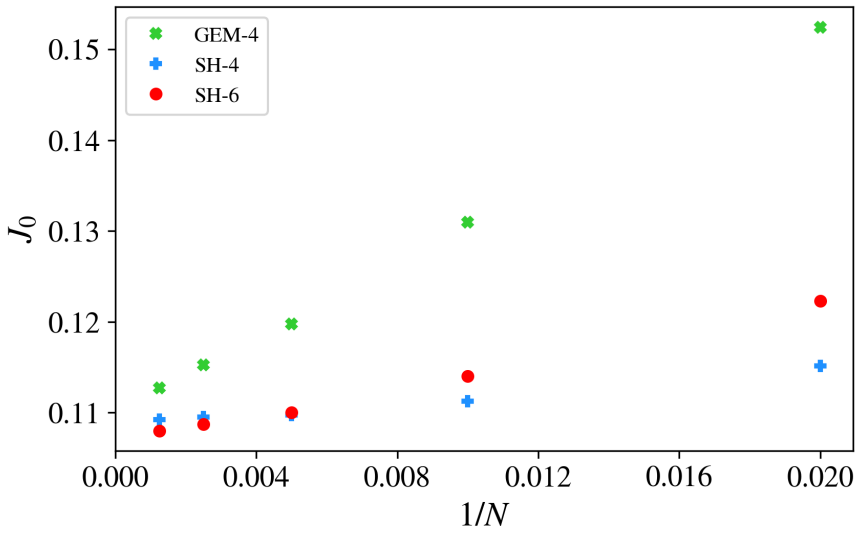

FIGURE 2.21: Results for J_0 as a function of the inverse number of soft particles, $1/N$. Reprinted from [1]

2.7 Universality of pseudo–spin dynamics in 1D clustering

In the previous sections we have established the emergence of effective Ising degrees of freedom via a nontrivial correspondence with a set of string variables in the soft particle systems under consideration. We observed that, for each model potential, a consistent t-dependent J can be extracted for $t \lesssim 0.06$, which seems to converge to a $t \to 0$ value. We now show that the ratio t/J is an approximate scaling variable for the pseudo–spin specific heat at temperatures $t \gtrsim 0.08J$, provided a suitable J is employed, which is not the low–temperature converged one.

In Fig. 2.22 we show the specific heat of the pseudo–spins in units of k_B, namely the data of Fig. 2.13 multiplied by J^2, as a function of t/J. The used values of J are 0.15, 0.0865, and 0.136 for the GEM-4, SH–4 and SH–6 potentials, respectively, and correspond to the values fitted from the pseudo–spin specific heat at its maximum. We also plot the Ising specific heat in the thermodynamic limit and for $N_s = 50$ in PBC (see Appendix E). With the selected values of J, by construction the three sets of data cross the Ising curve at their peak: what is not obvious is that the Schottky-like anomaly appears at a common $t/J \simeq 1$, which is slightly above the value for the Ising model $t/J \simeq 0.83$, and therefore display the same peak magnitude $C_I \simeq 0.44k_B$, akin to the Ising model. The scaling is apparently valid for $t/J \gtrsim 0.08$. At higher temperatures, the results from the considered

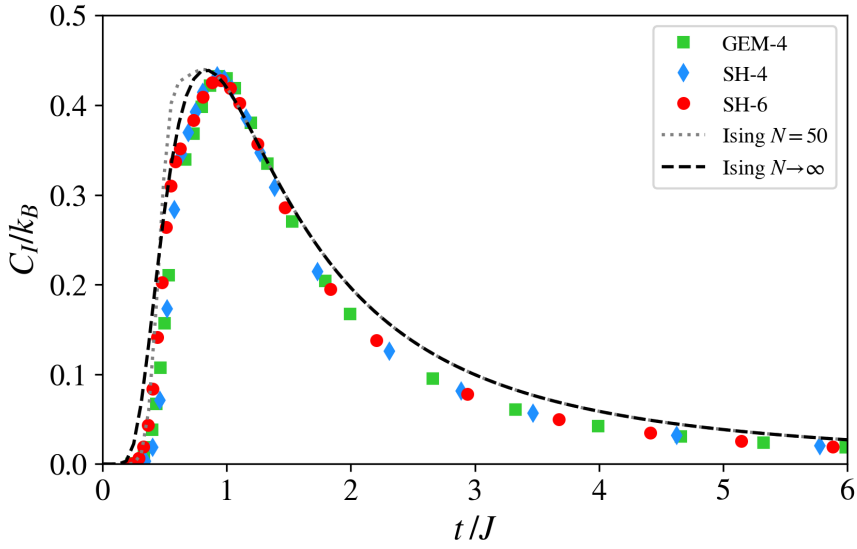

FIGURE 2.22: Specific heat in units of k_B of the pseudo–spins for the considered model potentials, as a function of the scaling variable t/J, where J is fitted from Fig.2.13 at the maxima of the specific heat. We also show the analytic results for the Ising model with $N_s = 50$ spins in PBC and in the thermodynamic limit. Reprinted from [1]

model potentials scale perfectly, independently of J, as can be appreciated in Fig. 2.13 where no multiplication by J^2 was performed. The reason is a high–temperature power-law decay of the specific heat with $1/t^2$. The coefficient in front of the $(J/t)^2$ behavior is however smaller than 1, which would hold for the Ising model. We speculate this scaling and its departure from the Ising model might be due to some coupling to the underlying phononic degrees of freedom. Conversely, discrepancies between the three sets of data can be seen at small temperature, which can be explained by both finite–size effects, which are known to be particularly large for the Ising model in PBC [37], and by the fact that we used values of J fitted in a different temperature range.

We also investigate whether there is a quantitative relation between the specific heat of the original soft systems, and the specific heat of the pseudo–spins. In fact, there is a striking similarity between Figs. 2.9 and 2.13. In particular, the maxima of the specific heat appear at similar temperatures. In Fig. 2.23, we thus plot again the data of Fig. 2.9 as a function of the scaling variable t/J, with the same values of J as reported in the previous paragraph. In the same figure, as a reference, we plot the Ising specific heat in the thermodynamic limit, $C_I/k_B = (J/t)^2/\cosh^2(J/t)$, shifted by 1, which, in the $t \to 0$ limit, accounts for the harmonic and kinetic contributions.

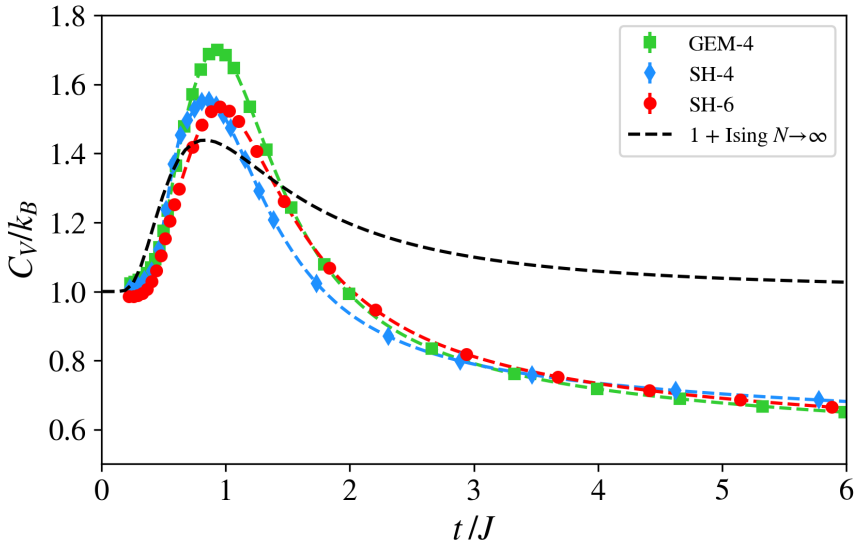

FIGURE 2.23: Specific heat in units of k_B of the soft particles for the considered model potentials, as a function of the scaling variable t/J, where J is fitted from Fig.2.13 at the maxima of the pseudo–spin specific heat. We also show the Ising model specific heat in the thermodynamic limit, shifted by 1. Reprinted from [1]

We observe that also for the clustering soft systems under consideration, the parameter $t/J \sim 1$, with the above specified values of J, marks the position of a peak in the specific heat. This is then a peculiar case of appearance of a Schottky anomaly in a classical non-magnetic system in the continuum. The magnitude of the anomaly varies and is in the range $0.5 - 0.7$ above 1. Interestingly, the high-temperature tails manifest a good scaling in t/J for $t/J \gtrsim 3$. This scaling depends on the chosen J, since it is missing in Fig. 2.9. In fact, at variance with the pseudo–spin specific heats, the behavior in this temperature range is not consistent with a t^{-2} power law.

2.8 Conclusions

In this chapter we have reported a study, via MC simulation, of the thermodynamic and structural properties of 1D fluids of particles interacting by soft-core, repulsive pair potentials of the $Q^{\pm}$ class [9], which allow spontaneous cluster formation. Three different functional forms of the interaction were considered, and for each of them the number density was fixed at a value commensurate with that of a dimer crystal. This investigation was prompted

by a former study of a one-dimensional quantum boson fluid at zero temperature [7] where, on increasing the strength of the inter-particle repulsion, a transition from a single-particle to a dimer Luttinger liquid was observed. Remarkably, mapping this fluid into a magnetic system of pseudo–spins by the introduction of pseudo–spin string variables revealed that the spin-spin correlation function across the transition behaves like that of the quantum transverse Ising model. It then comes as a natural question, whether a similar situation may occur in the corresponding classical system. Importantly, in the latter case, the nature of the fluctuations is deeply different from the ones of the bosonic system; nonetheless, we have observed a rich phenomenology which is surprisingly similar to the one of the quantum fluid. In the classical case one expects that, on lowering the temperature, the fluid will eventually freeze into an ordered cluster crystal [22]. Unlike in the quantum fluid, the transition takes place for any value of the repulsion strength, although in the one-dimensional system considered here, true long-range order is still expected to develop only at vanishing temperature [21].

Similarly to the quantum case, we then introduced a mapping procedure onto string variables whereby the continuum, configurational degrees of freedom of the original system are replaced by Ising-like spins. By construction, this mapping is such that a perfect or almost perfect dimer phase is turned into a ferromagnetic state, whereas a disordered configuration with no dimers corresponds to a paramagnetic state with random spin orientations. The remarkable point is that, in the low-temperaturelimit, the pseudo–spins thus introduced, whose dynamics is dictated by that of the underlying fluid of soft particles, do obey classical Ising statistics. We expect this result to be quite general, at least concerning soft-core 1D pair potentials, considered that the mapping procedure does not depend on the specific functional form of the interaction. The real phase transition in such system is not accessible at finite temperature, but the low-temperature limit already provides useful and interesting information about this. Therefore, our study clarifies the absence of any phase transition at temperature $T^* > 0$, for such a system.

Evidence of this was provided in several different ways:

i) The spin-spin correlation function is perfectly described by the corresponding expression of the classical one-dimensional Ising model. As the temperature is lowered, the correlations decay more and more slowly, pointing to the establishment of long-range order at zero temperature. Other thermodynamic quantities of the pseudo–spins, such as the internal energy, specific heat, and magnetic susceptibility, can also be described by their Ising expressions. In all cases, the spin-spin coupling constant J obtained by fitting those expressions to the simulation results is found to depend on temperature. This is not surprising, in the light of the fact that the introduction of the string variables implies some kind of average over the configurational degrees of freedom (e.g., phonons), which may then result in a state-dependent

effective J. Nevertheless, at low temperature the values of J obtained by this procedure become independent of the specific quantity under consideration, and approach a finite common limit as the temperature tends to zero.

ii) At a given temperature, the probability of occurrence of the first excited pseudo–spin state with respect to the ground state can be determined from the ratio of the soft-particle configurations which are mapped into either state. If the pseudo–spins obey Ising statistics, the coupling constant J can be extracted by relating this ratio to that of the Boltzmann weights of the Ising Hamiltonian. At low temperature, the values of J thus obtained fully agree with those determined from direct fit of the thermodynamic properties according to the procedure of point i).

iii) The value of J at zero temperature was estimated by comparing the energy of the ground state of the soft-particle system to that of its metastable state of lowest energy, determined via simulated annealing. The result is consistent with the extrapolation to zero temperature of the curves obtained by the procedures of points i) and ii) above.

Since the mapping of the configurations of the original soft-particle fluid into an assembly of Ising pseudo–spins is not trivial and necessarily implies a significant loss of degrees of freedom, there is not an obvious relationship between the thermodynamic observables of the fluid and their magnetic counterparts. Nevertheless, we think that the latter capture the role played by the discrete degrees of freedom of the system. In particular, the peak in the fluid specific heat as a function of temperature is mirrored by that in the specific heat of the pseudo–spins (the Schottky anomaly), and its position turns out to be nearly independent of the potential considered, provided the temperature is rescaled by the effective magnetic coupling constant J at the temperature of the peak. In the future, it would be interesting to study the temperature dependence of J beyond the phenomenological level considered here in order to clarify how this quantity is affected by the configurational degrees of freedom of the fluid.

Another potentially interesting development would consist in extending the present analysis to clustering involving more than two particles, or to systems in dimension larger than one. The latter development would allow to study the phase transition to cluster crystals at finite temperature, thereby making it more easily accessible to numerical simulation. While it is by no means obvious to us how the mapping considered here could be generalized to higher dimensions, since its present formulation clearly hinges on cluster formation in a 1D system, it is quite likely that the extension to larger clusters in 1D involves considering Potts models with higher spin. Clearly, the investigation of such a problem would represent a challenge due to the difficulty of introducing a suitable mapping onto corresponding spin variables; moreover, also testing the validity of such a mapping would be computationally extremely expensive, due to the very low temperatures involved.

This work required the usage of HPC resources: as usual, we resorted to the CINECA supercomputing facilities, via the *IscraC–SOFTONE* (2018) project.

Bibliography

[1] F. Mambretti, S. Molinelli, D. Pini, G. Bertaina, and D. E. Galli. Emergence of an Ising critical regime in the clustering of 1D soft matter revealed through string variables. *Physical Review E*, 102:42134, 2020.

[2] A. Stradner, H. Sedgwick, F. Cardinaux, W. C.K. Poon, S. U. Egelhaaf, and P. Schurtenberger. Equilibrium cluster formation in concentrated protein solutions and colloids. *Nature*, 432(7016):492–495, 2004.

[3] J. P.F. Lagerwall and G. Scalia. A new era for liquid crystal research: Applications of liquid crystals in soft matter nano-, bio- and microtechnology. *Current Applied Physics*, 12(6):1387–1412, 2012.

[4] Y. Y. Jau, A. M. Hankin, T. Keating, I. H. Deutsch, and G. W. Biedermann. Entangling atomic spins with a Rydberg-dressed spin-flip blockade. *Nature Physics*, 12(1):71–74, 2016.

[5] F. Cinti, T. Macrì, W. Lechner, G. Pupillo, and T. Pohl. Defect-induced supersolidity with soft-core bosons. *Nature Communications*, 5(1):1–6, 2014.

[6] S. Saccani, S. Moroni, and M. Boninsegni. Excitation spectrum of a supersolid. *Physical Review Letters*, 108(17), 2012.

[7] S. Rossotti, M. Teruzzi, D. Pini, D. E. Galli, and G. Bertaina. Quantum Critical Behavior of One-Dimensional Soft Bosons in the Continuum. *Physical Review Letters*, 119(21):1–6, 2017.

[8] M. Watzlawek, C. N. Likos, and H. Löwenen. Phase diagram of star polymer solutions. *Physical Review Letters*, 82(26):5289–5292, 1999.

[9] C. N. Likos, A. Lang, M. Watzlawek, and H. Löwen. Criterion for determining clustering versus reentrant melting behavior for bounded interaction potentials. *Physical Review E*, 63(3):031206, 2001.

[10] S. Prestipino and F. Saija. Hexatic phase and cluster crystals of two-dimensional GEM4 spheres. *Journal of Chemical Physics*, 141(18):184502, 2014.

[11] W. R. Magro and D. M. Ceperley. Ground state of two-dimensional Yukawa bosons: Applications to vortex melting. *Physical Review B*, 48(1):411–417, 1993.

[12] C. N. Likos, M. Watzlawek, and H. Löwen. Freezing and clustering transitions for penetrable spheres. *Physical Review E*, 58(3):3135–3144, 1998.

[13] L. van Hove. Sur L'intégrale de Configuration Pour Les Systèmes De Particules À Une Dimension. *Physica*, 16(2):137–143, 1950.

[14] N. D. Mermin and H. Wagner. Absence of ferromagnetism or antiferromagnetism in one- or two-dimensional isotropic Heisenberg models. *Physical Review Letters*, 17(22):1133–1136, 1966.

[15] J. A. Cuesta and A. Sánchez. General non-existence theorem for phase transitions in one-dimensional systems with short range interactions, and physical examples of such transitions. *Journal of Statistical Physics*, 115(3-4):869–893, 2004.

[16] R. Fantoni. Non-existence of a phase transition for penetrable square wells in one dimension. *Journal of Statistical Mechanics: Theory and Experiment*, 2010(7):P07030, 2010.

[17] L. Acedo and A. Santos. The penetrable-sphere fluid in the high-temperature, high-density limit. *Physics Letters, Section A: General, Atomic and Solid State Physics*, 323(5-6):427–433, 2004.

[18] C. Speranza, S. Prestipino, and P. V. Giaquinta. Thermodynamic and structural anomalies of the Gaussian-core model in one dimension. *Molecular Physics*, 109(23-24):3001–3013, 2011.

[19] S. Kirkpatrick, C. D. Gelatt, and M. P. Vecchi. Optimization by simulated annealing. *Science*, 220(4598):671–680, 1983.

[20] S. Prestipino. Cluster phases of penetrable rods on a line. *Physical Review E*, 90(4):042306, 2014.

[21] S. Prestipino, D: Gazzillo, and N. Tasinato. Probing the existence of phase transitions in one-dimensional fluids of penetrable particles. *Physical Review E*, 92(2):022138, 2015.

[22] C. N. Likos, B. M. Mladek, D. Gottwald, and G. Kahl. Why do ultrasoft repulsive particles cluster and crystallize? Analytical results from density-functional theory. *Journal of Chemical Physics*, 126(22):224502, 2007.

[23] T. Neuhaus and C. N. Likos. Phonon dispersions of cluster crystals. *Journal of Physics: Condensed Matter*, 23(23):234112, 2011.

[24] M. E. J. Newman and G. T. Barkema. *Monte Carlo Methods in Statistical Physics*. 1999.

[25] K. Binder and D. W. Heerman. *Monte Carlo Simulations in Statistical Physics*. Springer, 2010.

[26] A. Lang, C. N. Likos, M. Watzlawek, and H. Löwen. Fluid and solid phases of the Gaussian core model. *Journal of Physics: Condensed Matter*, 12(24):5087–5108, 2000.

[27] E. Gopal. *Specific Heats at Low Temperatures*. Springer, 1966.

[28] M. Teruzzi, D. E. Galli, and G. Bertaina. Microscopic Study of Static and Dynamical Properties of Dilute One-Dimensional Soft Bosons. *Journal of Low Temperature Physics*, 187(5-6):719–726, 2017.

[29] M. Teruzzi, D. Pini, S. Rossotti, D. E. Galli, and G. Bertaina. No. In *IOP Conf. Series: Journal of Physics Conf. Series 1041*, page 012009, 2017.

[30] S. Prestipino, A. Sergi, and E. Bruno. Clusterization of weakly-interacting bosons in one dimension: An analytic study at zero temperature. *Journal of Physics A*, 52(1):20, 2019.

[31] E. Vitali, M. Rossi, L. Reatto, and D. E. Galli. Ab initio low-energy dynamics of superfluid and solid 4He. *Physical Review B*, 82(17):174510, 2010.

[32] G. Bertaina, M. Motta, M. Rossi, E. Vitali, and D. E. Galli. One-Dimensional Liquid He 4: Dynamical Properties beyond Luttinger-Liquid Theory. *Physical Review Letters*, 116(13):135302, 2016.

[33] M. Motta, E. Vitali, M. Rossi, D. E. Galli, and G. Bertaina. Dynamical structure factor of one-dimensional hard rods. *Physical Review A*, 94(4):043627, 2016.

[34] G. Bertaina, D. E. Galli, and E. Vitali. Statistical and computational intelligence approach to analytic continuation in Quantum Monte Carlo. *Advances in Physics: X*, 2(2):302–323, 2017.

[35] P. Pfeuty. The one-dimensional Ising model with a transverse field. *Annals of Physics*, 57(1):79–90, 1970.

[36] J. Ruhman, E. G. Dalla Torre, S. D. Huber, and E. Altman. Nonlocal order in elongated dipolar gases. *Physical Review B*, 85(12):125121, 2012.

[37] J. Lee. Low-temperature behavior of the finite-size one-dimensional Ising model and the partition function zeros. *Journal of the Korean Physical Society*, 65(5):676–683, 2014.

Chapter 3

Simulation of complex behavior in electrical resistor networks

3.1 Introduction

It is becoming harder and harder to improve the quality of traditional computing architectures, due to the necessity of effective ways for dissipating energy while increasing the performance. Different approaches aim at reproducing the key structure and dynamical properties of the human brain (*neuromorphic computing*) [1], mimicking neurons and synapses to overcome the present limitations [2–6]. In fact, the human brain boasts a extremely high computational capability as well as a noticeable power efficiency. In such a view, it could be crucial to be able to imitate the processes of neuron–neuron communications, based on spikes separated by rest periods. The complex spatial–temporal correlation of these spontaneous (and apparently highly stochastic) firing events is expected to have a central biological role. For this reason, the development of neuromorphic software and hardware necessarily has to be based on probabilistic spiking units.

On the one hand, the field of (*software*) neuromorphic computing mainly relies on artificial neural networks. This research line is exponentially growing in recent years; many improvements have been achieved since the original ideas of Rosenblatt about the perceptron [7]. Since a few years, there is enough computing capability (thanks to GPU hardware and parallel supercomputing facilities) to translate theoretical ideas into effective computer programs. From a technological point of view, in order to obtain a high abstract ability and to satisfy the hypotheses of universal approximation theorem, neural networks must have many units and layers [8]. This directly affects the learning process since adjusting weights for each input is a time consuming operation. Moreover, the perceptron networks are implemented on digital computers where the von Neumann bottleneck (i.e. the reduced data transfer rate between the CPU and the memory, compared to the amount of available memory) strongly worsens the attainable performances.

On the other hand, many research lines aspire to fabricate *hardware* devices coherent with the neural networks architecture, focusing on the implementation within a material of artificial emulation of synapses and neurons, to overcome the intrinsic limitations of the digital computer paradigm [9]. The current project, as will be largely discussed later on, concentrates on the exploration of the possibility to use a condensed matter system (nanostructured metallic films), spontaneously arranged at the nanoscale, for useful logic computation. The long term goal concerns the exploitation of the nonlinear electrical properties of this nanostructured hardware for classification tasks (e.g. for pattern recognition in images, or similar tasks). Before discussing the specific details of the development of a computation model of the behavior of the samples investigated in this project, an introduction about the state-of-the-art of neuromorphic hardware computing is timely. The researchers aiming at developing materials with the aforementioned properties

have to face the problem that the highly complex interconnectivity of the biological systems can not be reproduced with traditional approaches [4]. In fact, in this regard, many issues presently emerge in the usage of classical CMOS architectures (Complementary Metal-Oxide Semiconductor, a technology typical of digital electronics used for integrated circuits), usually related to the scarce scalability and low efficiency of these devices [10]. *Memristors* represent an alternative to CMOS–based computing units, being two–end ideal electronic components that share some properties with resistors and others with non–volatile memories [11]. A memristor can be exploited to implement a reversible switching between two resistive states, without the need of voltage/current control, and without any external power supply. It is therefore considered an efficient element to implement the synaptic conductance changes; memristors were often used in recent years to produce artificial neural networks based on the perceptron model [12–14]. Unfortunately, memristors suffer from variability in the fabrication process, which generates huge variations of the performance among different devices, making the training procedure hard [15, 16]. To overcome these difficulties, the device has to be coupled to an external software (or integrated in an external circuit with other components [12, 17]), which clearly increases the time consumption and hinders the scalability. In addition, memristor–based devices rely on a learning procedure, such as backpropagation, that is energetically onerous and computationally rigid. The noise on the inputs or the devices imperfections contribute to the growth of the power consumption [16].

A large class of innovative approaches to neuromorphic computing that try to overcome these limitations is represented by *unconventional computing* methods [18]. In order to free the computing architecture from rigid traditional programming paradigms, many research activities started to consider a wide range of materials that can be utilized as computational substrates. On one hand, this allows to effectively exploit the intrinsic physical properties of the materials. On the other hand, a fine control of the material structure is not necessary, avoiding high cost fabrication methods and difficult integration processes. The advantages of this approach are summarized in the *in–memory computing* concept [19, 20]. It is essentially the ability of perform computation and data storage in the same physical unit, removing the latency and the energy cost usually associated to traditional computing hardware. The physical processes linked to the evolution of some physical parameter, such as current or conductance, allows to implement the elaboration of data inputs in the same place where the data are stored. To this extent, *self–assembly* and *self–organization* into the desired architecture are the key concepts that should guide the development of computing materials. Emerging physical properties that show dynamical evolution into *critical states* are a crucial feature: these systems should display high sensitivity to small external perturbations that generate avalanches of events in some physical observable of

the system [21].

Critical systems display scale–free phenomena and long range correlations; these features are retrieved, for instance, in percolating system, i.e. systems characterized by a regime where at least one fully connected path in a complex network of linked units is found [22]. Percolation theory provides powerful instruments to study and control the growth of systems composed by a high number of components with a complex organization (see e.g. an application in [23]). The most famous models which tried to exploit the state variability naturally embodied in the computing architecture are the *Boltzmann machines*, stochastic recurrent neural networks which leverage the natural sample stochastic noise as a resource for computation [24, 25], and the *reservoir computing* (RC) paradigm [2, 3, 5, 26, 27]. Both approaches present hardware and software implementations both and they started to dramatically change the traditional paradigm concerning neural networks and neuromorphic computing. In fact, in RC the output generated from the system is not fine–tuned through the careful regulation of a huge number of parameters (that is what happens during the training of traditional neural networks or when using traditional electronics approaches based on CMOS technology). Rather, the system is assembled in such a way that it generates a rich and complex output, consisting of many different signals. The role of the reservoir in RC is to nonlinearly transform sequential inputs into a high–dimensional space such that the features of the inputs can be efficiently read out by an ordinary learning algorithm. The goal becomes therefore to *select* the desired output among the complex full output produced by the sample. This task can be faced via a simple trainable neural network (called 'readout layer'), which has to choose the desired output in the reservoir of possible outputs produced by the sample. This is a formidable possibility, because the reservoir can be maintained and only the readout layer can be changed, in case the system is used for solving a different problem, making the training phase fast and not expensive. As evidenced by the review of Tanaka *et al.* [27], there is a variety of physical objects which can help in realizing a hardware implementation of this paradigm: nonetheless, there are major drawbacks related to development of a reservoir system that must satisfy all the previously discussed theoretical constraints. These constraints are hard to be implemented on the same physical substrate which performs the computation. Besides, the pre–processing of data to fit the reservoir interface mode, often adds a constraint to the computation process. It becomes therefore crucial to be able to exploit the autonomous evolution of some parameters strictly connected to a physical substrate. To this extent, the *evolution-in-materio* [28] represents an interesting technique with the goal to realize miniaturized, integrated and scalable computing devices. In this framework, a genetic algorithm evaluates the evolution of the physical substrate under the application of external

stimuli. This software is used to optimise and autonomously adjust the electrical control signals to induce the desired properties to the physical substrate. The response of the material to the external inputs can be used to accomplish computational tasks [29]. Although this method can achieve some intriguing results for programmable hardware, forcing the physical substrate to follow a precise evolution turns into a too low efficient processes [29, 30].

To date, the most promising experimental approach to neuromorphic computing consists in the bottom–up assembling of *nano–objects*; for instance, it has recently been shown by Fostner *et al.* that the complex connectivity of percolating networks of nanoparticles provides a natural solid–state system representing a route to realization of neuromorphic behavior [23]. These artificially synthesized materials present features which can be dramatically different from their bulk counterparts, are characterized by self–assembling processes and display an emergent response of their constituents to external signals. In recent years, systems generated by the assembling of structure confined at the nanoscale at least in one dimension, like nanowire networks [31], atomic-switch networks [4, 5], metallic nanoparticles networks [26] and cluster–assembled materials [6, 32–34], raised a high interest from the community in neuromorphic applications. In this context, our experimental collaborators, led by prof. P. Milani at the Università degli Studi di Milano, are studying cluster–assembled gold films characterized by random *resistive switching* (RS) activities due to the complex interactions of their constituents [6, 32–34]. Resistive switching is a physical phenomenon, occurring in a wide class of materials (including oxides, nitrides, chalcogenides, semiconductors, and organic materials), corresponding to the reversible jump in the resistance of a dielectric, as a consequence of the application of an external electric field. RS materials are becoming increasingly popular as possible solutions for a straightforward fabrication of complex architectures with neuromorphic features [14]: in fact, the sudden jumps in the sample resistance share some important features with neuron spikes in neuronal networks. It is important to observe, however, that the neuronal spikes correspond to a burst of activity, while RS events tend to hinder the current flow through the sample. Therefore, we underline that our collaborators are not trying to exactly reproduce neuron properties on a different hardware, but they rather take a loose inspiration from neuromorphic computing field in order to obtain self–assembled devices capable of acting as logic gates. In recent years, some researches have attempted to exploit material properties to enable logic operations [17, 30]. RS devices constitute a promising improvement, in this field, since one of their most important properties is the capability of exploring a rich variety of resistance levels on very short timescales. We underline that this stochastic behavior is not obtained as the result of the integration of specific devices, but this collective nonlinear dynamic switching property rather results from the

overall response of the nanoscale building blocks of the system to an external input (e.g. a particular applied voltage); this clearly supports scalability properties for these materials [33]. Moreover, it is also worthwhile to remark the intrinsic memristive behavior of such nanostructured materials. For memristors, Ohm's law holds instantaneously but, in general, the resistance of the sample also depends on the previous electrical history of the object: this is exactly the case of RS materials. In fact, after a 'conditioning' phase (whose nature will be detailed later but usually it modifies irreversibly the properties of the material), these objects keep track of their previous history, with their effective resistance showing a complex behavior as a function of time.

Motivated by the just discussed possibilities, and with the purpose of developing self–assembled hardware to be used as logic gates, Mirigliano *et al.* have recently demonstrated that metallic nanostructured Au films whose thickness is beyond the electrical percolation threshold show a non–ohmic electrical behavior and complex and reproducible resistive switching [34]. Fostner *et al.* [23] evidenced that, below the percolation threshold, the networks were formed by groups of particles separated by empty regions; on the contrary, while applying a given voltage, atomic scale wires form in the gaps, it generates an avalanche of switching events (similar to potentiation in biological neural systems). In fact, the strategy of our experimental collaborators, in order to tailor resistive switching behavior, is based on the careful control of the volume fraction of the nanoscale conducting phase that must be fixed close to the electrical percolation threshold [6, 34]. As shown in the following, the nonlinear electrical behavior of cluster–assembled Au films is stable and reproducible, thus allowing the straightforward training of the devices on precise resistive states. In data processing with artificial systems, nonlinear projection into a high–dimensional space is a computationally expensive operation that helps in the linear separation of the inputs, thus simplifying the classification of complex features. To overcome this obstacle, an energy efficient, inherently parallel way is the exploitation of cluster-assembled RS films to perform this nonlinear projection intrinsically, acting as self–assembled logic gates.

In the next section, we will delve deeper into the details of the experimental setup and measurements performed by our collaborators, before introducing the computational Stochastic Resistor Network Model (SRNM) we have developed to support the investigation of these systems.

3.2 Experiments

Our experimental collaborators from CIMaINa group investigated cluster–assembled gold films which, being not affected by oxidation of the nanoparticles during and after the deposition process, turn out to be highly promising

for the study of nanostructured metallic layers.

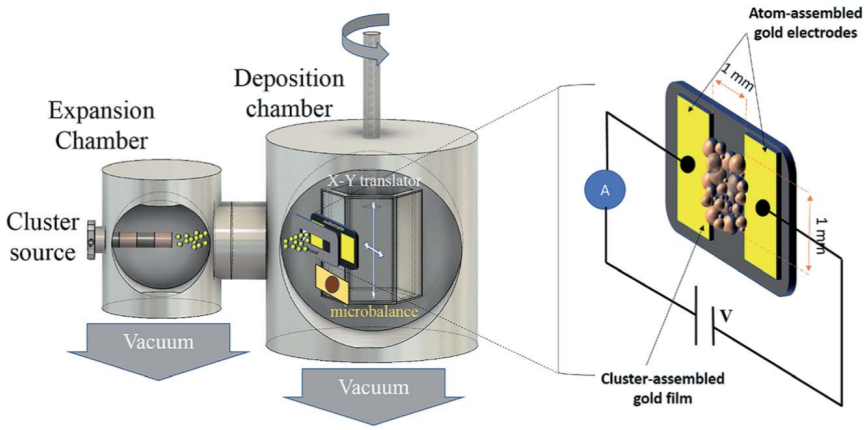

FIGURE 3.1: Scheme of the Au clusters deposition process. Reprinted from [34]

In Fig. 3.1 it is schematically shown the deposition procedure of the Au films, based on a Pulsed Microplasma Cluster Source that produces a supersonic expansion of an inert gas seeded with metallic clusters to form a cluster beam, that is deposited onto a insulating substrate. Local electrical characterization is performed during the cluster–assembled film growth, thus obtaining the time evolution of the electrical properties. The samples are thick enough (a few tens of nm) to be above the percolation threshold, i.e. avoiding the insulating behavior occurring when the films are made of isolated aggregates [6, 34]. In fact, for a low coverage of the insulating surface, the material behaves like a dielectric; upon increasing the film thickness, the isolated clusters start to form an interconnected network and the sample enters the metallic (conductive) regime. The thicker the sample, the lower the initial resistance: in particular, we can distinguish between Low Initial Resistance (LIR) and High Initial Resistance (HIR) samples. Further details about the setup and the morphological and structural characterization of the samples can be found in [6].

The first experimental result concerns the random switch events of the film effective resistance R_{tot}. Fig. 3.2 reports some examples of switching events in HIR and LIR samples both; apart from the different orders of magnitude of R_{tot} which characterize HIR and LIR samples, it is important to observe that the nature of the switching events is quite diverse. LIR samples host a large number of switches, marked by red circles in the pictures; conversely, R_{tot} in HIR samples displays a lower number of events. Remarkably, the increase of the overall applied voltage ΔV_{tot} from 5 to 15 V, in the HIR case, greatly enhances the switching events frequency.

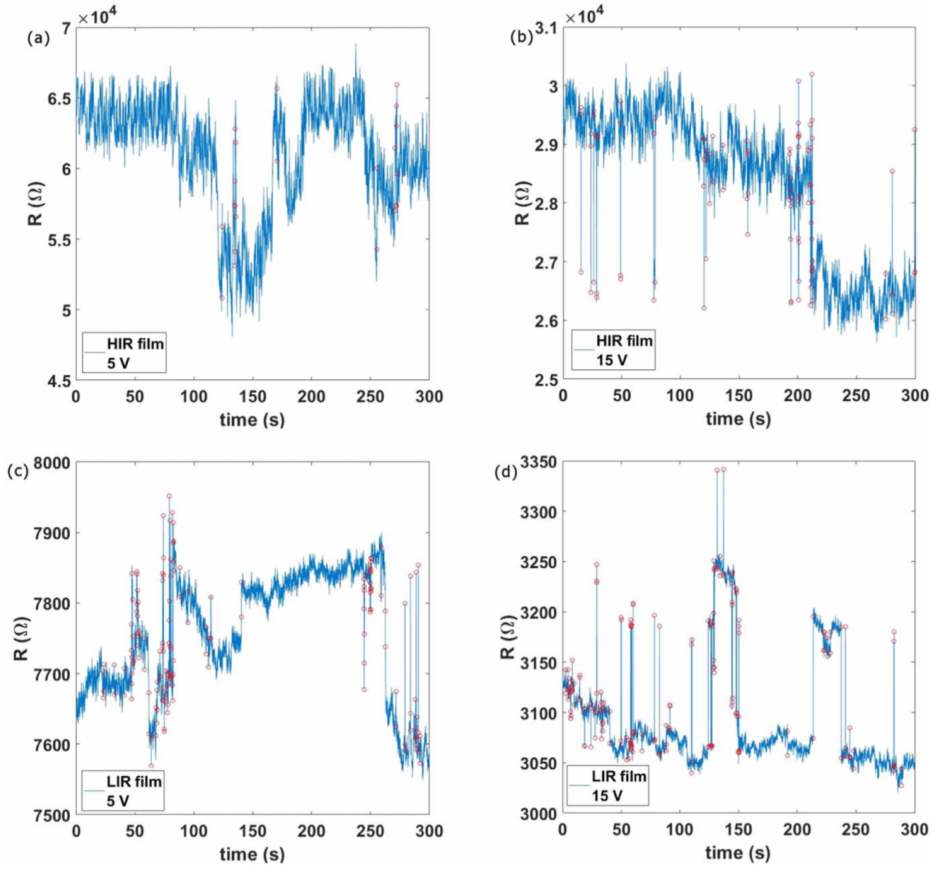

FIGURE 3.2: Examples of switching events in HIR and LIR, respectively a), b) panels) and c), d) samples. a) and c) panels are time windows captured at ΔV_{tot}5 V, while b) and d) are data taken when ΔV_{tot}= 15 V. Reprinted from [6]

Mirigliano and collaborators performed an extensive and quantitative analysis of the switches detected in the time evolution of R_{tot} of several samples. The distribution of temporal distances for consecutive switching events was deeply investigated, producing as a result that LIR samples are characterized by a power law decay of this quantity. This means that samples with high overall conductance show a higher correlation among switching events, similarly to the electrical activity of neurons [6]. In this parallelism, biological spikes of electrical current from neurons are usually grouped in time and are separated by time windows without any spike event. Oppositely to what happens in the brain, our gold films devices are characterized by bursts of correlated switching events, which correspond to a lower current flow.

The first experimental study of R_{tot} at fixed ΔV_{tot} highlights that R_{tot} displays jumps between discrete resistance levels [34]. The magnitude of the

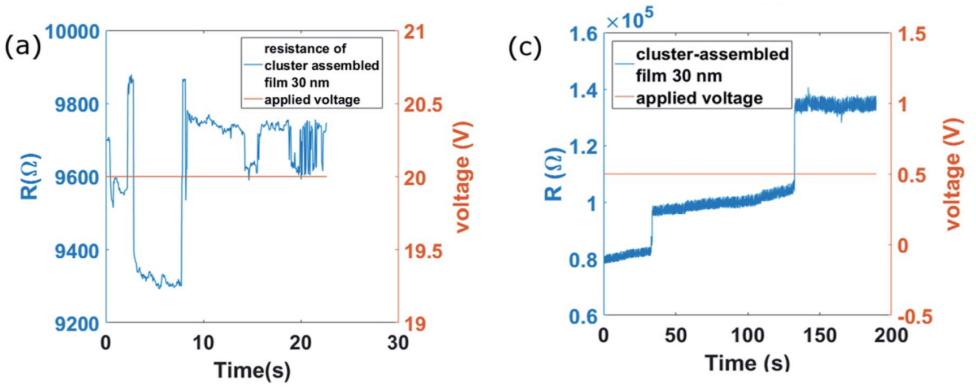

(a) R_{tot} as a function of time at high applied voltage (20 V)

(b) R_{tot} as a function of time at low applied voltage (0.5 V)

FIGURE 3.3: Resistive switching in experimental samples. Reprinted from [34]

jumps between the different levels explored is related to the applied voltage bias as shown in Figs. 3.3a and 3.3b: the higher the applied potential difference, the wider the resistance range explored by the sample.

In many samples, the authors observed a non–linear behavior of R_{tot} after a given threshold voltage which reproducibly depends on several factors, among which there is the initial resistance, the thickness, and the history of the film. Observing Fig. 3.3b, the switching activity clearly weakens, with a lower number of well distinct resistance values: this demonstrates the possibility to tune the switching activity of the sample by controlling the applied voltage in a reproducible manner. It is fundamental to recall that this phenomenology is totally absent in atomic–assembled gold thin films, which display simple linear electrical properties; in this case, conversely, the observed features largely depend on the granular structure of the samples. The building blocks are metallic but they form a much more complex system once assembled, as proved by their collective nonlinear response.

A simple picture of what happens at the nanoscale in these systems could be that local rearrangements and modifications of contacts among nanoparticles could induce the formation of new paths for the current [6, 34]. At the same time, an opponent mechanism tends to break connections upon increasing power dissipation. The balance between these two driving forces is thought to be the underlying mechanism behind the observed resistive switching. In particular, it is well known that in cluster–assembled gold films the granular structure at different length scales largely determines the non–ohmic electrical properties of the system. Despite being made of metallic particles, Au nanoclusters generate a collective non–ohmic response to external applied voltage. SEM and TEM imaging highlight the birth of polycrystallites, i.e.

a continuous network of aggregates rich of grain boundaries and stacking faults. The resulting film is porous and subject to frequent re–arrangements of the contacts, atom migration and re–crystallization processes. Obviously, the quality of the electrical conduction is strongly affected by these low conductance regions, which can generate a wide variety of diverse 'local' resistances. The current flow itself is able to modify the structure of grain boundaries and to determine their time evolution; besides, local nanoparticles re–arrangements, defect merging and breaking of the contacts also induce mismatches between the energy bands of different nanoparticles.

This simplified but effective microscopic picture can also be at the origin of the dissimilarities between HIR and LIR systems. HIR samples feature a lot of defects, their structure is full of gaps acting as an effective barrier for the electron flow, thus involving non–ohmic conduction mechanism and bridges, where current I can reach high density levels producing breaking (or formation) of intercluster connections. Conversely, LIR samples have a high number of interconnections, dissipate less energy and probably allow for an easier recombination of the defects.

Mirigliano *et al.* emphasized that this behavior is at the origin of non–ohmic $I(V)$ curves they found [34]: the determination of the total current I as a function of the applied voltage is another kind of experimental measurements that evidences the peculiarity of these devices. In this regard, Figs. 3.4a and 3.4b exemplify the noticeable departure from a ohmic behavior (note the y–log scale in the picture) and also the presence of some hysteresis effects (more visible in 3.4b) in a $I(V)$ cycle for such materials.

This was interpreted by Mirigliano *et al.* as the consequence of the passage of the system through the various accessible resistance levels. Over a given applied voltage threshold, the switching activity is activated and it is present in principle for any ΔV_{tot} value. In other words, the resistive switching in these systems requires a given applied voltage to be activated; afterwards, the phenomenon occurs repeatedly and randomly, independent of the applied potential. Therefore, being able to control the applied voltage means being able to control the switching activity of the sample.

As mentioned in the Introduction, the central target pursued by our collaborators is to verify whether these devices can be employed as self–assembled logic gates. For a physical reservoir to efficiently be used in computing applications, Tanaka *et al.* [27] emphasize that there is a number of requirements:

1. *high–dimensionality*, aiming to facilitate the separation of originally inseparable inputs in classification tasks (see also [29]). This property also allows to read out spatiotemporal dependencies of inputs in prediction tasks. They state that this property is strictly connected with the number of independent signals read from the reservoir. Concerning our RS

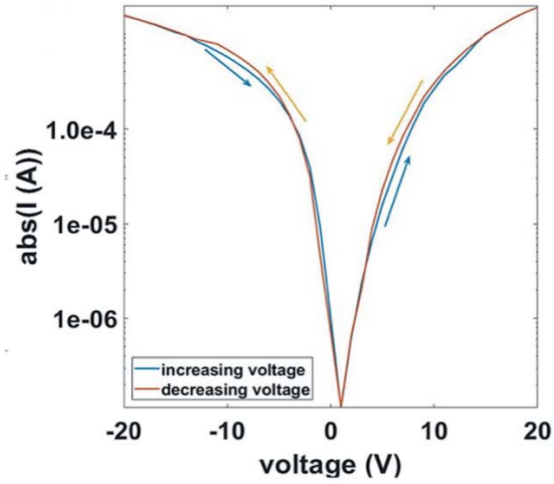

(a) $I - V$ experimental curve for a cluster–assembled Au film. Reprinted from [34]

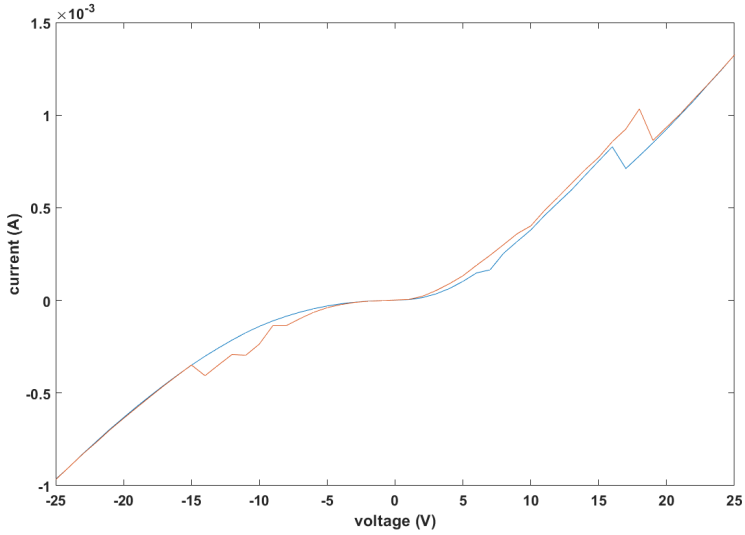

(b) $I - V$ experimental curve for another cluster–assembled Au film. Courtesy of dr. M. Mirigliano and prof. P. Milani, Università degli Studi di Milano

FIGURE 3.4

devices, this can be verified by deeply investigating how *rich* and *complex* can be the output signal. In particular, the group of CIMaINa labs conceived an experimental setup (see Fig. 3.5) that allows to identify input and output signals expressed by Boolean variables. In particular, one future point of investigation will be the identification of as many

os possible distinct output signals in the response of the network to a given logical input.

2. obviously, *nonlinearity* is another fundamental feature, necessary for classification tasks concerning non–linearly separable inputs and also for predicting nonlinear dependencies. From the analysis previously reported, it is apparent that our devices possess this property.

3. *short–term memory* is an important property, which means that the reservoir states as a dependence on previous input on a finite timescale. This claims for further investigation of memory effects in our devices, especially via the simulation tools that we made available.

4. least, *separation property* is required to classify the responses of a physical substrate to distinct signals into a finite number of separated groups. In this concern, a good reservoir is also stable with respect to small fluctuations (noise). The robust feedback that both experimental samples and simulated networks (see the following sections) provided during our studies suggests that this feature should be easily retrieved in our RS devices.

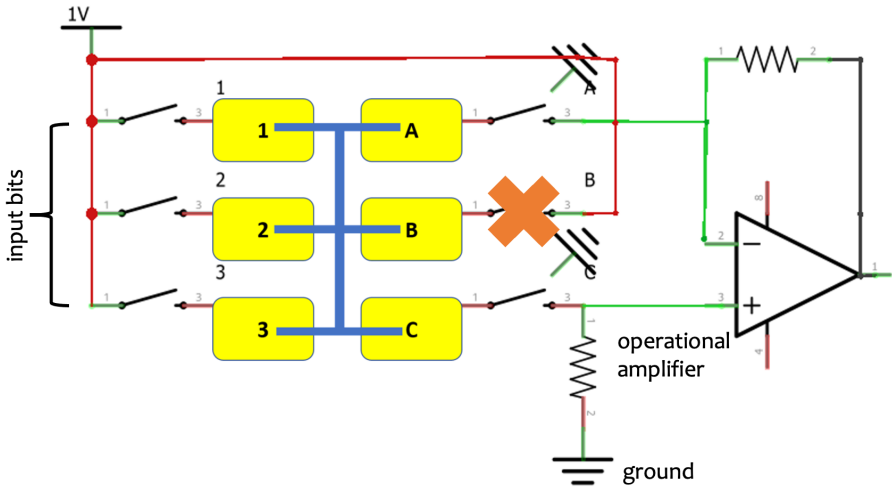

FIGURE 3.5: Scheme of the experimental setup for the study of Au nanostructured films as logic gates. Courtesy of dr. M. Mirigliano

Logic gates receive an input expressed as a certain number of 'bits' and generate a single bit as output; they can be hardware or software which is able

to perform Boolean operations. Our experimental collaborators developed an experimental setup with the target to test the exploitability of gold nanostructured films as key elements in neuromorphic computing. Their largely studied complex response to an input applied voltage is promising, because these devices seem to not require explicit programming in order to be used as logic gates.

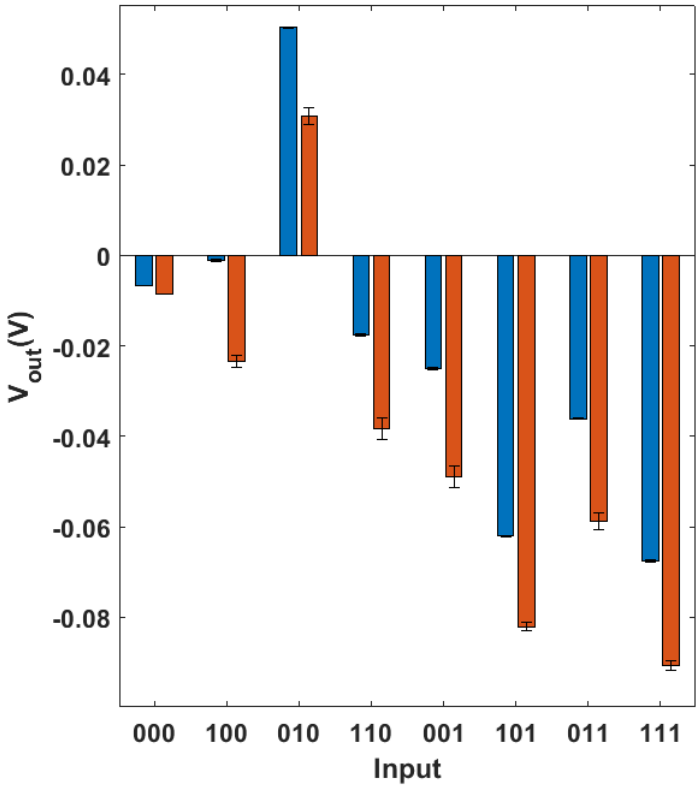

FIGURE 3.6: Example of experimental values of the output voltage, before the writing phase (blue bars) and after the writing phase (red bars), at 1 V. Courtesy of dr. M. Mirigliano

The experimental setup is sketched in Fig. 3.5. There are three input channels (left), which can essentially take two distinct values: '0' and '1'. The logic '0' corresponds to an open switch (infinite resistance, no current flows inwards); the logic '1' corresponds instead to a closed switch and an applied voltage (equal to 1 V in the reading phase and 15 V in the conditioning one, called also 'writing'). In the experiments, the voltage after the operational amplifier (whose presence is necessary for reading an output voltage) is the output signal, and it is thresholded (so that a 0/1 output bit

can be determined) and compared with the input voltage signal. Note that the output gate B is never used (there are always only two output channels). The experimental measurements in this concern are still not complete (and the choice of the threshold is a crucial point), but preliminary data show that there are differences between the measurements taken before the conditioning phase and those taken after it.

Fig. 3.6 contains the values of the output voltage read in the experiments, before the writing phase (blue bars) and after the writing phase (red bars), at low voltage (1 V). According to the peculiar set of 3 bits chosen in input, minor or major differences emerge between blue and red data. This is a rough and preliminary sign of a sort of memory present in the sample, which emerges from a set of local random events (about which we have largely discussed in the previous sections). If confirmed by more systematic investigations, this would mean that calculations can be performed on this hardware, which represents an innovative solution in the landscape of neuromorphic computing hardware.

There is great interest related to these experimental observations, also due to the possibility to exploit such class of systems for the fabrication of complex networks suitable for neuromorphic computing [6, 34]. To better understand the origin of the measured properties, we developed a theoretical simplified model that is largely described in the next section.

3.3 Computer modeling of electrical resistor networks

3.3.1 Overview

Systems based on nanoparticle networks are intrinsically complex, characterized by the loss of a periodic structure and by the presence of nanoscale aggregates with random and heterogeneous contacts. On the one hand, a theoretical modeling of such complexity which is not supported by numerical simulation can be hardly quantitative and directly comparable to the experiments previously described. On the other hand, the level of complexity itself implies that a microscopic numerical simulation can be applied only to the study of a small portion of these systems. In order to be able to model gold cluster–assembled aggregates at a mesoscopic/macroscopic level, as part of my PhD research activity I developed an abstract and simplified model of the network, representing effectually the phenomenology of these systems at these scales. In such a case, it is mandatory to use a model that reduces the degrees of freedom to take into account. Before entering into the details of the code implementation, here follows a concise description of the Stochastic Resistor Network Model we have built. We have introduced a

3D regular lattice of resistors, each one capable of a discrete number of conductive states, which evolve stochastically under a finite set of Monte Carlo probabilistic update moves. These moves were designed to model the thermal stability of the connections, i.e. the competition between Joule heating and thermal dissipation, but also other non-linear electron conduction mechanisms, due to inter-cluster and intra-cluster atomic rearrangements, which result in the dynamical creation and destruction of conduction pathways and triggers the switching events. Part of my work, as explained in detail later on, consisted of the development of a simulation code capable of efficiently solve Kirchoff's laws for our regular 3D resistor network. This code exploits the equivalence of a resistor network to a weighted undirected graph [35] to solve Kirchoff's laws using algorithms developed within Spectral Graph Theory (see e.g. [36, 37]) and efficiently implemented via the Armadillo library for linear algebra (`http://arma.sourceforge.net/`, which exploits OpenMP parallelization to speed up computationally expensive operations. The reader which is not interested into the details of the implementation of the code can directly go to the next section.

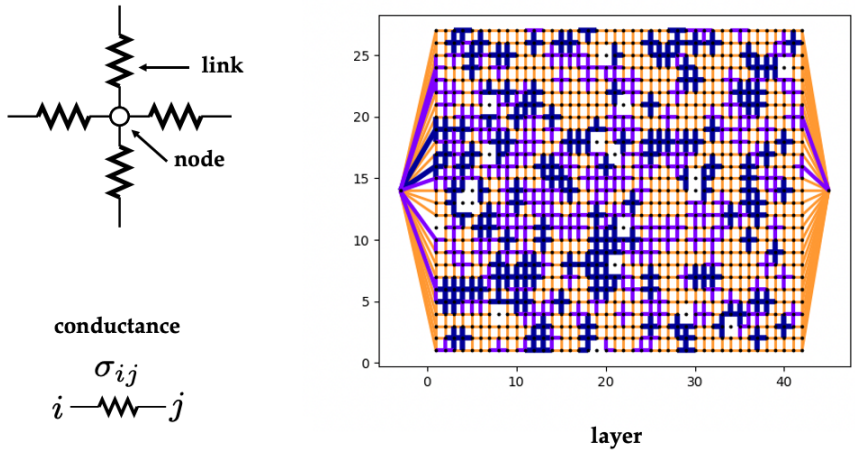

FIGURE 3.7: Schematization of a node, a link and a layer of our resistor network

The target was then to build a model that could reproduce RS events, share the essential features of the experimental samples and that could be exploited as a logic gate. As already mentioned, the main observable measured is the total resistance of the sample. In this sense, a smart choice is to study the behavior of a 3D resistor network, made of *nodes* (corresponding to small volumes of Au) connected in a regular fashion by *links*. Each link connecting

two nodes i and j is characterized by a conductance σ_{ij}. Links and nodes are regularly arranged to form a rectangular *layer*, as shown in Fig. 3.7, where the colors are associated to different link conductance values. All the pictures concerning the networks studied in this thesis are realized exploiting the powerful NetworkX Python library (`https://networkx.github.io/`). In our simulations, we pile up three layers, where vertical links mimic resistors connecting a node in a layer with the corresponding node in the upper/lower layer, as shown in Fig. 3.8.

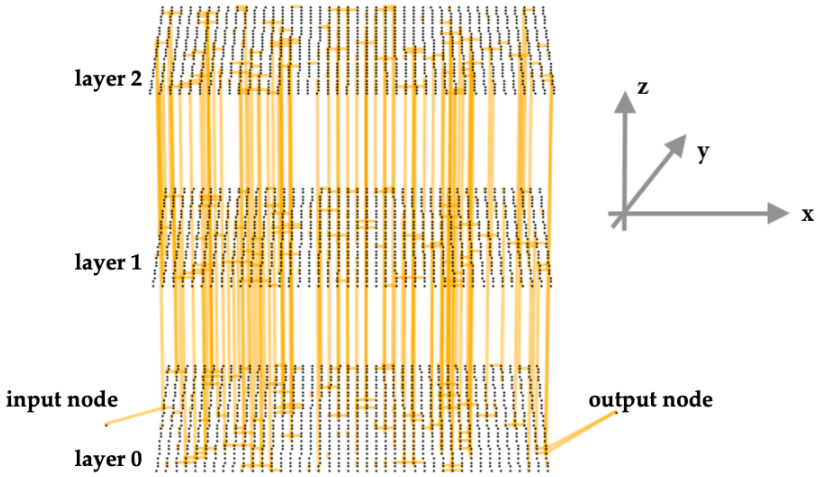

FIGURE 3.8: View of the 3D resistor network. Only edges with $\sigma_{ij} = 0.01\ 1/\Omega$ are colored.

There are two special nodes, i.e. the *input* (source) and *output* (sink) ones; to these nodes it is applied a constant overall voltage ΔV_{tot}. The total input current can be then easily derived as $I_{\text{tot}} = \dfrac{\Delta V_{\text{tot}}}{R_{\text{tot}}}$ via Ohm's law. Here, R_{tot} can be regarded as an *effective resistance* between the source and the sink: all the rest of the circuit can be replaced by a single component with a resistance given exactly by R_{tot} (see e.g. [38]).

We labeled the nodes in increasing order from the input one (index 0) to the output one (index $N_{\text{n}} - 1$), where N_{n} is the total number of nodes. The node 0 is only connected to all the nodes in the first column of the first layer, while the node $N_{\text{n}} - 1$ is only connected to the whole last column of the first layer. Only some links in Fig. 3.8 are colored, in particular only the ones with a conductance $\sigma_{ij} = 0.01\ 1/\Omega$. In fact, each link is described by a conductance level (that will, in general, stochastically vary over simulation time - see subsec. 3.3.3). To be as simple as possible, but at the same time willing to be able to describe the key properties of the network with

a model complex enough, we opted for having a limited number of possible conductance values. In particular, we restricted to 4 possible conductances; experimental analyses suggested that setting the conductance discrete levels to $\sigma_A = 0\ 1/\Omega$, $\sigma_B = 0.01\ 1/\Omega$, $\sigma_C = 0.02\ 1/\Omega$, $\sigma_D = 0.04\ 1/\Omega$ is a reasonable choice. Note that, in our computer simulations, $\sigma_{ij} = 0$ is not admissible (due to the algorithm we use to solve the network), and then a value of $\sigma_A = 10^{-10}\ 1/\Omega$ was adopted. Some simulations run with a slightly different set of possible σ_{ij} levels (of the same order of magnitude) indicate that this choice is not fundamental and small variations of these parameters generate similar results.

In this way, at the beginning of the simulations, each link is randomly assigned a conductance. Having the input current, the aim becomes to fully solve the network, in particular to calculate the ΔV_{ij} (and, as a consequence, the current) for each pair of connected nodes. To this end, we resorted to the *graph* theory, which is the most effective way to derive these properties for a huge circuit.

3.3.2 Graph theory for solving networks

Aiming to solve Kirchoff's equations for this huge circuit, a powerful tool is represented by the spectral theory of the Laplacian matrix of the graph associated to the network [35–40]. This approach turns out to be much more efficient, if compared to the classical brute–force method (and it is exact, which is obviously not true for numerical approximate methods). This is a crucial point, due to our interest for the time evolution of the resistor network, which will generate thousands of configurations to be analyzed (see next subsection for details).

The network we are dealing with could be regarded as a *weighted graph*. In general, a graph is an ordered pair $G = (V, E)$, where V is the set of N_{n} nodes making up the graph and E is the set of links (or *edges*) connecting the different nodes. The *order* of a graph $|V|$ is the number of its vertices; you define the *width* of a graph $|E|$ as the number of its links. A graph is said to be *undirected* if for each pair of nodes i and j the link ij connecting them is bidirectional. On the one hand, a resistor network can be thought of as a undirected graph, because the value of the resistance of each edge is clearly independent of the direction. On the other hand, considering the electrical currents flowing in each link as the elementary degree of freedom, a directed graph is naturally associated to the system (the current I has an algebraic sign indeed).

A fundamental quantity for solving the circuit is the *Laplacian matrix* $\mathbf{L}$ [36], defined as the difference between the *degree* matrix $\mathbf{D}$ and the *adjacency* matrix $\mathbf{A}$. $\mathbf{A}$ has a simple interpretation: one element A_{ij} of $\mathbf{A}$ is 0 if the nodes i and j are not directly connected, while it is 1 if a direct link between

them exists. On the other hand, **D** is a diagonal matrix and has the following definition:

$$D_{ij} = \begin{cases} d_i = \sum_{j=0}^{N_n - 1} A_{ij} & \text{if } i = j \\ 0 & \text{elsewhere} \end{cases} \tag{3.1}$$

In practice, you sum all the elements of a row of the adjacency matrix and obtain the only non–zero element of the corresponding **D** row: that element is the sum of the connections of the node i with all the other nodes of the graph. The Laplacian matrix, whose elements are thus defined as $L_{ij} = D_{ij} - A_{ij}$, has a number of interesting features that make it very useful for graph analysis:

- $L_{ij} = L_{ji}$ (symmetry)
- it is a semi–positive definite matrix
- due to the previous point, and also being symmetric and real–valued, the spectral theorem ensures that it is diagonalizable and all its eigenvalues are positive.
- it is not invertible, because its determinant is zero. It is easy to verify that, considering that the sum of any row or column of **L** equals zero.
- the elements on the diagonal of **L** indicate how many connections a node has with all the others (in practice, they are the elements of **D**).
- the non–vanishing off–diagonal elements indicate which pairs of nodes i and j are connected by a given edge (referred to as ij)

All these properties hold as well in the case of a weighted graph, i.e. for a graph in which a positive real number w (the weight, for example it can be the electrical conductance of a given link) is assigned to each link. The only difference is in the definition of **A** as:

$$A_{ij} = \begin{cases} w(i,j) & \text{if } i \text{ and } j \text{ are connected} \\ 0 & \text{elsewhere} \end{cases} \tag{3.2}$$

while **D** and **L** are defined as before. In this case, **D**'s non–vanishing entries contain the sum of the weighted links over a given row.

After this formal introduction to the properties of the Laplacian matrix, let us recall that the aim of all this machinery is to solve the network, i.e. to determine the voltage applied to the ends of each link (and then to determine the current flowing everywhere in the network and to calculate the overall network resistance). In general, people solve Kirchoff's equations; however, the method exposed here - called *nodal potentials* method - based on the spectral decomposition of **L** is a mathematically and conceptually simpler approach [40]. The interesting thing is that the solution for the currents

at each edge is derived in terms of the eigenvalues and eigenvectors of the Laplacian matrix of the network.

As described in [37], we begin with the assumption that Ohm's and Kirchoff's laws are valid at every edge and that charge at every node is conserved, except for the source and sink nodes (referred to in the following as s and t, respectively). The validity following properties is guaranteed (for the output node t there are analogous considerations):

- the input node has a net incoming current equal to the sum of all the currents going from s towards all the other nodes in the network: $I^{\text{in}} = \sum_{k=0}^{N_\text{n}-1} I_{sk} = -I^{\text{out}}$
- by applying Ohm's law for each link ij, one obtains: $I_{ij}^{(s,t)} = \dfrac{V_i^{(s,t)} - V_j^{(s,t)}}{R_{ij}} = \dfrac{\Delta V_{ij}^{(s,t)}}{R_{ij}}$, where the resistance R_{ij} of the link ij and the voltage difference $\Delta V_{ij}^{(s,t)}$ applied to the ends of the ij edge are computed for a given choice of the source and sink nodes (s,t).
- assume that disconnected nodes are characterized by infinite resistance (or conductance $\sigma_{ij} = 1/R_{ij} = 0$, equivalently)
- Kirchoff's law for a circuit's nodes yields:

$$\sum_{l=0}^{N_\text{n}-1} I_{kl}^{(s,t)} = \delta_{ks} I^{\text{in}} - \delta_{kt} I^{\text{out}}$$

- from this, it is straightforward to derive:

$$V_k^{(s,t)} \sum_{l=0}^{N_\text{n}-1} \frac{1}{R_{kl}} - \sum_{l=0}^{N_\text{n}-1} \frac{V_l^{(s,t)}}{R_{kl}} = I\left(\delta_{ks} - \delta_{kt}\right)$$

  where I is the absolute value of the input (output) total current

We can define the Laplacian matrix of the network, with entries $L_{kl} = \delta_{kl}\left(\sum_{l=0}^{N_\text{n}-1} \sigma_{kl}\right) + \left(\delta_{kl} - 1\right)\sigma_{kl}$. In fact, the non–vanishing adjacency matrix entries are the conductances between pairs of nodes and the degree matrix has, as usual, the sum of the corresponding $\mathbf{A}$ rows as diagonal elements. As a consequence, the following matricial equation holds:

$$\mathbf{L} \cdot \mathbf{V}^{st} = \mathbf{I}^{st} \tag{3.3}$$

where $\mathbf{V}^{st}$ is an array containing the list of the potentials calculated at each node, once assigned the source and the sink of the circuit, while $\mathbf{I}^{st}$ is an array where the only non–vanishing components are the two corresponding to the

total input and output currents (nodes s and t). Note that the potential of a node has no physical meaning; rather, the physically meaningful quantity is the voltage difference applied to a link between the nodes k and l:

$$\Delta V_{kl}^{(s,t)} = I \left[\sum_{n=1}^{N_n - 1} \left([\mathbf{v}_n]_k - [\mathbf{v}_n]_l \right) \frac{1}{\lambda_n} \left([\mathbf{v}_n]_s - [\mathbf{v}_n]_t \right) \right] \tag{3.4}$$

where $\mathbf{v}_n$ are the orthonormal eigenvectors of the Laplacian matrix, ordered with respect to their own eigenvalues λ_n in increasing order. Here, n starts from 1 because $\lambda_0 = 0$. The previous result have been demonstrated in a formal way, but the relative mathematical calculations are not relevant for the goal of this work; details can be found, e.g., in the work of Rubido *et al.* [37]. Here, it clearly appears that the knowledge of the eigenvalues and the eigenvectors of $\mathbf{L}$ represents the key element for the calculation of the voltage difference and of the current at the ends of each link.

The final point to address is, therefore, the calculation of the resistance of each link. This will also be useful for determining the effective network resistance, i.e. its R_{tot}. We start rewriting Eq. 3.3 as:

$$\mathbf{V}^{(s,t)} = I \left(\mathbf{e}_s - \mathbf{e}_t \right) \tag{3.5}$$

with $\mathbf{e}_i$ representing the vector of the canonical basis of $\mathbb{R}^{N_n - 1}$, which has its i-th entry equal to 1 (i is the vertex index within the graph G) and all the others are 0. In order to find $R_{\text{tot}} = R_{st}$ (or any other resistance R_{ij} between any pair of nodes i, j), one should be able to invert $\mathbf{L}$ and rewrite the previous equation as:

$$R_{st} = \frac{\left(\left[\mathbf{V}^{(s,t)} \right]_s - \left[\mathbf{V}^{(s,t)} \right]_t \right)}{I} \tag{3.6}$$

but, unfortunately, obtaining R_{st} from this equation is hindered by the fact that $\mathbf{L}$ is not a invertible matrix. It is then necessary to restrict ourselves to the space orthogonal to $ker(\mathbf{L})$, discarding from the basis of $\mathbf{L}$ eigenvectors the one corresponding to $\lambda = 0$, referred to as $\mathbf{v}_0$. As a consequence, the Moore–Penrose pseudo–inverse of the Laplacian matrix $\mathbf{L}^+$ can be introduced as [41–43]:

$$\mathbf{L}^+ \cdot \mathbf{v}_0 = 0 \quad e \quad \mathbf{L}^+ \cdot \mathbf{v}_n = \frac{1}{\lambda_n} \mathbf{v}_n \quad \forall n \neq 0 \tag{3.7}$$

where λ_n and $\mathbf{v}_n$ are, respectively, the eigenvalues and the eigenvectors of $\mathbf{L}$.

$\mathbf{L}^+$ is the used for the following theorem (proved elsewhere, such as in [44]).

Theorem 1. *For each graph $G(V, E)$ with weights w_{ij} for each link $(ij) \in E$, the corresponding link resistance is defined as $1/w_{ij}$. Therefore an* ***effective***

resistance *between a generic pair of nodes i and j (not necessarily directly connected) can be calculated as:*

$$R_{ij} = (e_i - e_j)^\top \cdot \boldsymbol{L}^+ \cdot (e_i - e_j) = \boldsymbol{L}^+_{ii} - 2\boldsymbol{L}^+_{ij} + \boldsymbol{L}^+_{jj} \tag{3.8}$$

This theorem is extremely important to our purposes, because otherwise it would have been impossible to determine the resistance between two nodes not directly connected by a single edge. In this way, the knowledge of the Laplacian matrix Moore–Penrose pseudo–inverse allows, for example, to retrieve the effective resistance between the input and the output nodes, R_{tot}, which represents the overall resistance of the network under investigation.

Connected graphs

A brief parenthesis on the meaning of the second smallest eigenvalue, λ_1, is noteworthy. In particular, the value of λ_1 contains the information about the graph G being *connected* or not. A graph is said to be connected if it is impossible to split it into two subgraphs without any shared links. It can be proved [44] that $\lambda_1 > 0 \Leftrightarrow G$ is connected. If $\lambda_1 = 0$, the graph is disconnected and it correspond to the physical situation where the resistor network is broken. In the code (whose structure will be presented in the following), a check about this is always performed. A broken network is, in principle, not able to conduct electrical current anymore, and we aim to avoid this condition. To this purpose, the knowledge of the full $\mathbf{L}$ spectrum is mandatory.

Numerical calculation of $\mathbf{L}^+$

The inversion of the Laplacian matrix is an extremely hard numerical problem. Among the several possible options and existing packages, one of the most efficient methods is to rely on the `pinv` method embedded in the powerful **Armadillo** `C++` library (`http://arma.sourceforge.net/` [45, 46]). All the Armadillo functionalities explained in this PhD thesis are guaranteed to work at least up to Armadillo v. 9.200.4. Armadillo is an open–source code, written in `C++` and provided with an automatic parallelization via OpenMP threads on multi–core computers (`https://www.openmp.org/`). Armadillo functions are capable of calculating the spectrum of $\mathbf{L}^+$, thus resolving the resistor network we are dealing with. As in the previous chapters, also in this research project the possibility of exploiting HPC resources is fundamental, due to the computational cost of the algorithm: in fact, given a network of N_{n} nodes, $\mathbf{A}$, $\mathbf{D}$ and $\mathbf{L}$ have $N_{\text{n}} \times N_{\text{n}}$ elements. This means that a network of 3404 nodes (as the ones studied in this work) produce matrices of 11587216

elements, which is a huge number and makes the calculation of $\mathbf{L}^+$' spectrum significantly expensive.Using Armadillo and its internal parallelization via OpenMP is straightforward and effective.

Here follows a brief description of the simulation code for solving the resistor network (and for its stochastic evolution) that was initially developed during the Bachelor Thesis of N. Pedrani [44], which I co–supervised. Part of my activity during the PhD has consisted of supervising the early stages of the developments of this code and of further widening the capabilities of the software on my own, for example by adding the possibility of adding a third layer, by optimizing some calculations, and by developing a complete framework of Python analysis tools. A relevant fraction of this code concerns topics that will be exposed in detail in the next subsection, especially about the physical model underlying the resistor network.

There are some mathematical calculations that are repeatedly performed in the code, aiming to solve the network for a given configuration (i.e., once assigned a conductance value σ_{ij} to each resistor in the network). These calculations are all completed exploiting Armadillo functionalities and are listed here below:

1. calculate adjacency matrix $\mathbf{A}$
2. calculate degree matrix $\mathbf{D}$
3. calculate laplacian matrix $\mathbf{L}$
4. find the spectrum of $\mathbf{L}$ via the `eig_sym` method, which yields eigenvalues in ascending order and the corresponding eigenvectors which are stored as column vectors
5. compute the effective resistance between the source and sink nodes, from the laplacian spectrum via Theorem 1
6. compute resistances among neighboring nodes pairs in the network and corresponding potential differences using the same Theorem and Eq. 3.4. This requires the knowledge of I_{tot}, i.e. the module of the input total current; this value is unknown because our input data is rather the overall potential difference between source and sink, ΔV_{tot}. Therefore, after the calculation of R_{tot}, the code computes the total current I_{tot} flowing in the network as $I_{\text{tot}} = \dfrac{\Delta V_{\text{tot}}}{R_{\text{tot}}}$. This allows to compute all the voltage differences at the ends of each edge according to Eqn. 3.4. It is not necessary, however, to compute R_{ij} and ΔV_{ij} for each i, j pair: the majority of these quantities vanish, so it suffices to compute them only for node pairs connected by a single edge.

Note that, in all the points of the algorithm described above, the fact the the network is 3D is not relevant: the physical positions of nodes and links in the space do not matter for this kind of analysis, if the nodes are increasingly ordered and each node ows the list of its neighbors. The adjacency matrix is not dependent on the spatial coordinates of the network, but just on the neighbor list of each node.

It is then clear how it is possible to completely solve the resistor network; the following steps consisted in developing a method for making the network stochastically evolve. In fact, we are interested in measuring network properties of the system over a wide number of steps, during which several resistance states can be explored, and many inner modifications of the network occur. A good way to obtain such information is to set some rules for the evolution of the single links conductance values based on physical insights (for example the microscopic mechanisms hypothesized in [6, 34]), and to apply these modifications to the network, measuring its properties along the algorithm steps.

3.3.3 Stochastic network evolution

The experiments take measurements on the samples for a given time interval, detecting resistive switching events and observing the time evolution of the film resistance. Thus, aiming to develop an abstract effective model of what happens in the experiments, we simulated a stochastic evolution of the resistor network. Clearly, it is very difficult to find a direct correspondence between our time step and a physical time; we employ a Monte Carlo algorithm for randomly updating the conductance state of each link, and in the simulation there is no notion of physical time in seconds.

The system is evolved via physically–inspired update moves which act on the (discrete) conductance state of each link, with a given probability to accept the move. Therefore, step after step, the set of values of the single resistors changes, due to stochastic acceptance of proposed updates. The initial levels of the conductances of all links are in general randomly chosen; the subsequent stochastic evolution tends to bring the system towards dynamic equilibrium configurations compatible with the applied voltage. It is straightforward to verify that the results that we are going to describe do not depend either on the choice of the initial conductance values relative abundance, or on their spatial distribution.

The links are allowed to change state only among the already introduced set of possible conductances: $\sigma_A, \sigma_B, \sigma_C, \sigma_D$. This choice was originally derived from considerations concerning the experimental data. In fact, the group at CIMaINa takes micrometer–sized SEM images of the gold clusters

over the SiO_x substrate; it is possible to perform a coarse–graining of SEM images and assign a single conductance value to each sub–region. The distribution of these values (automatically assigned through an algorithm) suggested that setting 4 distinct conductance values as the ones already described was the most reasonable option. During the MC steps, the conductances change with fixed probabilities, whose choice has already been extensively discussed elsewhere [44].

There are two physical mechanisms we have included in this model:

- the energy dissipated via thermal **Joule effect** (which has been recognized as a key feature also in the analysis of the experiments [6, 34])
- a **nonlinear activation function**, a kind of 'gate' loosely inspired to the behavior of diodes in electrical networks

Power dissipation

Each link can be characterized by a *dissipated power* $W_{ij}^{(d)} = \dfrac{\Delta V_{ij}^2}{R_{ij}}$ and an *absorbed power* $W_{ij}^{(a)} = c\,\dfrac{\sum_{N_{\text{neigh}}(kl)} \dfrac{\Delta V_{kl}^2}{R_{kl}}}{N_{\text{neigh}}}$, which is determined by the power dissipated from the N_{neigh} neighboring links, whose ends are indicized by k, l. Here c is a proportionality constant that takes into account the multiple usage of the same links for calculating the absorbed power for more than one link ij. In Fig. 3.9 it is represented the choice of the links that contribute to $W_{ij}^{(a)}$ in a 3D network.

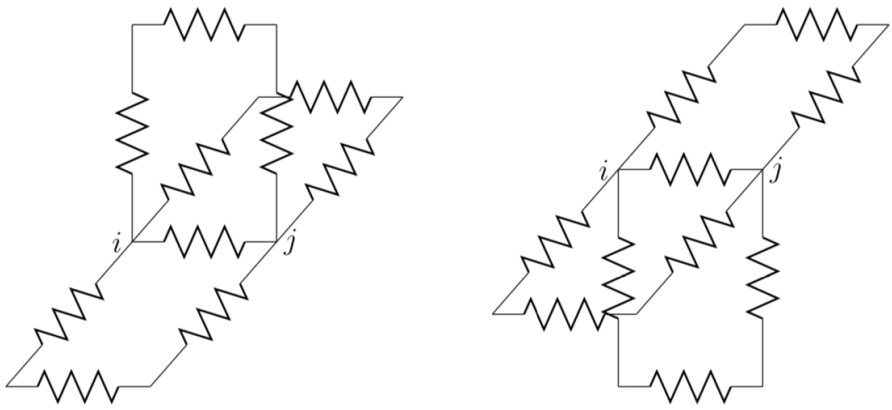

FIGURE 3.9: Left: links that contribute to W_{ij}^{a}, same ij level + upper level; right: analogously, same ij level + lower level. Reprinted from [44]

While $W_{ij}^{(d)}$ represents the energy emitted by thermal dissipation by the link ij, $W_{ij}^{(a)}$ collects the corresponding power amounts dissipated by neighboring links. These contributes can be microscopically interpreted as rearrangements of the inner conductive network structure, which can lead to an increase in the conductance of the link ij.

Therefore, in the code, a upgrade/downgrade of the conductance level of each link is proposed (and randomly accepted with a given probability), according to a specific procedure that will be detailed later on. When such an update is proposed, σ_{ij} jumps from an initial level up to a final one, depending on the comparison between $W_{ij}^{(a)}$ ($W_{ij}^{(d)}$) and a list of threshold power values W_{up}^{th} (W_{down}^{th}), which sets the minimum power requested for a transition between two conductance levels. Note that, for $W_{ij}^{(a)}$, the proportionality constant c is also present in the thresholds and, therefore, it gets simplified. On the one hand, the jump probabilities and the thresholds have been determined in order to reproduce as close as possible the experimental observations concerning RS events and the dependence of the electrical current on the applied voltage within hysteresis cycles. On the other hand, their values have also been carefully tuned in order to avoid breaking the network in the range of interest for ΔV_{tot} [44]. These values do not change across the simulations and are:

- $P_{\text{up}} = P_{\text{down}} = 0.0015$ (probability to accept any move that changes σ_{ij} upwards or downwards, regardless of the specific value of σ_{ij})
- $\sigma = 10^{-10} \leftrightarrow \sigma = 0.01 : W_{\text{up}}^{th_0} = 0.00002\, J/s = 2 \times W_{\text{down}}^{th_0}$
- $\sigma = 0.01 \leftrightarrow \sigma = 0.02 : W_{\text{up}}^{th_1} = 0.00001\, J/s = 2 \times W_{\text{down}}^{th_1}$
- $\sigma = 0.02 \leftrightarrow \sigma = 0.04 : W_{\text{up}}^{th_2} = 0.002\, J/s = 2 \times W_{\text{down}}^{th_2}$

We noticed that it is necessary to set higher thresholds for moves that attempt to raise the conductivity of resistor ('up' moves), in order to generate a behavior closer to the experimental one. In the code, for simplicity, we set up equal thresholds for both 'up' and 'down' trial moves and multiply $W_{ij}^{(a)}$ by a factor 0.5 before comparing the actual computed value with the thresholds. Clearly, this particular choice of the W^{th} values is not unique, but this one allows (as we will describe in the following) to approximately retrieve the essential experimental features in the simulated data. We tested that slight variations of these thresholds yield qualitatively analogous results.

An example will immediately clarify the link update mechanism: choose an edge ij, suppose that $\sigma_{ij} = \sigma_D = 0.04\ 1/\Omega$ and evaluate the dissipated power W_{ij}^{d}. If $W_{\text{down}}^{th_2} < W_{ij}^{d} \leq W_{\text{down}}^{th_1} + W_{\text{down}}^{th_2}$ the downgrade of σ_{ij} value to $\sigma_C = 0.02\ 1/\Omega$ is proposed (and accepted with probability 0.0015). But if

the dissipated power is large enough that $W_{\text{down}}^{th_2} + W_{\text{down}}^{th_1} + W_{\text{down}}^{th_0} > W_{ij}^{d} \geq W_{\text{down}}^{th_1} + W_{\text{down}}^{th_2}$, the link conductance will be decreased down to $\sigma_B = 0.01\ 1/\Omega$ with probability 0.0015, and so on. Clearly, links whose initial conductance is $\sigma_{ij} = \sigma_A = 10^{-10}\ 1/\Omega$ can not be further downgraded. The corresponding algorithm is applied when attempting to upgrade links conductance according to their dissipated energy.

In summary, our system embeds the possibility of increasing links conductance if their neighbors dissipate enough energy; conversely, a link can become more resistive if it is dissipating too much energy. Interestingly, even links with vanishing conductance can be 'reactivated' and contribute to the current flow towards the output node, which reproduces some properties hypothesized for the experimental samples [6, 34].

Nonlinear components

The observed experimental behavior of I_{tot}, at low voltages, is evidently a non–ohmic dependence on ΔV_{tot}; in particular, a huge increase of R_{tot} characterizes the samples for low applied potential difference [34]. This implies that we also need to insert a nonlinear element in the simulations: taking a loose inspiration from diodes, the edges of our network can be also compared with a voltage threshold ΔV^{th}. A diode allows the current passage only if it is subjected to a voltage larger than a threshold value. The motivation behind the insertion of such nonlinear elements is to model the current passage through two nanometric grains. In general, we can expect that two gold nanoparticles are characterized by different electrical conductance levels, according to their peculiar geometry, shape and position within the thin film. As a consequence, the conduction bands of the two nanoparticles will create a mismatch and the current will flow only if the local potential difference allows the electrons to jump through the gap. These events can be complemented by quantum tunnel effects, which are not separately taken into account in our SRNM, but are just included in the set of events modeled by the presence of nonlinear components.

In our system, an edge with $\sigma_{ij} = 10^{-10}\ 1/\Omega$ can favor the current passage (i.e. it increases its conductance up to $\sigma_{ij} = 0.01\ 1/\Omega$) if $|\Delta V_{ij}| > \Delta V^{th}$ with a given probability P_{nl}, where 'nl' stands for 'nonlinear'. Conversely, if $|\Delta V_{ij}| < \Delta^{th}$, and $\sigma_{ij} = 0.01\ 1/\Omega$, the link will decrease its ability to conduct electric current by lowering its σ_{ij} down to the lowest level (almost infinite resistance). $P_{\text{nl}} = 0.0003$ is the optimized value and 0.06 V is the chosen ΔV^{th}. In this regard, we noticed thanks to several tests that $P_{\text{nl}} < P_{\text{down,up}}$ is a fundamental condition to be met. In fact, in the opposite case the nonlinear gate function becomes too relevant and the overall resistance become dramatically reduced, leading us in conditions far away from the experimentally measurements.

This move involves, then, only the links with low conductance, leaving the others unaltered: this introduces the possibility for 'dead' edges to become conductive again and for edges with low conductivity to become temporarily infinitely resistant to current passage. For the aforementioned links, if this nonlinear move is attempted, the modifications of σ_{ij} based on power dissipation/absorption are not considered at that step. We also tested the effect of limiting this nonlinear behavior to the promotion of infinite–resistant links to the upper conductivity level; other simulations were instead performed only allowing the degradation of links with $\sigma_{ij} = 0.01\ 1/\Omega$ according to the just explained 'gate' mechanism. Both sets of simulations yielded results qualitatively different from the experimental ones, thus showing the necessity of including both possibilities in our Monte Carlo program. In particular, we observed that the nonlinear gate function necessarily has to act in both directions (downgrade and upgrade) in order to generate the non–ohmic behavior at low ΔV_{tot} during hysteresis loops.

Link update

Both mechanisms described in the previous paragraphs are included in the code in the `switch_on_off` function. At each step, after solving the network via graph theory, the code performs a loop over all pairs of directly connected nodes (i.e. over all the physical links). First of all, regardless of the link conductivity, $W_{ij}^{(a)}$ and $W_{ij}^{(d)}$ are computed. Afterwards, for each link, depending on its σ_{ij} value, a slightly different algorithm is applied:

1. if $\sigma_{ij} = \sigma_A$ the link can not be further upgraded:
   - if $W_{ij}^{(d)}$ is not smaller than $W_{\mathrm{down}}^{th_2}$, then attempt to decrease σ_{ij} depending on the comparison between $W_{ij}^{(d)}$ and the power thresholds for downgrade.
   - if, conversely, $W_{ij}^{(d)} < W_{\mathrm{down}}^{th_2}$, the link can not be downgraded
2. else if $\sigma_{ij} = \sigma_B$:
   - if $W_{ij}^{(d)} > W_{\mathrm{down}}^{th_1}$, then attempt to decrease σ_{ij} depending on the comparison between $W_{ij}^{(d)}$ and the power thresholds for downgrade.
   - else if $W_{ij}^{(a)} > W_{\mathrm{down}}^{th_2}$, then attempt to promote σ_{ij} to the maximum conductance value. Note that, even if the previous trial update is refused, nonetheless this move is not attempted.
3. else if $\sigma_{ij} = \sigma_C$:
   - if $|\Delta V_{ij}| < \Delta V^{th}$, try to downgrade σ_{ij} to $10^{-10}\ 1/\Omega$ with probability P_{nl}.

- else, if the condition for applying nonlinear gate is not satisfied, verify if $W_{ij}^{(d)} > W_{\text{down}}^{th_0}$, then attempt to decrease σ_{ij} to the minimum conductance value.
- else if both previous conditions are not met, compare $W_{ij}^{(a)}$ with $W_{\text{down}}^{th_1}$. If $W_{ij}^{(a)} > W_{\text{down}}^{th_1}$, then attempt to promote σ_{ij} to 0.02 or 0.04 $1/\Omega$, depending on the value of $W_{ij}^{(a)}$.

4. last, if $\sigma_{ij} = \sigma_D$, the trial updates can only attempt to increase σ_{ij}:
   - if $|\Delta V_{ij}| > \Delta V^{th}$, try to upgrade σ_{ij} to 0.01 $1/\Omega$ with probability P_{nl}.
   - else if the previous condition is false, compare $W_{ij}^{(a)}$ with the W_{up} values and, eventually, try to update σ_{ij}.

Importantly, we conducted many simulations and concluded that the order of the trial updates is not so relevant, in the end: checking $W_{ij}^{(a)}$ before $W_{ij}^{(d)}$ or vice versa generates, on average, approximately the same results. It turned out that it is instead slightly more important to apply, when possible, the nonlinear activation function before the other two update moves.

Code scheme

The software is capable of simulating either hysteresis loops (from a minimum to a maximum applied voltage value, with discrete increments, and then from the maximum down again to the minimum) or simple runs with fixed ΔV_{tot}. In the first case, the value $\Delta V_{\text{tot}} = 0$ is skipped by default, because we noticed that with $\Delta V_{\text{tot}} = 0$ the network resistance could assume non–numerical values, which vould compromise the rest of the simulation. Summarizing, the `C++` code developed in this code is structured as follows:

- read input data: applied voltage, initial A configuration (can be the last adjacency matrix of a previous simulation for a restart or a random one), number of steps n_s. In case of hysteresis cycles, specific parameters are read in addition, such as the starting and the end point of the loop, and the number intermediate ΔV_{tot} where to simulate at.
- for all the n_s MC steps (and, eventually, for all the ΔV_{tot} values which constitute the hysteresis cycle to be simulated)
  1. calculate $\mathbf{A}, \mathbf{D}, \mathbf{L}$ via graph theory
  2. calculate R_{tot}
  3. perform one stochastic evolution MC step, by attempting the update of all the links (some links must not be modified, but this will be detailed when necessary in subsections 3.4.5 and 3.4.4).

4. write output files (A and I matrices are periodically written on files, eventually for each MC step)

- write final A matrix for a possible restart

Network topology

Some tests performed during my PhD research suggest that, if L_x, L_y, L_z represent the number of nodes along the three directions:

- each layer should host at least about $L_x = 35 \times L_y = 20$ nodes (42×27 nodes is the final number chosen for the majority of the results showed in the present Chapter)
- $L_z = 3$ stacked layers with vertical connections are necessary

in order to mimic the essential experimental features, in particular aiming to reproduce the flattening of the $I(\Delta V)$ curve at low voltages (see Fig. 3.4a) and the RS events. We observe that even a 3D network, with 3 stacked layers, is not an appropriate choice if the number of nodes in each layer is too small (e.g. $L_x = 15$, $L_y = 8$ and $L_z = 3$ is a setup that will not reproduce the experimental properties). Some simulations were also performed using 3 layers made of 55×35 nodes each, but they required a much higher computational effort without any sensible gain, concerning the similarity with experimental data.

Figs. 3.10a-3.10d show four examples of $I(\Delta V)$ cycles from -8 V to 8 V and from 8 down to -8 V again, performed on networks with different number of layers and with different layers sizes. The $I(\Delta V)$ curve really flattens at low voltages only with the large resistor network simulated. In the other cases, especially with just a single layer, this feature disappears. Moreover, at high voltages, the smaller networks display nonphysical behavior with wild current oscillations. This can be ascribed to the smaller amount of links in the network which, in turn, induce huge fluctuations in the availability of effective paths for the current to flow through the system. From our simulations also appears that, given a number of stacked layers, the larger the size of a given layer, the higher the potential difference value for which this plateau starts. Interestingly, hysteresis effects such as those highlighted in experimental data (see Fig. 3.4b) are essentially always present independently on the specific network topology.

Therefore, in the following, we are always going to refer to a resistor network with $(L_x, L_y, L_z) = (42, 27, 3)$, plus a input and a output node: this means a total of 3404 nodes. The chosen network size represents a good trade–off between computational cost of the algorithm and physical plausibility of the results. We remark here that we are interested in determining the smallest possible network which allows to retrieve results comparable with

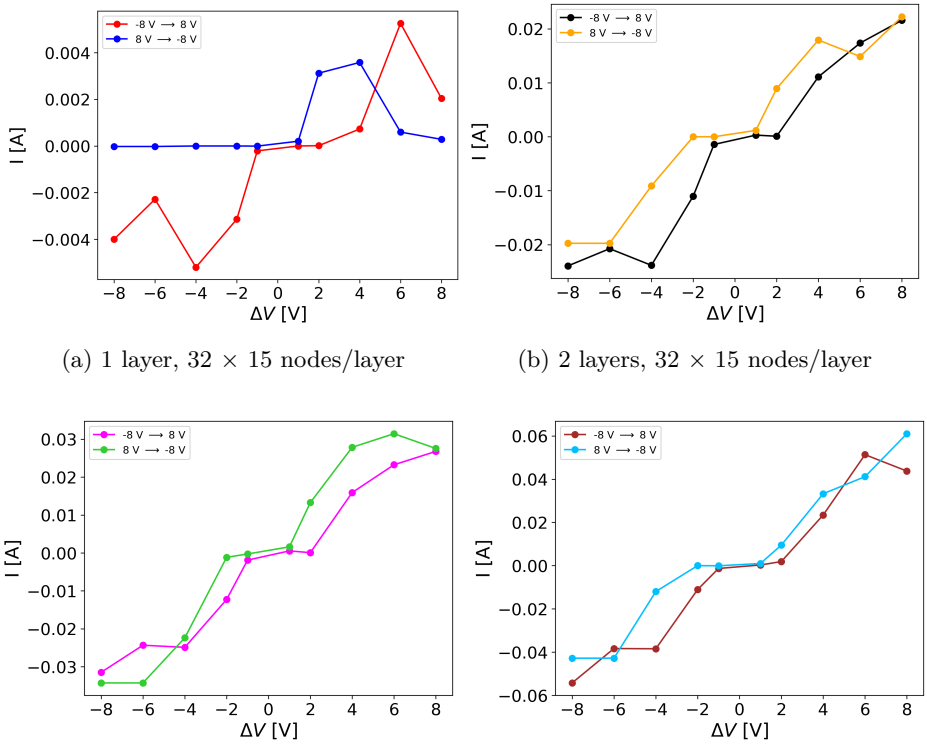

(a) 1 layer, 32 × 15 nodes/layer

(b) 2 layers, 32 × 15 nodes/layer

(c) 3 layers, 32 × 15 nodes/layer

(d) 3 layers, 42 × 27 nodes/layer

FIGURE 3.10: $I(\Delta V)$ cycle as a function of the number of layers and their size

the experiments. Additionally, the knowledge of the minimum size of such a simulated system also could provide a loose relationship between the spatial extension of the real sample and the length scale of our network.

We also checked that the main phenomenology is retrieved if one uses two different probabilities for the nonlinear update function (one for upgrading links with $\sigma_{ij} = 10^{-10}$ and another one for downgrading links with $\sigma_{ij} = 0.01$). As already noted, the key point is that it is mandatory to include this move, because without it our whole system essentially behaves like a trivial, large ohmic resistor. Another crucial observation is that modifying P_{up}, P_{down} or P_{nl} generates a slowdown or an acceleration of the system's dynamics, enhancing or suppressing local resistance fluctuations in the network. This could be easily grasped: increasing the acceptance probability of a move that changes the conductivity of a link - and, as a consequence, the state of the whole network - means that the dynamics becomes quicker, with a greater amount of resistors changing their σ_{ij} for each MC step.

A crucial experimental feature retrieved with this model is the overall trend of R_{tot}, i.e. the resistive switching highlighted e.g. in Figs. 3.3a and

3.3b. Concerning this, as an example, in the bottom panel of Fig. 3.11 we report the evolution of R_{tot} during a typical simulation of 20000 MC steps with $\Delta V_{\text{tot}} = 15$ V. Remarkably, it seems that the simulations are able to capture the main features evidenced in the experiments: there is a number of distinguished resistance levels that are repeatedly visited by the system with sudden variations of R_{tot} and subsequent fluctuations around a given resistance value. In the picture, the RS events occurring in the network are encircled in red.

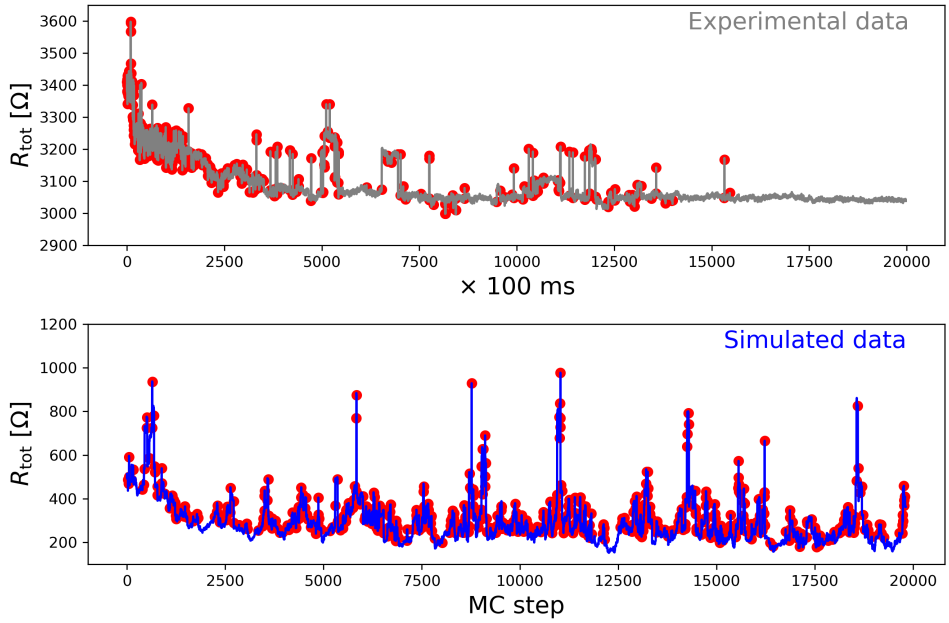

FIGURE 3.11: Comparison between a simulated (left panel) and an experimental (right panel) resistance time series, at $\Delta V_{\text{tot}} = 15$ V

The top panel of the same picture contains experimental measurements of the time evolution of R_{tot}, collected about every 0.1 s, at $\Delta V_{\text{tot}} = 15$ V, for a total of $\sim$ 20000 measurements. It is important to remark that the discrepancy between the order of magnitude of the experimental sample resistance and the one computed in our simulation can be due to many factors; we do not seek for a one-to-one correspondence between our SRNM and the experimental gold film, but for a qualitative recovery of the main experimentally observed features in the results of our simulations. From now on, all the exposed results refer to simulations where 'low voltage' corresponds to 4 V (or 1 V, where specified), while 'high voltage' means ΔV_{tot} =15 V (importantly, in general the network does not break down at this ΔV_{tot}, i.e. the associated graph is almost always connected). In particular, during the

experiments it turns out that the resistive switching behavior is enhanced if the network passes through a *conditioning* phase at high applied potential difference. Hence, our typical simulations comprise:

- n_s MC steps at 4 V (or 1 V, where specified), starting from a random coverage. This stage will be referred to as '4_pre' ('1_pre')
- n_s' MC steps at 15 V, i.e. the conditioning phase
- n_s'' MC steps at 4 V (or 1 V), after the conditioning. This last stage will be referred to as '4_post' ('1_post')

where n_s, n_s' and n_s'' usually range from a few thousand steps up to some ten thousand steps. The majority of the data analysis exposed in the next section will be referred to the investigation of the differences between the physical properties of the network at low applied voltage *before* and *after* the conditioning. To this extent, Fig. 3.12a displays, for a typical simulation, the amount of links featuring each one of the four conductance levels. This is a dynamic quantity, partly depending on the applied voltage and partly on the previous history of the system (the equilibrium values of the '4_post' phase are similar but not identical to those of the '4_pre' phase). These quantities oscillate during the simulation, unveiling the dynamic equilibrium that characterizes this network.

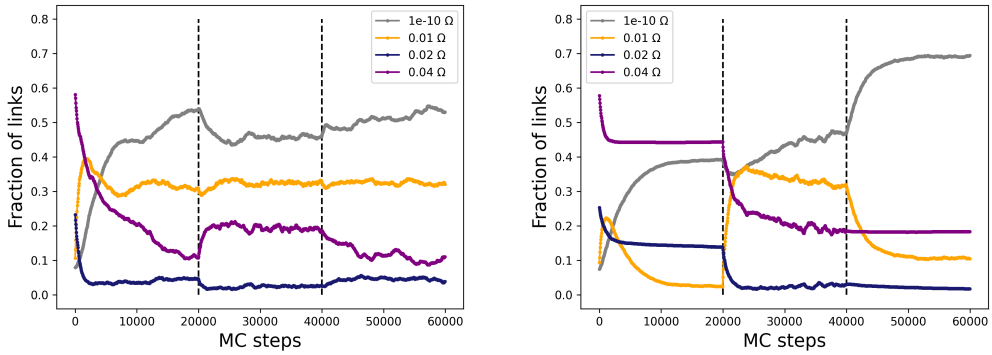

FIGURE 3.12: Fraction of links with $\sigma_{ij} = \sigma_A$ (grey), $\sigma_{ij} = \sigma_B$ (orange), $\sigma_{ij} = \sigma_C$ (navy) and $\sigma_{ij} = \sigma_D$ (purple), in a '4_pre'- 15 - '4_post' simulation (left) and in a '1_pre'- 15 - '1_post' simulation (right).

We have run preliminary simulations where the low voltage phases are characterized by ΔV_{tot} =1 V (indicated as '1_pre' and '1_post'). In this case, the fraction of links having a given conductance is an observable that is

largely affected by the system's previous history, as it is apparent by looking at Fig. 3.12b. Here, with the same color scale, we unveil that the non-Ohmic region of the networks presents an extremely interesting behavior: the large majority of links evolve towards a highly resistive state (grey color in the picture), while the fraction of resistors with $\sigma_{ij} = \sigma_B, \sigma_C, \sigma_D$ is smaller than it was during the '1_pre' phase.

The time scale issue

From the considerations exposed in the previous pages, it is clear that we lack a direct correspondence between a Monte Carlo step and the experiment time scale. We attempted some comparisons between our data and the experimental ones, but our idealized system can not completely be mapped onto the real sample. Preliminary analyses suggest that 0.1 s of measurement in the experimental framework approximately correspond to a 1-10 MC steps. This does not impede the possibility of comparing simulated and measured data, but it just implies that the stochastic evolution of the resistor network does not properly have the meaning of time evolution. As a consequence, also the frequency of the oscillations of R_{tot} could hardly be compared with the physical one. It is rather interesting to compare the overall trends of the relevant physical observables and to perform analysis on the simulated data concerning the underlying physical mechanisms. Nonetheless, as already discussed, the acceptance probabilities of the MC moves implemented in the code are important. They determine not only the amplitude of the R_{tot} jumps, but also the frequency of relevant network modifications: if the network state is changed too frequently, there will be less comparability with the experiments. In fact, as largely discussed in the previous section, the experiments clearly indicate the presence of strong *memory effects* in the system (especially after the conditioning phase at high ΔV_{tot}), marked by huge RS events. Fine tuning all the parameters we have already described is of crucial importance for closely mimicking the experimental behavior. In the simulations, we verified that this memory effect is retrieved if the system has been previously conditioned with a $\Delta V_{\text{tot}} \geq 10$ V (as already mentioned, in all the simulation the conditioning step was always performed at 15 V).

3.4 Network analysis and results

3.4.1 Resistance time autocorrelation and Power spectral density

While evaluating $R_{\text{tot}}(t_{MC})$, one shall take into account that a given R_{tot} can correspond to an extremely large number of equivalent resistors configurations. Thus, the system fluctuates around a given microscopic configuration;

fluctuations can be classified as *noise* and a noise is characterized by an amplitude and by some main frequencies. Signal theory investigates the nature of several kinds of noise, attempting to separate the physical information from the white background noise [47–49]. One of the main tools to investigate the fluctuations of the effective network resistance is its *time autocorrelation function*, defined as:

$$a(R_{\text{tot}}(\Delta t_{MC})) = \frac{\langle R_{\text{tot}}(\Delta t_{MC})\, R_{\text{tot}}(0)\rangle - \langle R_{\text{tot}}(\Delta t_{MC})\rangle \langle R_{\text{tot}}(0)\rangle}{\sigma^2(R_{\text{tot}})} \tag{3.9}$$

with $\sigma^2(R_{\text{tot}})$ as the variance of the total resistance and Δt_{MC} represents a gap expressed in MC steps. This quantity measures the time scale of the system correlations, ranging from -1 (anti-correlated data) to +1 (total correlation), where 0 indicates purely random fluctuations without any kind of correlation.

For short timescales, $a(R_{\text{tot}}(\Delta t_{MC}))$ can be fitted by an exponentially decaying function $e^{-\Delta t_{MC}/\tau}$, naturally providing a typical memory timescale as

$$\tau = \lim_{T\to\infty} \int_0^T a(R_{\text{tot}}(\Delta t_{MC}))d\Delta t_{MC}$$

For longer timescales, if the autocorrelation turns out to be $\propto 1/\Delta t_{MC}^{\alpha}$, $0 < \alpha \leq 1$, this means that

$$\tau \propto \int_0^T a(R_{\text{tot}}(\Delta t_{MC}))d\Delta t_{MC} \propto \frac{(\Delta t_{MC}^{1-\alpha})^{\infty}}{1-\alpha} \to \infty$$

In this case, our system would be characterized by a long–term memory, with correlations decaying only at an extremely low rate.

Considered that time is naturally coupled to frequencies, the other important quantity that can be computed is the *Power Spectral Density* (PSD), i.e. (for discrete values) the square modulus of the Discrete Fourier Transform (DFT) of $R_{\text{tot}}(\Delta t_{MC})$. There are several methods for computing PSD, for example Bartlett [50] and Welch [51] developed two different approaches for averaging several PSD estimations computed over different subdomains. Welch's method is already implemented in Python, via the Scipy method `scipy.signal.welch` (see, for more details, [52]). As explained on the website and in the cited paper, the PSD by Welch's average periodogram method is computed over the array containing the discrete time series $R_{\text{tot}}(\Delta t_{MC})$ as described in the next lines. The autocorrelation data are divided into segments of given length; each segment is detrended and windowed, and the different segments can be partly overlapped in the time domain. The square modulus of the Fast Fourier Transform (FFT, an efficient algorithm for the determination of the DFT) [53] of each segment is computed and these values are averaged to compute PSD, with a scaling to correct for power loss due

to windowing. In [44] the Bartlett method was used, but the Welch one provides some improvements and then we will refer to this last approach. Note that the PSD of the total resistance is symmetric on its own domain, thus it is sufficient to show just half of its domain. What is mostly relevant is the shape of the PSD and its dependence on frequency f, rather then absolute frequency values (which are referred to MC steps and not to a physical time). In particular, a key quantity that can be compared between experimental and simulated PSD of the effective total resistance is the α exponent of the fit function $1/f^{\alpha}$.

Briefly, if the autocorrelation function of R_{tot} has only an exponential decay, it can be shown [47–49] that, for the power spectrum $S(f)$:

$$S(f) = \frac{2\tau}{1 + (2\pi f)^2 \tau^2}$$

We are interested in the behavior of $S(f)$ for $f \gg \frac{1}{\tau}$; if $S(f) \propto \frac{1}{f^2}$, the system becomes rapidly uncorrelated, but if $S(f) \propto \frac{1}{f^{\alpha}}$ with $1 < \alpha < 2$, this implies that a kind of long–term memory is present in the evolution of R_{tot}. In particular, if $a(R_{\text{tot}}(\Delta t_{MC}))$ decays as $\frac{1}{\Delta t_{MC}^{\gamma}}$, $S(f) \propto \frac{1}{f^{\alpha}}$ and $\alpha = (1-\gamma)^2$. Thus, for $f \to 0$ $S(f) \to \infty$, and also the correlation time diverges. Physical systems with fluctuations of relevant observables (such as R_{tot} in our case) displaying a PSD with long–term memory are said to be characterized by *pink noise*, which is neatly different from the purely random white noise. Therefore, in experiments and simulations both, it is possible to fit $S(f)$ with a function like $\frac{1}{f^{\alpha}}$, for frequencies far away enough from the origin. The largest frequencies correspond to the inverse of the time between two consecutive experimental measurements (about 0.1 s for us, i.e. 10 Hz), or the the inverse of a single MC step in the simulations. Conversely, the smallest frequency can be readily obtained from the inverse of the maximum measurement time. We compare in Fig. 3.13 the PSD at 1 V (blue points) and at 15 V (green points) respectively, for simulated and experimental data both. Note that analogous properties hold for any voltage comprised between them. In both cases, we computed the PSD from the total resistance time series via Welch method, more specifically exploiting the `scipy.signal.welch` tool (sampling n_d data points, with a sampling factor equal to 1 and no overlap between the windows of the algorithm, in a frequency range between 0 and 0.5). $n_d = 5000$ for the simulated data (the first 15000 steps of each phase are discarded in this analysis), while $n_d = 20000$ for experimental data. The log-log representation of the PSD values helps the visualization and the fitting procedure (in log-log scale, the fit function is a straight line with slope α, represented as a dashed red line at 1 V and as a dashed black one at 15 V).

In the experimental measurements reported in [6], the typical PSD graphs look like the blue and green data in the right panel of the picture.

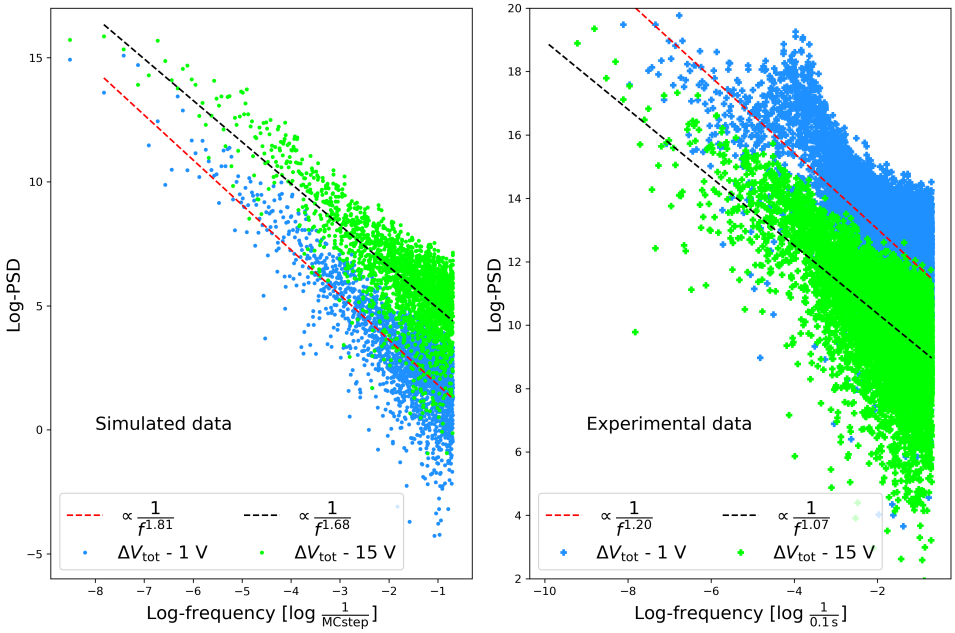

FIGURE 3.13: Left panel: PSD of two simulated R_{tot} time series (log-log scale), respectively at 1 V (blue points) and at 15 V (green points). Right panel: experimental PSD at the same voltages. In both cases, dashed red and black lines represent power law fits of blue and green data, respectively. In log-log scale, the α exponents of the frequency power-law dependence of the two PSD coincide with the slopes of red and black straight lines.

In particular, the majority of the measured resistances of cluster–assembled films show a $\dfrac{1}{f^{\alpha}}$ scaling behavior (in the frequency range considered), with $1 < \alpha < 2$, in line with the findings of [4, 54]. This holds for HIR and LIR devices both, while the exponent α shows a weak dependence on the applied voltage. In the example reported in the picture, $\alpha = 1.20 \pm 0.03$ at 1 V and $\alpha = 1.07 \pm 0.02$ at 15 V. In order to assess whether the computational model we developed contains the essential features for generating long–term memory effects, PSD deriving from simulations at 1 V and at 15 V, respectively, were produced starting from two series of simulated $R_{\text{tot}}(t_{MC})$ values. Here, the PSD at 1 V scales as $\alpha = 1.81 \pm 0.05$, while at 15 V the fitting power-law exponent is $\alpha = 1.68 \pm 0.05$. Importantly, also in this case, the Power Spectral Density of the network resistance is characterized by a pink noise. I remark here that the specific value of the PSD exponent is not fundamental;

what really matters, instead, is that $\alpha \in (1, 2)$ at any voltage in the range of interest. As shown, for instance, in [54], the PSD frequency dependence can even vary during the same experiment, taking arbitrary values in the aforementioned interval, depending on sample properties.

We observed that the exponent α which characterize the noise produced by the simulated system is not strongly influenced by the details of the network topology. The value of α rather depends on the jump probabilities between conductance levels for each link, thus underlining that these parameters actually represent a way to effectively influence the physical behavior of the system. The network that originated the PSD shown in the left panel of Fig. 3.13 was made up by the usual stacking of $L_z = 3$ layers, with $L_x = 42$ and $L_y = 27$. This is an additional proof that the computational setup we have built contains in itself many elements in common with the real system properties.

As a last comment, note that the frequency is measured in the units of measurement for time, which are clearly different in the experiments (seconds) and in the simulations (MC steps). Preliminary comparisons between experimental and simulated data seem to indicate that a single experimental measurement can approximately correspond to a number k of MC steps, being $k \in (1, 10)$. Our SRNM, however, despite being oversimplified with respect to the real sample, appears to possess the key elements for modeling the crucial physical features of the real sample.

3.4.2 Shortest paths

The fluctuations of the overall network resistance are not the only quantity that can be inspected. In fact, an intriguing view considers our simulated resistor network, as already discussed, as a graph. Distances between pairs of nodes within a graph can be measured, once that a metrics has been chosen. The code provides the matrices $\mathbf{I}$ and $\mathbf{A}$ as a function of time, step by step. This means that, aided by NetworkX tools, we investigated the graph structure of the network, looking for possible predominant paths (such as in [31]), shortest paths (SP) from source to sink nodes and other information coming from network topology and inner organization. Importantly, the analysis of the shortest paths where the current could pass through that is developed in the next pages is not obviously related to the fluctuations of the R_{tot}. The aim of this subsection of my work is to explore the possibility to employ such network analysis tools to obtain useful topological information about network conductivity. Further connections between these optimal pathways and resistance fluctuations constitute one of the future developments of this project, especially in order to determine whether the behavior of the system can be interpreted in terms of different pathways available for the current in different conditions.

The most important information is related to how many ways are there to reach sink node from source node and, given a metrics, how 'long' are these paths [55]. In particular, we aim at investigating the group of shortest paths that connect node 0 and node $N_\mathrm{n}-1$; a very important quantity, in this regard, is the minimum length L_{min} among all the possible paths that connect source and sink nodes [56, 57]. An interesting approach to this problem considered the $\mathbf{I}$ matrix (which is 3404×3404 matrix) as a weighted graph, which constituted the input for the following procedure, executed within a dedicated Jupyter Notebook:

- load, for each time frame t saved during the simulation, the corresponding matrices $\mathbf{I}|_t$ and $\mathbf{A}|_t$ into 2D `numpy` arrays.
- loop over $\mathbf{I}|_t$ elements: each entry I_{ij} of $\mathbf{I}|_t$ corresponds to a weight $W_{ij} = \dfrac{1}{|I_{ij}|}$, if $A_{ij} \geq 0.01\ 1/\Omega$, otherwise $W_{ij} = \infty$. The current values cover a wide range, typically between $10^{-12}A$ and $10^{-3}A$. The rationale behind the construction of this weight matrix $\mathbf{W}$ is that those links where the conductance is non–vanishing should be used by the current, while connecting node 0 and node $N_\mathrm{n}-1$. Conversely, highly (infinitely) resistive edges are essentially never crossed by the electrical current; assigning them an infinite weight means excluding these edges (because the nodes they link are substantially disconnected) from the search of the SP connecting the source and sink nodes.
- once built the weight matrix $\mathbf{W}$, given two nodes i and j, it is possible to calculate the shortest path between them, where the notion of distance is given by the weight matrix $\mathbf{W}$. NetworkX includes some methods for calculating the shortest path between a pair of nodes, in particular those by Dijkstra [58] and Bellman-Ford [59, 60]. We resorted to `shortest_path_length` function, which accepts a `method` keyword ('dijkstra' or 'bellman-ford'). This method requires, as input, also the graph `G` (i.e. the list of nodes and connecting edges), the two indexes of the nodes that are connected by the path(s) we are looking for and a reference to the weight to be employed. Note that using the absolute value of I_{ij} makes the graph a directed graph (we have a source and a sink) with non–negative weights, while it should have been regarded as a directed one with negative weights in the opposite case. We decided to avoid negative weights because optimization methods are known to fail in some cases with negative weights. A NetworkX `DiGraph` object is used, for the following analyses.

A typical SP between source and sink is shown in Fig. 3.14: interestingly, there are nodes belonging to each layer that are involved in the shortest path,

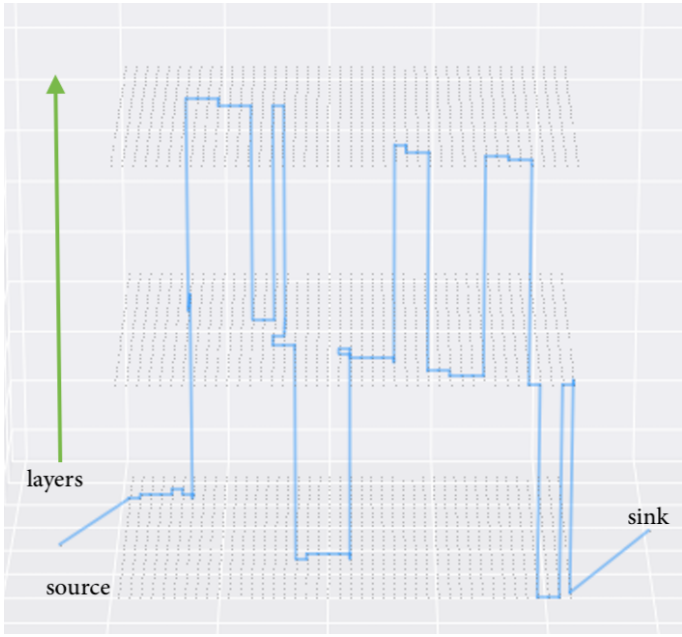

FIGURE 3.14: One shortest path between source and sink nodes, in a frame taken from a simulation at 15 V, with $W_{ij} = \frac{1}{|I_{ij}|}$ as metrics for distance. The small grey dots represent the nodes of the network, piled up in 3 layers.

and also z links are fundamental We stress again that the one represented is only an example within a class of equivalent shortest paths.

The following results were obtained for simulations with this schedule:

1. $n_s = 20000$ steps, 4 Volt
2. $n'_s = 40000$ steps, 15 Volt
3. $n''_s = 40000$ steps, 4 Volt

where the **A** and **I** matrices were saved every 50 steps. It is important to underline that we checked that all the following results remain qualitatively similar if the distance function is changed and the weights are calculated as $W_{ij} = \frac{1}{|I_{ij}|^m}$, with $m = 0.5, 2, 3$.

Both Dijkstra and Bellman-Ford algorithms yielded the same SP length (see Fig. 3.15), but the Bellman-Ford method implemented in NetworkX systematically detected a much higher number of equivalent paths (i.e. with the same length) between source and sink nodes, as appears from Figs. 3.16a and 3.16b. Once defined a distance function, the two methods are guaranteed to produce the same exact L_{min}, for a given graph. Fig. 3.15 is an example,

for a typical run with the above described schedule, of the variation of the optimal path length found via these algorithms along the simulation steps.

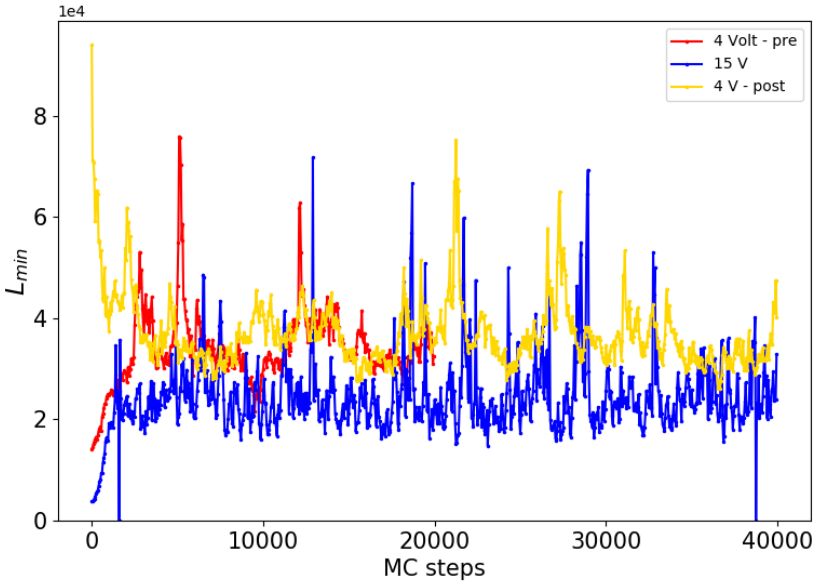

FIGURE 3.15: Shortest path length L_{min} for a typical simulation, as a function of the MC step. Data sampled every 50 MC steps, for a run with the usual ΔV_{tot} schedule (4 V, 15 V, 4 V) are reported.

For all the three stages of the simulations, the count of the corresponding MC steps starts from 0, for a better visual comparison of the L_{min} trend in the three situations. The red data points ('4_pre') have a domain which is half of the other two sections of the simulations, due to the schedule we adopted. For all the curves, there is an initial equilibration, and a following phase where L_{min} oscillates but does not show systematic increasing or decreasing trends. Fluctuations can be huge but some clear features emerge: first of all, it seems that L_{min} strongly depends on the applied voltage (and, obviously on network topology), but it probably does not depend on the previous electrical history of the network, considered that the first (red data) and the last (yellow data) phases with $\Delta V_{\text{tot}} = 4$ V yield statistically similar L_{min} series. Besides, for the highest the applied potential the optimal path is much shorter, probably because of the higher amount of current flowing in the network; in other words, at 15 V it is usually easier for the current to flow in the network, due to the fact An observation about the two blue data points where $L_{min} = 0$: in these two cases, at least one of the links excluded (i.e. a link with almost null conductance) is necessary for completing any path from the source to the sink

node. It is a extremely rare situation (only the 0.01% of the analyzed frames presents this kind of issue) and it comes from the fact that we assigned a finite σ_{ij} as the minimum possible conductance for an edge, and so the current can sometimes (rarely, because it is however an extremely small conductance) pass through links with such a high resistance.

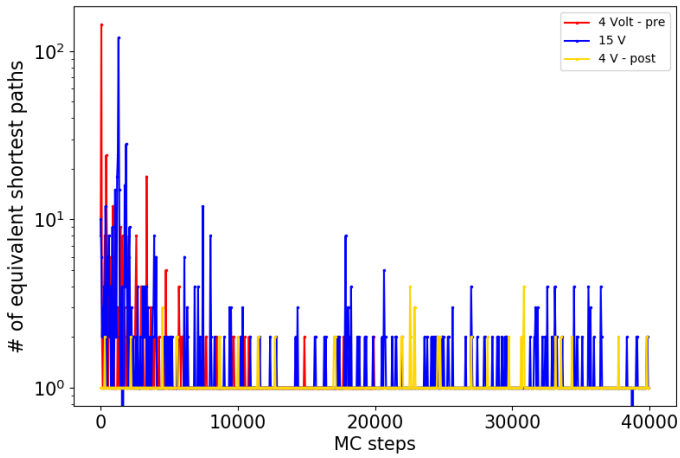

(a) Data obtained using Dijkstra optimization procedure

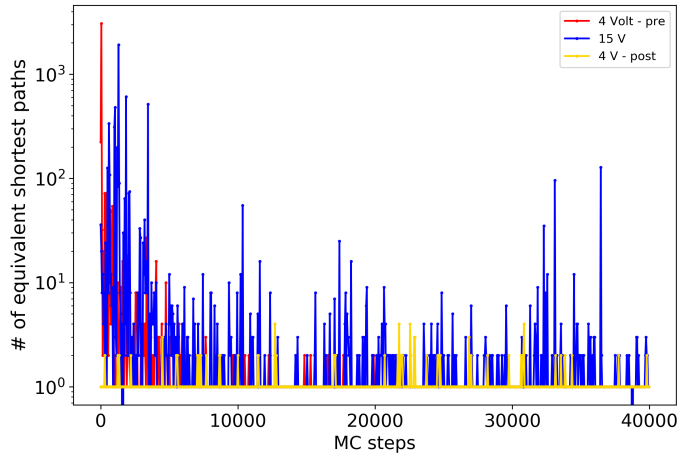

(b) Data obtained using Bellman-Ford optimization procedure

FIGURE 3.16: Number of SP as a function of MC steps. Data sampled every 50 MC steps, for a run with the usual ΔV_{tot} schedule (4 V, 15 V, 4 V) are reported.

As aforementioned, Figs. 3.16a and 3.16b refer instead to how many

equivalent shortest paths can be found in the network, step by step, for all the stages of the schedule adopted (this can be simply obtained by counting the number of elements individuated by `all_shortest_paths` NetworkX tool).

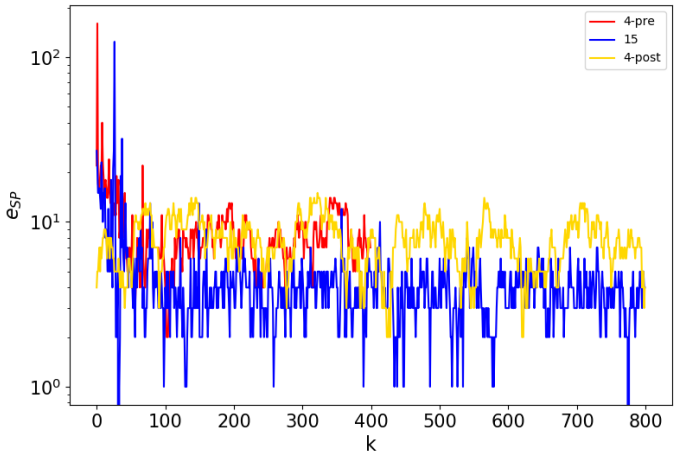

(a) Data obtained using Dijkstra optimization procedure

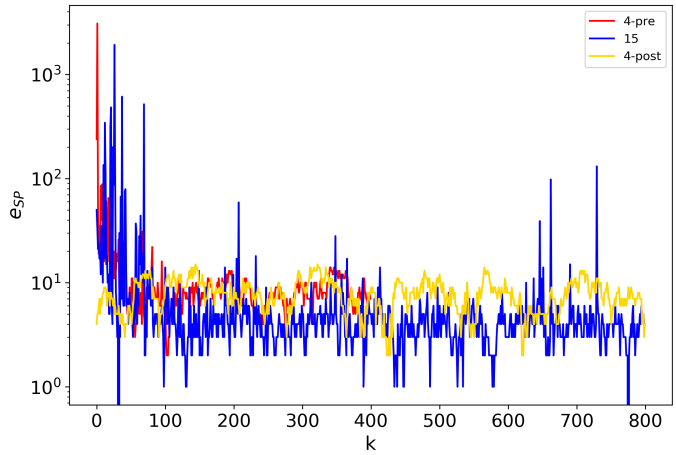

(b) Data obtained using Bellman-Ford optimization procedure

FIGURE 3.17: e_{SP} as a function of the iteration k of the algorithm which removes from G the nodes involved in any SP at iteration k-1. k consecutive values are separated by 50 MC steps.

Dijkstra and Bellman-Ford algorithms detect a different number of equivalent shortest paths (even by a factor of 10, sometimes), but the key information they both suggest is that, interestingly, the '4_post' simulations are

characterized by a sensibly smaller number of equivalent shortest paths. This means that the current, after the conditioning phase, has lost some alternative ways for reaching the output node. As a consequence, RS events, on average, are expected to increase.

The previous observation must be complemented by the consideration that, however, the current can choose many paths and not necessarily the shortest one. Therefore, a low number of equivalent shortest paths does not imply automatically that there is a small number of ways for the current to flow within the network. To follow this physical intuition, we decided to artificially remove from the graph G all the nodes which are involved in *any* shortest path, apart from nodes 0 and $N_{\mathrm{n}} - 1$. This generates a new graph G^*, which can be further analyzed, seeking for its shortest path(s). The procedure can be iterated k times, by progressively reducing the number of nodes. In Figs. 3.17a, 3.17b are represented the results of this analysis for both Dijkstra and Bellman-Ford methods. We can in fact inspect the number e_{SP} of $k-$th level (i.e. the shortest path at the k-th iteration of the algorithm which progressively deletes the nodes used by the shortest paths) equivalent shortest paths that are found for each iteration. This is clearly a rough and approximate procedure, because, for example, the second-level shortest paths could have used some nodes in common with the shortest paths, if these nodes would still have been present. $e_{SP}(k)$ presents, in all cases, an initial decrease, followed by oscillations around a given value, which appear to be dependent only on the ΔV_{tot} applied. We verified that this algorithm does not distinguish statistically between '4_pre' and '4_post', but only between 4 V and 15 V phases. The number of alternative paths available at a generic iteration k of our algorithm is almost identical in the two phases of the simulation performed at 4 V, within one standard deviation. Therefore, this analysis was not able to give us more details about the differences between the initial and the final simulation stages.

3.4.3 Origin of resistive switching

Our simulation and analysis framework allowed us to deeply investigate another fundamental question: are there in the network any local signals related to RS events? For example, is it possible to establish a quantitative relationship between local resistance changes and the overall network properties? Aiming to detect any possible inner rearrangements of the network corresponding to resistive switching events, we analyzed several time windows, drawing a 3D network representation and highlighting only the edges whose electrical current was found in fixed ranges. Figs. 3.18, 3.19, 3.20, are referred to three network configurations where R_{tot} as a function of the MC step is compared with a 3D representation of the network whose edges ij are colored according to their respective instantaneous electrical current value I_{ij}. The

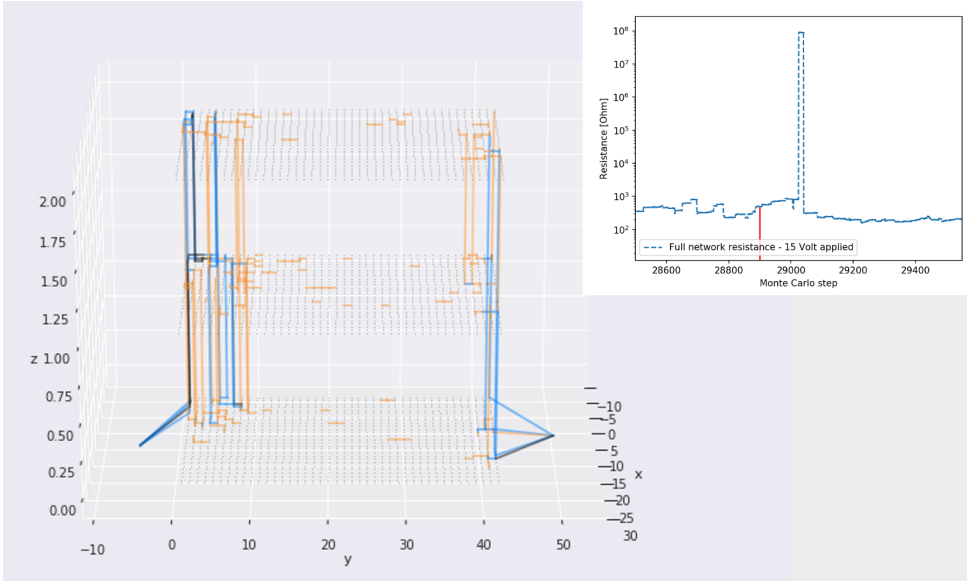

FIGURE 3.18: Typical configuration before the switching event, links are colored according to their current as explained in the main text.

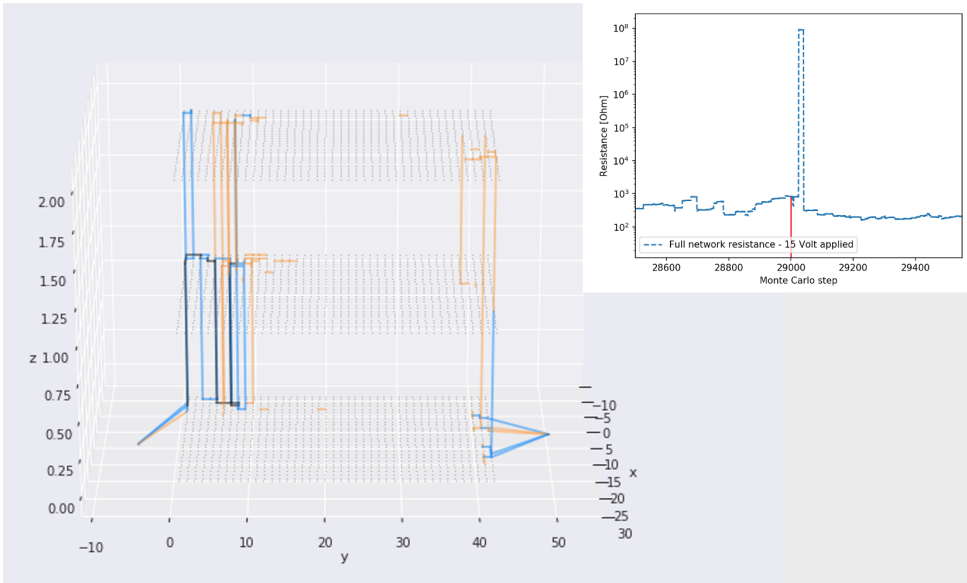

FIGURE 3.19: Immediately before the switching event, links are colored according to their current as explained in the main text.

color scale is adapted with respect to the largest current I_{max} measured at

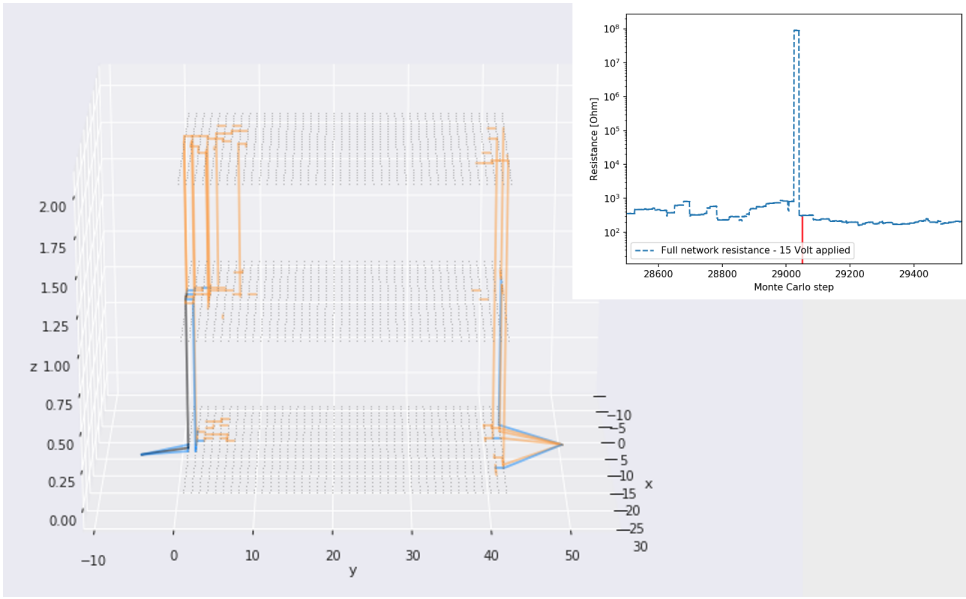

FIGURE 3.20: Immediately after the switching event, links are colored according to their current as explained in the main text.

each step in the network. Black links are crossed by a current $I > 0.5\, I_{max}$; orange links by a current I such that $0.15\, I_{max} < I \leq 0.5\, I_{max}$ and blue links by a current I such that $0.05\, I_{max} < I \leq 0.15\, I_{max}$. Edges that are not colored correspond to links where the flowing current is smaller than $0.05\, I_{max}$. All these frames are found close to a RS event (note the y-log scale for R_{tot} in the insets): a few steps before, immediately before and immediately after the resistive switch. The red segment in the inset of each Figure indicates the MC step. Noticeably, we are finally provided with a tool that aids inspecting the possible localized origin of resistive switching behavior. In fact, it is evident that RS events with jumps towards higher values are usually marked by a significant decrease of the number of links characterized by a high enough electrical current. It is worth to observe that the majority of the colored edges is found near the source and the sink nodes due to their special role, and due to the fact that all the incoming current I_{in} is subdivided into a few edges that link node 0 with the nodes of the first column of the first layer (and vice versa, all the edges linking the last column of that layer must collect all the outcoming current $I_{\text{out}} = -I_{\text{in}}$).

Note that all the measurements performed to obtain the results exposed in the present subsection were all instantaneous and did not include any kind of average. In principle, one can accumulate for a given number of MC steps (e.g. 50 MC steps, the same sampling frequency adopted here - but also 25

and 100 MC steps have been tested) and average the quantity of interest over the 50 timeframes considered. We do not report here the corresponding results, which are extremely similar to the ones already shown. Some fluctuations became smaller, but the key observations persisted: when the network experiences a kind of collective 'switch off' of the currents flowing through the edges, a sudden jump in R_{tot} is detected. Averaging over timeframes, substantially, does not yield any clear improvement.

3.4.4 Spatial coarse-graining and information

Seeking for methods that allow to distinguish the low–voltage phase preceding the 'writing' step from the low–voltage phase that follows, we pursued an approach based on Information Theory. In fact, many studies where the brain is investigated and modeled as a network [55, 57, 61, 62] exploit tools proper of Information Theory while analyzing brain electrical signals. The electrical patterns from neurons, in particular in Tononi's (and collaborators) view, can be measured by introducing a notion of *complexity* as integration of information. Motivated by these studies, we opted for applying as well these tools to delve into the properties of the neuromorphic devices we simulated. In particular, one can perform a *spatial coarse–graining* (CG) of the network, by dramatically reducing the degrees of freedom involved in the analysis. If L_x, L_y and L_z represent the number of nodes along the three directions in the original network, L'_x, L'_y and L'_z are the number of degrees of freedom of the coarse–grained system; in this work L'_z is kept equal to 1, therefore the coarse–grained system will be a two–dimensional matrix. Let us assign to each node three (discrete) spatial coordinates x, y, z. We will refer to the degrees of freedom of the reduced 2D system as 'pixels'; they are indicized in increasing order, from 0 to $n_{\text{pix}} - 1$, n_{pix} being the total number of coarse–grained degrees of freedom (see Fig. 3.21).

The ratio between L_x and L'_x (and the same holds for y and z) identifies the pixel into which each link is sent by the coarse–graining procedure. It has also to be considered that the number of edges that are sent onto a specific pixel is not the same for all the pixels. For example, a $42 \times 27 \times 3$ network can be reduced to a 3×2 rectangle, with $L'_x = 3$, $L'_y = 2$ (and $L'_z = 1$). Now, each row has 42 nodes and 41 edges; by construction, we assign the first 13 horizontal edges of each row to the pixel $p = 0$, the second 14 to $p = 1$ and the last 14 to $p = 2$. Instead each pixel, in this peculiar case, receives contributions from 13 vertical links (because the original network has 26 links in every column). If a node i in the layer 0 contributes to the average of a given pixel, also the two corresponding nodes of the above layers ($i + 42 \times 27$ and $i + 2 \times 42 \times 27$ in this example) will contribute to the same average, as well as the two $z-$links connecting layers 0 and 1 and layers 1 and 2, in correspondence of i. The links which connect node 0 with the first column

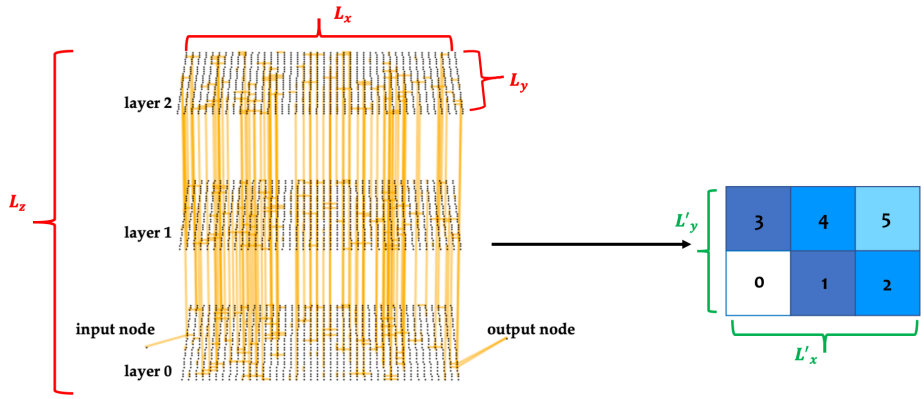

FIGURE 3.21: Passage from the original 3D network to the coarse–grained matrix. The length of the original network sides is indicated in red, while the size of the sides of the CG matrix are evidenced in green.

and $N_\mathrm{n} - 1$ with the last columns of the network are 27, in this case; they are subdivided in a group of 14 and a group of 13, connected to pixels 0 and 3 or 2 and 5, respectively.

An averaged conductance value $\overline{\sigma_p}$ can be assigned to each pixel, by averaging over the conductances σ_{ij} of all the links whose x, y, z are such that the link is mapped into the pixel p. First of all, an histogram of the values assumed by the various $\overline{\sigma_p}$ along a simulation can be performed. The MC simulations we will refer to will be divided into three stages, i.e.:

1. '4_pre' phase, $n_s = 20000$ steps with $\Delta V_\mathrm{tot} = 4$ V
2. '15' phase, $n'_s = 20000$ steps with $\Delta V_\mathrm{tot} = 15$ V
3. '4_post' phase, $n''_s = 20000$ steps with $\Delta V_\mathrm{tot} = 4$ V

where the three phases are concatenated, which means that the last configuration of the first phase is the input one for the second phase and so on. As a first attempt, we decided to discard from the analysis the first 10000 steps of each phase, i.e. the first half, in order to skip possible effects due to equilibration following voltage change. We presently ignore contributions coming from this stage of the simulation, but given that this work is conceived as the starting point of a much larger project, we are currently investigating the opportunity to exploit also non-equilibrium stages of the MC simulations for

measuring other properties we are interested in, such as the efficiency of the device in reproducing Boolean logic functions. As an example, in Fig. 3.22 we report the time-averaged correlation matrix M for the CG conductances (being $L'_x = 3$, $L'_y = 2$) of two typical simulations, for the three simulation phases. The top row and the bottom left corner of the picture present the correlation maps for the 6 $\overline{\sigma_p}$ values, computed over 200 MC steps (once every 50 steps, in the last 10000 MC steps of each phase). In particular, I have employed the following formula for each entry M_{ab} of the matrices drawn in the picture (very similar to the autocorrelation for the total resistance expressed in Eq. 3.9):

$$M_{ab} = \frac{\sum_{t=0}^{n_s}(\overline{\sigma_p}^a(t) - \langle\overline{\sigma_p}^a\rangle)(\overline{\sigma_p}^b(t) - \langle\overline{\sigma_p}^b\rangle)}{\sqrt{\sum_{t=0}^{n_s}(\overline{\sigma_p}^a(t) - \langle\overline{\sigma_p}^a\rangle)^2 \sum_{t=0}^{n_s}(\overline{\sigma_p}^b(t) - \langle\overline{\sigma_p}^b\rangle)^2}}$$

where a and b are two pixels with CG conductance $\overline{\sigma_p}^{a,b}$ and n_s is replaced by n'_s, n''_s in the following phases. Clearly, if the configurations are sampled once every k steps, the sum index t will be increased by k each time. Note that the numerator is the covariance of the $\overline{\sigma_p}^a$ and $\overline{\sigma_p}^b$ conductances.

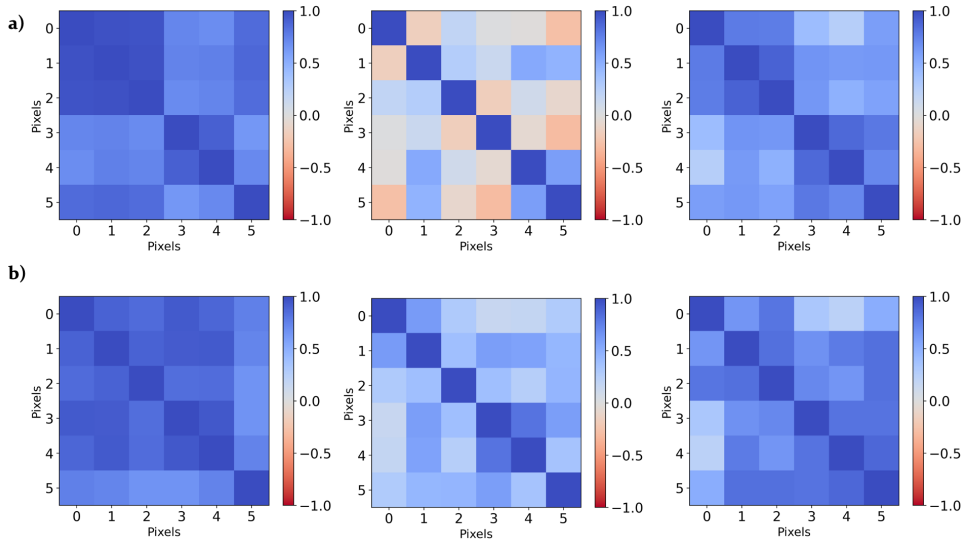

FIGURE 3.22: Example, relative to two single simulations, of the time correlation matrix M, computed over 200 configurations, sampled every 50 MC steps, in the last 10000 steps of each phase. Top row and bottom row contain data for all the three simulation phases, from left to right, referring to two independent simulations.

The correlation matrices which refer to the pre-writing phases result to be very close one to each other, but this is largely dependent on the random

initial conditions of the network (which, at low voltages, experiences only small changes). Interstingly, as shown in the example, two writing phases so different as witnessed by the matrices M appearing in the central column of the picture, can both induce some modifications. In both cases, the '4_post' correlation matrices show inner correlations among the sub-regions (i.e. the pixels), which are partly different from the initial simulation stage. This is ascribable to the nature of the conditioning phase, regardless of its details: the application of a high voltage affects in any case the pathways for the current in the system, changing its inner correlations.

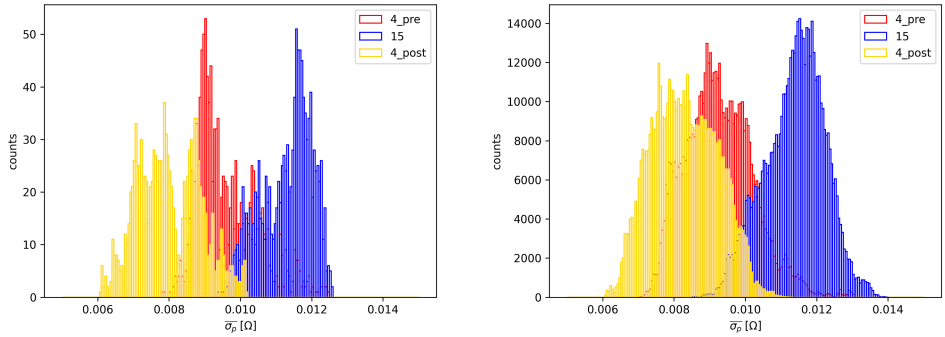

(a) Data relative to a single simulation. (b) Data taken by merging 9 independent runs.

FIGURE 3.23: Histograms of the coarse–grained conductances ($L'_x = 3$, $L'_y = 2$), for the last 10000 MC steps of the '4_pre' phase (red), the '15' (blue) and the '4_post' (yellow).

In Fig. 3.23a we report a typical distribution of the $\overline{\sigma_p}$ values for the '4_pre' (red), '15' (blue) and '4_post' (yellow) phases, for a single simulation (sampled every 50 steps, i.e. each histogram contains $10000/50 \times 6 = 1200$ entries). The right panel (Fig. 3.23b) merges the same data, taken from 9 independent runs. This means that the right panel contains, for each of the three histograms reported, $9 \times 10000/50 \times 6 = 10800$ contributions: 9 simulations of 200 single frames each of a CG matrix with 6 pixels. Remarkably, a difference emerges between the phase of the simulation preceding the high–voltage conditioning and the following one: the red and yellow histograms are only partially overlapped. In particular, statistically the '4_post' stage displays a distribution peaked in slightly lower conductance values (approximately 0.008 vs 0.009 $1/\Omega$). This coarse–graining procedure evidences that there is a deep change in the conductivity of the whole system before and after applying a high voltage: in the last phase, the system visits less frequently high-conductance states, and the edges with high conductance are in a smaller number (see Fig. 3.12a).

Moreover, note that in this analysis emerges how $\overline{\sigma_p}$ is not a discrete variable, but it is real-valued in the interval $[10^{-10}, 0.04]$ $1/\Omega$. The entries of the histograms can be uniformly divided into a finite number of sub–groups s, in order to recover a discretized conductance space state for each pixel. The shades of blue, from white to dark blue, in Fig. 3.21 represent exactly an example of this conductance discretization.

Having a discrete number of states accessible to each pixel allows then to use statistical tools to build a probability distribution, based on the occurrence of each pixel state in long simulations; this probability can be used to obtain an entropy of the CG system, which can in turn be utilized in quantities typical of the Information Theory, such as the Mutual Information and the Integrated Information [55, 61–63], which will be widely discussed later on. The following results obtained through the present analysis were obtained by studying *each* configuration generated by the system (i.e. data are sampled every single MC step). We verified the diverse consequences of using $s = 2, 3, 4$. The data were divided into s groups, according to the interval in which their conductance value falls, in the hypothesis of uniform conductance distribution: the first group of data comprised conductances between 0 and $1/s$, the second group between $1/s$ and $2/s$, ...

Fig. 3.24 contains an example of three plots of the occurrences of a given coarse–grained state (i.e. a particular configuration of the CG network, which is a particular set of 6 values for the 6 pixels) as a function of an integer index which identifies the CG state, for $s = 2, 3, 4$ (top left, top right and bottom, respectively). This case is referred to a single simulation. For all the values of s considered, the writing phase evidently affects the number of CG states visited during the '4_post' phase of the simulation. In fact, in this peculiar example (but the tendence is similar in the majority of the simulations we run), the distribution of the CG states before the application of $\Delta V_{\text{tot}} = 15V$ (red) is very different from the one after the writing phase (yellow data in Fig. 3.24). From such kind of analysis emerged that, despite the large number of possible elements of the space state, it was definitely possible to define an (approximate) probability distribution for these CG states.

The fact that many CG configurations repeatedly occur within 9 independent simulations (i.e. that some states are more probably visited than others) not only allows us to build an approximate probability distribution for the electrical conductance, but also is a significant proof that the configurations generated by our MC code are physically plausible and correlated. Conversely, a flat distribution of states all different from each other (each visited only once) would mean that the code samples configurations in a uniformly random way. Summarizing, the histograms drawn in Fig. 3.24 *are precisely* the probability distributions we will refer to. Obviously, all the quantities derived from these distributions slightly depend on the number of pixels chosen for the coarse–graining.

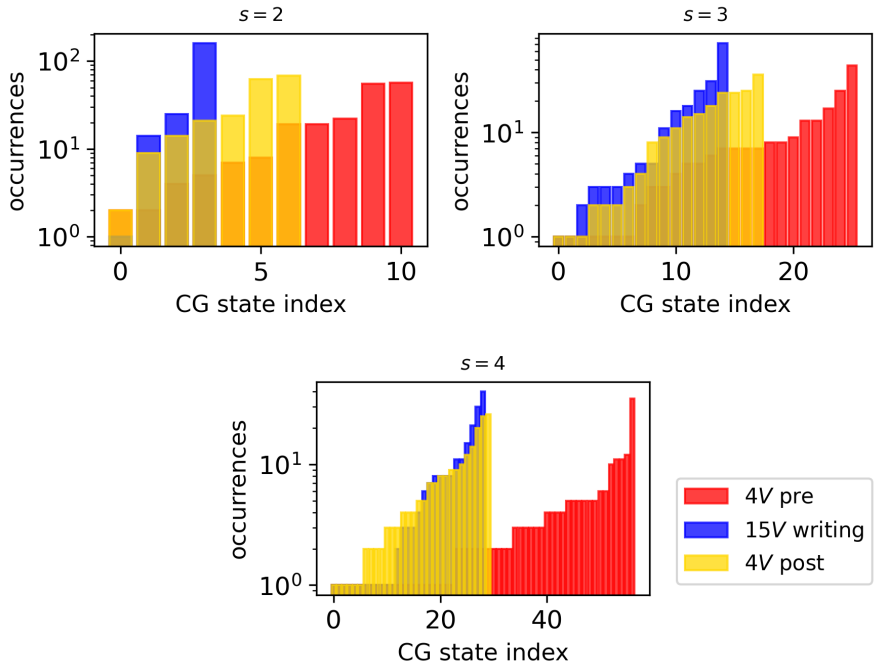

FIGURE 3.24: Occurrence of the CG states for a simulation of the $(L'_x, L'_y) = (3, 2)$ CG network. Data taken from a single simulation, 1000 MC steps each. Top left: $s = 2$, top right: $s = 3$, bottom: $s = 4$.

The most fundamental quantity that can be computed, in presence of a known probability distribution, is the *entropy*, i.e. the function that measures the uncertainty contained in a variable: essentially all the other functions are obtained starting from entropy H. Following the approach of many papers and textbooks (see e.g. [61–63]), let us assume that a random variable X (e.g. the complete state of a 3×2 CG matrix), whose possible states are a set of individual values $\{x\}$ (e.g. the simultaneous conductance state of the 6 pixels), the entropy of X is:

$$H(X) = \sum_{x \in X} p(x) \log_2 \left(\frac{1}{p(x)} \right) \tag{3.10}$$

being $p(x)$ the probability that a particular state x occurs (it is the joint probability of the states of the pixels of the CG matrix). Entropy is therefore a quantity that is accessible, in the simulations we analyzed. In fact, we know $p(x)$, where x is a particular state of the CG system (every entry of the data reported in Fig. 3.24 corresponds to a particular CG state) and $p(x)$ is exactly the value of the histogram for that abscissa. Note that this definition uses

the logarithm in base 2, therefore expressing the entropy in bits. $H(X) \geq 0$ and grows as long as the uncertainty about X increases. Two important concepts related to the simple entropy are the *conditional entropy* $H(X \mid Y) = \sum_{x \in X, y \in Y} p(x,y) \log_2 \left(\frac{1}{p(x|y)} \right)$ (related to the probability that $X = x$ if $Y = y$) and the *joint entropy* $H(X,Y) = \sum_{x \in X, y \in Y} p(x,y) \log_2 \left(\frac{1}{p(x,y)} \right)$ (related to the probability that $X = x$ and, simultaneously, $Y = y$). These three quantities are connected by the useful relation:

$$H(X,Y) = H(X) + H(Y \mid X)$$

As already mentioned, entropy quantifies uncertainty, i.e. it is a way to measure correlation between variables. In this sense, if $H(Y \mid X)$ contains the entropy that remains in X, once the state of Y is known, $H(X)$ will be equal to $H(Y \mid X)$ plus the information $I(X;Y)$ provided by Y about X. For this reason, $I(X;Y)$ is often named *mutual information* and henceforth referred to as MI in this text. The following identity, which evidences that MI is positive and symmetric, can be easily retrieved:

$$\begin{aligned} MI = I(X;Y) = I(Y;X) = H(X) - H(X \mid Y) = \\ = H(X) + H(Y) - H(X;Y) = \\ = \sum_{x \in X, y \in Y} p(x,y) \log_2 \left(\frac{p(x,y)}{p(x)p(y)} \right) \end{aligned} \tag{3.11}$$

MI is null if X and Y do not contain any reciprocal information; in general $MI \geq 0$ and the higher it is, the higher is the amount of knowledge about X that knowing the state of Y automatically yields. As observed by Timme *et al.* [63], MI can be regarded as the distance (according to Kullback-Leibler metrics) between the true joint distribution $p(x,y)$ and the joint distribution under the hypothesis that X and Y are independent, $p^{\text{ind}}(x,y) = p(x)p(y)$. Considering the CG systems previously discussed, computing MI on the conductance states of the pixels is an important tool to determine how much information is available about the $\overline{\sigma_p}$ of the pixels belonging to a subsystem, given the knowledge of the conductance state of the pixels belonging to the rest of the CG matrix. It can be shown that MI is a fine and powerful estimator, capable of capturing both linear and nonlinear dependencies [61, 62].

The *integrated information* II measures, instead, the total entropy loss as the difference between the sum of the entropies of the individual elements of a (sub)system and the entropy of the (sub)system:

$$II = -H(X) + \sum_{k=1}^{l} H(x_k) \tag{3.12}$$

where $H(x_k)$ is the entropy of each element which constitutes the subsystem under investigation. For our CG matrices, $H(x_k) = \sum_{m=1}^{s} p_m^k \log_2 \left(\frac{1}{p_m^k}\right)$, being in our case p_m^k the probability that the $k-$th element of the (sub)system (i.e. a single pixel among the l pixels that made up the (sub)system considered) assumes the $m-$th value among the s possible states. For example, if X represents the overall state of a CG matrix with $L'_x = 3, L'_y = 2$, II will be equal to the sum of the entropies of the $l = n_{\text{pix}}$ 6 single pixels minus the total entropy of the system. Analogously, if X represents the first column of the CG system, II in this case will be given by the sum of entropies of the $l = 2$ pixels belonging to the first column minus the total entropy of the first column. Note that determining the entropy of a subsystem requires the knowledge of the related probability distribution, which means counting the occurrence on a vast dataset of each possible state of the subsystem, and obtaining from this histogram the probability of every conductance state. Fig. 3.25 schematizes an hypothetical neural system whose elements are the grey dots indicized by the integer k. The scope of this picture is to clarify the meaning of mutual information (red arrow, measuring the correlations between X and the rest of the system) and of integrated information (green arrows, measuring internal correlations among the elements of X).

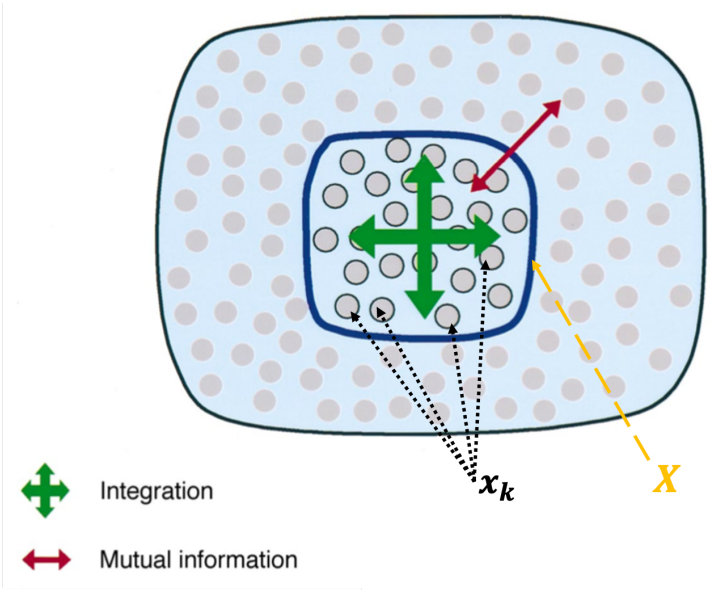

FIGURE 3.25: Picture adapted from [62]. A subset X of a neural system is drawn as a collection of individual elements x_k (grey points); the meaning of MI (red arrow, relationship between X and the rest of the system) and II (green arrows, internal correlations among the elements of X) is evidenced.

Let us now discuss the results obtained for MI and II as a function of the size of the fraction of the resistor network chosen (i.e. number of pixels): only curves for $s = 4$ are shown, because data for $s = 2, 3$ are qualitatively similar but we assumed that higher s values are more accurate in approximating the true probability distribution for pixel conductances. Figs. 3.26 and 3.27 show MI and II as a function of the subsystem size for $s = 4$ and a 3×2 CG matrix shape, for all the three phases of the simulations. Each data point is averaged over 9 independent runs (whose standard deviation of the mean produces the represented errorbars). Importantly, the shape of the curves computed for the single simulations are very similar one to each other, where each abscissa corresponds to a number of different realizations of a subsystem of that size.

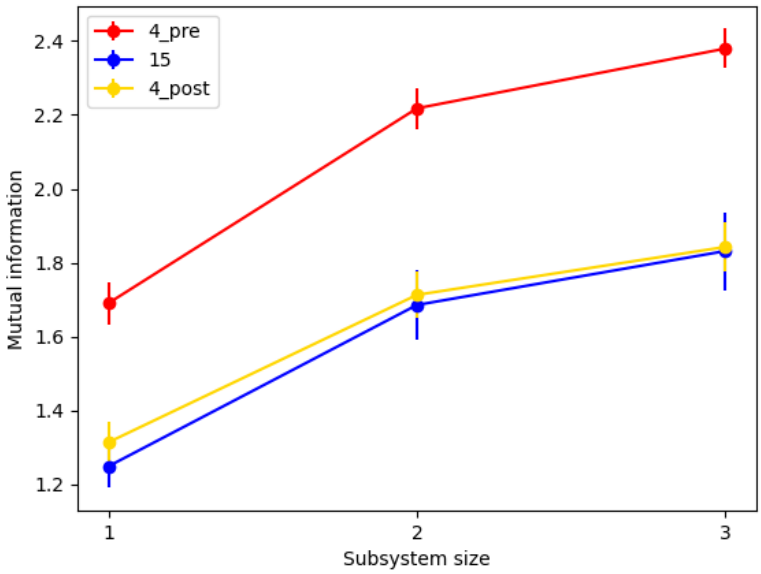

FIGURE 3.26: Mutual information as a function of the subsystem size for $s = 4$ and $(L'_x, L'_y) = (3, 2)$. MI values are averaged over 9 independent simulations.

Both pictures display very interesting features:

- the difference between red and yellow data is evident → the system is strongly conditioned by the passage through 15 V, and its entropy-related properties during the '4_post' stage are much more similar to the ones at high voltage. In particular, the '4_post' systems has a lower MI and a lower II, with respect to the '4_pre', which can be connected to the reduction in the number of available paths for the electrical current.

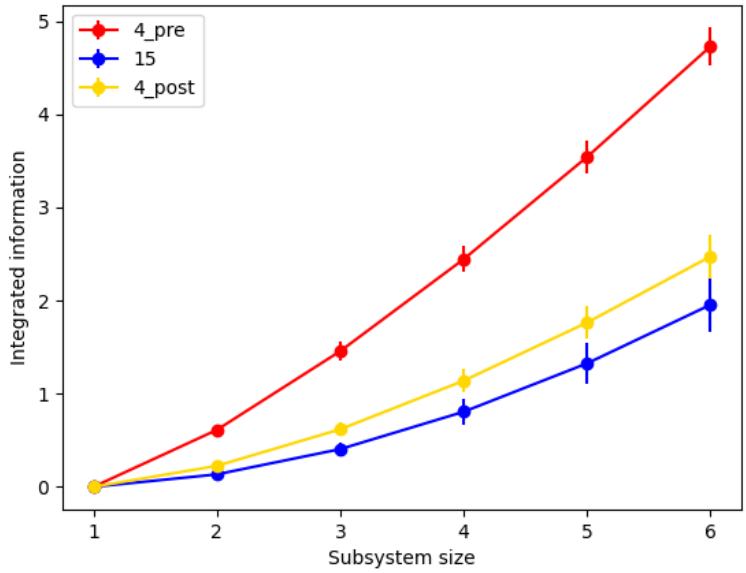

FIGURE 3.27: Integrated information as a function of the subsystem size for $s = 4$ and $(L'_x, L'_y) = (3, 2)$. II values are averaged over 9 independent simulations.

- all the quantities plotted grow as a function of the subsystem size. In the case of MI this means that a knowledge of a larger portion of the system automatically yields a greater knowledge on the rest of the system. On the other hand, as forecast by the theory, II grows as a function of the subsystem size as well. For instance, 4 pixels will be, on averaged, more integrated among themeselves than 2 pixels (which can be much more easily uncorrelated).

- the reported trends are remarkably similar to those discussed in [62], where neural complexity of the human brain is schematically examined. In Fig. 3.28 are reported the simulated II (left) and MI (right) values for primary visual areas, calculated for different patterns of intergroup connections. Remarkably, the trend of this two quantities as a function of subsystem size closely resembles our simulated data. This is noticeable, because our coarse–grained systems are very simple, in principle, and not explicitly programmed for displaying such a behavior.

  From the data presented in Fig. 3.27 it is possible to estimate the neural complexity of the network. In particular, starting from II, it coincides with the area comprised between the II curve and a straight line connecting the first and the last point (see the left panel of Fig. 3.28).

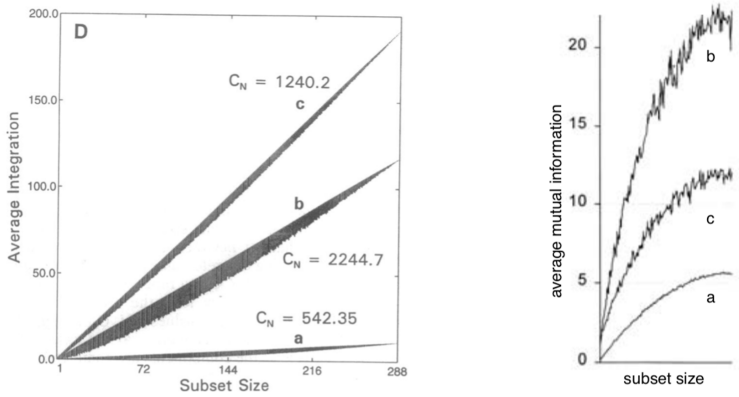

FIGURE 3.28: Left: average integration and complexity C_N (shaded area) from simulations of a primary visual area, calculated for different patterns of intergroup connections (a, b, c), reprinted from [61]. Right: analysis of simulations of a primary visual cortical area, via mutual information, for three cases (a, b, c) with different connectivity, reprinted from [64]

We analyzed the '4_pre' and the '4_post' phases, concluding that their respective neural complexities were influenced absence/presence by the conditioning stage. Importantly, different writing configurations generate different effects in the MI and II curves, which turn into different neural complexities. Moreover, the post-writing phases data seem to be characterized by a larger complexity, with respect to the the pre-writing. This information must not be retained as being fundamental, due to the arbitrary nature of the random initial configuration. As already mentioned, it is rather crucial to verify that a different writing setup would in general yield different properties in the subsequent low-voltage phase. Conversely, preliminary data we are presently analyzing, taken at 1 Volt, seem to suggest instead that the post-writing stage features a systematically larger neural complexity, which in turn corresponds to a system with preferential pathways for the current and nontrivial inner correlations.

These observation could, in principle, depend on the peculiar initial conditions, such as the initial configuration of the edges conductances. To rule out this hypothesis, we verified with dedicated simulations that changes in the initial state only affect the first part of the '4_pre' phase, which is essentially needed to equilibrate the system. Another interesting test consisted in adding other two phases to the simulation, namely a second conditioning

phase ('15_bis') and a third phase at low voltage ('4_post_bis'). Interestingly, the behavior of the CG network during these two additional stages of the MC simulation remained similar to the previous ones, thus strengthening the validity of our results: the key factor that introduces a novelty in network properties is the first encoding (conditioning) phase.

The possible study for a coarse–grained matrix with a much larger number of pixels is still to be performed, due to the fact that it is computationally intensive and we got aware that this task can not easily completed by NetworkX in a reasonable time. For example, computing II for a subsystem size equal to l requires the determination of all the possible combinations of l elements, the calculation of the entropy of the whole subsystem and the calculation of the entropy of the single pixels (to this extent, the Python `itertools.combinations` tool greatly helps); these operations need to be repeated for each configuration which contributes to the finale average and could take days. One important future improvement to SRNM will be the development of analysis tools in a compiled programming language, in order to perform all the analysis just described on systems with a higher number of CG pixels.

A final remark about electrical current: I values were analyzed in a very similar way, by applying constraints on their averaged pixel values $\bar{I}_p$, and repeating all the investigation described in this subsection. We observed that a probability distribution for $\overline{I_p}$ can be built, but the II and MI computed do not distinguish between '4_pre' and '4_post' as neatly as the same quantities based on $\overline{\sigma_p}$ distribution do. However, the number of distinct current states of the CG systems, for $s = 2, 3, 4$ are of the same order of magnitude of the ones based on conductance. The other noticeable point is that the current–based integrated information and mutual information, computed as a function of the subsystem size considered, turn out to be sensible to the applied voltage (but not much, as already mentioned, to the previous history of the system).

3.4.5 Logic gates

In this last subsection, the aim is to introduce a theme that will be intensively developed after the conclusion of this PhD Thesis, in my research group. During my PhD research activity, I started exploring the possibilty of using these Au nanostructured films (modeled as resistor networks) as logic gates, i.e. elements that can be used in physical realizations of neuromorphic computing, as largely discussed in the Introduction of this Chapter. Experimentally, our collaborators begin to have evidence that Au nanostructured films can effectively be used as logic gates (see e.g. Fig. 3.6).

Concerning the simulations, instead, the simple idea is to find a suitable arrangement of the links near the source and the sink nodes, in order to make them mimic open and close switches of Fig. 3.5. Our network does not

explicitly include switches that can be opened or closed, but let us consider the group of 27 links which connect node 0 with the first column of the first layer: a configuration with $N_b = 2$ separate 'bits' could be obtained by assigning a conductance equal to 10^{-10} $1/\Omega$ to the 7 central links, thus creating two separated groups of 10 links. We established that, if all the links in a group are set to maximum conductance, this corresponds to a bit equal to '1' in that input channel; conversely, turning off all the 10 links in the group is approximately equivalent to opening an input gate in the experimental system (which essentially means to stop the current passage in that region, which we named a '0' state. With this particular configuration, we retrieve a situation quite close to the experimental arrangement. Similarly, we could mimic 3 input bits by creating two groups of 3 links (connecting input node and first column) which are always turned off, which separate three groups of 7 links each which can take the conductances corresponding to bits '0' and '1', as described above. The choice of the numbers of links which contribute to the input gates is arbitrary and we believe that it does not qualitatively affect the output of the simulations. In our simulations, the conductances of the $0j$ edges maintained their value for all the duration of the run. In the following, only the results concerning the simulations with $N_b = 2$ are shown, because their analysis was also completed.

The insertion of a complex nonlinear element such the operational amplifier present in the experiments (see Fig. 3.5) in our network is not feasible. However, to be as close as possible to the experimental situations, in these simulations we opted for setting $\sigma_{ij} = 0.04$ $1/\Omega$ for all the links ij belonging to the last column of the first layer: this makes the last column substantially identical to a wire which allows the largest possible current flow. The links connecting last column with sink node ($i\,(N_\mathrm{n} - 1)$ edges) are always subdivided in two groups of 10 links each (which are always kept at the highest conductance level), separated by a region of 7 'turned off' links. Clearly, the output configuration in the experiments is much more complicated than in our SRNM (due to the presence of the operational amplifier). Moreover, out code does not output a voltage, which is a fixed parameter for the simulations, but an effective total resistance. Therefore, a first rough analysis can be done by looking at R_tot, but is not a variable for which it would be reasonable to set a threshold and binarize the output.

A solution for this problem consists in subdividing the resistor network in regions (the CG pixels of the previous subsection), assigning an average resistance to that region and use these values for feeding an analytical model of a simple circuit which should mimic the Au nanostructured film. We conceived a small circuit, made by 7 resistors, which is exactly solvable (sketched in Fig. 3.29); this circuit also contains an operational amplifier, and its output voltage is therefore directly comparable with the experimental measurements.

Therefore, the aim of the simulations previously described was to provide

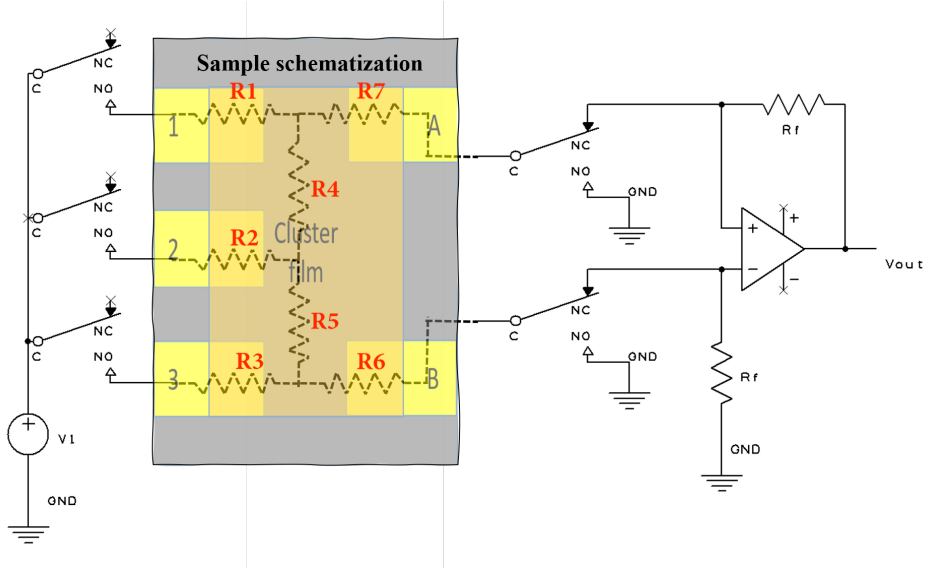

FIGURE 3.29: Sketch of the schematization of the Au nanostructured film as an analytically solvable model of 7 resistances ($R1 \dots R7$ in the picture). Courtesy of dr. M. Mirigliano

a set of 7 coarse–grained resistances, to be substituted into the $R1 \dots R7$ resistances which made up the circuit in Fig. 3.29. Each of these values was obtained by time–averaging (at equilibrium) the spatially coarse–grained value of the resistance. The spatial coarse–graining procedure was identical to the one detailed in the previous subsection about Information Theory analysis of our simulations. The optimal CG configuration was identified in a network subdivided in 7 pixels, with a first column of 3 pixels on the left that carries information about the region connected to the input channels, while the other 4 pixels, divided in a 2×2 rectangle, contain information about the rest of the system. The output voltage V_{out} of this exactly solvable circuit, built with coarse–grained resistances coming from simulations, was compared with the input applied voltage, in order to test whether the writing phase introduced any differences in the output voltage read from the op. amp. during the two reading phases. This analysis, for each input signal, was repeated on 10 independent simulations, aiming to collect significant statistics.

For all the results shown in the following, the simulation protocol consisted of:

1. low applied voltage (1 V or 4 V, we tested both) phase ('first reading'). 2000 equilibration steps + 1000 steps for measurements. 2 input channels with one of the possible input combinations: 00, 01, 10, 11.

2. 'writing' phase at 15 V, 2000 equilibration steps + 1000 steps for measurements. Note that the specific input signal adopted during the writing stage can, in general, be different from the one used during the two reading phases.

3. low applied voltage (1 V or 4 V, we tested both) phase ('second reading'). 2000 equilibration steps + 1000 steps for measurements. Here some differences with the first reading stage should arise, despite having the same combinations of inputs.

It turned out that it was necessary to perform an equilibration after each ΔV_{tot} change, before beginning to measure, because there are trends in observables which must not be included in the calculation of equilibrium CG resistances. Note that the specific input signal adopted during the two reading phases can, in general, be different from the one used during the writing stage: for example, one can read having a '01' as input signal and write having a '11' as input signal.

The analysis about these data is preliminary, but it is promising: with 2 bits, we were able to qualitatively reproduce what happens in the experiments, i.e relevant differences were detected between the first and the second reading phases. When referring to all zero inputs, clearly there is no current passing through the gates in the experiment and, at the same time, the network in the simulation is broken immediately after the input node (and thus it is not simulated). Fig. 3.30 shows the results of the analysis for all the independent simulations we performed. For them all, comparing the output voltage during the reading stages before and after the writing phase evidences differences. In particular, the logic NAND gate can be easily retrieved (in more than the 90% of the simulations); in fact, naming '0' the output bit when $|V_{out}^{\text{pre}}| > |V_{out}^{\text{post}}|$ and '1' when $|V_{out}^{\text{pre}}| \leq |V_{out}^{\text{post}}|$, we have that a 00 input $\rightarrow$ in output generates a logical '1' ($|V_{out}^{\text{pre}}| = |V_{out}^{\text{post}}|$). For any other input, in almost all the simulations, $|V_{out}^{\text{pre}}| > |V_{out}^{\text{post}}|$ and the corresponding output is '0'. The errorbars shown in the picture were obtained via error propagation, starting from the errors computed within the simulations on the single coarse–grained resistances. This is a very clear and important proof of concept, because NAND is a universal logic gate: any boolean function can be implemented by using a combination of NAND gates. This property is called functional completeness and it represent a crucial element for building devices capable of performing computations.

We also investigated the behavior of the simulations with '1_pre', '15' and '1_post' phases (being all the other parameters kept fixed); the results, having 2 bits as input, are qualitatively similar to the previously analyzed runs and variations well beyond the errorbars in the output voltage were registered.

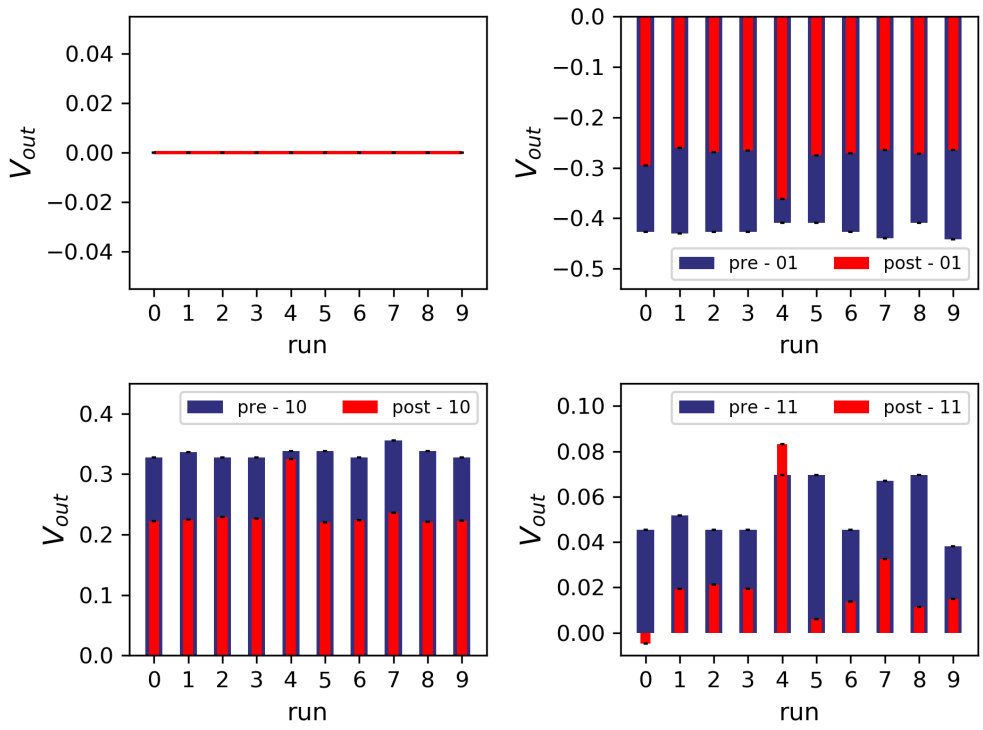

FIGURE 3.30: Comparison between the V_{out} in the first ('pre', blue) and second ('post',red) reading phases, from the analytically solvable circuit with 7 coarse–grained resistances. From top lef to bottom right, the inputs 00, 01, 10 and 11 are examined, for all the 10 simulations performed. Errorbars are in black.

As already mentioned, in this Thesis only the $N_b = 2$ case is discussed. The analogous runs with $N_b = 3$ are in program; a higher number of input bits clearly corresponds to configurations closer to real-world applications. The importance of the results shown in this section resides in the proof of concept about the possibility of exploiting this devices as logic gates, without explicitly programming them (which is the main limitation, for instance, evidenced in the interesting article of Chen *et al.* [29]).

3.5 Conclusions and further perspectives

In this Chapter I have described the experimental realization of nanostructured gold films, characterized by spontaneous assembly of deposited clusters, realized by the group of prof. P. Milani, at the CIMaINa labs at the Università degli Studi di Milano. These nanoscale devices represent a promising

and innovative approach to the vast field of neuromorphic computing. We have supported the experiments with a tailored abstract model of a resistor network, stochastically evolved in time via a Monte Carlo code, capable of catching the essential details of the real sample. Resistive switching phenomena which characterize the experimentally measured resistance as a function of time were retrieved in simulations. The associated noise was analyzed via the study of the Power Spectral Density. Detailed investigations about the network topology and its inner structure, about the paths followed by the electrical current were performed, identifying interesting ways to separate the behavior of the system before and after a high–voltage encoding phase. Moreover, in the attempt to unveil the origin of RS phenomena, we observed a dramatic change in the spatial distribution of electrical currents in the network in correspondence of resistive switching events. Due to the fact that these synthetic devices are loosely brain–inspired, with a structure resembling the interconnected architecture of neurons and spiking synapses, we adopted tools typical of Information Theory, analyzing entropy–based observables. A coarse–grained reduction of the original network evidenced the emergence of remarkable differences in the network state after the conditioning phase, i.e. a detectable memory effect. The last stage of this work was represented by the first attempts to probe the possible usage of these devices as logic gates in hardware computing applications.

This last topic is worth to be further developed; in particular, we have the goal to systematically delve deeper into the comprehension of the reasons behind the efficiency of the experimental samples in realizing logic gates. An analysis of the simulated network concerning its efficiency in generating rich outputs (i.e. its ability as a reservoir) is on schedule. Moreover, it would also be useful to extensively use an approach based on Information Theory concepts and observables, in particular on data from simulations with logical bits in input. This would strengthen also the comparison between the devices we are investigating and developing and the essential features of probabilistic spiking units, loosely inspired to neurons (but very similar to traditional logic gates). The novelty (and the ambition) of this work mainly resides in the innovative hardware used to realize logic gates with an arbitrary number of input channels.

In all this work, the usage of HPC resources proved fundamental, especially through the usage of CINECA supercomputing facilities, via the *IscraC–RENNA* (2019) and *IscraB-PANDA* (2020) projects. We also thank INDACO supercomputing structure (Università degli Studi di Milano) for the usage ot their resources, in particular through the CRYSTALGROWTH project (2019).

Bibliography

[1] D. Marković, A. Mizrahi, D. Querlioz, and J. Grollier. Physics for neuromorphic computing, 2020.

[2] D. Verstraeten, B. Schrauwen, and D. Stroobandt. Reservoir Computing with Stochastic Bitstream Neurons. In *Proceedings of the 16th Annual ProRISC Workshop*, pages 454–459, 2005.

[3] D. Verstraeten, B. Schrauwen, M. D'Haene, and D. Stroobandt. An experimental unification of reservoir computing methods. *Neural Networks*, 20(3):391–403, 2007.

[4] A. V. Avizienis, H. O. Sillin, C. Martin-Olmos, H. H. Shieh, M. Aono, A. Z. Stieg, and J. K. Gimzewski. Neuromorphic atomic switch networks. *PLoS ONE*, 7(8):e42772, 2012.

[5] H. O. Sillin, R. Aguilera, H. H. Shieh, A. V. Avizienis, M. Aono, A. Z. Stieg, and J. K. Gimzewski. A theoretical and experimental study of neuromorphic atomic switch networks for reservoir computing. *Nanotechnology*, 24(38), 2013.

[6] M. Mirigliano, D. Decastri, A. Pullia, D. Dellasega, A. Casu, A. Falqui, and P. Milani. Complex electrical spiking activity in resistive switching nanostructured Au two-terminal devices. *Nanotechnology*, 31(23), 2020.

[7] F. Rosenblatt. The perceptron: A probabilistic model for information storage and organization in the brain. *Psychological Review*, 65(6):386–408, 1958.

[8] K. Hornik. Approximation capabilities of multilayer feedforward networks. *Neural Networks*, 4(2):251–257, jan 1991.

[9] D. Kuzum, S. Yu, and H. S. Philip Wong. Synaptic electronics: Materials, devices and applications, 2013.

[10] E. Chicca, F. Stefanini, C. Bartolozzi, and G. Indiveri. Neuromorphic electronic circuits for building autonomous cognitive systems. *Proceedings of the IEEE*, 102(9):1367–1388, 2014.

[11] L. O. Chua. Memristor—The Missing Circuit Element. *IEEE Transactions on Circuit Theory*, 18(5):507–519, 1971.

[12] F. Alibart, E. Zamanidoost, and D. B. Strukov. Pattern classification by memristive crossbar circuits using ex situ and in situ training. *Nature Communications*, 4(May):1–7, 2013.

[13] L. Chen, C. Li, T. Huang, H. G. Ahmad, and Y. Chen. A phenomenological memristor model for short-term/long-term memory. *Physics Letters, Section A: General, Atomic and Solid State Physics*, 378(40):2924–2930, 2014.

[14] Z. Wang, H. Wu, G. W. Burr, C. S. Hwang, K. L. Wang, Q. Xia, and J. J. Yang. Resistive switching materials for information processing, 2020.

[15] S. Ambrogio, P. Narayanan, H. Tsai, R. M. Shelby, I. Boybat, C. Di Nolfo, S. Sidler, M. Giordano, M. Bodini, N. C.P. Farinha, B. Killeen, C. Cheng, Y. Jaoudi, and G. W. Burr. Equivalent-accuracy accelerated neural-network training using analogue memory. *Nature*, 558(7708):60–67, 2018.

[16] I. Boybat, M. Le Gallo, S. R. Nandakumar, T. Moraitis, T. Parnell, T. Tuma, B. Rajendran, Y. Leblebici, A. Sebastian, and E. Eleftheriou. Neuromorphic computing with multi-memristive synapses. *Nature Communications*, 9(1):2514, 2018.

[17] J. Borghetti, G. S. Snider, P. J. Kuekes, J. J. Yang, D. R. Stewart, and R. S. Williams. Memristive switches enable stateful logic operations via material implication. *Nature*, 464(7290):873–876, 2010.

[18] A. Adamatzky. Unconventional computing. *International Journal of General Systems*, 43, 2014.

[19] D. Ielmini and H. S. P. Wong. In-memory computing with resistive switching devices. *Nature Electronics*, 1(6):333–343, 2018.

[20] Q. Xia and J. J. Yang. Memristive crossbar arrays for brain-inspired computing. *Nature Materials*, 18(4):309–323, 2019.

[21] P. Bak and M. Paczuski. Complexity, contingency, and criticality. *PNAS*, 92(15):6689–6696, jul 1995.

[22] D. Stauffer and A. Aharony. *Introduction To Percolation Theory*. Taylor & Francis, dec 2018.

[23] S. Fostner and S. A. Brown. Neuromorphic behavior in percolating nanoparticle films. *Physical Review E*, 92:52134, 2015.

[24] D. H. Ackley, G. E. Hinton, and T. J. Sejnowski. A learning algorithm for boltzmann machines. *Cognitive Science*, 9(1):147–169, jan 1985.

[25] M. Ernoult, J. Grollier, and D. Querlioz. Using Memristors for Robust Local Learning of Hardware Restricted Boltzmann Machines. *Scientific Reports*, 9(1):1851, 2019.

[26] S. K. Bose, S. Shirai, J. B. Mallinson, and S. A. Brown. Synaptic dynamics in complex self-assembled nanoparticle networks. *Faraday Discussions*, 213:471–485, 2019.

[27] G. Tanaka, T. Yamane, J. B. Héroux, R. Nakane, N. Kanazawa, S. Takeda, H. Numata, D. Nakano, and A. Hirose. Recent advances in physical reservoir computing: A review. *Neural Networks*, 115:100–123, 2019.

[28] J. F. Miller and K. Downing. Evolution in materio: Looking beyond the silicon box. In *Proceedings - NASA/DoD Conference on Evolvable Hardware, EH*, volume 2002-Janua, pages 167–176. Institute of Electrical and Electronics Engineers Inc., 2002.

[29] T. Chen, J. van Gelder, B. van de Ven, S. V. Amitonov, B. de Wilde, H. C. Ruiz Euler, H. Broersma, P. A. Bobbert, F. A. Zwanenburg, and W. G. van der Wiel. Classification with a disordered dopant-atom network in silicon. *Nature*, 577(7790):341–345, 2020.

[30] S. K. Bose, C. P. Lawrence, Z. Liu, K. S. Makarenko, R. M.J. Van Damme, H. J. Broersma, and W. G. Van Der Wiel. Evolution of a designless nanoparticle network into reconfigurable Boolean logic. *Nature Nanotechnology*, 10(12):1048–1052, 2015.

[31] H. G. Manning, F. Niosi, C. G. da Rocha, A. T. Bellew, C. O'Callaghan, S. Biswas, P. F. Flowers, B. J. Wiley, J. D. Holmes, M. S. Ferreira, and J. J. Boland. Emergence of winner-takes-all connectivity paths in random nanowire networks. *Nature Communications*, 9(1):1–9, 2018.

[32] F. Borghi, M. Mirigliano, P. Milani, and A. Podestà. Quantitative Analysis of Gold Nano-aggregates by Combining Electron and Probe Microscopy Techniques. In *Toward a Science Campus in Milan*, pages 67–80. Springer International Publishing, 2018.

[33] C. Minnai, M. Mirigliano, S. A. Brown, and P. Milani. The nanocoherer: An electrically and mechanically resettable resistive switching device based on gold clusters assembled on paper. *Nano Futures*, 2(1):011002, 2018.

[34] M. Mirigliano, F. Borghi, A. Podestà, A. Antidormi, L. Colombo, and P. Milani. Non-ohmic behavior and resistive switching of Au cluster-assembled films beyond the percolation threshold. *Nanoscale Advances*, 1(8):3119–3130, 2019.

[35] W. Xiao and I. Gutman. Resistance distance and Laplacian spectrum. *Theoretical Chemistry Accounts*, 110(4):284–289, 2003.

[36] N. K. Vishnoi. Lx = b Laplacian solvers and their algorithmic applications. *Foundations and Trends in Theoretical Computer Science*, 8(1-2):1–141, 2012.

[37] N. Rubido, C. Grebogi, and M. S. Baptista. General analytical solutions for DC/AC circuit-network analysis. *The European Physical Journal - Special Topics*, 226:1829–1844 (2017), 2017.

[38] M. Mahoney. Lecture: Modeling graphs with electrical networks, 2017.

[39] R. Quinlan. Spectral Graph Theory MA500-1: Lecture Notes Semester 1 2016-2017, 2017.

[40] M. Kagan. On equivalent resistance of electrical circuits. *American Journal of Physics*, 83(1):53–63, 2015.

[41] A. Dresden. The fourteenth western meeting of the american mathematical society. In *Bulletin of the American Mathematical Society*, volume 26, pages 385–396, 1920.

[42] R. Penrose. A generalized inverse for matrices. *Mathematical Proceedings of the Cambridge Philosophical Society*, 51(3):406–413, 1955.

[43] A. Berman. Generalized Inverses of Linear Transformations. *SIAM Review*, 23(4):545–546, 1981.

[44] N. Pedrani. *Modellizzazione e simulazione di trasporto elettrico in nanostrutture*. Bachelor thesis, Università degli Studi di Milano, 2019.

[45] C. Sanderson and R. Curtin. Armadillo: a template-based C++ library for linear algebra. *The Journal of Open Source Software*, 1(2):26, 2016.

[46] C. Sanderson and R. Curtin. *Mathematical Software – ICMS 2018*, volume 10931. 2018.

[47] S. Engelberg. *Random Signals and Noise - A Mathematical Introduction*. Press, CRC, 2008.

[48] D. K. C. MacDonald. *Noise and Fluctuations - An Introduction*. Dover, 2006.

[49] W. C. Van Etten. *Introduction to Random Signals and Noise*. 2006.

[50] M. S. Bartlett. Periodogram Analysis and Continuous Spectra. *Biometrika*, 37(1/2):1, 1950.

[51] P. D. Welch. The Use of Fast Fourier Transform for the Estimation of Power Spectra. *Digital Signal Processing*, (2):532–574, 1975.

[52] https://docs.scipy.org/doc/scipy/reference/generated/scipy.signal.welch.html.

[53] J. W. Cooley and J. W. Tukey. An algorithm for the machine calculation of complex Fourier series. *Mathematics of Computation*, 19(90):297–297, 1965.

[54] A. Diaz-Alvarez, R. Higuchi, P. Sanz-Leon, I. Marcus, Y. Shingaya, A. Z. Stieg, J. K. Gimzewski, Z. Kuncic, and T. Nakayama. Emergent dynamics of neuromorphic nanowire networks. *Scientific Reports*, 9(1):1–13, 2019.

[55] O. Sporns. Theoretical Neuroanatomy: Relating Anatomical and Functional Connectivity in Graphs and Cortical Connection Matrices. *Cerebral Cortex*, 10(2):127–141, 2000.

[56] D. Poli, V. P. Pastore, and P. Massobrio. Functional connectivity in in vitro neuronal assemblies. *Frontiers in Neural Circuits*, 9:1–14, 2015.

[57] M. W. Cho and M. Y. Choi. Brain networks: Graph theoretical analysis and development models. *International Journal of Imaging Systems and Technology*, 20(2):108–116, 2010.

[58] E. W. Dijkstra. A note on two problems in connexion with graphs. *Numerische Mathematik*, 1(1):269–271, 1959.

[59] R. Bellman. On a routing problem. *Quarterly of Applied Mathematics*, 16(1):87–90, 1958.

[60] L. R. Jr Ford. Network Flow Theory. Technical report, Defense Documentation Center for Scientific and Techinical Information, Cameron Station, Alexandria, Viriginia, 1956.

[61] G. Tononi, O. Sporns, and G. M. Edelman. A measure for brain complexity: Relating functional segregation and integration in the nervous system. *PNAS*, 91(11):5033–5037, 1994.

[62] G. Tononi, G.M. Edelman, and O. Sporns. Complexity and coherency: integrating information in the brain. *Trends in Cognitive Science*, 2(12):474–484, 1998.

[63] N. M. Timme and C. Lapish. A tutorial for information theory in neuroscience. *eNeuro*, 5(3), 2018.

[64] G.M. Edelman and G. Tononi. *A Universe of Consciousness*, volume 66. Basic Books, 2001.

Chapter 4

Phase diagram and structural properties of trivalent DNA nanostars

This Chapter concerns a part of my research activity which is not yet completed; nonetheless, since the development of the model and of the code took a considerable fraction of time during my PhD, I opted for the insertion of these contents in this thesis. Moreover, the description of the experiments (conducted by the group of from the University of Milan led by prof. T. Bellini and in collaboration with dr. G. Nava) involved in this project is merely functional to provide a motivation for my work. A real comparison between experimental and simulated results has not been possible yet, and it will be the subject of future research activity about this topic.

4.1 Low valence systems

Atomic systems, in general, feature a crystalline ground state: spherosymmetrical inter–particle interactions, at low temperature, usually produce an ordered state with long–range periodicity. In such cases, particles do not have a limited number of possible bonds, and the interplay between energy and entropy always favors low energy ordered states as the temperature T is decreased [1]. Conversely, colloidal particles with limited *valence*, i.e. with a low number of attractive sites on their surface (some examples are reported in Fig. 4.1), naturally set an upper threshold for the number of bonds built, and these anisotropic interactions generate peculiar structures [1–5]. These objects can be either synthesized in laboratory with tailored properties or already exist in nature (we refer for example to complex biological molecules): they can be described by isotropic effective potentials only as a zero-th order approximation [4].

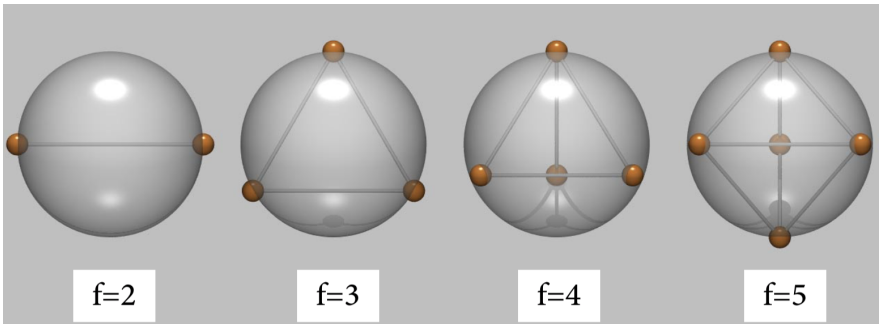

FIGURE 4.1: Schematic representation of the location of the square–well interaction sites (centers of the small spheres) on the surface of the hard–core particle, being valence $f \in [2, 5]$. Reprinted from [2]

These colloids are called *patchy particles*, and they are essentially hard–core (less frequently, soft–core) spheres decorated by a few sticky spots on their surface [2]. The capability of assembling such molecules in a laboratory

(see, e.g., Refs. 1-5 in [2]), provided with specific and strongly directional interactions, has recently introduced the possibility not only to reproduce molecular systems on the nano and micro scale, but also to detect and investigate novel collective behaviors. In particular, these objects display *self–assemble* capability, i.e. they spontaneously aggregate into *clusters* and form some kind of order resulting from the competition between enthalpic and entropic factors, without external controlling tools. Self–assembly is also something that can happen in atomic systems, but colloids turn out to be much easier to inspect due to their larger size [4].

A number of theoretical studies focused on the temperature–density (T, ρ) phase diagram of such particles, in particular concerning the gas–liquid phase separation region and its dependence on the particles' valence f [1–3, 5]. Moreover, also clustering and gelation of these systems were accurately studied, via Monte Carlo simulations and Wertheim thermodynamic perturbation theory [6] both. As already mentioned, a key element in this analysis is represented by the number of (usually square–well) attractive patches which decorate the surface of such colloids. Bianchi *et al.* [3] showed that the relative position of the sticky spots is almost irrelevant, for the most important physical properties of these systems. Nonetheless, on the one hand it seems that a regular position of the patches on the surface enhances the formation of bonds and networks; on the other hand, they also noted that the theoretical predictions for the critical point location in the phase diagram are closer to the geometric case model rather than the random one. As a consequence, in general people works with patchy particles whose patches have a symmetric geometric distribution on the surface (e.g., for $f = 3$, the sticky spots are located on an equator and evenly spaced on the vertexes of an equilateral triangle inscribed in the circumference), and we adopted as well this convention for the present work. Fig. 4.1 shows the chosen arrangement of the patches on the surface for valence between 2 and 5.

In their first study, Bianchi *et al.* [2] initially concentrated on a system of hard–spheres whose surface was provided by a small number f of attractive sites and they identified f as the key ingredient controlling the location of the critical point. Monte Carlo simulations generated the location of the critical point in the temperature–density plane (in the original paper the packing fraction ϕ is used instead of the density), which turns out to be strongly dependent on f. Wertheim theory complemented the analysis of the simulations, and both approaches signaled a tendency of the critical point to move towards smaller T and ϕ values upon decreasing f (and a shrinking of the coexistence region, as a consequence, as shown in Fig. 4.2 for $f \in [3, 5]$).

Therefore, the authors hypothesized that it should be possible to realize, even in an experiment, equilibrium liquid states at a temperature lower than the gas–liquid critical one, with arbitrary small packing fraction (density), referred to as *empty liquids*. For tetrahedral patchy colloids, for example,

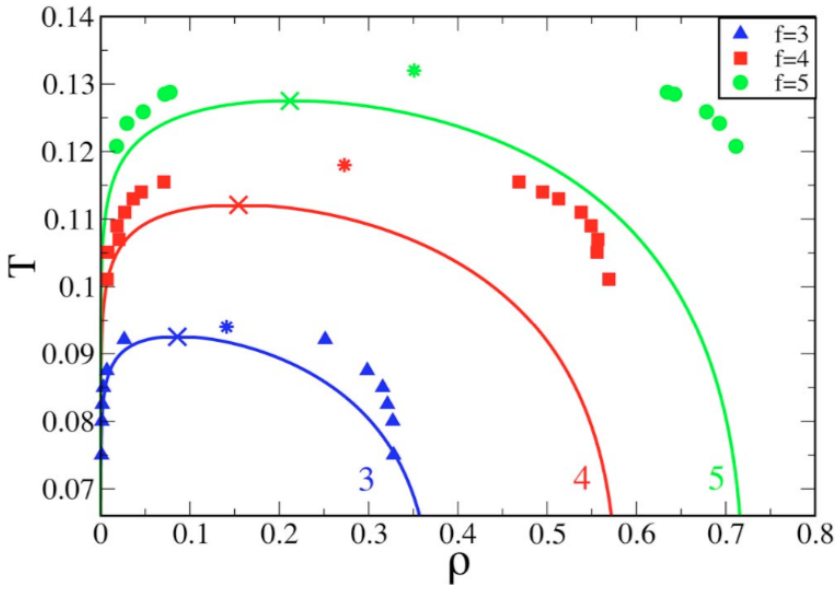

FIGURE 4.2: Gas-liquid coexistence regions in the (T, ρ) plane on varying f from 3 to 5. Reprinted from [3]

the typical volume fraction occupied by particles in the empty liquid state is approximatively 25–30%, as compared to the $\sim 60\%$ packing in simple liquids [7]. In such a state, the colloids are interconnected, and the system is found in an equilibrium disordered configuration: an homogeneous disordered material is obtained, where the bond lifetime is comparable with the experimental observation time, and then the network persists in time [3]. In that article, the authors suggested that, at low T and ϕ, it should be possible to approach dynamically arrested states continuously from equilibrium and to generate a real material as close as possible to an *ideal gel* (see e.g. Fig. 4.3). This is a surprising new possibility, clearly not even conceivable with particles interacting via spherosymmetrical potentials, with a crystalline fundamental state. They also underlined that their predictions are relevant to a large class of functionalized particles (e.g. Janus particles, nanocolloidal polyhedra, rods, ...), provided that they attract each other only through a limited number of sites. From this computational and theoretical investigation it emerges the centrality of particle valence for building collective structures with a peculiar geometry. We remark that all the previous discussion is supported by the *single-bond-per-patch* hypothesis, which is also explicitly present in the Wertheim theoretical framework as a fundamental condition: when a patch is engaged in a bond with another one, no other sticky spot can be further

involved in the bond. As evidenced in a recent review about patchy particles simulation methods, the single-bond-per-patch condition is essential to control the valence [8].

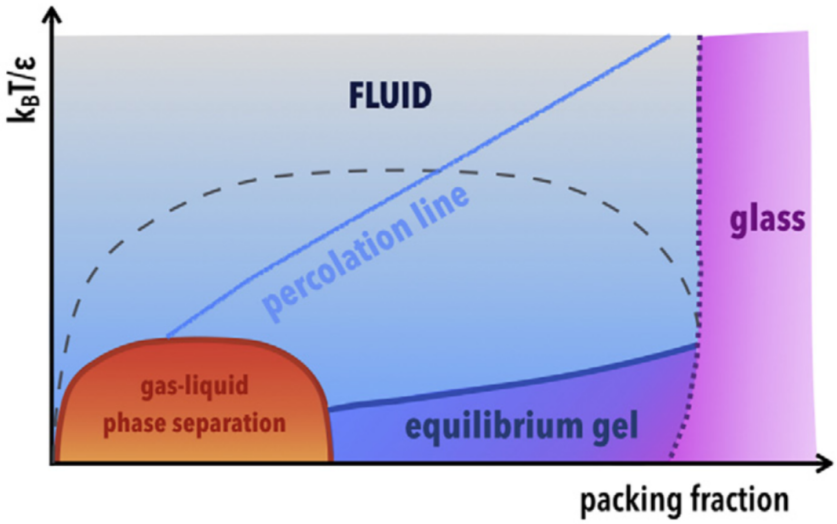

FIGURE 4.3: Schematic phase diagram of limited valence particles. Note the 'equilibrium gel' region at low temperature and relatively small packing fraction. Reprinted from [7]

Rovigatti *et al.* [1] remarked that the full–bonded states described a few lines above are thermodynamically stable and, in these cases, present a lower free energy with respect to the ordered crystal. Noticeably, in limited valence systems, the network phase has a potential energy very close to the one of the crystal and can thus compete with it even at low temperature. Once the system is in its fully bonded disordered state, a further decrease of T has only a small effect on its dynamics. The number of bonds and the network topology shall not change much upon further lowering of the temperature. In the picture of Rovigatti and co–workers, this new state is constructed through the progressive onset of all possible bonds, avoiding either a more stable crystal phase or a phase separation. In their view, a key element is found to be the bond flexibility: having the same energy, the crystal and the network state compete regarding entropy. In this sense, the configurational entropy is smaller in the crystal, and an increased bond flexibility should make it overwhelm the vibrational entropy (typically larger in the crystal) [1, 9]. Sciortino *et al.*[7] emphasized that equilibrium limited valence gels are peculiar, considered that they do not coarsen neither age with time, differently from conventional colloidal gels. In the end, limited valence is a fundamental requisite to generate open stable equilibrium phases at low temperature.

In this framework, the *DNA nanostars* (NS) - nanoparticles entirely made of DNA, structured with an inner core and a small number of arms terminated by sticky ends - constitute a promising innovation, being flexible enough to represent the first laboratory example of a liquid more stable than a crystal, in the soft matter field [1, 10]. A brief introduction to DNA nanotechnology is then the first natural step to better understand the importance of this relatively recent research area.

4.2 DNA nanostars

In the last decades, DNA has acquired an increasing relevance as a building block in materials science applications [11]. Double helix DNA is an object with a typical nanometer length scale: its diameter is about 2 nm and the basis–basis separation is ≈ 0.34 nm. In nanotechnology, DNA constructs are presently considered as very powerful and interesting options, in order to assemble more complex structures whose 'bricks' are DNA polymers [4, 7, 10, 12]. In this sense, DNA is characterized by some properties which make it a powerful tool to explore fundamental phenomena of soft matter and statistical physics. Thanks to the sophisticated control on the base–pairing mechanism, in fact, DNA nanoparticles and DNA origami of complex shape and binding ability have been conceived and experimentally realized, providing an alphabet of building blocks which can be properly combined to assemble new materials with desired properties. For example, Bellini and co–workers showed that it is possible to build up f–valent DNA constructs, called nanostars due to their core-and-arms shape, which are able to bind with other constructs simply by mutually connecting their open ends [10, 12, 13].

In fact, in their experiments, each NS arm is terminated by a *CGATCG* self-complementary sequence, which promotes nanostar–nanostar bonding via Watson-Crick pairing. These nanostars mimic molecules with controlled limited valence f which, due to their directional interactions, are key in the realization of new colloidal materials with possibly unconventional phase behaviors, as discussed in the first section of this Chapter. Fig. 4.4 shows an example of a DNA trimer and a DNA tetramer; each nanostar is composed by exactly f single filaments, which form double helices with unpaired (open) overhangs. Bellini and co–workers realize these nanometer–sized objects by dissolving in water equimolar quantities of f distinct 49–base–long oligonucleotides, whose sequence for a $f = 3$ case is reported in Fig. 4.5.

Concerning the inner structure of the NS, in Fig. 4.5 it is remarked by a black circle the presence of two adenine bases located at the center of each filament; this is fundamental for the rotational degrees of freedom of the nanostar arms, creating at the same time a inner excluded volume. One

FIGURE 4.4: Cartoon of a 3–valent and a 4–valent DNA nanostar. Reprinted from [10]

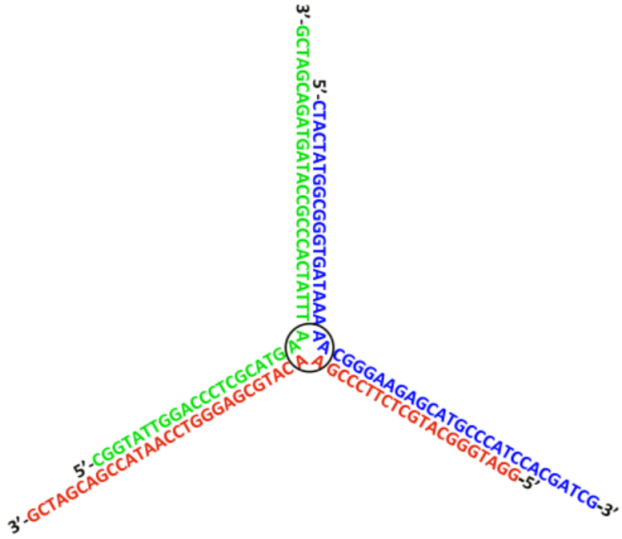

FIGURE 4.5: Scheme of the nucleotides building up a trivalent DNA nanostar. Reprinted from [10]

additional *A* base has been added immediately before the terminating sequence *CGATCG* in each arm, in order to favor a further rotational degree of freedom to the two arms involved in a link. These adenine bases located

at fixed positions constitute rigid points around which 3D rotations can be performed. By construction, given that each arm contains 49 nucleotides, if we eliminate 6 nucleotides belonging to the sticky end, 1 adenine bases that is found immediately before the overhang and 2 adenine bases in the middle, there are two 20–nucleotides long segments left. Two segments of such length belonging to different NS can join and form a mutually exclusive bond via their sticky terminations. As a consequence, each nanostar is involved in up to f links made by double strands of 20 nucleotides each; further details are provided for example in [10, 12]. The particular direction of the helix winding determines whether a DNA NS possesses a left–handed (LH) or right–handed (RH) *chirality*. In nature, DNA only exists as a right–handed helix; left–handed DNA can be artificially synthesized (and it is sometimes referred to as Z-DNA). Importantly, only nanostars with the same chirality can have a reciprocal attractive interaction; the interspecies potential is instead repulsive, i.e. LH and RH nanostars are not allowed to form shared bonds. They only repel each other due to mutually excluded volume.

Regardless of the chirality, the behavior of these DNA constructs strongly depends on temperature: as evidenced by Fig. 4.6, according to the temperature of the solution, the DNA can pass from a gaseous single–stranded phase to the formation of a full–bonded network at lower temperatures.

Let $T_{sa} \sim 65$ °C be the temperature over which DNA only exists in single strands; for $T \sim T_{sa}$ the single strands begin to hybridize and this leads to the self–assemble of NS with valence f. If T_b represents the higher temperature which allows for the formation of links among different nanostars (binding temperature), for temperatures between T_b and T_{sa} we have a diluted system of isolated nanostars. As it is depicted in Fig. 4.6, for $T \lesssim T_b \sim 42$ °C, single NS start to bond together by connecting two single–stranded arms and form higher order geometrical arrangements. This observation implies that at this temperature the attractive energy term is well-balanced with the thermal energy of the system. Upon further decreasing T below T_b, the DNA nanostars aggregates grow in size, forming larger and larger clusters; in particular, as it is explained in the next section 4.3 it was shown that for both $f = 3$ and $f = 4$, these anisotropic colloids are capable of generating networks, with a very small packing fraction [10, 12]. In such networks, the majority of inter–particle links are effectively stable, with slow inner rearrangements of the global structure, as suggested e.g. by Nava *et al.* [13]. We therefore have an experimental realization of a dynamically arrested system, essentially a gel as described in the introductory part of this Chapter. It is important to highlight again that this happens only because these colloidal nanoparticles have asymmetrical potentials, and this aids the formation of complex structures when they bind together. Note that, in these experiments, the binding force between sticky overhangs is tuned in such a way that it is stronger than

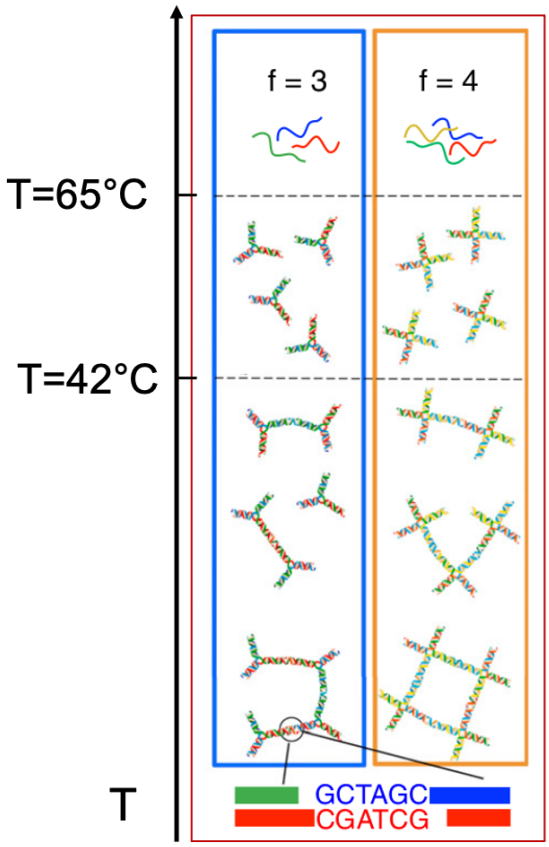

FIGURE 4.6: DNA trimers and tetramers form geometrical arrangements, depending on the sample temperature. Adapted from [10]

all other interparticle interactions (excluded volume, van der Waals, electrostatic), thus making DNA NS an optimal model for highlighting the role of the valence in such samples. In general, DNA structures have turned out to be unique particles for investigating the phase behavior of systems in which it is possible to carefully tune binding selectivity (via the DNA sequence), strength of interaction (via the DNA length), and valence [4, 10].

4.3 The experiments

The first study performed by the group of prof. Bellini concerned the equilibrium properties of $f = 3, 4$ DNA nanostars, whose major findings were reported in the paper by Biffi *et al.* [10]. These results will be detailed in the next subsection 4.3.1, but the most important feature that emerged was that

these objects displayed a critical curve in the (T, ρ) plane (see Fig. 4.7), below which the system experienced phase separation. The two phases involved were, essentially, a DNA–rich one and a DNA–poor one.

Successively, they exploited the aforementioned fact that the well–defined chirality of these molecules prevents a left–handed DNA NS from bonding with a right–handed one. Our experimental collaborators cleverly leveraged this property, inquiring about the consequences of mixing in the same sample a fraction of LH and a fraction of RH DNA nanostars, both in critical conditions, aiming to test whether the critical behavior persisted (this last experimental campaign is still in progress). These bi–component systems are referred to as *mixtures*, in the remainder of the Chapter, while mono–component ones are termed *pure*. Here, the fundamental question to address is how the structures and the properties of the pure system are affected by the insertion of a second species, where the reciprocal interaction is only a repulsion due to the excluded volume. This is a unprecedented idea, both for the question in itself and for the possibility to investigate about that in a suitable experimental framework. Note that, in the last 10 years, some works focused on mixtures of nanostars with different values of f [14, 15], but this is - to our knowledge - the first study concerning mixtures of elements with opposite chirality.

As explained in [10, 16], the experimental measurements reported in the following are essentially based on fluorescence microscopy, in particular confocal microscopy. This allows to reconstruct 3D sample images, which are also much neater than traditional microscopy. The two components of the mixtures were identified based upon fluorescent markers. The details of the preparation of experimental samples are not reported here, but a note concerning the role of the salt in the water (solvent) is important. The role of the salt in the solution consists in screening the electrostatic interactions and its concentration is thus a key element for these systems. In fact, the DNA filaments are negatively charged; as a consequence, they repel each other. A higher salt concentration has a higher screening effect and raises the importance of the other interactions. The negative filament charges become less important and the DNA–DNA interactions related to bases pairing become more and more relevant at higher temperatures. This clearly simplifies the experimental procedure, stabilizing the interactions among DNA nanostars; the more recent study on trivalent NS by De Chiara [16] uses a salt concentration of 200 mM and, as a consequence, the critical temperature (see Fig. 4.7) moves from about 10 °C (for Biffi *et al.* [10] the salt fraction was only 23 mM) to about 25 °C.

4.3.1 Equilibrium measurements

Biffi *et al.*[10] completed the first systematic equilibrium measurements on DNA NS samples, determining the phase diagrams of nanostars with 3 and 4 sticky terminals for small DNA concentrations in water and salt solutions ($x-$axis in the picture). The main results of their experiments and analyses are reported in Fig. 4.7 (which was adapted with respect to the original one).

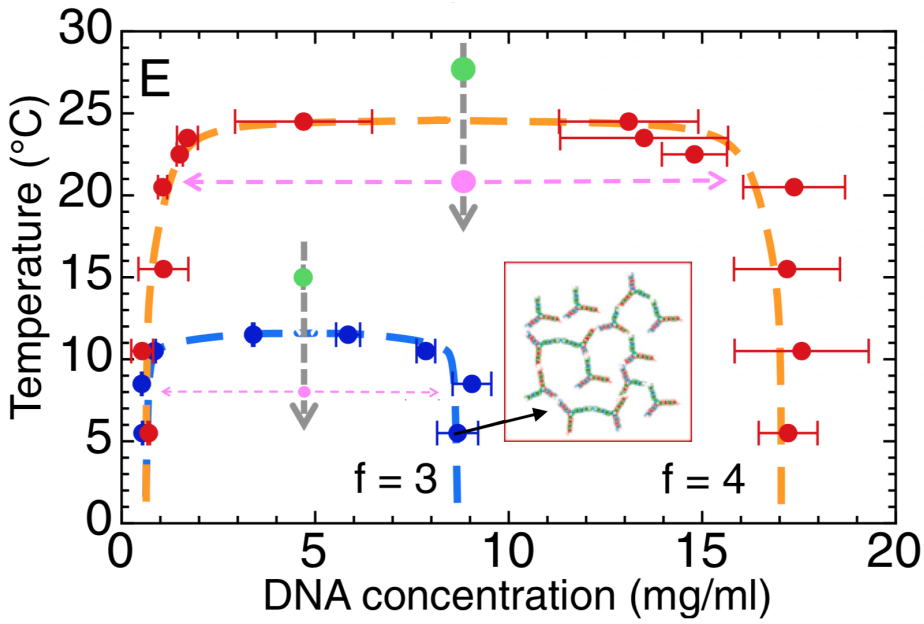

FIGURE 4.7: Phase behavior of DNA nanostars with valence $f = 3$ and $f = 4$. Grey lines indicate the quench, while magenta lines indicate the spinodal decomposition process. Image adapted from [10]

The authors, for each DNA concentration examined, executed a isochoric quench process (grey arrows) from a high temperature down to a low one (e.g. from green to pink circle in the picture). This procedure allowed them to identify a consolution curve, drawn in Fig. 4.7 as a dashed line obtained as a fit of the experimental data for $f = 3$ (blue) and $f = 4$ (orange). In the region above each consolution curve, the NS form a disordered system of independent particles, which may occasionally also form aggregates. Below that curve, the sample was observed to phase–separate in DNA–rich and DNA–poor subregions (marked by the ends of the magenta arrows). In fact, when the DNA concentration is small (e.g 1 mg/mL), the DNA nanostars do not occupy all the space, and their volume fraction is extremely low. Conversely, at higher DNA concentrations (for example, to a solute concentration

≈ 8.5 mg/mL for the $f = 3$ system) the NS form aggregates which fill the majority of the available volume and generate liquid networks with low packing fraction. For DNA concentrations lying at the right of the consolution curve (e.g 10 mg/ml for $f = 3$), the system is a full–bonded network (an example is sketched inside Fig. 4.3) as the one forecast by the theoretical models for low valence systems described in the introductory part of this Chapter. Blue and orange dashed lines represent than *spinodal lines* corresponding to phase coexistence, which separate two different regimes. The experimentally determined consolution curve necessarily terminates, at high T, in a critical point (T_c, c_c) corresponding to the divergence of DNA concentration fluctuations. Experimentally, this has been studied for example via the scattering intensity $I(q)$ dependence on the scattered wavevector q in the critical region.

Obviously, Biffi *et al.* could not inspect the ground state of the system (due to the accessible temperature range and due to the entropy cost of such a state), but only study the NS network, which does not have a regular structure. However, in the Supplementary Information of Ref.[10], they hypothesized a simple model for the ground state of these systems, assuming that the NS are arranged in a regular lattice. From a theoretical point of view, concerning $f = 4$ nanostars, at low temperatures they are supposed to be ordered in a diamond–like lattice (see left half of Fig. 4.8). Clearly, this ground state is intrinsically highly degenerate, because any bond swap that preserves the diamond structure is allowed and corresponds to a configuration with the same energy. Experimental data analysis suggests that the distance between the centers of bonded nanostars is ≈ 17 nm, which corresponds to the length obtained when the arms joined in a bond and the duplex formed by the paired overhangs are all perfectly straight and aligned in a line [10, 12]. Such a network would have a density of 0.22 mM, corresponding to a DNA concentration of 13.3 mg/mL. From now on, we are only going to deal with trimers; in this case, we lack an obvious lattice to refer to. However, the diamond lattice can be modified and adapted to trimers by replacing every $f = 4$ nanostar with two $f = 3$ NS connected through one bond; our experimental collaborators speculated that the ground state of our system is a crystalline *z–stretched diamond lattice*. As evidenced in the right half of Fig. 4.8, when two trimers bond, they are supposed to form an elongated structure in a sort of generalization of what happens for tetramers[10].

If we call $L = L_x = L_y$ the size of x and y sides of the unit diamond cell, the z side is $L_z = L \times \dfrac{3\sqrt{3}}{2}$ long, while the nearest neighbor distance along z is $L \times \frac{\sqrt{3}}{4}$. Considering again the center–to–center distance for bonded trivalent NS, we obtain that such a crystal would have a density of 16 mM, corresponding to a DNA concentration of 7.3 mg/mL. Importantly, this is a lower

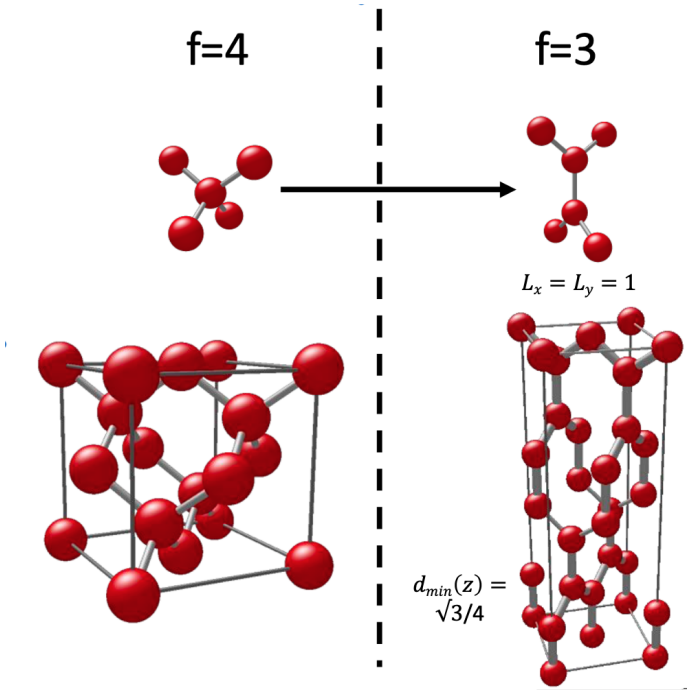

FIGURE 4.8: Scheme of the unit cell of the modified diamond lattice. Courtesy of dr. G. Nava

bound estimation, because any bending or fluctuation of the bonded nanostar arms reduces their distance and thus increases the effective concentration (and in fact the experimental measurements yield slightly larger densities for the full–bonded phases). Obviously, such considerations are merely theoretical and are only loosely related with the experimentally observed structures, due to the extremely low temperatures (at the right fixed density) that would be required to find such configurations.

It is important to note that experimental data match theoretical predictions such as the one of Fig. 4.2, which forecast a significant shrink of the unstable region in the temperature—concentration plane, with critical temperature T_c and critical concentration c_c decreasing and approaching zero as the valence of the colloids is reduced: in fact the $f = 3$ NS have a noticeably smaller coexistence region with respect to $f = 4$ NS.

The presence of such a consolution curve holds for pure LH and pure RH systems both. When the two species with different chirality are mixed, and rapidly quenched from a high–T state towards a low–T one, under weak electrostatic screening provided by the solvent, they were observed starting a quick demixing process but it is not clear how their behavior is related to the original phase diagrams. One of the main goals of my research activity in this field was to study via simulations the effects of the interpenetration

among elements of the two species.

For the sake of completeness, next subsection addresses the topic of the cluster formation process and the spinodal decomposition dynamics which are not directly faced in this Chapter but provide the reader with a complete overview of the experimental achievements.

4.3.2 Spinodal decomposition dynamics

A second set of experimental measurements concerned the observation of the early stages of the spinodal decomposition in a bi–gel sample, i.e. in a sample with 50% of type–A nanostars and 50% of type B and both components found at critical density, thus generating a total density which is two times the critical one. A preliminary observation via fluorescent markers of such a mixture is reported in Fig. 4.9, where the two colors correspond to the volumes occupied by LH and RH nanostars.

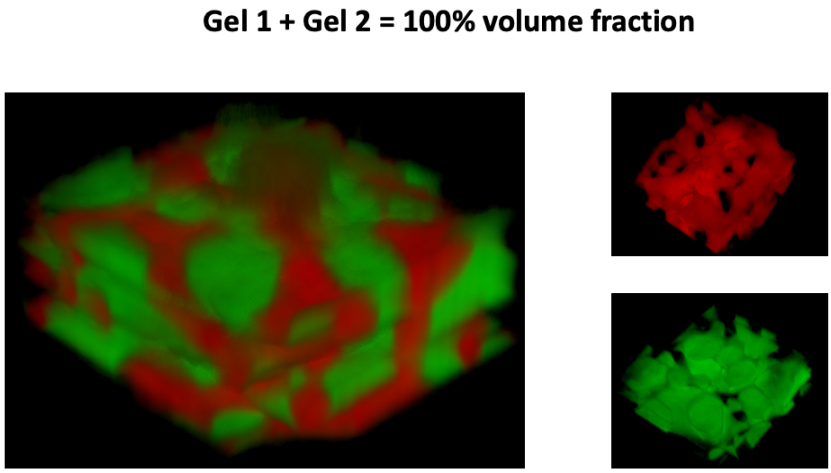

FIGURE 4.9: Experimental observation of the spinodal decomposition in a sample where the two gels occupy all the available volume. Courtesy of G. Nava and T. Bellini

In the example reported, the spinodal decomposition process was still in progress; important experimental measurements on schedule regard the determination of the average cluster size growth in time. An hypothesis of our experimental collaborators (to be tested with computer simulations) is that, at the very beginning, the shape and inner structure of each cluster experience some rearrangements before allowing for an effective growth and coalescence. These rearrangement processes are nontrivial and in general depend on a subtle balance between the surface tension of the cluster and the

viscoelasticity of the gel. In the Conclusions of this Chapter, we hypothesize a computational method for supporting experiments also in the study of the early clusterization stages.

4.4 Theoretical model

The remarkable properties of DNA NS encouraged us to try to characterize via computer simulations the equilibrium properties of networks of DNA trimers. In particular, aiming to compare equilibrium measurements with simulated results, we performed classical Monte Carlo simulations (with Metropolis algorithm) in order to investigate for the first time the phase diagram of $f = 3$ DNA NS binary mixtures. We underline here that this choice is particularly interesting because, before the pioneer investigation of Biffi *et al.* [10], such systems were essentially unexplored. Besides, $f = 3$ is the minimum valence necessary to obtain a gel, and this makes this system interesting also from a theoretical point of view. Other recent articles address with a different computational approach the study of $f = 4$ DNA nanostars [12, 15, 17].

Following some recent papers [17], we opted for a simplified description of a DNA nanostar, without explicitly accounting for the atomic structure of DNA. A different approach would have resorted to a coarse–grained model of DNA, for example based on the popular oxDNA software [18]. Instead, aiming to reduce the computational cost and with the goal of a general description of limited valence systems, we decided to model a single DNA trimer as a *soft–core patchy particle*. An equatorial (maximum diameter) section of a typical soft patchy particle with effective radius r_n is schematized in Fig. 4.10.

Each particle has a central r_{hc}–sized *hard–core* region (green in the picture) which prevents particles from completely overlapping, which would be nonphysical. A concentric larger (blue) sphere surrounds the inner core, characterized by a *soft–core* repulsion with radius r_{sc}: the soft potential allows for partial overlapping between two or more patchy particles. This is a simple way to reflect the flexibility of the nanostars arms, aided by the adenine bases: the centers of the NS can be closer than the respective effective radius, because of the rotational degrees of freedom. On an equator of a sphere of radius $r_{hc} + r_p$ are placed $f = 3$ attractive spheres of radius r_p, the *patches*, mimicking the sticky tips of DNA nanostars. The patches represent in an abstract way the valence sites; DNA nanostars are characterized by overhangs which occupy a much lower volume portion, but here each spherical patch represents an effective ideal volume spanned by DNA NS terminations during their fluctuations. We underline here that the sticky ends are the same for all the NS arms, which is well represented by the fact that all the patches are equivalent. The details of the rest of the arm (i.e. the nucleotides involved in the double helix) are not relevant here. Concerning the relations among

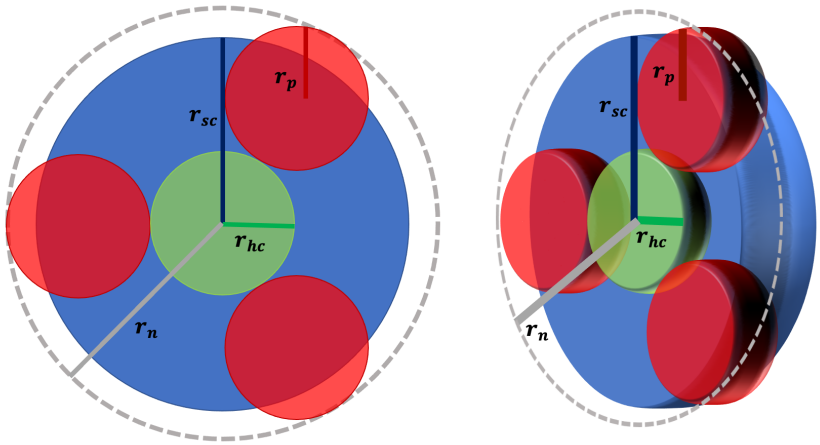

FIGURE 4.10: Left: planar equatorial section of a trivalent soft patchy particle. Right: the corresponding rotated view of a 3D equatorial section. The patches and the inner core are drawn transparent for a better comprehension.

r_p, r_{hc} and r_s, we decided to keep $r_{sc} > r_{hc} + r_p$ in order to better reproduce the expected peaks of the modified diamond structure in the radial pair distribution function. This arrangement leaves less than half a patchy sphere to emerge from the soft–core region; we noticed, during some test simulations, that the condition $r_{sc} = r_{hc} + r_p$ (i.e. with the patches centers lying on the external boundary of the blue sphere in Fig. 4.10) did not allow to retrieve the expected diamond–like structure at low temperature. Moreover, a reasonable choice was to set $r_{hc} = r_p$. From now on, let us introduce the following notation: $\sigma_{hc} = 2\,r_{hc}, \sigma_{sc} = 2\,r_{sc}, \sigma_p = 2\,r_p$ for the respective diameters.

With the goal of keeping the model simple, all the aforementioned interactions are included in the code as step potentials, independent of distances. In particular, the potential energy $V_{ij} = V_{ij}^{\text{rep}} + V_{ij}^{\text{attr}}$ for a given nanostar pair (i, j) interaction reads:

$$V_{ij}^{\text{rep}} = \begin{cases} +\infty & \text{if } r \leq \sigma_{hc} \\ +\epsilon_{sc} & \text{if } \sigma_{hc} \leq r \leq \sigma_{sc} \end{cases} \tag{4.1}$$

for the hard–core and soft–core repulsive terms, with r as the distance between the centers of two patchy particles. The patch–patch interaction term for patchy particles of the same type is modeled as an attractive square well, being r_{kl} the distance between the centers of two patches labeled by k and l

indexes, belonging to i and j particles, respectively:

$$V_{ij}^{\text{attr}} = \sum_{k=0}^{2}{}' \sum_{l=0}^{2}{}' V_{ij}^{kl,\text{attr}} = \sum_{k=0}^{2}{}' \sum_{l=0}^{2}{}' - \epsilon_p \qquad \text{if } r_{kl} \leq \sigma_p \tag{4.2}$$

while it vanishes for particles belonging to different species and for patches belonging to particles already sharing a link (so to delete the energy gain coming from a further bond formation, aiming to rule out double or triple shared links). In these cases, only the repulsive term V_{ij}^{rep} is present. The $'$ apex in the sum symbols recalls the presence of boundary conditions on the interactions (single bond per patch, only pairs of free patches can form new bonds, and others that will be discussed in the next section) which limit the effective number of potential energy amounts contributions. Each energy term can be conveniently expressed in units of the patch–patch energy, $|\epsilon_p|$. We remark also that the effects of the interaction potentials are additive, and then that in general - when the patchy particles interact - there is an interplay between the cores overlap cost and from the bonded patches energy gain. In this concern, the total potential energy of the system reads as:

$$E = \sum_{i=0}^{N-2} \sum_{j=i+1}^{N-1} \left(V_{ij}^{\text{rep}} + \sum_{k=0}^{2}{}' \sum_{l=0}^{2}{}' V_{ij}^{kl,\text{attr}} \right) \tag{4.3}$$

We observe that the inner hard–core term is meant to model the excluded volume: DNA nanostars can not fully compenetrate one with each other. The soft–core external region, instead, takes into account the vast empty space left by these nanoparticles when they aggregate and form network–like structures. There is in fact a huge degree of freedom in this sense, and two nanostars are allowed to form a bond and get quite close.

In Fig. 4.11 are depicted the step potentials chosen for our model; quantities on y axis are in reduced units, while distances on x axis are expressed in nanometers (their exact values will be clarified in a few lines). Note that d is the distance along an axis connecting the centers of the two particles, being their patches placed in symmetrical positions with respect to a common reference frame whose x axis is exactly the straight line connecting the centers of the particles (see the inset for a graphical view).

Obviously, the real interaction energy of the system is much more complicated than the simple sum of pairwise step potentials we have employed. For example, as detailed in the article by Spinozzi *et al.* [12], it depends on temperature; our simplified description only works as an effective picture which comprises many different contributions. As already mentioned, there is also the possibility of a totally different approach, consisting in a coarse–grained atomic description of DNA–DNA interaction based on the oxDNA model [18]; many simulation articles used this approach [1, 15, 17], which

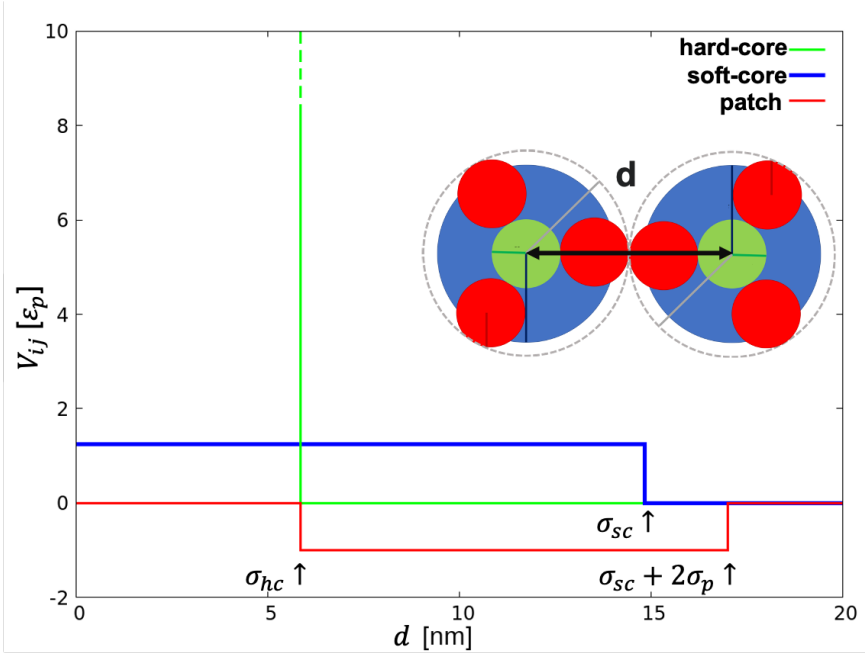

FIGURE 4.11: Representation of the three potential energy contributions for the $f = 3$ soft patchy particles model developed. These contributions to the potential energy are referred to the situation where the distance d is measured along a straight line connecting the centers of two particles and, at the same time, connecting the centers of two patches.

is on the contrary limited by the small number of DNA nanostars that can be studied and by the fact that the result found are quite specific and not easily extendible to other systems. Our idealized model has been refined after many different attempts, and it was not obvious *a priori* which was the best geometrical arrangement in order to develop a suitable model for Monte Carlo simulations and for a fair comparison with experimental data. Our choices were subjected to some boundary conditions, but we believe that our patchy particle model is flexible and general enough to be representative for a large class of systems. Other patchy particles models were used in previous works, but we introduced the peculiar feature that our colloids are soft–core objects, differently from those used for example by Bianchi *et al.* [3], De Las Heras *et al.* [14] and Rovigatti *et al.* [8]. On the other hand, we share with those models the fact that, when two patchy particles are already linked by a bond, no other bonds can form within that particle pair (no double or triple shared bonds). This can be obtained either by substituting the soft–core region with a hard–core one, or explicitly prohibiting the formation of double shared links. Our model presents a hard–core inner region, surrounded by

an external soft core representing a finite overlapping probability, aiming to maintain the peculiarity of soft–core interactions in the Hamiltonian. Therefore, in the simulations described in this Chapter, only free patches pairs can become part of new links.

Concerning the numerical values used in this work, here follows a list of the exact values of the quantities of the model chosen, derived from a comparison with experimental data. As already mentioned, lengths are expressed in nanometers, while energies are expressed as ratios with respect to a reference energy (the patch-patch potential energy term). We assume that $k_B = 1$, and so also temperatures are expressed as T^*, in units of $|\epsilon_p|$. Typical reduced temperature values are of the order of 0.1, because a rough experimental estimation yields patch-patch interaction energies 10 or 20 times larger than k_BT.

- $r_p = 2.85$ nm. This was derived from a comparison with the experimental estimation of the NS diameter, similar to the calculations described in [12] for tetramers.
- $r_{sc} = 7.4$ nm. This value guarantees the formation of the modified diamond lattice at zero temperature, with a typical inter–particle distance almost identical to the theoretical one.
- $r_{hc} = 2.85$ nm. r_{hc} was set equal to r_p for convenience. It must be large enough to prevent full particle overlap and can be varied in a relatively wide range.
- ϵ_p: sets the reference for the energies in the system.
- $\epsilon_{sc}/\epsilon_p = 1.25$. This was accurately chosen after many test simulations. It was a tradeoff between the target of having a soft–core potential ($\epsilon_{hc} \gg \epsilon_{sc} \gtrsim \epsilon_p$) and the need of adding a reasonable energy cost for overlapping colloids (so $\epsilon_{sc} \geq \epsilon_p$).
- $\epsilon_{hc}/\epsilon_p = 10000$, but it can be any value such that $\epsilon_{hc} \gg \epsilon_p$ and $\epsilon_{hc} \gg \epsilon_{sc}$

Note that, as a consequence of the previous choices, the patches lie on a circumference of radius $r_p + r_{hc} = 5.7$ nm, centered in the particle center. Besides, r_n=r_{hc} + 2r_p=8.55 nm; this is a sort of effective patchy particle radius, referred to the dashed grey circumference in Fig. 4.10.

4.5 Development of the code

Here follows the description of the structure of the program I have developed during part of my PhD activity for the simulation of DNA nanostars modeled via soft–core patchy particles and $f = 3$.

4.5.1 Overall structure of the code

The main program is a `C++` code with MPI parallelization, very similar to the one described in the previous Chapter for 1D soft particles. Also here, each of the n_{MPI} MPI ranks, for each block of s_b MC steps, works on a subset of $s_r = n_{MPI}/s_b$ steps. The contributions from each rank are combined to form unique block averages; this assumes that the system is at equilibrium in each rank and so the sampled configurations are equivalent and comparable. Obviously, the main difference with the scheme represented in Fig. 2.3 is that, for each step s the following operations are performed:

- trial single–particle moves (translation, rotation, switch)
- update of the list of particles belonging to each cluster → trial cluster moves (translation, rotation, reshape)
- measure $O(s)$
- accumulate $O|_r = \dfrac{\sum_{s=1}^{s_r} O(s)}{s_r}$
- periodic print of configuration and clusters list

where the details of the single–particle and cluster moves are provided in the following. All the rest of the code structure is essentially identical to what explained in Chapter 2.

4.5.2 Input and setup

Before effectively performing the MC simulation, the initial system configuration is generated via a external Python script which replicates the unit diamond cell into the 3D space. The majority of the simulations described in section 4.6 have been run in a box made of $4 \times 4 \times 2$ unit cells, where each unit cells contains 16 patchy particles, i.e. 16 cores and 48 patches (N=512 particles in total). The script takes the unit cell and replicates it along x, y, z for the specified number of lattice steps, at the given density. The patches of each nanostar are placed onto the vertices of an equilateral triangle, at distance $r_p + r_{hc} = 5.7$ nm from the center. The script deals with systems with any relative concentration x_A of particles of type A. This configuration is read by the program, and placed in a 3D simulation box with PBC. Given that the simulation box is not a perfect cube, PBC along each axis are different. A typical modified diamond simulation box filled of patchy particles with $f = 3$ appears like the one in Fig. 4.12; straight red lines evidence the modified diamond structure described also by Biffi *et al.* [10].

The `C++` code, uses structs of type `particle`, containing information about each particle coordinates, the status of the three patches (free/bonded

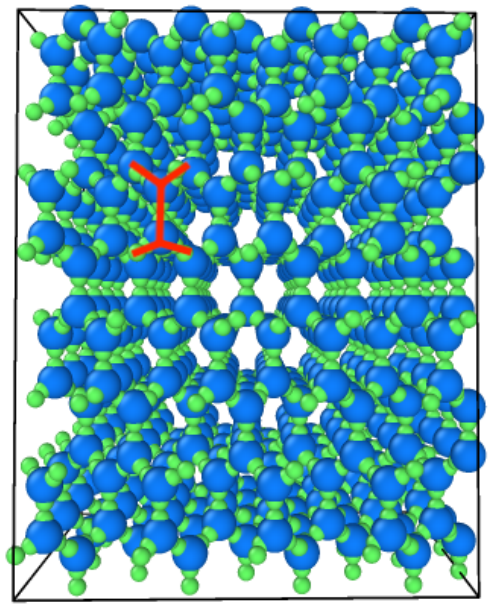

FIGURE 4.12: Modified diamond simulation box, N =512 trivalent patchy particles. Realized with OVITO [19]

and the identity of their neighbors), particle type (corresponding to the DNA nanostar being LH or RH), particle index, index of the cluster the particle belongs to and particle cell index (see next paragraph about neighbor cells). After initial operations, concerning the reading of input parameters (temperature, density, box sides size, parameters for neighbor cells, initial configuration), and the measurement of the initial potential energy (that has contributions from core–core overlaps and from patch–patch interactions both), the first list of the clusters formed in the system is built via the `Build_clusters` method. We underline that this list is necessarily re–built before each cluster move, to guarantee that the following move is performed considering the updated clusters. There are several possible methods for building the list of the clusters present in the system. The algorithm implemented here is not necessarily the most efficient one, but has a transparent structure: chosen a particle, the cluster is progressively built starting from the other (from 0 to 3) particles linked to the one considered via a patch–patch bond. Iteratively, the procedure is repeated for these particles on their connected neighbors and so on. Obviously, clusters made of single–particles do exist but Monte Carlo cluster moves are only performed on larger clusters ($\geq$ 2 particles in

the cluster).

4.5.3 Equilibration/restart

Unless otherwise specified, the `run_equilibration` function initially simulates the system at high temperature (e.g. $T^* = 1$); this stage is followed by a second equilibration process at the target temperature of the simulation, which is longer for the simulations at lower temperature. The duration of these phases was the result of many test attempting to eliminate any possible drift in the observables measurements. The high temperature range starts from $T^* = 0.17$ for the pure and from $T^* = 0.19$ for the equimolar mixture. Each rank equilibrates its own configuration; during the equilibration phase, all the Monte Carlo update moves (described later) are executed.

After the equilibration, the effective simulation is performed in the canonical ensemble, with Metropolis acceptance criterion for MC moves. Data blocking averages are computed, configurations and clusters list are periodically printed during the simulation. At very low temperatures, it turned out that our simulation method was not able to bring the system towards a real equilibrium state; rather, several metastable states are visited by the system, which continues to decrease its energy without reaching a stable condition (similar to what analyzed e.g. in [17]). Therefore, for $T^* \lesssim 0.12$, data blocking can not be performed and our simulations do not converge.

4.5.4 Tricks for speedup: neighbor cells

The pair potential of the system (illustrated above) is short–ranged, in fact particles do not interact as long as they do not touch each other, at least. Aiming to reduce the computational cost of the interaction computation, we took the wise choice of dividing the simulation box in sub–cells (within the `setup_neighbor_lists` method), whose smallest side must be larger than $2\,r_n$. Each sub–cell shares at least one face with other 26 other sub–cells, in PBC; a patchy particle in a given sub–cell may in principle interact only with a subset of all the particles, i.e. precisely those belonging to the 26 neighboring cells of that sub–cell. If these sub–cells are small enough (but still larger than a patchy particle diameter), for each particle only a few possible interacting neighbors are considered, and this considerably speeds up the computations. After each move, the list of particles found in the sub–cells involved in the MC move is readily updated. Summarizing, each sub–cell has a fixed list of the indexes of the neighboring sub–cells; for each sub–cell, the particles found in that sub–cell are readily updated based upon the accepted MC moves.

4.5.5 The Monte Carlo steps

An effective and clever sampling of the configurational space is the core point of any Monte Carlo simulation, especially for a soft/condensed matter system experiencing a phase transition. In particular, it becomes very relevant to make smart MC moves when dealing with complex objects such as our patchy particles, characterized by (partially) non–spherical interactions. To this extent, here follows a brief description of the moves present in the program; this moves are proposed and accepted via Metropolis criterion based on the Boltzmann energy weight associated to the move. Some kind of MC moves have been inspired by [17], other were specifically designed for our system.

Ghost patchy particles

Before passing to the description of the update moves, a general remark is mandatory. Consider that, due to bond exclusivity of the bonds, when a bond is broken (after a generic MC move), it is possible that 'ghost' patches play a role. Suppose that patches α and β were linked and that β moves away, enough to break the link. If there is a third patch (that belongs to a trimer that was already there) γ with a distance from α $r_{\gamma,\alpha} < \sigma_p$, then α and γ form a new link with Boltzmann probability, computed via the `search_ghost` function included in the code.

A possible example of what a ghost link is effectively is sketched in Fig. 4.13a-4.13c for a two–dimensional case.

Throughout the code this is monitored and taken into account for all the possible situations; this can be extremely tricky, because there are lots of possible complicated configurations which involve the possible activation of ghost links. We decided that the priority is given to the new links formed by the particle being moved, for example particle i; the new mates of i can not be involved in the possible activation of ghost links with the old mates of i. Another thing to be careful about concerns the fact that patches involved in a ghost link during the current move can not, clearly, be used for the formation of other ghost links at the same time. Besides, also patches belonging to the particle being moved can activate ghost links (this is easy to imagine if one considers a single–particle rotation where only the position of the patches on the sphere surface changes). The energy associated to each ghost is accounted for as all the other contributions in the overall energy balance evaluated with the Metropolis criterion. We observe that this issue only arises, with the chosen patchy particle shape and geometry, due to the presence of a soft-core repulsive interaction (an hard core of radius r_{sc} would prohibit any superposition of three patches). Including such a move partly enhances the quality of the exploration of the configuration space by the code.

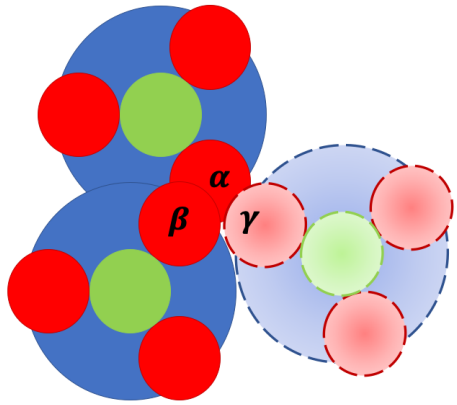

(a)

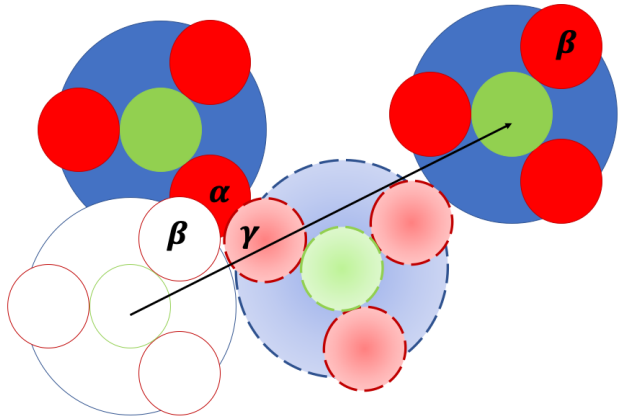

(b)

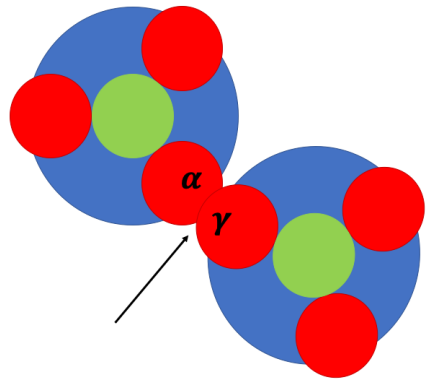

(c)

FIGURE 4.13: Stages of the formation of a new bond with a ghost patch.

The moves

- *Single particle translation* The simplest move concerns particle translations in a random direction in the 3D space. Three moves of this type are present in the current version of the code, respectively characterized by small ($< 10\%$), intermediate ($\approx 50\%$) and high ($> 80\%$) acceptance ratios. This is tuned by suitably regulating the maximum translation range along each axis, δ: the exact numerical values strongly depend on temperature, but δ_{small} is typically in the range of Å, $\delta_{\text{intermediate}}$ between 1 and 5 nm and δ_{high} runs from 5 to 100 nm (in the T^* ranges explored here). A new position for the chosen particle is proposed and accepted via Metropolis criterion, based on the potential energy before and after the move. To simplify calculations, only contributions coming from the selected particle are considered, beyond those due to possible new links formed due to the ghost particles; in fact the rest of the system is not affected by such a move and does not contribute to the energy difference caused by the trial move.

- *Single particle rotation* Single particles, regardless of the links they form, can perform a random 3D rotation around an axis passing through their center. If a particle is free, this move does not generate energy variations and it is accepted with probability 1. In the code, each rotation is performed in a new reference frame, where the center of the trimer is translated at the origin, the patches are rotated without PBC, and then all the coordinates are reverted back (in PBC) into the original system.

  Single particle moves are both performed N times for each MC step.

- *Switch links* As already explained for the formation of links with ghost patches, it can happen that two particles share a bond, and a third patch is placed within σ_p from at least one of the patches already bonded. To enhance the exploration of the configurational space, for all these cases it is proposed a switch of the links with probability 0.5, once for each MC step. In other words, if patches α and β were linked and $r_{\gamma\alpha} < \sigma_p$ (or $r_{\gamma\beta} < \sigma_p$) for a third patch γ, it is proposed a move that breaks the old link and form a new link between α and γ (or α and β), being $r_{\gamma\alpha}$ and $r_{\gamma\beta}$ the respective distances. This MC update move does not affect the energy, and it is accepted with a random uniform probability $\frac{1}{2}$.

- *Cluster translation* Once for each MC step, a cluster (i.e. a group of at least 2 bonded particles) is randomly chosen, and a rigid random translation in 3D PBC of its barycenter (and then of all its particles) is attempted. The barycenter here is calculated by only weighing the position of particles centers, without considering their asymmetry. Note

that this move does not change the relative particles positions, but other particles could join the cluster at the end (i.e. two or more clusters can merge and form a larger one). Typical cluster translation span a few nanometers (the largest the cluster, the more difficult for a configuration update to be accepted).

- *Cluster rotation* Once a step, it is attempted the random rotation of a cluster around a randomly chosen axis passing through a randomly chosen particle belonging to the selected cluster. Also here, we underline that the number of particles in the cluster at the end can be higher (or equal to) than at the beginning, because of possible merging of different clusters. In the code, the whole cluster is mapped into a new reference frame where the 'seed' particle for rotation is placed at the origin, it is rotated without PBC and then it is brought back into the box reference frame.

  One observation concerning cluster translation and rotation moves is that, if the cluster is too large, the move is rejected with probability 1 by construction. Consider, in fact, that a cluster whose extension (i.e. the distance in PBC between the two most distant particles) is larger or equal to half the smallest box side risks to be artificially split into two clusters, after the trial MC move, because of the PBC. The motivation behind this issue can be readily understood if one considers that clusters can be found, before attempting to rotate them, in a situation like the one sketched (in 2D) in Fig. 4.14:

  Referring to the picture, the two halves A and B of the initial (schematized in orange) cluster are connected. A rotation of a given angle around the point O (which is a particle belonging to the cluster chosen as the center for the rotation) can move the two halves up to new positions A' and B' which are not connected anymore. It can be shown that this only happens if the cluster size is larger than 0.5 times the shortest box side; a check for this is present in the code for both cluster translation and rotation, aiming to avoid to rotate potentially disconnected cluster halves.

- Cluster translation and rotation moves are both built to be highly efficient and the code is not provided with moves that can break a cluster in two or more smaller clusters in one step. At high temperatures, this is not a problem; at low temperatures, this could make the system not ergodic enough. This means that, once a cluster is formed, our code does not easily allow for the cluster to break apart: this would require many single–particle moves involving particles that detach from their original cluster (which implies an energy cost to be compensated). On the one hand, this can be a severe issue because the system is biased in

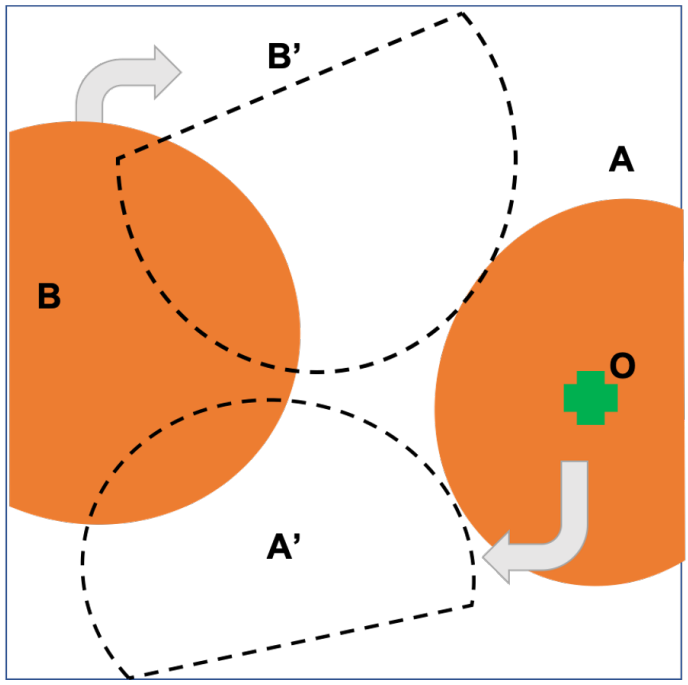

FIGURE 4.14: Example: a 2D cluster which has two halves connected in PBC that would be no more connected under some rotations or translations.

order to form clusters; on the other hand, this is exactly what the experimental samples do, at the right temperatures, and so, in our code, the formation of states corresponding to the cluster phase is enhanced.

- *Reshape cluster* Detaching a particle from a cluster is a move that usually increases the energy of the system, because of the broken link (increase the energy by ϵ_p) without being sure to form a new one at the end of the move, thus being only rarely accepted. Conversely, a move that guarantees that at least one link is maintained has a higher acceptance probability. Therefore, we introduced a function that randomly takes a nanostar in a cluster and moves it in a new position such that:

  1. the original link is replaced by a link with another free patch in the cluster
  2. the moved particle still belongs to the cluster

See also Fig. 4.15 for a 2D example of this move: a patchy particle member of a cluster changes its position with respect to all the other particles by moving into a new position such that at least one link is maintained.

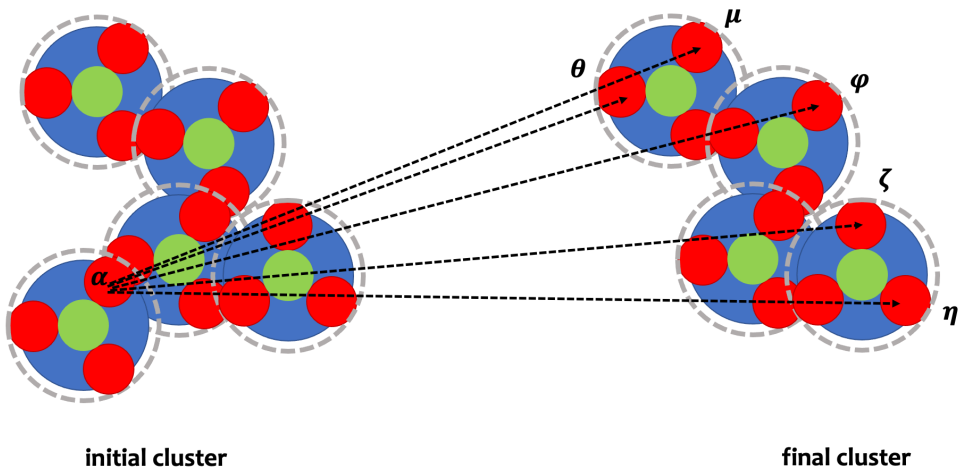

FIGURE 4.15: Example: a 'reshape cluster' move for a 2D case. The particle in the lower left of the cluster, linked to the rest of the cluster via patch α, is tentatively moved in one of the randomly chosen position corresponding to free patches $\theta, \mu, \phi, \zeta, \eta$

4.5.6 Measurements

Several observables were computed, accumulated and averaged, according to the scheme presented in Fig. 2.3. In particular, in order to retrieve structural information about the configurations generated, the code computes the radial distribution function and the static structure factor along the Cartesian axes. In particular, the $g(r)$ (whose general formula was introduced in Chapter 2) is calculated for:

- particle pairs, regardless of their type. This $g^{sc}(r)$ usually contains information about the overall order of the system.
- particle pairs of the same type, separating 'mixed' correlations: $g^{sc}_{AA}(r)$, $g^{sc}_{AB}(r)$, $g^{sc}_{BB}(r)$ (the apex ^{sc} stands for 'soft-core').
- patches pairs (i.e. where r is the distance between the centers of two patches), distinguishing also here $g^{p}_{AA}(r)$, $g^{p}_{AB}(r)$, $g^{p}_{BB}(r)$, with ^{p} indicating patches. In the calculation of these observables, the two patches belonging to the same particle of the patch considered are not taken into account (in order to ignore the considerable contribution to the g^p that they would generate at fixed distance).

In addition, the static structure factor projections along coordinate axes $S(q)|_x$, $S(q)|_y$, $S(q)|_z$ are computed for discrete wavevector values commensurate with the finite box size. For each of these quantities, they were determined both including the contributions coming from every particle and also separating in AA, BB and AB accumulators depending on the scatterer particle type. Biffi *et al.* exploited, in the analysis of their experimental data, the small-q behavior of the 3D version of the static structure factor, easily available from scattering measurements [10]. In particular, $S(|\overrightarrow{q}| \to 0)$ allows to detect critical behavior (and that experiment represented the first report of such a behavior in a DNA solution). In fact, $S(|\overrightarrow{q}| \to 0), T$ is linearly proportional to the isothermal compressibility $\chi(T)$ of the system, which is an important order parameter that represents an effective tool for locating the spinodal decomposition temperature T_s, via the relation:

$$S(|\overrightarrow{q}| \to 0, T) \propto \chi(T) \propto (T - T_s)^{-\gamma} \tag{4.4}$$

being $\gamma = 1.25$ the critical exponent for the liquid–gas transition and for the Ising universality class [17]. We have a set of simulated (or measured) estimations of $S(|\overrightarrow{q}| \to 0, T)$ at different temperatures T, from which the spinodal temperature can be deduced. How to concretely recover the $S(|\overrightarrow{q}| \to 0, T)$ limit? The Ornstein–Zernike relation for $S(|\overrightarrow{q}| \to 0)$ reads as [10, 17]:

$$S(|\overrightarrow{q}| \to 0, T) = \frac{S(0)}{1 + q^2\xi^2} \tag{4.5}$$

where ξ is a correlation length. Therefore, one could measure the complete $S|\overrightarrow{q}|$, fit these values for small $|\overrightarrow{q}|$ and obtain $S(0)$ (and also ξ). For each T, fit the curve $S(0, T)$ in order to estimate T_s, i.e. the temperature at which the isothermal compressibility diverges. In general, it must also be taken into account that $\chi = \dfrac{1}{\rho k_B T} S(|\overrightarrow{q}| \to 0)$; given that we explore a temperature range, this inverse temperature dependence can not be ignored. A possible future improvement of the measurement tools included in our Monte Carlo code is represented by the implementation of the calculation of this observable, which is however an extremely demanding computation.

Concerning instead thermodynamic quantities, the first observable that can be analyzed is the total reduced potential energy E^*:

$$E^* = \sum_{i=0}^{N-2} \sum_{j=i+1}^{N-1} \left(V_{ij}^{\text{rep}} + \sum_{k=0}^{2}{}' \sum_{l=0}^{2}{}' V_{ij}^{kl,\text{att}} \right) \tag{4.6}$$

where the first term represents the overlap among the particles cores (soft and hard both) and the second term represents the attractive patch-patch interactions. Note that the reduced energy per particle E^*/N can only assume values larger than (or equal to) -1.5, which corresponds to a situation where

all the patches of *all* the particles form links; each link brings in a contribution equal to -1 in units of ϵ_p, therefore if all the three links are formed for every patchy particle, $E^*/N = -3/2 = -1.5$, where the 1/2 comes from the fact that bonds are shared between two particles.

The fluctuations of the potential energy, via the fluctuation–dissipation theorem, directly provide the potential energy contribution to the specific heat. Exactly as in the case of Eq. 2.7 in the previous Chapter, the kinetic energy additive contribution to the specific heat is constant ($1/2k_B$) and can be neglected. In the code, the potential energy contribution to the specific heat is computed only at the end of each block as:

$$C_v = \frac{1}{N} \frac{\langle (E^*)^2 \rangle - (\langle E^* \rangle)^2}{(T^*)^2}$$

and it represents a crucial tool for the estimation of the spinodal temperature at fixed density. In fact, as explained in the previous Chapter for the 1D soft particle system, second order phase transitions feature a divergence of the specific heat near the critical temperature. Here we are in 3D and a phase transition is allowed, but the finite size of the simulation box will be reflected into the mere presence of a peak (not a real divergence) in C_v.

Moreover, we implemented the computation of the number of particles with 0/1/2/3 patches involved in a bond, which is an effective way to observe the possible formation of a full–bonded network. The fraction of bonded arms is also monitored. The code also stores the number of clusters n_c, which is an important information about the internal order of the system, indicating the tendency to form aggregates. Last, acceptance rates for each move are computed, and - for single particle moves - they are separately printed for totally free particles and for bonded particles.

4.6 Results

Here follows the presentation of the first results obtained for equilibrium MC simulations of mixtures of trivalent soft patchy particles with different chirality. These findings are preliminary and lots of further investigations are in program and will be detailed in the next section. It is fundamental to stress that the natural tendency of these systems, especially at low temperatures, is to form gels. The possibility of performing equilibrium simulations, in this case, is seriously affected by the intrinsic physics of the patchy particles, which hinders and slows down the equilibration process. We run 5 sets of independent stochastic simulations of a pure system and a mixture with $x_A = 0.5$, over a range of temperatures $T^* \in [0.12, 0.24]$. In order to establish the numerical density values for the simulations we recall that, in the modified diamond structure, each elementary cell contains n_{elem} =16 nanostars and

the following relation holds:

$$n_{\text{elem}} = \frac{V_{\text{elem}}}{V_{\text{box}}} N$$

being V_{elem} the volume of the elementary cell and V_{box} the volume of the simulation box. If we name N_A is the Avogadro number and $M = \dfrac{N}{N_A\, V_{\text{box}}}$ the molarity of the solution (i.e. the number of moles per liter), the previous equation transforms into:

$$\frac{n_{\text{elem}}}{V_{\text{elem}}} = M\, N_A$$

where the first term is the numerical density of the system. As a consequence, for a gel of trimers occupying all the available volume, whose molecular weight is 45 kDa/nanostar, with a solute concentration of ($\approx$ 10mg/mL), $M = 10/45000 = 222\ \mu M$, we have that the numerical density for a full–bonded network spanning the whole simulation cell is then equal to $\rho_{fb} = 0.0001337\ \text{nm}^{-3}$. Thus, the critical density is equal to 0.5 times this value, $\rho_c = 0.00006685\ \text{nm}^{-3}$. All the following results were obtained by fixing $\rho = \rho_c$ for $x_A = 1.0$ and $\rho = \rho_{fb}$ for the equimolar binary mixture. In fact, our primary goal is to investigate the critical behavior of a pure system and to verify whether the criticality of the two components is maintained when they are mixed but separately kept at the critical density.

The simulations at fixed ρ and x_A were analyzed by plot the observables computed against the reduced temperatures. Each physical observable appearing in the following was obtained as the average of its estimations in 5 independent runs and errorbars were calculated as the maximum of the errorbars (calculated via the data blocking method exposed in Chapter 2). The errorbars considered are those relative to the best estimation of the running average, which is a reasonable choice but it almost certainly underestimates the real fluctuations. Another possibility to estimate errors is to use the standard deviation (not the standard deviation of the average because the estimations contributing to the average are not 'atomic' but are already an average over the MPI processes and over the blocks of steps).

The first useful quantities to be inspected are the radial distribution function $g^{sc}(r)$ and the static structure factor along the z axis, $S(q)|_z$, which corresponds to the box side commensurate with the $z-$stretched modified diamond lattice. The top panels of Figs. 4.16 and 4.17 contain the $g^{sc}(r)$ for the pure system and the equimolar mixture simulated at three different temperatures, respectively low (brown and purple), intermediate (grey and orange) and high (black and yellow). The lower panels of both pictures show, for the same simulations, the $S(q)|_z$; note that all the panels feature a y axis log-scale. The data shown here were not averaged over the 5 different simulations sets, but were obtained from just 1 set.

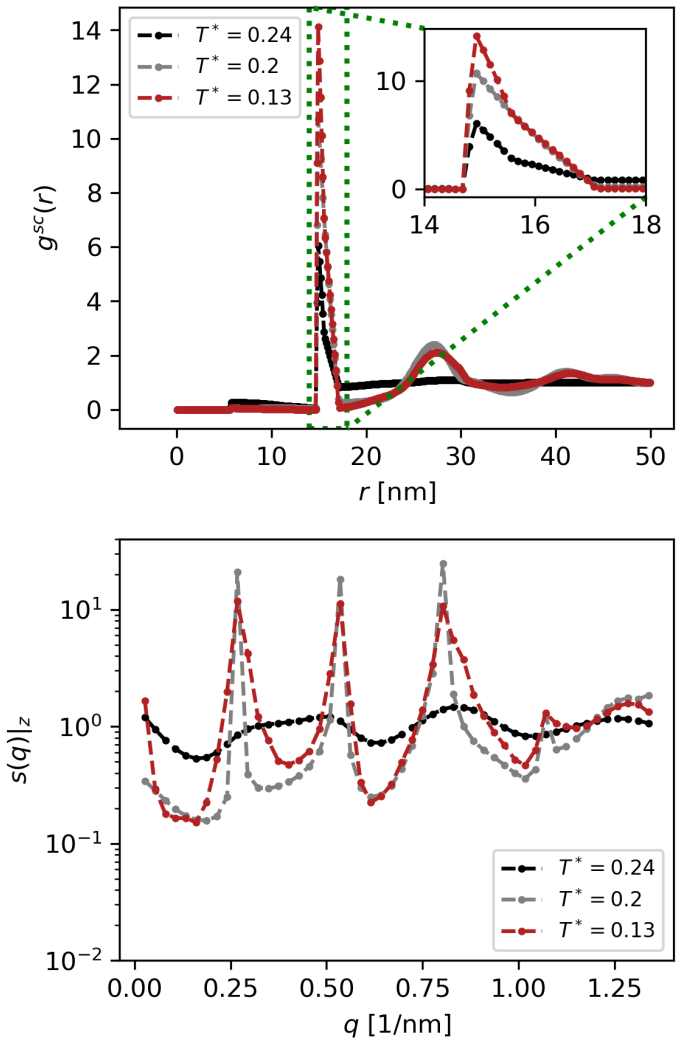

FIGURE 4.16: Top: three $g^{sc}(r)$ for a system with $x_A = 1.0$, $\rho = 0.00006685\text{nm}^{-3}$ respectively at $T^* = 0.13$ (red), 0.20 (grey), 0.24 (black). In the inset, a magnification of the peak region. Low: three $S(q)|_z$ in the same conditions. Note the logarithmic y scale.

The radial distribution function considered here did not distinguish between particles of different species. In both cases, upon increasing temperature, the (smaller) first peak grows, while the second (and taller) one presents a slight decrease. The data for the runs at $T^* = 0.24$, drawn in black and yellow respectively, evidenced a lack of long–distance structure, with a $g^{sc}(r)$ which is essentially flat from ≈ 20 nm. The tall peak, in all the cases, was

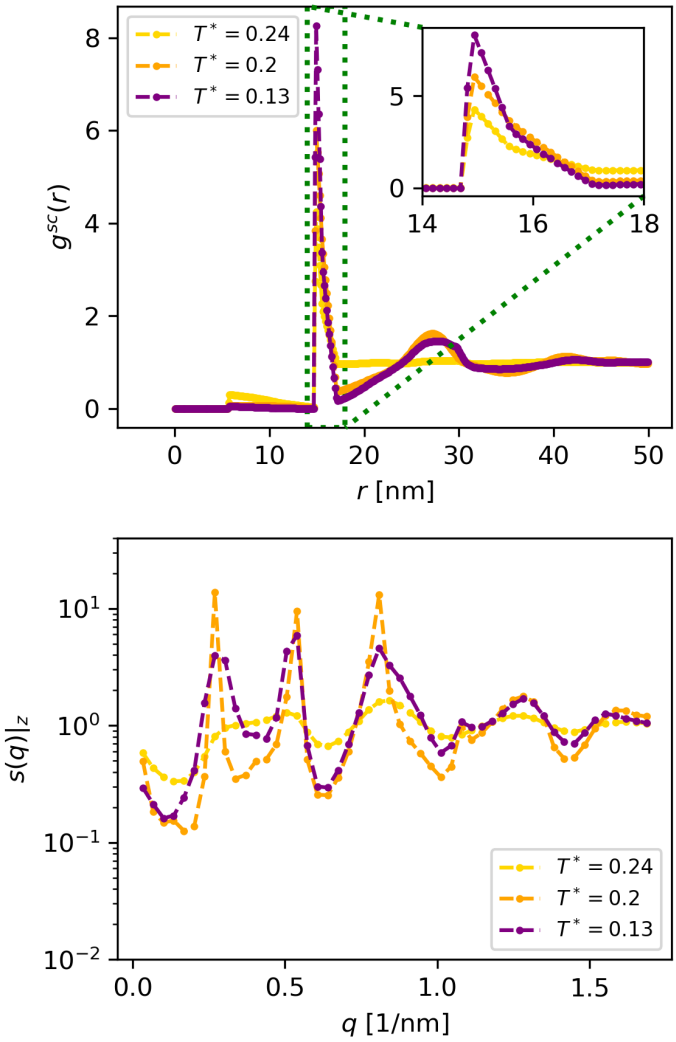

FIGURE 4.17: Top: three $g^{sc}(r)$ for a system with $x_A = 0.5$, $\rho = 0.0001337\text{nm}^{-3}$ respectively at $T^* = 0.13$ (purple), 0.20 (orange), 0.24 (gold). In the inset, a magnification of the peak region. Low: three $S(q)|_z$ in the same conditions. Note the logarithmic y scale.

located at the characteristic distance $2r_n$, representative of first–neighbors bonds. All the data also reflected the presence of the inner hard–core and of the external soft–core region. Concerning instead the z component of the static structure factor, the black and yellow data points lack any Bragg peak, indicating that those systems are substantially liquid. Lowering the temperature originated some Bragg peaks, which signal solid–like structures along

that axis, whose origin we identify into the to patch–patch bonds which form structures in the network. All the examples reported display a finite value of the static structure factor for low q, highlighting the presence of some surface at large distances (spinodal decomposition).

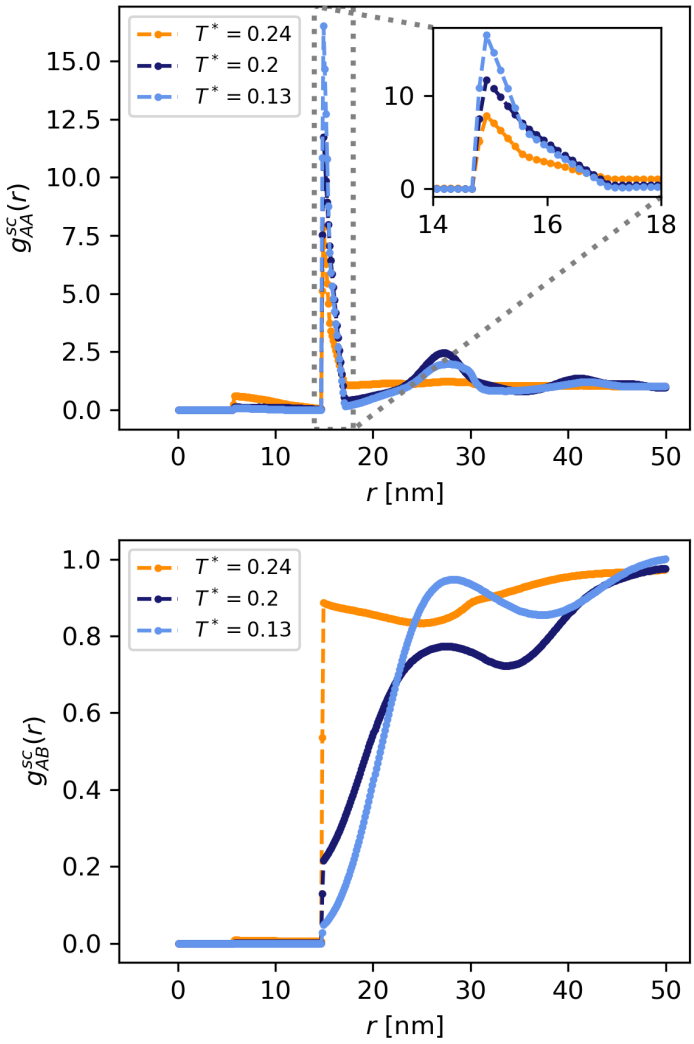

FIGURE 4.18: Top: $g^{sc}_{AA}(r)$ for a system with $x_A = 0.5$, $\rho = 0.0001337\text{nm}^{-3}$ respectively at $T^* = 0.13$ (lavender), 0.20 (blue), 0.24 (orange). In the inset, a magnification of the peak region. Low: $g^{sc}_{AB}(r)$ for a system with the same composition and density, at the same temperatures.

Fig. 4.18 shows, for the same representative temperatures used in Figs. 4.16 and 4.17, and for a mixture with $x_A = 0.5$ and $\rho = 0.0001337\text{nm}^{-3}$,

the radial distribution function for the soft cores $g^{sc}(r)$ restricted only to AA particle pairs (top panel) or only to AB particle pairs (lower panel).

Interestingly, the $g^{sc}_{AA}(r)$ (whose features are substantially equal to the ones of $g^{sc}_{BB}(r)$) is very similar to the pair distribution functions shown in the above pictures, indicating that the two species equally contribute to the global behavior of the system, and form analogous structures, on average.

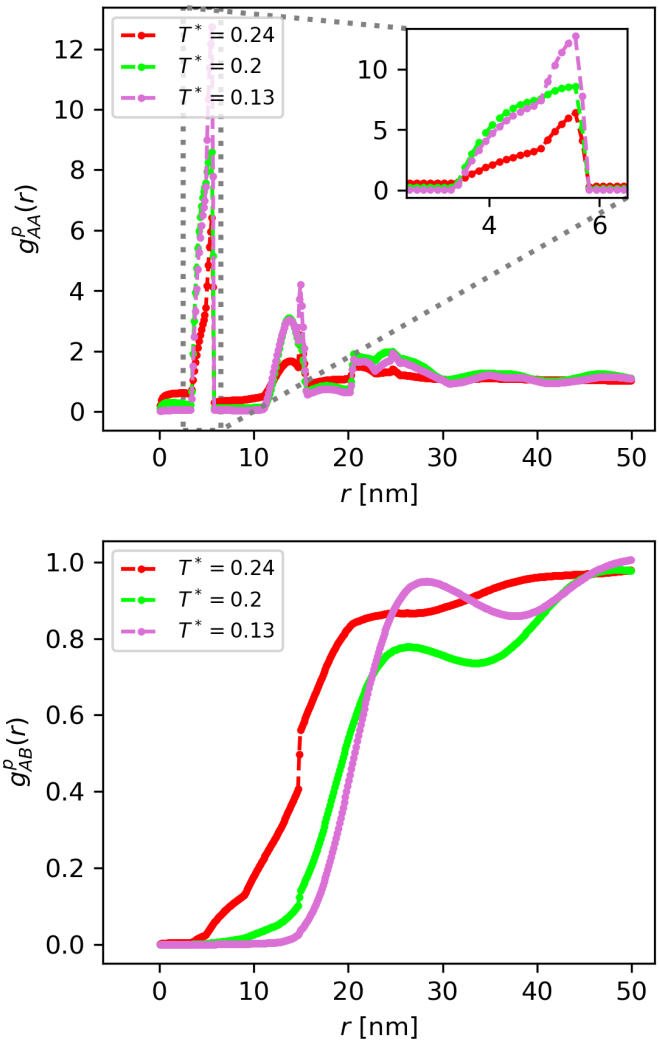

FIGURE 4.19: Top: $g^p_{AA}(r)$ for a system with $x_A = 0.5$, $\rho = 0.0001337\text{nm}^{-3}$ respectively at $T^* = 0.13$ (fuchsia), 0.20 (green), 0.24 (red). In the inset, a magnification of the peak region. Low: $g^p_{AB}(r)$ for a system with the same composition and density, at the same temperatures.

The $g^{sc}_{AB}(r)$ is instead characterized by a zero value up to $r = \sigma_{sc}$: in fact, in this case, particles of different types would pay the overlap cost without the energy gain of the patch-patch interactions (only at high temperatures some of these overlaps can rarely occur, see orange data). For larger distances, at high temperatures the system's properties resemble those of the ideal gas, while upon lowering T^* the $g^{sc}_{AB}(r)$ is dramatically reduced, forming small peaks in the range between 20 and 30 nm. These signs of structures should not be ascribed to structures formed by A and B–type particles together, but are simply to be interpreted as the consequence of the separated networks that the members of the two species are generating on their own. For the largest r values investigated, $g^{sc}_{AB}(r) \to 1$, which is the value for the ideal gas.

Regarding instead $g^{p}_{AA}(r)$, the top panel of Fig. 4.19 displays many peaks and contains information about the patch–patch bonds (the main peak), and about the bonds formed by the other two patches belonging to the same particle of the patch placed in $r = 0$ (second peak). There is also a larger and broader peak, between about 20 and 30 nm, which includes the contribution from patches belonging to the same cluster but not directly linked to the selected particle. The height of the first two peaks scales with the temperature. The low panel of this picture presents, instead, the contribution of mixed patch-patch interactions (whose reciprocal energy is zero). These curves resemble the corresponding curves of $g^{sc}_{AB}(r)$, with the important property that at $r = \sigma_{sc}$ they display a sudden jump, more evident for the red curve but present also in the others. That jump is caused by the fact that, for particles of different types, the soft–core overlaps are energetically unfavorable, because they are not compensated by the energy gain of patch–patch links. Therefore, where $g^{p}_{AB}(r) > 0$ for $r < \sigma_{sc}$, the presence of patches belonging to particles of different species is only due to thermal motion and to the structures separately formed by the two species.

The structural information can be complemented with the analysis of the thermodynamic observables. For example the potential energy per particle E^*/N carries interesting information: observing the data reported in Fig. 4.20, upon lowering the temperatures E^*/N tends to -1.4, which is a energy indicating that *almost all* the links are formed (the full–bonded energy is -1.5, represented in the picture by a dashed horizontal gray line). For $T^* \leq 0.13$ a small energy increase is visible, which can be ascribed to the scarce ergodicity of the corresponding low–temperature simulations.

Importantly, while at higher temperatures some small differences can be detected between the pure (black) and the binary equimolar (orange) system, at low temperatures ($T^* \leq 0.16$) the two curves are statistically identical (errorbars are smaller than the symbols). For higher temperatures, the potential energy per particle increases, becoming less and less negative: the importance of repulsive contributions grows and the number of stable patch–patch bonds decreases.

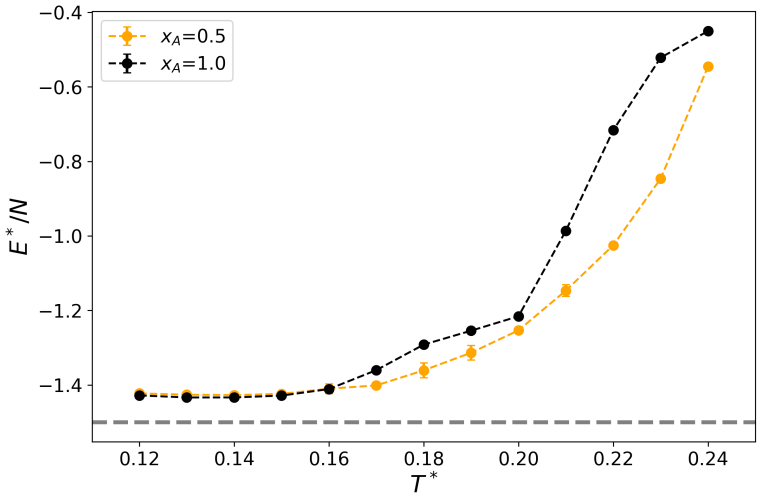

FIGURE 4.20: Potential energy per particle E^*/N as a function of reduced temperature T^*, for $x_A = 0.5, 1.0$. Data averaged over 5 independent simulations. Errorbars are smaller than symbol size.

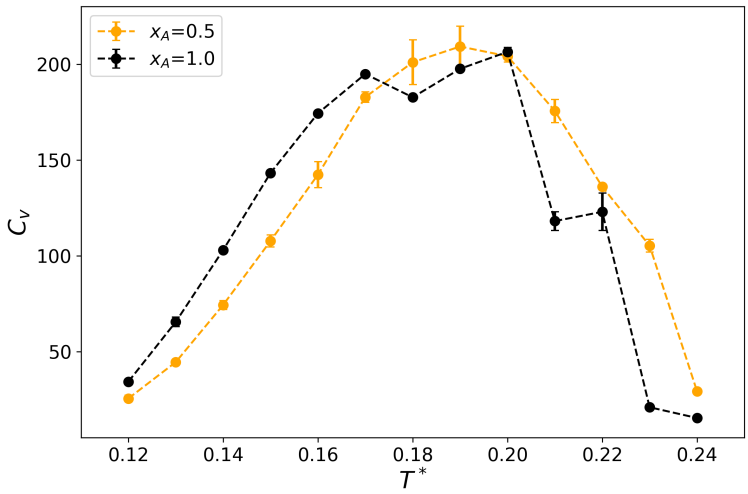

FIGURE 4.21: Potential energy contribution to the specific heat C_v as a function of reduced temperature T^*, for $x_A = 0.5, 1.0$. Data averaged over 5 independent simulations. Errorbars are smaller than symbol size.

In order to perform a comparison with experimental measurements concerning the spinodal decomposition curve, we also investigated the fluctuations of the potential energy, i.e. its contribution to the specific heat C_v. As unveiled by Fig. 4.21, this quantity is one of the best order parameters, in the attempt to locate the spinodal temperature T_s^* for a fixed density and a given mixture. C_v in the picture displays a marked peak; it is neat for the mixture (orange curve) at $T^* = 0.19$, while the data are not as smooth for the $x_A = 1.0$ case, but the spinodal temperature for that case seems to be similar.

It should be observed that, in the range $T^* \in [0.16, 0.20]$, because of the proximity to the critical region, it is difficult to effectively sample configurations via equilibrium MC simulations. In particular, an effective simulation of the equilibration phase is complicated, and the odd behavior of the black curve in the temperature range between 0.17 and 0.23 (partly present also in the pictures of the other scalar observables discussed in this section) indicates that these simulations can not be considered completely reliable. Further improvements may require a different equilibration protocol, or the variation of some simulation settings. We anticipate that one step which is scheduled for future studies is to distinguish, in the mixture, energy contributions for particles belonging to the two species and interspecies terms, evaluating also separate specific heats.

The fact that $T^* \approx 0.19$ approximately marks the passage between two different regimes is reflected also in the temperature dependence of the fraction of full–bonded particles, i.e. the fraction of colloids with all the three patches engaged in a bond with another patch.

Fig. 4.22 reveals an easily interpretable trend: for the highest temperatures investigated, only a small fraction of the patchy particles has all the valence sites involved in a patch–patch bond. As long as the temperature of the simulation is decreased, this fraction grows up to the lowest investigated temperatures, where it amounts to about the 80%/90% of the total number of particles N (the value for a completely bonded network is 1 and it is marked in the picture by a horizontal dashed gray line). Also here, the apparent small decrease of the curve for $T^* \leq 0.14$ is caused by the reduced ergodicity of the corresponding simulations. Nava *et al.* highlighted that an effective way of inspecting the network structure is the fraction of nanostar arms (i.e. of patches, in our idealized system) which are involved in a bond [13]. Fig. 4.23 evidences that at high temperatures, about only half of the patches are involved in some link, while this fraction grows and overcomes 0.8 in proximity of the estimated T_s^*, up to more than 0.9 at the lower temperatures investigated. For a system with all the patches involved in some bond, this quantity is equal to 1, which is marked in the picture by a dashed horizontal gray line.

Also the average number of clusters (i.e. groups made up by at least

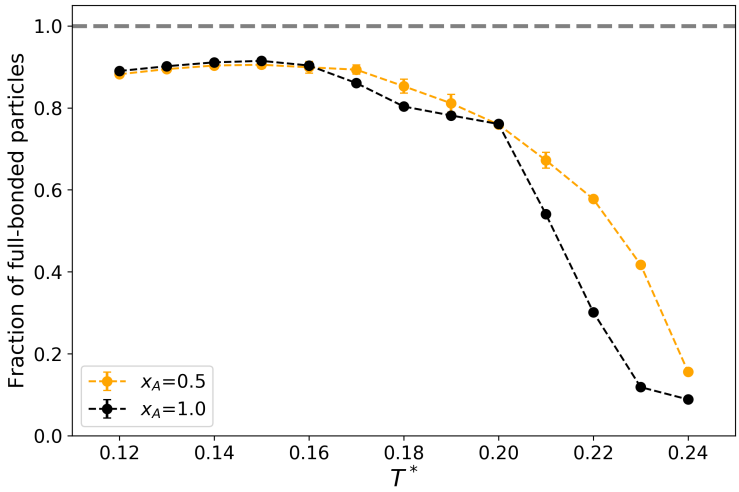

FIGURE 4.22: Fraction of full–bonded patchy particles as a function of reduced temperature T^*, for $x_A = 0.5, 1.0$. Data averaged over 5 independent simulations. Errorbars are smaller than symbol size.

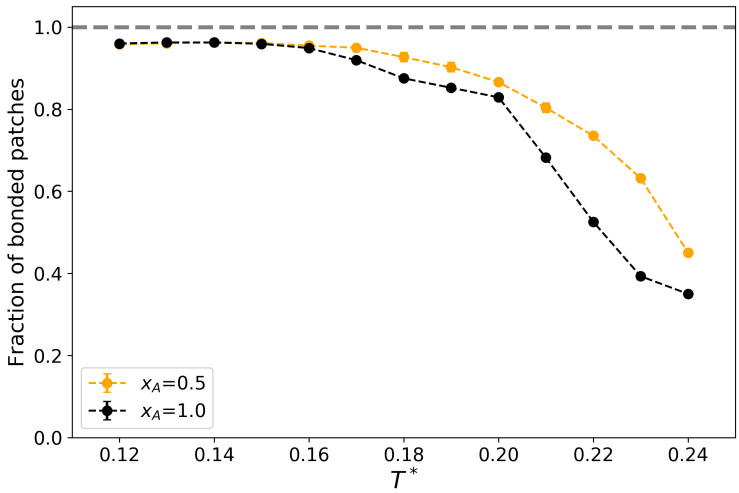

FIGURE 4.23: Fraction of bonded patches as a function of reduced temperature T^*, for $x_A = 0.5, 1.0$. Data averaged over 5 independent simulations. Errorbars are smaller than symbol size.

two particles) is characterized by a similar temperature dependence, with the presence of a huge number of (presumably small) clusters for high temperatures and less than 10 clusters for $T^* \leq 0.15$ (see Fig. 4.24). The logarithmic scale on the y-axis highlights a slope change for the lowest temperatures explored, where the number of clusters tends to some limit value (which would be equal to 1 only in the case of a pure system at zero temperature and high density). We underline that the knowledge of n_c does not carry any information about the number of members of each cluster. In fact, the clusters could be characterized by a very diverse number of components each. MC equilibrium simulations do not represent the correct tool to inspect the time evolution of the structure of patchy particles clusters. We plan to delve deeper into this topic by exploiting Brownian Monte Carlo methods [21], as explained in the Conclusions. To gain some information about the nature of these clusters, we need to exploit other computational tools. However, the orange curve at high temperature appears to be systematically under the black one. This may be interpreted by thinking that particles of opposite types can not form patch–patch bonds, and this repulsion could induce the formation of a lower number of clusters made by slightly more particles with respect to the mono–component case at the same temperature.

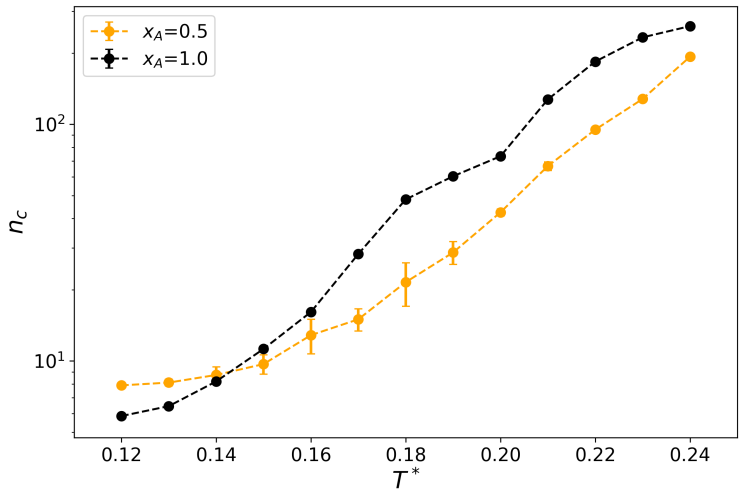

FIGURE 4.24: Number of clusters as a function of reduced temperature T^*, for $x_A = 0.5, 1.0$. Each data point is averaged over 5 independent simulations. Errorbars are smaller than symbol size in linear scale.

For a better visual comprehension, in Figs. 4.25 and 4.26 the OVITO software [19] was exploited in order to show the n_c temperature dependence for a

pure and a binary equimolar system (upper and lower picture, respectively).

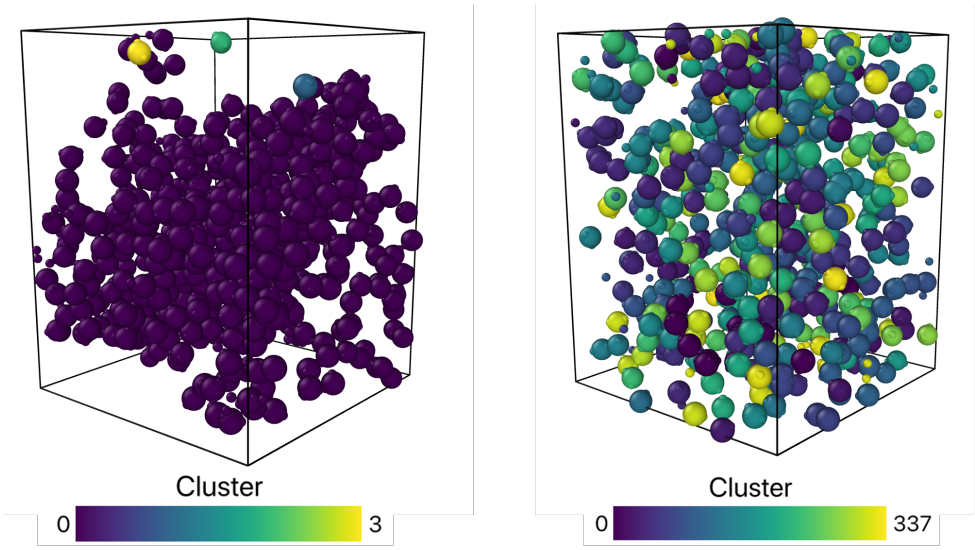

FIGURE 4.25: Configuration of a $x_A = 1.0$, $\rho = \rho_c$ system, represented with OVITO. Left: $T^* = 0.12$, right: $T^* = 0.24$. Color scale for cluster index indicated below each subfigure.

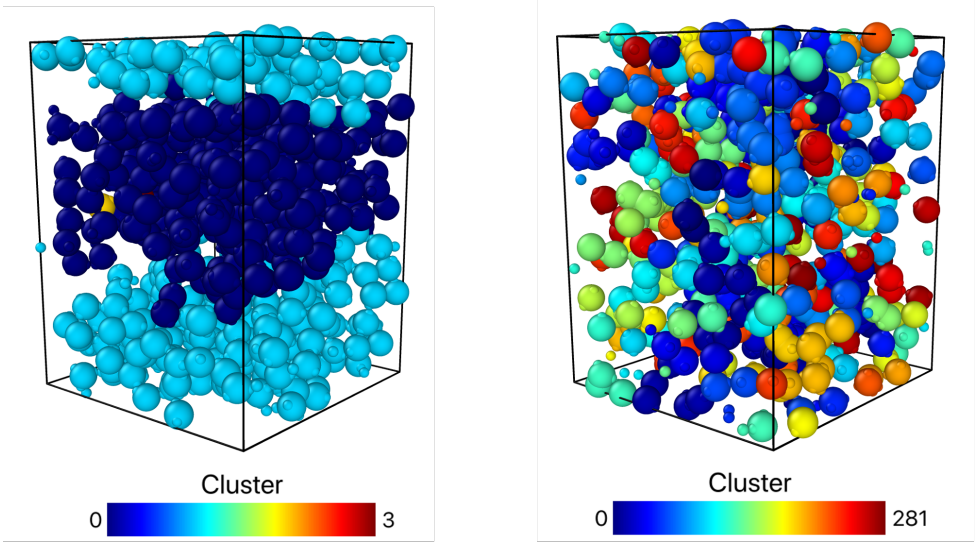

FIGURE 4.26: Configuration of a $x_A = 0.5$, $\rho = \rho_{fb}$ system, represented with OVITO. Left: $T^* = 0.12$, right: $T^* = 0.24$. Color scale for cluster index indicated below each subfigure.

In both pictures, on the left we show a snapshot of the simulation box for $T^* = 0.12$, with the particles colored according to their cluster index; on the

right, a configuration taken from the simulation at $T^* = 0.24$ is taken. In both cases, the maximum of the cluster index–based color scale at $T^* = 0.24$ is two order of magnitude larger than the corresponding value at $T^* = 0.12$.

Concerning the pure systems, they are not able to fill the box due to their density; at low temperature, the patchy colloids tend to form a unique aggregate with the shape of a compact globule which is surrounded by huge empty regions. At high temperature, conversely, the system is essentially constituted by small clusters (337 in the frame drawn in Fig. 4.25, against a total of $N = 512$ particles), which better fill the space but do not form a significant amount of bonds.

The $x_A = 0.5$ mixture, at high temperature, forms many clusters; as already hypothesized a few lines above, the number is slightly smaller than in the pure case also because particles of different species do not bond. At $T^* = 0.12$ the mixture appears definitely phase–separated: the simulation box is filled by two large cluster with two neatly defined boundary surfaces.

Once again, it is important to underline that these are equilibrium data, so we cannot infer anything about the growth of clusters in time. Moreover, the small size of the simulation box represents a severe bias, concerning the measurement of the topological and geometrical properties of patchy particles aggregates.

4.7 Conclusion and further perspectives

These preliminary results emerging from our Monte Carlo equilibrium simulations indicated that the pure system at critical density effectively shows a critical behavior, phase–separating with the void (in the experiments, with water and salt). Mixing together particles of two species with purely repulsive interspecies potential, separately found at critical conditions, yielded similar results: the critical behavior is maintained. Beyond the improvements already mentioned throughout the Chapter, concerning better implementations of observables computed during the simulations and a new equilibration protocol, many other points still have to be addressed.

First of all, the experimental measurements on DNA nanostars mixtures with $f = 3$ are still in progress. For instance, our collaborators mean to vary the respective concentration of LH and RH DNA nanostars, by studying non–equimolar mixtures. Moreover, they are also going to explore densities larger than ρ_{fb}, to test the response of the system to a further reduction of the available volume. More specifically, we wonder whether the two components will persist in their critical behavior and how could become more complex the pathway towards phase separation in these new conditions.

A point that can only be faced by simulations regards the 'softness' of the repulsive potential, in particular we aim to delve deeper into the dependence

of our findings on the specific value of ϵ_{sc}, which is a parameter that can be easily changed in our code. In fact, it will be crucial to understand how and quantify how much a soft–core potential differs from a hard–core one in present and future results.

On the other hand, as mentioned when introducing the measurements of the cluster aggregation and growth, we aim to support experiments also by adapting our MC code in order to simulate an approximate dynamics. I was the co-supervisor of a Bachelor Thesis [20] which attempted to modify the program, aiming to transform it into a Brownian Monte Carlo [21]. The idea is to change translation and rotation moves (both cluster and single–particle) by only allowing small Gaussian displacements, so to closely mimic a diffusive process. This should generate physically meaningful trajectories, providing the time evolution of the system in the early stages of the clusterization process. More specifically, we are interested in observing the time dependence of the average cluster size, and also to investigate (for example with graph theory tools, or inspiring to the analysis of loops for elastic transient networks described in [22]) the internal structure of the network while it is growing. Clearly, we shall reject the hypothesis of spherical clusters, given that clusters of odd and irregular shapes are expected to form. It will also be fundamental to understand in which simulation regime the quantitative and geometrical information about clusters formation and growth will be reliable.

All the simulations described in this Chapter were run on CINECA supercomputers, in particular exploiting the *IscraB-PANDA* (2020) project on Galileo. We also exploited INDACO supercomputing structure (Università degli Studi di Milano), in particular through the CRYSTALGROWTH project (2019).

Bibliography

[1] L. Rovigatti, F. Smallenburg, F. Romano, and F. Sciortino. Gels of DNA nanostars never crystallize. *ACS Nano*, 8(4):3567–3574, 2014.

[2] E. Bianchi, J. Largo, P. Tartaglia, E. Zaccarelli, and F. Sciortino. Phase diagram of patchy colloids: Towards empty liquids. *Physical Review Letters*, 97(16):1–4, 2006.

[3] E. Bianchi, P. Tartaglia, E. Zaccarelli, and F. Sciortino. bianchi2008.pdf. *Journal of Chemical Physics*, 128:144504–1, 2008.

[4] E. Bianchi, B. Capone, I. Coluzza, L. Rovigatti, and P. D.J. Van Oostrum. Limiting the valence: Advancements and new perspectives on patchy colloids, soft functionalized nanoparticles and biomolecules, 2017.

[5] F. Sciortino. Gel-forming patchy colloids and network glass formers: Thermodynamic and dynamic analogies. *European Physical Journal B*, 64(3-4):505–509, 2008.

[6] M. S. Wertheim. Fluids with highly directional attractive forces. I. Statistical thermodynamics. *Journal of Statistical Physics*, 35(1-2):19–34, 1984.

[7] F. Sciortino and E. Zaccarelli. Equilibrium gels of limited valence colloids. *Current Opinion in Colloid & Interface Science*, 30:90–96, 2017.

[8] L. Rovigatti, J. Russo, and F. Romano. How to simulate patchy particles. *European Physical Journal E*, 41(59):1–12, 2018.

[9] F. Smallenburg and F. Sciortino. Liquids more stable than crystals in particles with limited valence and flexible bonds. *Nature Physics*, 9(9):554–558, 2013.

[10] S. Biffi, R. Cerbino, F. Bomboi, E. M. Paraboschi, R. Asselta, F. Sciortino, and T. Bellini. Phase behavior and critical activated dynamics of limited-valence DNA nanostars. *Proceedings of the National Academy of Sciences of the United States of America*, 110(39):15633–15637, 2013.

[11] N.C. Seeman. *Structural DNA Nanotechnology*. Cambridge University Press, 2015.

[12] F. Spinozzi, M. G. Ortore, G. Nava, F. Bomboi, F. Carducci, H. Amenitsch, T. Bellini, F. Sciortino, and P. Mariani. Gelling without Structuring: A SAXS Study of the Interactions among DNA Nanostars. *Langmuir*, 36(35):10387–10396, 2020.

[13] G. Nava, M Rossi, S. Biffi, F. Sciortino, and T. Bellini. Fluctuating Elasticity Mode in Transient Molecular Networks. *Physical Review Letters*, 119(7):1–5, 2017.

[14] D. De Las Heras, JJ. M. Tavares, and M. M. Telo Da Gama. Phase diagrams of binary mixtures of patchy colloids with distinct numbers of patches: The network fluid regime. *Soft Matter*, 7(12):5615–5626, 2011.

[15] E. Locatelli, P. H. Handle, C. N. Likos, F. Sciortino, and L. Rovigatti. Condensation and Demixing in Solutions of DNA Nanostars and Their Mixtures. *ACS Nano*, 11(2):2094–2102, 2017.

[16] L. De Chiara. *Gelazione e separazione di fase in miscele binarie di DNA enantiomerici*. Bachelor thesis, 2019.

[17] L. Rovigatti, F. Bomboi, and F. Sciortino. Accurate phase diagram of tetravalent DNA nanostars. *Journal of Chemical Physics*, 140(15), 2014.

[18] B. E.K. Snodin, F. Randisi, M. Mosayebi, P. Šulc, J. S. Schreck, F. Romano, T. E. Ouldridge, R. Tsukanov, R. Nir, A. A. Louis, and J. P.K. Doye. Introducing improved structural properties and salt dependence into a coarse-grained model of DNA. *Journal of Chemical Physics*, 142(23):234901, 2015.

[19] A. Stukowski. Visualization and analysis of atomistic simulation data with OVITO-the Open Visualization Tool. *Modelling and Simulation in Materials Science and Engineering*, 18(1), 2010.

[20] S. Zinzani. *Simulazione della decomposizione spinodale in miscele binarie di nanostelle di DNA*. PhD thesis, Università degli Studi di Milano, 2020.

[21] F. Romano, C. De Michele, D. Marenduzzo, and E. Sanz. Monte Carlo and event-driven dynamics of Brownian particles with orientational degrees of freedom. *Journal of Chemical Physics*, 135(12):124106, 2011.

[22] M. Zhong, R Wang, K. Kawamoto, B. D. Olsen, and J. A. Johnson. Quantifying the impact of molecular defects on polymer network elasticity. *Science*, 353(6305):1264–1268, 2016.

Appendix A

Details about experiments on supercooled Ar-Kr liquid mixtures

Experimental determination of thermodynamical quantities for the analytic calculation of crystal growth rates

In order to calculate the crystal growth rate of a mixture according to eq. 1.1, $g_{\mathrm{B}}^{\mathrm{L,C}}(T)$ and $g_{\mathrm{A}}^{\mathrm{L,C}}(T)$ are needed. These can be obtained from respective heat capacities. The symbols in Fig. A.1 represent experimental heat capacity data for argon (violet) and krypton (red) in the liquid (circle) and solid (square) phases.

As remarked in the main text, we assumed the heat capacities of the supercooled liquids as linear extrapolations for $T < T_m$ of experimental data at higher temperatures, fitted by $c_p^{\mathrm{L}}(T) = a_0 + a_1 T + a_2 T\, e^{a_3 T}$. Similarly, the experimental heat capacities of the pure solids were fitted for $T > 10$ K via: $c_p^C(T) = \sum_{k=0}^{4} b_k T^k$. Tabs. A.1 and A.2 contain fit parameters for liquid and solid phases of Ar and Kr heat capacities.

TABLE A.1: Fit parameters for argon and krypton heat capacity in the liquid phase.

a_i	**Argon**	**Krypton**
a_0[J/(mol K)]	28.6384	40.5517
a_1[J/(mol K^2)]	0.1744	0.0349
a_2[J/(mol K^2)]	4.66×10^{-8}	1.7169×10^{-6}
a_3[1/K]	0.111	0.0599

TABLE A.2: Fit parameters for argon and krypton heat capacity in the solid phase.

b_i	**Argon**	**Krypton**
b_0[J/(mol K)]	-10.2982	-7.9314
b_1[J/(mol K^2)]	1.5792	1.7226
b_2[J/(mol K^3)]	-0.00252	-0.332
b_3[J/(mol K^4)]	1.6155×10^{-4}	2.8317×10^{-4}
b_4[J/(mol K^5)]	-9.4934×10^{-8}	-8.3907×10^{-7}

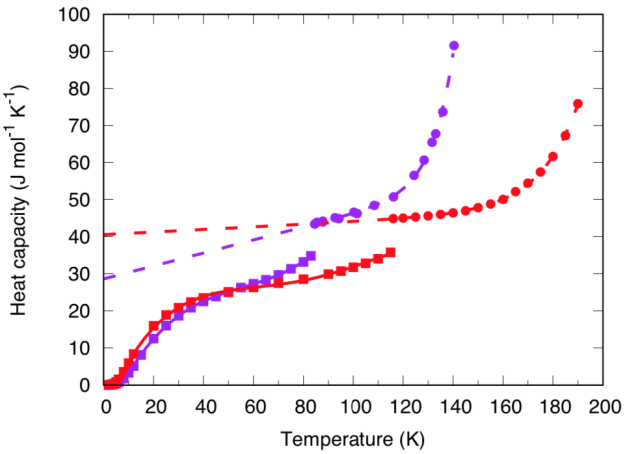

FIGURE A.1: Experimental heat capacity for Ar and Kr as a function of temperature. Dashed lines indicate the linear extrapolation for low temperatures of the liquid data.

Experimental details

Here are some technical details about the realization of the experiment:

- The liquid jets were generated by gas condensation in a glass capillary cryogenically cooled to temperatures slightly above the equilibrium liquidus line of mixtures of argon and krypton.
- The mixtures were prepared at room temperature by continuous mixing of 99.999% purity argon and krypton gases at specific ratios set by two mass flow controllers, one for each gas.
- The liquid jet velocities were determined from the Bernoulli equation $v = \sqrt{2P/\rho}$, where P is the applied gas supply pressure and ρ is the density of the liquid.

- The source pressure varied between 20 and 40 bar, depending on the specific mixture, providing jet velocities between 55 and 77 m/s.

Scattering data analysis

The scattering images resembled virtual powder diffraction patterns as a consequence of the 100–s–long acquisition time, during which up to $\sim 10^8$ individual sampled volumes crossed the $\sim 24\mu$m-wide focus of the X-ray beam. Diffraction images were thus recorded by employing a Pilatus 300k (Dectris) pixel array detector, placed slightly sideways with respect to the X-ray beam direction at a distance of 229 ± 0.9 mm from the jet. For analysis, the two-dimensional diffraction patterns were azimuthally integrated and background-subtracted, and subsequently corrected for polarization and geometric effects. The q values were initially calibrated by recording diffraction patterns from the thin layer of hexagonal ice that formed by condensation at the capillary tip of water molecules invariably present as residual gas in the vacuum chamber. The background images were, then, recorded at each z at a radial distance of $\sim 50\,\mu$m from the jet axis where no scattering from the filament was expected. However, the fact that the transmitted X-ray beam was attenuated by the liquid jet resulted in different contributions to the diffraction intensity of the X-rays scattered from the thin Kapton foil placed between the jet and the detector. We removed this distortion by comparing background diffraction images measured at different distances from the nozzle.

TABLE A.3: JMAK fit parameters employed in the analysis of our experimental data.

Kr mole fraction x	**k** ($\times 10^4$ **s**$^{-1}$)	$\tau(\mu)$ **s**	n
0	6.0	3.1	0.8
0.03	3.2	4.2	0.7
0.07	2.3	2.1	0.9
0.15	1.5	1.0	1.0
0.4	1.3	4.2	1.4
0.85	3.4	4.3	1.0
0.93	4.8	5.1	0.7
1	5.6	4.8	0.7

The scattering profiles such as the one exposed in Fig. 1.7a had to be analyzed separating the contributions to the diffraction intensity of the disordered liquid and crystalline phases. To this aim, we used up to eight Voigt functions to fit the experimental diffraction profiles.

The contribution of the disordered liquid was modelled by assuming three Voigt functions with fixed area ratios and relative peak positions. The fraction crystallized was calculated by dividing the sum of the integrated face-centred cubic (fcc) peak intensities by the total integrated intensity. To estimate the uncertainty, we considered two different integration ranges, one containing the full measured diffraction profile, and one limited to 1 $\text{Å}^{-1} \leq q \leq 2.5$ Å^{-1} and containing only the two most intense fcc peaks. We fitted the experimental data by the Johnson–Mehl–Avrami–Kolmogorov rate equation 1.15, reported in Chapter 1, with the parameters exposed in Tab. A.3.

Jet temperature determination

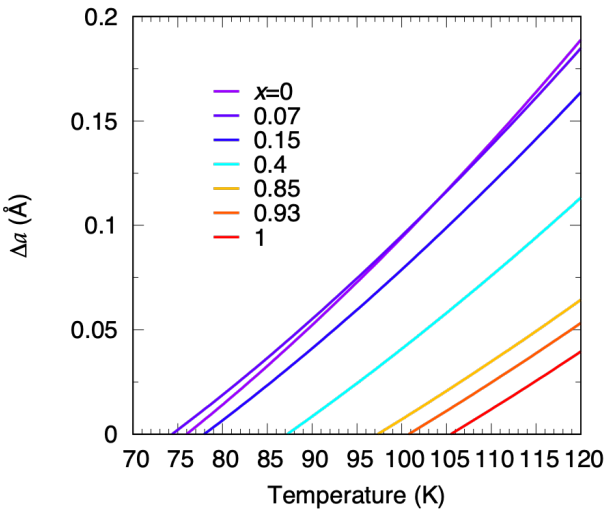

FIGURE A.2: Graphical determination of the jet temperature at the onset of crystallization. Reprinted from [Schottelius *et al.*, *Nat. Mater.*, 2020]

Here are furnished the details of the jet temperature determination, at the onset of crystallization. They are based on the analysis of the first visible (111) fcc peak in the integrated diffraction patterns. The associated q value was used to extract, by means of Bragg's law, the lattice constant a_{exp} of the growing crystal in each investigated system. Remeber that, for a cubic unit cell, the lattice constant a is related to the density ρ by $a^3 = N\,M_{mol}/(N_A\,\rho)$, with M_{mol} being the molar mass and N_A the Avogadro number. For the fcc crystal structure (rare gases form fcc lattices), the number of atoms per unit cell is $N = 4$. Accordingly,

the lattice constant as a function of x and T becomes:

$$a(x_{Kr}, T) = \left[4\frac{m(x_{Kr})}{\rho(x_{Kr}, T)}\right]^{1/3} \tag{A.1}$$

where the mixture's mass $m(x_{Kr})$ is equal to $m_{Kr}\, x_{Kr} + m_{Ar}\,(1 - x_{Kr})$ and $\rho(x_{Kr}, T) = \rho_{Kr}(T)\, x_{Kr} + \rho_{Ar}(T)\,(1 - x_{Kr})$. Clearly, m_{Kr} and m_{Ar} represent respectively the atomic mass of argon and krypton; $\rho_{Kr}(T)$ and $\rho_{Ar}(T)$ are the densities of the solid phases of argon and krypton, determined from fits to experimental molar volume data [Ferreira *et al. J. Chem. Therm.*, 2008]. The validity of this equation was verified by comparing it with lattice constants measured in solid mixtures of argon and krypton at 7 K [Kovalenko *et al. Phys. St. Sol. (a)*, 1972].

The solid lines in Fig. A.2 represent, for each krypton mole fraction, the difference $\Delta a(T) = a(x_{Kr}, T) - a_{exp}$, where a_{exp} is the experimental lattice constant determined by means of Bragg's law from the q-value of the first visible (111) fcc peak in the integrated diffraction patterns. The jet temperatures at the onset of crystallization were then obtained as graphical solution to the equation $a(x_{Kr}, T) - a_{exp} = 0$, for each x_{Kr}.

Appendix B

LAMMPS input script

Here follows the LAMMPS input script used to perform the simulations described in the first Chapter of this PhD thesis. The whole example refers to the simulations of the 40% Kr - 60% Ar mixtures along (100) growth axis. The lines where the script for the (111) simulation differs are explicitly described, as well as the lines distinguishing the simulations of pure systems.

Please also note that the z axis mentioned in the following (for (111) and (100) directions both) is the x axis of the main text.

```
1
2  ###################################
3  # INIZIALIZATION
4  ###################################
5  units       real
6  dimension   3
7  atom_style  atomic
8  boundary    p p p
9  atom_modify map array
10
11 ###################################
12 # ATOMS AND REGIONS DEFINITION
13 ###################################
14 variable lat_sp equal 5.6155 #(100) lattice constant in Angstrom
       comes from last set of experimental data
15
16 variable elem_cell_vol equal $(v_lat_sp^3) \#volume elementary fcc
       cell, expressed in units of σ^3
17
18 lattice fcc ${lat_sp} # create fcc lattice with this lattice constant
        - ok for (100) and (111) both
19
20 variable x_side equal 36.0 #lattice units. i.e., box size along x is
       = to (x_side × lat_sp) in \AA
21 variable y_side equal 8.0
22 variable z_side equal 8.0
23 variable x_side2 equal $(v_x_side/2)
24 variable y_side2 equal $(v_y_side/2)
25 variable z_side2 equal $(v_z_side/2)
```

```
26
27 #x_side, y_side and z_side become respectively 36.0, 10.0 and 6.0 for
       the study of the crystal growth along the (111) surface
28
29 region box block 0.0 ${x_side} 0.0 ${y_side} -${z_side2} ${z_side2}
      units lattice
```

The first difference concerning (111) simulations is that these few lines are added:

```
1 # lattice spacing multiplicative factors for (111) direction
2 variable x_lat_const equal 1.1547
3 variable y_lat_const equal 0.7071
4 variable z_lat_const equal 1.2247
```

in order to take into account the particular shape of elementary (111) cells.

In fact, if the x axis was oriented as (100), in the notation of Miller indexes, and it is now rotated to be aligned with (111), also the other two axes must be rotated accordingly. The new set of vectors for the conventional unit cell must be right-handed. This yields many degenerate solutions for the two remaining vectors; we chose to orient the y axis as (1-10) and the z axis as (11-2).

Therefore, the `lattice` command is modified as follows:

```
1 lattice fcc ${lat_sp} orient x 1 1 1 orient y 1 -1 0 orient z 1 1 -2
      spacing ${x_lat_const} ${y_lat_const} ${z_lat_const}
```

Now, the general formula for the interplanar distance d between two consecutive layers along the (ijk) direction is:

$$d = \frac{a}{\sqrt{i^2 + j^2 + k^2}}$$

where a is the interplanar distance when $i = 1$ and $j = k = 0$ (or the two equivalent (010) and (001) faces). As a consequence, for the orientation we chose, the interplanar distances are:

- $d_x = \frac{a}{\sqrt{3}}$
- $d_y = \frac{a}{\sqrt{2}}$
- $d_z = \frac{a}{\sqrt{6}}$

LAMMPS allows to scale d_x, d_y, d_z by three corresponding factors s_x, s_y, s_z, which adjust the aspect ratio of the box (via the `spacing` keyword). Aiming to maintain the density of the system between the simulations where x axis coincides with (100) and the simulations where

the x axis is instead oriented along (111), the following condition must be verified:

$$(s_x\, d_x)\,(s_y\, d_y)\,(s_z\, d_z) \equiv 1$$

This corresponds to impose that $s_x^2\, s_y^2\, s_z^2 \equiv 36$. Now, one of our goals is to deform as less as possible the simulation box, thus to make the ratio between y and z sides as close to unity as possible. $s_x^2\, s_y^2\, s_z^2 \equiv 36$ has two sets of degenerate solutions: $\{1, 2, 3\}$ and $\{1, 1, 6\}$. Considering that $d_y > d_x > d_z$, the most reasonable choice is to take $s_y = 1, s_x = 2, s_z = 3$. As a consequence, $s_x\, d_x \simeq 1.1547, s_y\, d_y \simeq 0.7071, s_z\, d_z \simeq 1.2247$, which are exactly the values I used in the LAMMPS input script as values for the `spacing` keyword.

Then, for a mixture, one has to create a simulation box and fill it with atoms of two species:

```
create_box 2 box  # 1 for pure Ar/Kr

read_data ${fullpath}/start_001.40 add append #read initial
    configuration from an external file, prepared via an external BASH
     script. These coordinates overwrite the ones of create_box
```

In the `start_001.x` files, the atoms of both chemical elements are placed in the fcc lattice sites; their identity (being Ar or Kr) is randomly extracted, according to the chosen mixing ratio. The `read_data` command is replaced, in pure systems, by:

```
create_atoms 1 box
```

Now, all the operations concerning the creation of the liquid and of the central crystal seed, as described in section 1.4 of Chapter 1 take place:

```
displace_atoms all move 0 0 0.25 units lattice  #center crystal
    lattice, for full symmetry with respect to the origin
variable dens equal $(4.0/v_elem_cell_vol) #numerical density, dens
    =4/lat_sp^3
variable ratio equal $(v_dens/v_liquid_dens) #liquid_dens is a
    numerical density, too
variable new_z_side equal $(v_z_side*v_ratio) # new length of z side

variable N equal atoms # pre-defined LAMMPS variable: total number of
     atoms

###################################
# OUTPUT FILES
###################################
variable fullpath string ./${ada_thermo}/${random_loop}
```

```
12
13 shell mkdir ${frigo}
14 shell mkdir ${fullpath}
15
16 variable toler equal 0.00001 #numeric tolerance for comparisons
17
18 ###################################
19 # CRYSTAL SEED
20 ###################################
21 # Define the regions of the groups related to the central harmonic
       wall
22 region wall_4layers block -${toler} $(v_x_side+v_toler) -${toler} $(
       v_y_side+v_toler) -$(0.75+v_toler) $(0.75+v_toler)  units lattice
       # central wall made by 4 harmonic layers
23 group wall_4layers region wall_4layers # atoms assigned to this group
        for the whole simulation
24
25 # 4 separate groups for the 4 separate layers of the wall
26 region 1la_le block -${toler} $(v_x_side+v_toler) -${toler} $(v_y_side
       +v_toler) -$(0.25+v_toler) -$(0.25-v_toler)
27 group 1la_le region 1la_le
28
29 region 1la_ri block -${toler} $(v_x_side+v_toler) -${toler} $(v_y_side
       +v_toler) $(0.25-v_toler) $(0.25+v_toler)
30 group 1la_ri region 1la_ri
31
32 region 2la_le block -${toler} $(v_x_side+v_toler) -${toler} $(v_y_side
       +v_toler) -$(0.75+v_toler) -$(0.75-v_toler)
33 group 2la_le region 2la_le
34
35 region 2la_ri block -${toler} $(v_x_side+v_toler) -${toler} $(v_y_side
       +v_toler) $(0.75-v_toler) $(0.75+v_toler)
36 group 2la_ri region 2la_ri
37
38 group mobile subtract all wall_4layers # atoms free to move: static
       group - i.e., assignement is once for all
39
40 # these groups are only for the starting displacement of atoms
41 region mobile_right block -${toler} $(v_x_side+v_toler) -${toler} $(
       v_y_side+v_toler) $(0.75+v_toler) $(v_z_side2+v_toler) units
       lattice
42  region mobile_left block -${toler} $(v_x_side+v_toler) -${toler} $(
        v_y_side+v_toler) -$(v_z_side2+v_toler) $(-0.75-v_toler) units
        lattice
43 group mobile_left region mobile_left
44 group mobile_right region mobile_right
45 region mobile union 2 mobile_right mobile_left
46
47 ###################################
48 #SIMULATION BOX
49 ###################################
50 # Initial change of box shape and atoms positions: the aim is to have
        a perfect crystal in the middle of the box, and an "average"
       liquid in the rest of it
```

```
51
52 change_box all z final $(-v_new_z_side/2) $(v_new_z_side/2) remap
       units lattice # change density along z
53
54 #bring back the 2 internal layers of the central wall - (ratio-1) is
       the relative elongation coefficient
55 displace_atoms 1la_le move 0 0 $(0.25*(v_ratio-1)) units lattice
56 displace_atoms 1la_ri move 0 0 $(-0.25*(v_ratio-1)) units lattice
57
58 #bring back the 2 external layers of the central wall
59 displace_atoms 2la_le move 0 0 $(0.75*(v_ratio-1)) units lattice
60 displace_atoms 2la_ri move 0 0 $(-0.75*(v_ratio-1)) units lattice
61
62 #bring back all the other atoms, maintaining the liquid density
63 displace_atoms mobile_left move 0 0 $(0.75*(v_ratio-1)) units lattice
64 displace_atoms mobile_right move 0 0 $(-0.75*(v_ratio-1)) units
       lattice
65
66 #new length of half of the simulation box along z, in lattice units
67 variable new_z_side2 equal $(v_new_z_side/2 - 0.75*(v_ratio-1))
68
69 #cut the empty edges of the box
70 change_box all z final $(-v_new_z_side2) $(v_new_z_side2) units
       lattice
71
72 # spatial binning of temperature and density - it lasts for the whole
        run
73 # the spacing between neighboring layers is 0.5 lattice units, i.e.
       0.5*lat_sp
74 compute clayers all chunk/atom bin/1d z 0.0 0.5 units lattice
       compress no
75 fix layers_fix all ave/chunk 100 10 1000 clayers density/number temp
       file ${fullpath}/dens_temp_layers.dat
```

Here below is reported the part of the LAMMPS input script relative to the pair potential and to the time–integration scheme. Also atomic masses are set.

```
1 ###################################
2 # FORCE FIELDS
3 ###################################
4 variable cutoff_radius equal 20.4 #\AA
5 pair_style lj/cut ${cutoff_radius}
6 pair_coeff 1 1 0.238066 3.405 # species_i species_j epsilon_ij
      sigma_ij
7 pair_coeff 2 2 0.330669 3.636
8 pair_coeff 1 2 0.277486 3.5205
9 pair_modify tail no #with such a long cutoff, they are not necessary
10
11 ###################################
12 #NEIGHBOR LISTS
13 ###################################
```

```
variable skin_distance equal 1.7 # \AA # distance to add to cutoff in LJ units
neighbor ${skin_distance} bin # after checking if some atom has moved beyond half of the skin distance...
neigh_modify every 10 delay 0 check yes #... update neighbors list every 10 steps

###################################
#TIME INTEGRATION
###################################
run_style verlet #Velocity-Verlet integrator
timestep 2 #fs

###################################
#MASSES
###################################
mass 1 39.948 # atom type and mass in amu
mass 2 83.798
```

Now comes the proper simulation, starting from the high-temperature melting of the initial crystal:

```
################################
# FIX - MELTING1
################################
# initial velocity distribution - T in Kelvin
velocity mobile create 300 ${seed_random} dist gaussian mom yes rot yes
velocity wall_4layers create 160 ${seed_random} dist gaussian mom yes rot yes

###################################
# FIXES
###################################
# give different starting temperatures and thermostat to different temperatures the wall and the rest of the system
fix nvt1_fix mobile nvt temp 150 150 200 #last value is the thermostat's relaxation time. 100 steps is ok, in general
fix wall_nve_fix wall_4layers nve
#apply an harmonic spring to each atom in the group. the rest position of each atom is the starting one. k is in LJ units.
fix harmonic_fix wall_4layers spring/self 1.67 # k=k_LJ*epsilon/(sigma)^2
fix wall_thermo wall_4layers temp/csvr ${temp} ${temp} 200 ${seed_random}

###################################
#COMPUTES
###################################
# in questo modo termostato la regione e non solo il gruppo di atomi wall_4layers
compute temp_wall all temp/region wall_4layers
```

```
#use the temperature measured within the wall to keep it under thermostat
fix_modify wall_thermo temp temp_wall

###################################
# OUTPUT
###################################
log            ${fullpath}/log.nvt1
dump           dump_nvt1 all atom 1000 ${fullpath}/dump_nvt1.lammpstrj
dump_modify    dump_nvt1 sort id scale no
thermo         1000
thermo_style   custom step temp press pe ke etotal

###################################
#RUN
###################################
run 2000

unfix nvt1_fix
undump dump_nvt1

# active: thermostat + NVE fix + harmonic confinement of the atoms in the crystal seed
```

The subsequent equilibration of the liquid at a slightly lower T:

```
################################
# FIX - MELTING2
################################
variable T2 equal 130
fix nvt2_fix mobile nvt temp ${T2} ${T2} 200

###################################
# OUTPUT
###################################
log            ${fullpath}/log.nvt2
dump           dump_nvt2 all atom 1000 ${fullpath}/dump_nvt2.lammpstrj
dump_modify    dump_nvt2 sort id scale no
thermo         1000
thermo_style   custom step temp press pe ke etotal

###################################
# RUN
###################################
run 2000

unfix nvt2_fix
undump dump_nvt2
```

A key step is represented by the supercooling of the system:

```
###################################
```

```
# LINEAR SUPERCOOLING
###################################

variable T_scale equal 42 #supercooling temperature
variable loops equal 50
variable decrease equal (${T2}-${T_scale})/${loops} #temperature
    decrease at each step
variable superc_temp equal ${T2}-${decrease}

# begin the loop on supercooling steps
label superc_loop
variable i loop ${loops}

###################################
# FIXES
###################################
fix superc_fix mobile temp/rescale 1 ${superc_temp} ${superc_temp}
    0.012 1.0
fix nve_fix mobile nve

###################################
# OUTPUT
###################################
log           ${fullpath}/log.superc append
dump          superc_dump all atom ${loops} ${fullpath}/dump_superc.
    lammpstrj
dump_modify   superc_dump sort id append yes scale no

###################################
# ACTIONS
###################################
run 1 # single step

unfix superc_fix
unfix nve_fix
undump superc_dump
variable superc_temp equal  ${superc_temp}-${decrease}

next i
jump SELF superc_loop

variable loops delete
variable i delete
```

Setup the control regions:

```
###################################
# CONTROL REGIONS SETUP
###################################
variable ELDAR_start equal  $(v_z_side2-v_ELDAR_buffer_size) #
    lattice units
variable estart equal  $(v_ELDAR_start*v_lat_sp) #ELDAR_start_buffer
    in \AA
```

```
region ELDAR_left block 0.0  $(v_x_side) 0.0  $(v_y_side) EDGE - $(v_ELDAR_start) units lattice
region ELDAR_right block 0.0  $(v_x_side) 0.0  $(v_y_side)  $(v_ELDAR_start) EDGE units lattice
region ELDAR union 2 ELDAR_left ELDAR_right

group ELDAR_left dynamic all region ELDAR_left
group ELDAR_right dynamic all region ELDAR_right
group ELDAR dynamic all region ELDAR

group ELDAR2 region ELDAR

variable N_ELDAR_r_target equal  $(v_liquid_dens*v_x_side*v_y_side*(v_new_z_side2-v_z_side2+v_ELDAR_buffer_size)*v_elem_cell_vol)
variable N_ELDAR_l_target equal  $(v_liquid_dens*v_x_side*v_y_side*(v_new_z_side2-v_z_side2+v_ELDAR_buffer_size)*v_elem_cell_vol)

############################
# PARTICLES INSERTION
############################
variable excluded equal 3.808 #radius of the excluded spherical volume, in Angstrom, for the insertion of new atoms in the control regions

variable mySeed equal round(random(1,1000001,${seed_random}))
variable choice equal random(0,1,${seed_random})

#read the velocities of this new particles from external files, created via dedicated BASH scripts
#the velocities satisfy a Gaussian distribution at the chosen temperature
variable appo0 file ${fullpath}/vx70K.dat
variable appo1 file ${fullpath}/vy70K.dat
variable appo2 file ${fullpath}/vz70K.dat
```

And finally, run the proper simulation of the crystallization of the supercooled liquid:

```
############################
# OUTPUT
############################
compute_modify thermo_temp dynamic yes

dump nve_dump all custom 500 ${fullpath}/dump_nve.* id type x y z
dump_modify nve_dump sort id
log ${fullpath}/log.nve
thermo 10000
thermo_style custom step temp press pe ke etotal

fix PT_fix all ave/time 100 100 10000 c_thermo_press c_thermo_temp file ${fullpath}/PT.dat mode scalar

fix nve_fix mobile nve  #microcanonical time-integration
```

```
15
16 ############################
17 # ADAPTIVE THERMOSTAT
18 ############################
19 fix ELDAR_thermo ELDAR temp/csvr ${temp} ${temp} 2000 ${seed_random}
20
21 variable k index 0 1 2 3 4 5 6 7 8 9 10 11 12 13 14 15 16 17 18 #
       number of layers in the analysis region
22 region central_thermo block -${toler} $(v_x_side+v_toler) -${toler} $(
       v_y_side+v_toler) -$(0.75+v_toler+v_k*0.5) $(0.75+v_toler+v_k*0.5)
        units lattice
23 group central_thermo region central_thermo
24
25 variable z_hi equal $(zhi/v_lat_sp)
26 variable z_lo equal $(zlo/v_lat_sp)
27
28 variable endTime equal $(v_ada_thermo*18) #stop the action of the
       adaptive thermostat at this timestep
29
30 label final_loop
31 variable i loop 1100000
32
33 ###################################
34 # CONTROL REGIONS SETUP
35 ###################################
36 #  the barostat modifies the simulation box sides
37 region CTRL_REG_left delete
38 region CTRL_REG_right delete
39 region CTRL_REG delete
40 group CTRL_REG2 delete
41 region CTRL_REG_left block 0.0 $(v_x_side) 0.0 $(v_y_side) EDGE -$(
       v_CTRL_REG_start) units lattice
42 region CTRL_REG_right block 0.0 $(v_x_side) 0.0 $(v_y_side) $(
       v_CTRL_REG_start) EDGE units lattice
43 region CTRL_REG union 2 CTRL_REG_left CTRL_REG_right
44 group CTRL_REG2 region CTRL_REG
45
46 ###################################
47 # BAROSTAT SETUP
48 ###################################
49 fix press_fix CTRL_REG2 press/berendsen z 0.0 0.0 2000 modulus 4154.0
        dilate partial
50 variable CTRL_REG_natoms_r equal count(all,CTRL_REG_right) # count
       atoms of the 'all' group found in these regions
51 variable CTRL_REG_natoms_l equal count(all,CTRL_REG_left)
52 variable N_CTRL_REG_r_target equal $(v_liquid_dens*v_x_side*v_y_side
       *(v_z_hi-v_z_side2+v_CTRL_REG_buffer_size)*v_elem_cell_vol)
53 variable N_CTRL_REG_l_target equal $(v_liquid_dens*v_x_side*v_y_side
       *(-v_z_lo-v_z_side2+v_CTRL_REG_buffer_size)*v_elem_cell_vol)
54
55 variable trial equal 1000 #try to insert an atom this number of times
        per step
56
```

```
57 if "${choice} < 0.60" then "variable specie equal 1" else "variable
       specie equal 2" #chooe its species
```

Clearly, in the simulation of a pure system, this last command does not exist, and all the inserted particles have the same species than the others.

Here follows the trial of inserting atoms to compensate the removal of particles from the control regions due to the crystal growth, as well as the action of the adaptive thermostat.

```
1  ###################################
2  # APPLY BAROSTAT
3  ###################################
4  if "${CTRL_REG_natoms_r} < ${N_CTRL_REG_r_target}" then &
5  "next appo0" &
6  "next appo1" &
7  "next appo2" &
8  "fix insert_r mobile deposit 1 ${specie} 1 ${mySeed} region
       CTRL_REG_right near ${excluded} units box attempt ${trial} vx ${
       appo0} ${appo0} vy ${appo1} ${appo1} vz ${appo2} ${appo2}" &
9  else "fix insert_r mobile deposit 1 ${specie} 1 1 region
       CTRL_REG_right near 100.0 units box attempt 1"
10
11 if "${CTRL_REG_natoms_l} < ${N_CTRL_REG_l_target}" then &
12 "next appo0" &
13 "next appo1" &
14 "next appo2" &
15 "fix insert_l mobile deposit 1 ${specie} 1 ${mySeed} region
       CTRL_REG_left near ${excluded} units box attempt ${trial} vx ${
       appo0} ${appo0} vy ${appo1} ${appo1} vz ${appo2} ${appo2}" &
16 else "fix insert_l mobile deposit 1 ${specie} 1 1 region
       CTRL_REG_left near 100.0 units box attempt 1"
17
18 ###################################
19 # APPLY ADAPTIVE THERMOSTAT
20 ###################################
21 #progressive expansion of the thermostatted region
22 if "$i >= ${ada_thermo} && $(v_i%v_ada_thermo)==0 && $i<=${endTime}"
       then &
23 "unfix wall_thermo" &
24 "region central_thermo delete" &
25 "group central_thermo delete" &
26 "next k" &
27 "region central_thermo block -${toler} $(v_x_side+v_toler) -${toler}
       $(v_y_side+v_toler) -$(0.75+v_toler+v_k*0.5) $(0.75+v_toler+v_k
       *0.5) units lattice" &
28 "group central_thermo region central_thermo" &
29 "fix wall_thermo central_thermo temp/csvr ${temp} ${temp} 2000 ${
       seed_random}"
30
31 run 1 #run 1 step
32
```

```
33 variable mobileN equal count(mobile)
34 print "${CTRL_REG_natoms_r}, ${CTRL_REG_natoms_l}, ${
       N_CTRL_REG_r_target}, ${N_CTRL_REG_l_target}, ${mobileN}, ${z_lo},
        ${z_hi}" append ${fullpath}/CTRL_REG.dat
35
36 unfix insert_r
37 unfix insert_l
38 unfix press_fix
39 variable z_hi equal $(zhi/v_lat_sp)
40 variable z_lo equal $(zlo/v_lat_sp)
41
42 next i
43 jump SELF final_loop
44
45 write_restart ${fullpath}/restartFile #very useful in case of
       simulations that are too long and require restart
46
47 unfix CTRL_REG_thermo
48 unfix nve_fix
49 unfix PT_fix
```

Note that we run just 1 step at a time. Then, all the quantities have to be re-calculated: the actions of the barostat, in particular, changes step-by-step due to the fact that atoms enter into and exit from the control regions and the analyisis regions as well. At each step, the groups of atoms to which barostats/thermostats and all the other tools are applied change; this has to be taken into account.

Appendix C

Appendix: convert reduced LJ into physical units

LAMMPS allows for usage of *reduced* Lennard–Jones units and physical real units both. After the choice of the mapping between the reduced and physical values of ϵ, σ and m, every other quantity is determined. This Appendix contains a list of the useful conversion formulas and some typical orders of magnitude. See also https://lammps.sandia.gov/doc/units.html.

It is worth underlining that, throughout this work, reduced LJ units have been sometimes employed in the simulations, but never in the presentation of results. In any case, Lennard–Jones parameters for pure Argon have been chosen equal to 1; therefore, all the other reduced quantities are referred as scaled with respect to 100% Argon corresponding values.

For argon, as stated in the first Chapter of the present PhD thesis, the physical values chosen for ϵ, σ and m are 0.996 kJ/mol, 3.405 Åand 39.948 amu (i.e. $6.6335209E-26$ kg) respectively. Given that the corresponding values for krypton are: $\epsilon_{KrKr} = 1.33$ kJ/mol, $\sigma_{KrKr} = 3.636$ Åand $m = 83.798$ amu (i.e. $1.3914984E-25$ Kg), in reduced units these last quantities would be expressed as $\epsilon* = \frac{\epsilon_{KrKr}}{\epsilon_{ArAr}} = 1.335$, $\sigma* = \frac{\sigma_{KrKr}}{\sigma_{ArAr}} = 1.068$ and $m* = \frac{m_{Kr}}{m_{Ar}} = 2.1$.

To convert time from real units to reduced ones, remember that the reduced time is defined as: $\tau* = \sqrt{\frac{\epsilon}{m\sigma^2}}$, where ϵ, σ and m are the argon ones, in this work. Therefore, $\tau* = 1$ corresponds to a physical time of about 2.15 ps. A good MD simulation timestep is then around $\tau* = 0.001$, i.e. 2 fs.

Concerning pressure, $P* = P\frac{\sigma^3}{\epsilon}$ and $P* = 1$ equals about 421.5 bar.

The numerical density conversion is straightforward, considered that $\rho* = N/V*$, where $V*$ is the volume expressed in length reduced units. For pure argon, a reduced density equal to 1 implies a fcc lattice constant of 5.39716 Å.

Obviously, temperature is related to energy by a simple relation involving Boltzmann's constant k_B and then $T* = \frac{T k_B}{\epsilon}$, which means having $T* = 1$ at 120 K.

Appendix D

Appendix: LAMMPS input lattice constants

TABLE D.1: Input parameters for the simulations of the mixtures at various temperatures.

x_{Kr}	**T [K]**	a **[Å]**
1	40	5.67328
1	50	5.6916
1	80	5.75472
1	93.4	5.78828
1	103.4	5.81688
1	105.5	5.82288

x_{Kr}	**T [K]**	a **[Å]**
0.85	40	5.63644
0.85	50	5.65608
0.85	80	5.72408
0.85	97.2	5.7718
0.85	99.1	5.77936

x_{Kr}	**T [K]**	a **[Å]**
0.40	30	5.4774
0.40	35	5.48804
0.40	40	5.49912
0.40	50	5.52248
0.40	60	5.54816
0.40	65	5.56184
0.40	70	5.57628
0.40	76.2	5.59456
0.40	80	5.60828
0.40	82.4	5.61548
0.40	86.2	5.62952
0.40	87.2	5.63292

x_{Kr}	**T [K]**	a **[Å]**
0.15	40	5.4048
0.15	50	5.43032
0.15	60	5.45848
0.15	78	5.5144
0.15	79	5.52352

x_{Kr}	**T [K]**	a **[Å]**
0	30	5.3148
0	40	5.33916
0	55	5.38020
0	60	5.39548
0	64.7	5.41072
0	70	5.42916
0	74.7	5.4504
0	76	5.45044
0	80	5.46836

Appendix E

Appendix: Ising formulae for finite number of spins

We report here the exact formulae for the Ising thermodynamical properties discussed in Chapter 2, analytically calculated for a finite number of spins N_s in PBC. In this Appendix we again normalize energy and temperature to the coupling parameter U.

Starting from the simple expression for the first–neighbor Ising energy $E_I = -J \sum_{i=1}^{N_\mathrm{s}} \sigma_i \sigma_{i+1}$ (where the Bohr magneton μ_B is set equal to 1, and PBC are assumed), the partition function of the system can be easily derived, and the transfer matrix as well. Calling the eigenvalues of the transfer matrix λ_+ and λ_-, the free energy reads $F = -t \log(\lambda_+^{N_\mathrm{s}} + \lambda_-^{N_\mathrm{s}})$. Setting $\zeta = J/t$, all the thermodynamic properties can then be derived, such as the internal energy per spin in units of J:

$$\frac{\langle E_I \rangle}{J N_\mathrm{s}} = -\tanh\zeta \left(\frac{1 + \tanh^{N_\mathrm{s}-2}\zeta}{1 + \tanh^{N_\mathrm{s}}\zeta} \right), \tag{E.1}$$

the specific heat C_I in units of $k_B J^2$:

$$\frac{C_I}{k_B J^2} = \frac{1}{t^2 \cosh^2\zeta} \left[1 + \frac{\tanh^{N_\mathrm{s}}\zeta \,\mathrm{csch}^2\zeta}{(1+\tanh^{N_\mathrm{s}}\zeta)^2} \times \right. \\ \left. \times \left(N_\mathrm{s} - (1+\tanh^{N_\mathrm{s}}\zeta)\cosh(2\zeta) \right) \right] \tag{E.2}$$

the spin–spin correlation function:

$$g_i^\sigma = \frac{\sum_j \langle \sigma_j \sigma_{j+i} \rangle}{N_\mathrm{s}} = \tanh^i\zeta \left(\frac{1 + \tanh^{N_\mathrm{s}-2i}\zeta}{1 + \tanh^{N_\mathrm{s}}\zeta} \right), \tag{E.3}$$

and finally the magnetic susceptibility:

$$\chi_I = \frac{e^{2\zeta}}{t} \left(\frac{1 - \tanh^{N_\mathrm{s}}\zeta}{1 + \tanh^{N_\mathrm{s}}\zeta} \right). \tag{E.4}$$

Grazie

Mi fa un po' strano girarmi indietro, arrivato a questa tappa del cammino, e riguardare tutti questi anni. Ricordo molto bene il mio primo vero giorno in LCP, da neo-tesista triennale, 17 settembre 2014. Da allora, quella stanzetta è pian piano diventata casa, i suoi occupanti volti noti, poi compagni di lavoro e addirittura anche amici. Quella stanza ha spesso ospitato i miei amici, a volte alla ricerca di un luogo dove studiare, un caffè o due chiacchiere in compagnia. Sono contento e riconoscente di quel che è stato, e curioso di quel che sarà, nel lasciare questo posto dove ho imparato e sono cresciuto tanto. Sono grato di molte vicende capitate in questi sei anni e mezzo, e dell'incontro con tante persone in questi anni di dottorato. Mi ha impressionato scrivere per ciascuno il nome e, a volte, un po' del perchè. Sono in buona compagnia! Provo nelle prossime righe a ricordarvi tutti, non tanto per non far torto a nessuno, ma proprio per dire grazie a ciascuno di esserci stato, poco o tanto.

Grazie:

- alla mia famiglia. A **papà** e **mamma**, per avermi voluto, messo al mondo, cresciuto, educato, fatto diventare grande. Grazie mamma per le infinite e buonissime schiscie, i bottoni ricuciti, la pazienza, l'incoraggiamento quando le cose non andavano bene e i richiami alla necessità di far fatica quando ce n'è stato bisogno. Grazie perchè sei come le seconde linee e i flanker a rugby, che fanno un sacco di lavoro sporco, dietro le quinte. Grazie papà per l'affetto dietro l'apparenza burbera, per le pause caffè a casa a metà mattina, per le tasse, le questioni finanziarie che hai provato a spiegarmi, la storia medievale, la tua voce quando leggi un racconto. Grazie **Lucia**, sister. Come farei senza le tue battutacce? E senza la tua compagnia in tanti viaggi? Grazie per aver trovato la tua strada a un certo punto, perchè apprezzi il rugby e perchè ti si può spesso schiacciare un cinque senza ragioni particolari. Grazie ai miei quattro nonni: nonno **Vittorio** ormai in Cielo da tanto, così burbero ma sotto sotto affettuoso, nonna **Chicca** che lo hai raggiunto da poco (quante serate ti sei sorbita mentre facevo un sacco di baccano suonando coi miei amici, e quante caramelle mi hai portato mentre studiavo, solo o in compagnia). Grazie nonno **Franco** perchè negli ultimi anni hai provato a capire che cosa studiavamo io e Lucia e ti sei interessato a noi come potevi; grazie nonna **Maria** per la matematica, le circonferenze con la buccia del salame e i cerchi con le zucchine.

- grazie a te, **Davide**, che mi hai preso come tesista triennale nel lontano 2014. Ero un fisico in erba e tuttora so di avere molto da imparare. Grazie per avermi fatto crescere come fisico e come uomo, per avermi

mostrato che chi vive bene lavora bene e viceversa, che non c'è separazione tra come metti il cuore nel Monte Carlo e come lo metti davanti agli altri, dall'ultimo studente al professore ordinario. Grazie per avermi sopportato, corretto, lanciato in mille progetti. Grazie per le focaccine del 'Pizza a Pezzi', gli infiniti caffè, le mail nel cuore della notte. E infine, grazie per essere stato così libero con me da suggerirmi di andare a Padova a fare il post-doc, per la mia crescita e il mio bene. Lo apprezzo tantissimo.

- a **Robert Grisenti** per tutte le avventure in Germania, le mangiate al Birrificio di Lambrate, la tua passione per le cose buone e per la ricerca scientifica vera fatta con dedizione. Devo ringraziare anche tutti quelli del tuo gruppo che mi hai fatto conoscere: **Alex**, per il gran lavoro insieme, le notti di veglia a DESY e XFEL, le mega-cotolette ad Amburgo; **Claudia**, **Jan**, **Anton**, **Ruslan**, **Johannes**, **Luca** e tutti gli altri, inclusi i nostri amici spagnoli **Tiberio Ezquerra** e **Josè Ma Fernandez**.

- grazie al prof. **Santi Prestipino-Giarritta**, e al prof. **Peter Harrowell** per le loro correzioni alla mia prima versione della tesi, puntuali e attente. Grazie al prof. **Alberto Parola** per aver accettato di far parte della mia commissione.

- al prof. **Paolo Milani**, per avermi massacrato durante un esame tanti anni fa, avermi fatto capire che non sono uno sperimentale, e per dire sempre ciò che pensa, lasciando stare galateo e formalità. E per avermi ricordato che noi fisici siamo pagati per giocare coi Lego.

- al prof. **Tommaso Bellini**, per le domande inquiete e costanti, la voglia di capire, gli scorci ad allargare l'orizzonte.

- grazie al dott. **Davide Pini**, per il suo umorismo tagliente, l'autoironia, la fisica divertente e tutto il lavoro in collaborazione.

- grazie ai professori che in triennale prima e in magistrale poi sono stati più determinanti per me. **Maura Salvatori**, spietatamente precisa, **Elide Terraneo**, che mi ha mostrato che non tutti i professori di Analisi divorano gli studenti, **Dario Tamascelli**, per avermi spiegato che l'informatica non era mia nemica. E poi **Leonardo Carminati**, per il suo modo placido e chiaro di spiegare, **Gianluca Colò**, per il sorrisetto di chi si diverte quando spiega, come i mitici **Matteo Alaimo**, per la fisica dei supereroi, e **Giuseppe Bozzi**, pronto a raccogliere le nostre lacrime disperate durante la preparazione di Meccanica Quantistica. Grazie a **Gianluca Alimonti** e **Maurizio Maugeri**, per lo sguardo allargato sui fenomeni energetici e atmosferici, mia iniziale intuizione

di interesse, diventata poi passione (chissà se avessi intrapreso questa via alternativa da fisico...). Sono molto grato a **Guido Tiana** per i suoi bellissimi corsi di Fisica delle Proteine e Biofisica Computazionale, oltre che a **Bruno Bassetti** per il corso più divertente e l'esame più incredibile che abbia mai sostenuto. Grazie a **Giuliano Zanchetta** per tue belle ore di lezione durante il corso del primo anno al dottorato. Sono molto grato ai professori **Paolo Arosio**, **Alessandro Lascialfari** e **Cristina Lenardi** per avermo coinvolto nel campo del Machine Learning applicato alla Fisica Medica.

- **Matteo Mirigliano**, perchè negli anni abbiamo imparato a collaborare, per le chiacchierate sul futuro e la tua risata pulita.

- **Giovanni Nava**, per le discussioni sulla fisica della materia soffice, il tuo entusiasmo e la voglia di vedere coi tuoi occhi come si dispongono davvero le molecole su piccola scala. Ce la faremo!

- a chi ha passato almeno un po' del suo tempo nella grande famiglia di LCP. Grazie a **Ciccio**, grazie per avermi suggerito di fare un salto nell'ufficio di Davide molti anni fa. Grazie per la tua pronta assistenza quando c'è bisogno col computer, e per la tua scurrilità venata di genio. Grazie a **Mario** per avermi insegnato ad aprire la porta e cedere il passo, specialmente alle ragazze; grazie a **Gianluca**, per la tua ironia fine, la tua calma sicura quando lavori sulla fisica e per starci agli scherzi; ai membri storici **Maurizio** (il Santissimo MR), **Ettore** e **Filippo** e poi **Simo, Gabry, Marta, Martina, Ivan, Nicolò** e tutti gli altri, inclusi i nuovi arrivati **Christian** e **Davide**.

- ai miei tesisti (qualcuno che è stato anche in tesi con me, ma non solo, compare più in là nei ringraziamenti... non preoccupatevi). Grazie **Rodolfo**, per quel libro arrivato prima di Natale alcuni anni fa, segno inatteso della tua gratitudine per il lavoro insieme, mentre eri a piedi nel cuore della Siberia. Grazie **Fabio** per la tua placidità, **Tommaso** per essere stato così nerd da riuscire a insegnarmi qualche trucco al pc, **Daniele** così metodico e rilassato. Grazie **Matteo** (Tine) per la tua serietà e la passione nel lavoro. Grazie **Andrea** per la gita in Germania e la compagnia, l'ordine nell'esposizione e la serietà. **Marco**, come faremmo senza la tua macchinetta del caffè in LCP? **Michele**, grazie per le conversazioni sulla fisica e sulla vita, le risate, le battute a raffica, il lavoro serrato, il salame d'oca e l'avermi mostrato che esiste sempre un metodo alternativo per fare le cose (quale sprovveduto userebbe mai Power Point per fare una presentazione?). Grazie **Elisa** per l'incredibile estetica dei tuoi grafici, la tua gentilezza e la tua grinta negli studi.

- sono debitore di profonda riconoscenza e stima verso le due insegnanti che più mi hanno formato prima dell'università: la maestra **Giovanna Lilla**, per avermi letto ad alta voce le Cronache di Narnia, per avermi insegnato a scrivere i temi e per avermi fatto vivere in modo serio la scuola elementare. E la professoressa **Maria Adele Lavazzetti**, l'insegnante più decisa che abbia mai conosciuto, per il suo grande rigore, per la sua idea che a scuola si va per imparare e non per socializzare o altre cose strane, per l'assoluta mancanza di buonismo e il grandissimo affetto che ha avuto e ha nei miei confronti. Ricordo entrambe con stima e gratitudine.

- grazie a **Tiziana**, che in questi anni ho incrociato frequentemente la mattina presto mentre faceva le pulizie. Grazie per le chiacchiere, i sorrisi e il buonumore.

Sono moltissimi gli amici che voglio ringraziare, davvero non sono mai stato solo in questi anni. Grazie:

- **Samu** per essere sempre silenzioso e discreto, ma in prima linea, una spalla quando ce n'è bisogno. Grazie per avermi chiesto di farti da testimone e per la tua casa sempre aperta e perchè ogni tanto ti sei addirittura aperto con me. Grazie per come mi conosci anche negli angoli meno illuminati e per avermi richiamato indietro, tante volte in cui stavo per mollare tutto, specialmente un pomeriggio di tanti anni fa in cui la Meccanica Quantistica stava per sconfiggermi. Grazie (Maria) **Chiara**, per le chiacchierate, per avermi salvato a Parigi, per le cene.

- **Cap**, grazie per tutti i passi insieme, i libri, le playlist su Spotify, Euresis, il Capitano Grandi, l'Irlanda, la birra, la montagna, il Meeting, e tutte le altre faccende in cui ci siamo trascinati a vicenda. Non sarebbero le stesse senza di te. Low, lie the fields of Athenry ...

- **Luigi** per la tua intelligenza un po' caustica, per le chiacchierate sul nostro lavoro e sulla vita, la cucina buona e il tuo esempio con la CUSL. Il tuo biglietto di auguri natalizi coi Deep Greetings è appeso nella bacheca in camera mia! **Betta**: grazie per la tua serietà che ogni tanto si apre in risate di cuore, non avere paura, è una bella cosa ridere.

- **Pierh** o come cavolo si scrive, probabilmente non lo sai neppure tu. Per il tuo italiano goffo e caloroso, per i porciui estremi, la barba da monaco bizantino e le grandi bevute mentre si parla della vita.

- **Anna** e **Andre** (con **Alice** e **Matteo**!): so bene che siete due persone diverse, ma guardandovi vedo che cosa vuol dire che quando ci si sposa sul serio si diventa una cosa sola. Grazie per la nostra amicizia semplice,

di lunga data. Grazie per casa vostra, le cene, le risate, le vacanze e i consigli semplici e diretti.

- **Tommy** perchè mi hai insegnato la fedeltà, mi fai spesso ridere e per la tua precisione nello scandire il ritmo quando suoniamo.

- **Giò** per le schitarrate, la bici e gli snaffoli, i numeri primi, le favole e il rock and roll.

- **Nico**, perchè ti togli le scarpe in pubblico (e mi hai insegnato a farlo), hai un cuore enorme e mi fai ridere un sacco. Per la tua passione calcistica nell'affrontare ogni pezzetto di vita, per come gioisci e come te la prendi. Non ti è bastato lavorare con me a Milano, ora ti tocca sopportarmi anche a Padova!

- **Ale**, per la tua acidità divertente e l'amicizia implacabile, per il catechismo vissuto insieme quest'anno e il tuo grande affetto per ciò che hai davanti.

- **Simo**: calamaretto! Per la tua ironia e le mitiche schiscette. Per Aldo Baglio e le partite al due. **Nicol**: grazie per essere sempre stata diretta con me, tendenzialmente per contestare le mie idee, ma con sincerità e interesse. Cura il calamaretto!

- **Bira** per il due, il treno insieme, la cultura, il tuo essere un comunista cattolico di destra simpatico e buono. Grazie **Fra** (e Marti!) perchè anche se ti (vi) conosco poco non ti (vi) sento estranea (i). Verrò da voi per quella pizza! E che bello essere andati in gita insieme quest'inverno.

- **Matteo Luciani**: grazie per avermi fatto scoprire la Fisica (e la musica!) molti anni fa, in una notte stellata nella neve, con chitarra e vin brulè.

- **Mauro**, per la tua calma romana, e per la richiesta sincera e diretta di amicizia nata dentro Euresis e poi proseguita negli anni. Grazie perchè metti sul piatto tutto, desiderando in grande. Sono davvero contento di aver conosciuto anche tua moglie **Valeria**: bravo, tipa tosta!

- **Sbalki**, per il tuo cuore grande, perchè mi hai portato di peso in fondo a quella Macerata-Loreto e perchè fai il tifo per me. Grazie **Alessia** anche se ci conosciamo meno, per il tuo affetto e la tua amicizia.

- **Andrea, Deborah, Giovanni e Stefano**, per la vostra amicizia, l'accoglienza a braccia aperte e la scoperta della tenda in alta quota. T-hanks! (;-))

- **Cri e Teo**, per le grigliate, la vostra timidezza, l'amicizia che pian piano stiamo scoprendo. Per lo stinco, le wurstellate e perchè c'è sempre posto alla vostra tavola. E con voi, sono grato a **Botolo** per le chiacchiere, le risate, le grandi mangiate, la sua generosità da fuochi d'artificio e le infinite birre.

- **Guasta**, per la tua disponibilità fraterna, le birre rare ma importanti, la tua passione nel lavoro, le tue soluzioni tecniche brillanti.

- **Brio** per l'amicizia durata negli anni, ormai a centinaia di chilometri di distanza, ma non si molla. Come a rugby.

- **Sofia**: grazie per il tempo insieme, prima, durante e dopo. Per il treno e lo sci, e tutto il resto che sai. Non so bene perchè sia andata come è andata, ma grazie, davvero.

- al gruppetto che mi ha accompagnato per un bel po' a Fisica: a **Monica**, per i dolci, la tua disponibilità, le calze con le fragoline, perchè hai imparato a chiedere quando c'è bisogno e per la tua fede sincera (e brava per la Laurea!). A **Lore**, scusa per averti distrutto il lampadario in montagna urtandolo con la testa! Grazie perchè sei diretto e desideri cose belle. A **Jack** e **Michela**: Jack grazie per i libri, i passaggi, la tua placida tranquillità. Michi, non siamo così tanto amici, hai una personalità particolare, ma grazie per la grinta, per metterci la casa o l'appa quando serve e perchè non ti sei tirata indietro per giocare al due. A proposito, grazie a tutti per il due. **Dani**: grazie per le colazioni da Scaringi, perchè qualche volta mi hai recuperato per i capelli, grazie perchè la pensiamo diversamente su un mucchio di cose ma c'è sempre stato posto per me alle tue grigliate.

- grazie Astro**Marta** per la tua sincerità e per Bruce Springsteen.

- grazie **Cesare** e **Gabon** per farmi ridere, lo studio insieme, le cavolate e tutto questo tempo.

- alle matematiche: **Maria**, perchè sei un tornado e **Katia** perchè sei l'esatto opposto e perchè mi hai salvato al Meeting con le schiscie della tua mamma. **Irene** per il tuo animo chic che si mescola a un grande cuore, **Vale** per il tuo sorriso e la tua decisione nell'andare dietro a quel che conta.

- agli amici di Euresis, senza i quali anche il mio lavoro avrebbe un orizzonte ridotto. **Paolo** per le cene e i pranzi, il vino immancabile, i passaggi in macchina e le lunghe chiacchierate. **Elio** per la granita, la zuppa inglese e la tua fedeltà. **Benny**, perchè negli anni ho imparato ad apprezzarti, per la tua nettezza di giudizio e i piedi per terra. **Bino**,

per il modo chiaro, lucido e bello che hai di intervenire. **Carlo**, perchè ci riporti sempre al punto. Grazie anche a **Piero**, per i kiwi e gli aneddoti incredibili, **Mauro** per la tua disponibilità e a tutti gli altri, compreso **Alessandro Vato** che abbiamo incontrato per poco ma in modo intenso. Grazie **Sergio** per la tua ironia, la tua ospitalità, l'enorme numero di cose fatte bene che fai, la cena a Genova e la tua guida. Grazie **AZ**, perchè ci sei da sempre, sei appassionato e ami divertirti. Grazie **Nicola** per avermi invitato al direttivo tanti anni fa e per le numerose mostre preparate insieme, spinti dalla tua curiosità. Grazie a **Sergio**, **Mario**, **Aldo** e a tutti gli altri. Sono molto grato anche dei tantissimi incontrati in questi anni lavorando al Meeting, **Elena** di Padova per il tuo accento e le punzecchiature continue, **Michele** eroico nella fatica, **Chiara**, **Franci**, **Giulia**, **Lalla**, **Filippo**, **Gianni**, **Mario** e **Anna**, **Ettore** (mitico filosofo che sopravvive alla grande fra scienziati), **Marco**, **Assa**, **Filippo**, **Spugna** con le tue invenzioni superlative, mitico **Tullio** dal cuore grande, **Gianni**, **Desko** "Stakanov" e infine **Chiarina** e **Chicca** (le mie preferite, lo sapete). Grazie alla fantastica **Sara Mulone**, che traduce in disegni stupendi le nostre idee vaghe.

- sono estremamente grato di averti conosciuto, **Samir**, e di poter lavorare con te nei prossimi anni, con la tua incredibile curiosità per poter applicare ovunque gli strumenti del fisico. Non vedo l'ora di iniziare a tempo pieno!

- **Giulia**, per la tua lenta e paziente ricerca della verità, per la tua calma proverbiale che ci ha fatto e ci fa tanto ridere. Mi mancherai in Liguria, ma Giò ha la testa sulle spalle, fai bene a sposarlo! Invitateci al mare!

- grazie a tutti gli altri amici di Villasanta: **Rosy** e **Antonio**, **Franco** e **Luisa**, **Roberto** e **Chiara**, **Matteo** e **Marta**, **Cristian** e **Silvia**, **Edo** (volevo dire prof. Pacchetti!) e **Adele** perchè siete dei begli esempi di famiglie e di amici che camminano insieme. E grazie **Alby** per il Boss e la folle gita a Roma, **Cate** per la tua timidezza che nasconde una grande sensibilità e intelligenza, al **Fra Galimba**, per la nostra lunga amicizia, la tua calma rocciosa, la musica. Grazie **Simo Sala** per le chiacchierate sul dottorato e la tua impulsività piena di affetto alle cose. Grazie **Sabri** per l'organetto e le grigliate. A **Ludo**, che ho imparato ad apprezzare nel tempo, e a **Sofia** per la tua 'r' e il tuo affetto sincero. Grazie **Pietro** per i calzini pieni di stile, le tante domeniche pomeriggio in RSA e il tuo stile. Infine sono grato a **Jacques** per le sue incredibili barzellette.

- grazie a **Tiziano**, al **Maestro Villa**, **Bon**, **Cecco**, **Luca** e **Betti**, **Pinuccia** e tutti gli altri di Stand By Me, per questo luogo meraviglioso. L'importante è starci alle cose! Grazie alle mie piccoline diventate grandi, **Cate**, **Benny**, **Alice** e **Sara**.

- a **Davide Gandini** per gli sciatori, uno rosso e uno blu, seduti sull'orlo di un burrone...

- **Giorgio Frangi** per i tuoi messaggi di Natale, i libri, l'intelligenza.

- a **Francesco** e **Nicole** (con **Ginevra**!): grazie per tanti anni di amicizia, le discussioni infinite sull'attualità, il vostro sorriso.

- a **Pis** per le discussioni sull'informatica e la tua voce da basso.

- a tutti gli amici del **Coro Capitano Grandi** e in particolare ai veri **bassi**. Grazie a **Gio Pale**, **Nerd**, **Bubba**, **Merlo**, **Nello** e a tutti gli altri. Cantare con voi è stato spaziale.

- a **Lidia**, **Geoffroy** e la piccola **Elena**. Grazie Lidia per come mi hai accolto a Fisica e il tuo sincero affetto negli anni.

- a tutti gli amici dell'auletta: **Samu Geretti**, **Simo Dotti**, **Max**, **Monte**, **Bella**, **Tappo**, **il Diablo**, **Abbo**, **Enri**. E poi **Nonno Pozzi**, **Vigo**, **Gulco**, **Jashna** (mitico compagno di labo!), **Ciondolo**, **Gio Killer**, **Chiarina** e **Benny** e tutti gli altri che ho sicuramente dimenticato.

- grazie ai grandi di Fisica, solo negli anni ho capito quanto siete stati importanti. Grazie a **Frasa**, **Feo**, **Annina**, **C2**, **Agne**, **Male**, **Gaffo** e **Ambrogio**.

- ai miei ragazzi dell' **oratorio di Groppello**, perchè sto imparando a volervi bene e per la vostra spontaneità.

- ai mitici fratelli **Marì** e **Dario** Bonati, per essere così diversi. Grazie Marì per il tuo sorriso furbo, per come ti sei data da fare nella tua scuola e per i capelli colorati. Grazie Dario per la calma e l'arguzia.

- agli amici del calcetto, quanto mi mancate **Pier**, **Giulio**, **Ste**, **Paolino**, **Giaggia** e **Gitta**, vecchio amico e compagno di scuola e di oratorio. Che voglia di tornare sul campetto!

- sono molto grato a tutti gli amici incontrati l'anno scorso in Croce Rossa, che mi hanno dato una grande spinta nei difficilissimi mesi della scorsa primavera.

- a **Bruna** e **Pierangelo** per il catechismo da piccolo, le visite prima di Natale, i cioccolatini e le tirate d'orecchie anche se ormai io e Lucia siamo grandi.

- sono grato di essere stato accompagnato anche da **Graziella** e **Giovanni**. Grazie, Graziella, per la tua testimonianza enorme di fede nella prova. Sono grato di avere avuto Giovanni come padrino di cresima, grato per il salame, le gite che siamo riusciti a fare in montagna e il rosario a maggio nel vostro condominio. Grazie **Saverio** per l'informatica quando ero matricola e la tua infinita pazienza, grazie **Luca** (con **Camilla** e il piccolo **Samuele**) per i film piratati e le discussioni sulla scienza.

- grazie **Giuse** e **Antonio** per l'esempio roccioso e tenace che siete, per le Collette Alimentari, le cene e i pranzi da voi, la casa su Marte e il risotto alla zucca.

- grazie **Loredana** e **Alfredo**, per essere amici dei miei genitori, per gli enormi e immeritati regali, i fantastici Lindt natalizi e l'accoglienza di casa vostra, dalla quale si esce solo ingrassati di un paio di chilogrammi.

- a **Davide Forgia** per il Gran Gelato, il tuo essere un lavoratore infaticabile e le battute con cui accogli chiunque entri in gelateria. Nelle scoperte scientifiche che ho fatto in questi anni, il tuo gelato e il tuo esempio sono stati importanti.

- grazie ai tanti sacerdoti che ho incontrato negli anni. Grazie **don Dino**, per il tuo fare burbero, la testimonianza limpida e ragionevole, la tua voce solida e la tua grinta da guerriero anche in tarda età. Grazie **don Pietro** per come mi hai cresciuto, per le vacanze in Umbria, la passione per la montagna, il fuoco e l'ironia pungente. Sono grato di aver conosciuto la fede diretta e il modo amichevole di **don Alessio**, che ha per me un affetto immeritato che mi sorprende. Grazie **don Davide**, perchè è sempre bello venire a Forlì, per la musica, la storia, la Messa celebrata come si deve, le piade, il gelato e la tua infinita curiosità. A proposito, sono terribilmente grato anche per tutti gli amici forlivesi incontrati in questi anni, fra piadinate, gelati, musica e accoglienza calorosa: **Flavio, Federica e Ale**, **Sandro** mitico frequentatore delle mostre al Meeting, grande appassionato di musica e di bellezza, e tutti gli altri, soprattutto le famiglie **Pace**, **Soffiantini** e **Pizzol**. Grazie **don Marco**, per avermi accolto matricola tanti anni fa, per il tuo sorriso e la tua risata contagiosa. Grazie **don Cesare**, per il tuo cuore grande che si nasconde dietro le sembianze rudi da orso. Grazie soprattutto a **don Giacomo**, grazie per avermi accolto, per tutte le volte che mangiamo insieme, per quando con pazienza mi ascolti che ti racconto di aver

combinato le stesse sciocchezze. Per il catechismo, le passeggiate, le risate, lo sguardo lucido sul mondo. Grazie per la porta di casa tua sempre aperta, la preghiera, l'entusiasmo e la fede limpida. Grazie per la Villa, l'oratorio estivo, le serate di musica e giochi, ma soprattutto per guidarmi e accompagnarmi nella fede oggi.

- grazie a tutti gli altri che non saprei bene dove collocare, **Pepe**, **Patrick**, gli amici dell'**Iride**, tutte le famiglie dei miei amici che ho conosciuto per poco o tanto tempo.

- E infine, . . . sì, sì. Lo so. Cara **Fede**, avrai scorso questi ringraziamenti, avrai arricciato il nasino battendo il piede con impazienza meditando così "E io? Dove sono? Mi avrà dimenticata o, peggio, inclusa nei ringraziamenti confusa con qualcun altro?". In effetti, la pazienza è proprio una virtù che devi esercitare. Invece volevo dirti che con gli imprevisti, le torte, i giudizi chiari e netti, l'altruismo, i desideri su grande scala... beh, con questi sei a buon punto! Grazie per la pizza, perchè non lasci quasi mai neppure le briciole nel piatto, grazie per essere misteriosamente apparsa a un certo punto (forse non dovrei ringraziare te per questo ma più in alto...). Grazie per come vuoi bene agli amici (e perfino a me!). Grazie per avermi accompagnato in questi ultimi mesi a Milano (nonchè i primi insieme!), grazie per gli gnocchi al cavolo cappuccio rosso in fonduta di gorgonzola, per la tua risata cristallina e il tuo inconfondibile stile. Non ti avrei mai neppure considerata, ma intuisco che con te ogni cosa ha più intensità, più colore, mi si sono un po' riaperti gli occhi. È decisamente vero che le vie del Signore sono infinite... proprio tu?!

Chiudo queste pagine nella speranza, come scrisse Bilbo Baggins, che questo viaggio a Padova sia solo una 'andata e ritorno', per fare emergere il mio lato avventuroso. Gli Hobbit, e un po' anche alcuni fisici, non sembrano fatti per i salti verso l'ignoto, ma ogni tanto ci vuole qualcuno che dia loro 'una spintarella fuori dall'uscio'. There and back again.